Montanuniversität

Dissertation

Characterization of fatigue crack growth with the configurational force concept

Dipl.-Ing. Walter Ochensberger

Leoben, October 2015

Erich Schmid Institute of Materials Science
Austrian Academy of Sciences
Jahnstraße 12
A-8700 Leoben

Materials Center Leoben Forschung GmbH
Roseggerstraße 12,
A-8700 Leoben

Affidavit

I declare in lieu of oath,
that I wrote this thesis
and performed the associated research myself,
using only literature cited in this volume.

Walter Ochensberger
Leoben, October 2015

Dedication

To
Petra

Acknowledgements

This thesis has been carried out in the years between 2011 and 2015 during my occupation at the Materials Center Leoben (MCL) Forschung GmbH and the Erich Schmid Institute of Materials Science, Austrian Academy of Sciences.

Financial support by the Austrian Federal Government and the Styrian Provincial Government within the research activities of the K2 Competence Center on "Integrated Research in Materials, Processing and Product Engineering", under the frame of the Austrian COMET Competence Center Programme, is gratefully acknowledged (strategic projects A4.11-WP4 and A4.20-WP3).

I would like to express my deepest gratitude to my principal collaborator and supervisor Prof. Otmar Kolednik of the Erich Schmid Institute for the possibility to work as his PhD student, his excellent support and many valuable discussions.

In addition, I would like to thank Prof. Franz Dieter Fischer at the Institute of Mechanics, Montanuniversität Leoben, for his helpful advices and for acting as second examiner of my thesis.

Special thanks go to my colleagues at the MCL, Masoud Sistaninia, Darjan Kozic, Dr. Ronald Schöngrundner, René Hammer, Markus Mikl-Resch, Jürgen Maierhofer, Dr. Hans-Peter Gänser, who are responsible for pleasant working atmosphere and among which I have found not only excellent partners for discussions but also friends. Furthermore, Dr. Werner Ecker, MCL, is gratefully acknowledged for letting me be part of his team, Dr. Ronald Schöngrundner for support especially at the beginning of my work, and Dr. Guoxin Shan, Siemens VAI Metals Technologies GmbH, for providing the Python code for the configurational force post-processing.

I also would like to thank the staff of the Erich Schmid Institute, in particular Prof. Reinhard Pippan for very useful discussions and his interest in my work, Viktoria Schrutt, Johannes Zechner and Andreas Umgeher.

Finally, I thank my parents for enabling my studies and permanent support. I am especially grateful to my partner Petra for her patience and support during my time as PhD student. Without her encouragement, affection and tolerance, this thesis could not have been completed.

Walter Ochensberger, Leoben, October 2015

Abstract

This thesis deals with the characterization of crack propagation in cyclically loaded elastic–plastic materials in a new way, namely, by using the concept of configurational forces.

Crack extension under cyclic loads, i.e. fatigue crack growth, is the most common failure mechanism in engineering. In order to assess the lifetime of cyclically loaded components it is necessary to predict the growth rate of fatigue cracks. Cracks under low-cycle fatigue conditions and short fatigue cracks are of great practical importance, but cannot be treated with the conventional stress intensity range ΔK concept, since linear elastic fracture mechanics is not valid. An engineering approach is to apply the experimental cyclic J-integral ΔJ^{exp} in such cases. However, the conventional J-integral is based on deformation theory of plasticity, which is not applicable for cyclic loading and crack extension due to the non-proportional loading conditions. Therefore, severe doubts arise whether ΔJ^{exp} is appropriate to characterize the growth rate of fatigue cracks.

The concept of configurational forces provides an elegant solution to this problem, since it enables the derivation of a J-integral for real elastic–plastic materials with incremental theory of plasticity. This new type of J-integral, J^{ep}, keeps, in contrast to the classical J-integral, the physical meaning of a true thermodynamic driving force term in elastic–plastic materials and is applicable even under strongly non-proportional loading conditions. However, J^{ep} is, in general, path dependent.

The aim of the current thesis is to find out, how J^{ep} can be used for the evaluation of the driving force of a fatigue crack in elastic–plastic materials. A cyclic J-integral term ΔJ^{ep} is determined from the variations of J^{ep} during whole load cycles. The path dependence of J^{ep} is investigated by analyzing the distribution of configurational forces in two-dimensional fracture mechanics specimens with *long* cracks under cyclic Mode I loading. Hereby the configurational forces and the values of J^{ep} are computed by a post-processing procedure after a conventional finite element stress and strain analysis. Stationary and growing cracks are considered. Different load ratios, between pure tension and tension-compression loading are investigated. Loading parameters are varied in order to study the influences of contained and uncontained plasticity on the properties of ΔJ^{ep}.

The results provide a new, physically appropriate basis for the application of the J-integral concept for characterizing fatigue crack growth in the regime of non-linear fracture mechanics. It is shown that the experimental cyclic J-integral ΔJ^{exp}, which has been strongly challenged up to now, is correct for a stationary fatigue crack. It is not strictly correct, if the fatigue crack propagates. In addition, it is demonstrated that the new parameter ΔJ^{ep} is also able to accurately reflect crack growth retardation following a single overload. Moreover, in combination with a configurational force analysis, new insights are obtained into the most important mechanism for the overload effect, which is still a contentious issue among fatigue experts.

Kurzzusammenfassung

Die vorliegende Arbeit befasst sich mit einer neuen Art der Charakterisierung des Risswachstums in elastoplastischen Materialien unter zyklischer Belastung. Hierzu wird das Konzept der konfigurellen Kräfte (concept of configurational forces) verwendet.

Ermüdungsrisswachstum, d.h. Risswachstum unter zyklischer Belastung, ist der am häufigsten auftretende Schadensmechanismus. Um die Lebensdauer von zyklisch belasteten Bauteilen abzuschätzen, ist es notwendig, die Wachstumsrate von Ermüdungsrissen vorherzusagen. Die Bestimmung der Risswachstumsraten im Bereich der Kurzzeitfestigkeit (low-cycle fatigue) oder für kurze Ermüdungsrisse ist für die Praxis von großer Bedeutung. Dafür kann aber nicht die konventionelle Spannungsintensitätsschwingweite ΔK verwendet werden, weil die Voraussetzungen für die linear elastische Bruchmechanik nicht gegeben sind. Stattdessen wird das experimentelle zyklische J-Integral ΔJ^{exp} angewandt. Allerdings basiert das konventionelle J-Integral auf der Deformationstheorie der Plastizität, die aber aufgrund der nichtproportionalen Belastungsbedingungen bei zyklischer Belastung und Rissfortschritt nicht verwendet werden darf. Dies hat zu starken Bedenken an der Gültigkeit von ΔJ^{exp} zur Charakterisierung der Risswachstumsrate bei der Ermüdung geführt.

Das Konzept der konfigurellen Kräfte bietet eine elegante Lösung für dieses Problem, da es die Herleitung eines J-Integrals für „reale“ elastoplastische Materialien mit inkrementeller Plastizitätstheorie ermöglicht. Dieses neue J-Integral, J^{ep}, hat—im Unterschied zum klassischen J-Integral—die physikalische Bedeutung einer wahren treibenden Kraft in elastoplastischen Materialien und ist auch unter stark nichtproportionalen Belastungsbedingungen anwendbar. Allerdings muß man berücksichtigen, dass J^{ep} vom Integrationsweg abhängt.

Das Ziel dieser Dissertation ist herauszufinden, wie man J^{ep} für die Bestimmung der treibenden Kraft eines Ermüdungsrisses anwenden kann. Dazu wird aus der Variation von J^{ep} in einem vollständigem Lastzyklus ein zyklischer J-Integralterm ΔJ^{ep} bestimmt. Die Wegabhängigkeit von J^{ep} wird mittels Analyse der Verteilung der konfigurellen Kräfte in zweidimensionalen Bruchmechanikproben mit *langen* Rissen unter zyklischer Mode I Belastung untersucht. Die konfigurellen Kräfte und die J^{ep}-Werte werden mit einer Post-Processing Routine nach einer konventionellen Finiten Elemente Analyse berechnet. Stationäre und wachsende Risse werden betrachtet. Verschiedene Lastverhältnisse, vom Zugschwell- bis zum Zug-Druckbereich, werden untersucht. Die Belastungshöhe wird variiert, um den Einfluss der Größe der plastischen Zone auf die Eigenschaften von ΔJ^{ep} zu studieren.

Die Ergebnisse liefern die Grundlage für die physikalisch korrekte Anwendung des J-Integrals zur Beschreibung der Risswachstumsrate bei Ermüdung im Bereich der nichtlinearen Bruchmechanik. Es wird gezeigt, dass das experimentelle zyklische J-Integral ΔJ^{exp}, welches seit langem stark umstritten ist, für stationäre Ermüdungsrisse korrekt ist. Es ist aber nicht ganz korrekt, wenn der Ermüdungsriss wächst. Zusätzlich wird gezeigt, dass der neue Parameter, ΔJ^{ep}, auch die Risswachstumsverzögerung nach einer einzelnen Überlast mit hoher Genauigkeit beschreiben kann. Darüber hinaus erhält man sogar neue Erkenntnisse über

den wichtigsten *Mechanismus* für den Überlasteffekt, was noch immer ein brisantes Thema unter Ermüdungsexperten ist.

Content

Nomenclature

Vector and tensor notation

Scalars are denoted by lightface letters, *vectors* by lowercase boldface letters (with the exceptions of the reference coordinate $\mathbf{X}$ and the *J*-integral vector $\mathbf{J}$), and *tensors* by uppercase boldface letters (with the exceptions of the Cauchy stress tensor $\boldsymbol{\sigma}$ and the linear strain tensor $\boldsymbol{\varepsilon}$). A dot, as in $\mathbf{a}\cdot\mathbf{b}=a_i b_i$, with summation of repeated indices, designates the *inner product* of vectors; a dot, as in $\mathbf{A}\cdot\mathbf{B}=A_{ij}B_{ij}$ designates the inner product of tensors. The expressions $(\mathbf{Aa})_i=A_{ij}a_j$ and $(\mathbf{AB})_{ij}=A_{ik}B_{kj}$ denote *matrix products*. The expression $\mathbf{A}:\boldsymbol{\Lambda}$, with $\mathbf{A}$ as second-order and $\boldsymbol{\Lambda}$ as third-order tensor, gives a *vector* defined by $(\mathbf{A}:\boldsymbol{\Lambda})_k=A_{ij}\Lambda_{ijk}$.

List of parameters

a	actual crack length
a_0	initial crack length
Δa	crack extension
$\Delta(\Delta a)$	incremental crack extension during a single load cycle
Δa_d	delay distance after an overload
Δa_OL	total crack growth distance affected by an overload
$\Delta a_{r\mathrm{pl,OL}}$	distance where active plastic zone has escaped from the overload plastic zone
A	area below load–displacement (F–v) curve
ΔA	area below a single loading (or unloading) branch of F–v-curve
ΔA_n	element area corresponding to a specific node n in a finite element mesh
b	ligament length
B	specimen thickness
$\mathcal{B}$	body in (deformed) current configuration
$\mathcal{B}_0$	body in (undeformed) reference configurationan
$\partial\mathcal{B}$	boundary of $\mathcal{B}$
$\mathbf{C}$	(second rank) configurational stress tensor
C_p	plasticity influence term
$\mathrm{d}a/\mathrm{d}N$	fatigue crack growth rate
$\mathcal{D}$	part of deformed body $\mathcal{B}$, e.g. bounded by integration contour Γ
$\mathcal{D}_0$	part of undeformed body $\mathcal{B}_0$
$\mathcal{D}_r$	disk (area) of radius r centered at crack tip
$\mathcal{D}(t)$	migrating control volume in a body
$\partial\mathcal{D}$	boundary of $\mathcal{D}$
$\mathbf{e}$	unit vector in nominal crack growth direction
E	Young's modulus
$\mathbf{f}$	bulk configurational force vector
$\mathbf{f}_\mathrm{S}$	surface configurational force

$\mathbf{f}_{\text{tip}}$	configurational force emanating from the crack tip
$\mathbf{f}_{\Sigma}$	configurational force emerging on an interface
$\mathbf{f}^{\text{def.pl}}$	configurational force for deformation plasticity
$\mathbf{f}^{\text{ep}}$	incremental plasticity bulk configurational force
f_x^{ep}	x-component of $\mathbf{f}^{\text{ep}}$-vector
f_y^{ep}	y-component of $\mathbf{f}^{\text{ep}}$-vector
$\mathbf{f}^{\text{nlel}}$	nonlinear elastic configurational force
F	loading force
ΔF	applied load amplitude, $\Delta F = F_{\max} - F_{\min}$
F_{cl}	crack closure load, i.e. where crack flank contact appears during unloading
F_{op}	crack opening load, i.e. where crack flank contact disappears during re-loading
$F_{\delta_t=0}$	crack *tip* opening load at time $t_{\delta_t=0,\text{op}}$
F_{OL}	magnitude of overload
$\mathbf{F}$	deformation gradient tensor
G	elastic energy release rate
H	height of Compact Tension specimen
$\mathbf{I}$	identity tensor
J	conventional J-integral
$\mathbf{J}$	J-integral vector
ΔJ	cyclic J-integral, $\Delta J = J_{\max} + J_{\min} - 2\sqrt{J_{\max} J_{\min}}$
J_{tip}	near-tip J-integral
J_{Γ}	J-integral evaluated for an arbitrary contour Γ
J_{far}	far-field J-integral or driving force inserted into the specimen by the applied load
J_{actPZ}	J-integral evaluated for a contour Γ_{actPZ} around the *active* plastic zone
J_{PZ}	J-integral evaluated for a contour Γ_{PZ} around the *total* crack tip plastic zone
J^{ep}	incremental plasticity J-integral for elastic–plastic materials
$\Delta J_{\text{actPZ}}^{\text{ep}}$	driving force for *growing* fatigue cracks
$\Delta J_{\text{PZ}}^{\text{ep}}$	driving force for *stationary* fatigue cracks
J^{exp}	experimental J-integral evaluated from the load–displacement (F–v) curve
ΔJ^{exp}	experimental cyclic J-integral
J^{nlel}	nonlinear elastic J-integral
J^{VCE}	ABAQUS J-integral calculated via virtual crack extension method
K	stress intensity factor
K_{op}	stress intensity factor at F_{op}
ΔK	stress intensity factor range, $\Delta K = K_{\max} - K_{\min}$
ΔK_{eff}	effective stress intensity fator range, $\Delta K_{\text{eff}} = K_{\max} - K_{\text{op}}$
$l_{\text{proc.z}}$	length of process zone
m	Finite Element mesh size
$\mathbf{m}$	unit normal vector in the reference configuration
n	average strain hardening exponent
$\mathbf{n}$	unit normal vector in the current configuration
N	load cycle number

$\mathbf{p}$	unit normal vector to the crack flank
$\mathcal{P}$	potential energy
r	distance from the crack tip
r_{pl}	plastic zone radius
$r_{\mathrm{pl,cyc}}$	radius of cyclic plastic zone
$r_{\mathrm{actPZ},y}$	extension of active plastic zone in y-direction
R	load ratio, $R = F_{\min} / F_{\max}$
R_{OL}	overload ratio, $R_{\mathrm{OL}} = F_{\mathrm{OL}} / F_{\max}$
$\mathbf{S}$	first Piola–Kirchhoff stress
t	time
t_{cl}	crack closure time
t_{op}	crack opening time
$t_{\delta_{\mathrm{t}}=0,\mathrm{cl}}$	crack *tip* closure time
$t_{\delta_{\mathrm{t}}=0,\mathrm{op}}$	crack *tip* opening time
$\mathbf{t}$	surface traction vector
$\mathbf{u}$	displacement vector
u_y	displacement in y-direction
$\mathcal{U}$	strain energy
v	load-line displacement
$\mathbf{v}$	material point velocity in reference configuration
$\mathbf{v}_{\mathrm{tip}}$	crack tip velocity
$\mathbf{w}$	material point velocity in current configuration or motion velocity
W	specimen width
$\mathcal{W}$	working rate
$\mathbf{x}$	position vector in the current coordinate system (x, y, z)
$\mathbf{X}$	position vector in the reference coordinate system (X, Y, Z)

Greek symbols

Γ	arbitrary integration contour for the evaluation of the J-integral
Γ_r	contour at distance r around crack tip
Γ_{tip}	contour around the crack tip
$\Gamma_{\mathrm{proc.z}}$	contour around the process zone
Γ_{actPZ}	contour around the active plastic zone of the current crack tip
Γ_{PZ}	contour around the total crack tip plastic zone
Γ_{far}	far-field contour
δ_{t}	crack tip opening displacement
$\Delta\delta_{\mathrm{t}}$	cyclic crack tip opening displacement, $\Delta\delta_{\mathrm{t}} = \delta_{\mathrm{t,max}} - \delta_{\mathrm{t,min}}$
Δ_j^i	relative difference betweentwo values i and j
ε	(engineering) strain
$\Delta\varepsilon$	cyclic strain or strain range
ε_{e}	elastic strain

ε_{p}	plastic strain
$\varepsilon_{\mathrm{eq}}^{\mathrm{p}}$	equivalent plastic strain (PEEQ in ABAQUS)
$\boldsymbol{\varepsilon}$	linear strain tensor
η	nondimensional geometry factor for evaluation of J^{exp} and ΔJ^{exp}
ν	Poisson's ratio
σ	(engineering) stress
$\Delta\sigma$	cyclic stress or stress range
$\boldsymbol{\sigma}$	Cauchy stress tensor
σ_{xx}	normal stress component in x-direction
σ_{yy}	normal stress component in y-direction
σ_{eq}	equivalent stress or von Mises stress
σ_{u}	ultimate tensile strength
σ_{y}	yield stress
ϕ	strain energy density or (Helmholtz) free energy per unit volume
ϕ_{e}	elastic (reversible) part of strain energy density
ϕ_{p}	plastic (dissipated) part of strain energy density
ψ_{tip}	dissipation due to crack tip propagation
ψ_{bulk}	bulk dissipation per unit volume

Acronyms

CL	subscript denoting constant cyclic loading
conv	superscript denoting the conventional J-integral
contact	superscript denoting that crack flank contact is considered in the simulation
CT	Compact Tension (specimen)
E–PFM	elastic–plastic fracture mechanics
FE	Finite Element
gy	general yielding
HRR	Hutchinson-Rice-Rosengren (crack tip field)
LCF	low-cycle fatigue
LEFM	linear elastic fracture mechanics
lsy	large-scale yielding
OL	subscript denoting cyclic loading with a single overload
overlap	superscript denoting crack flank overlap, i.e. without crack flank contact
sly	severe ligament yielding
ssy	small-scale yielding

“Alles in der Welt endet durch Zufall und Ermüdung”
“Everything in the world ends by chance and fatigue”

Heinrich Heine, 1797–1856

1 Introduction

This thesis is an output of a strategic project within the Austrian COMET Competence Center Programme. The main objective of the project was to develop a new computational tool for the physically correct evaluation of the crack driving force in cyclically loaded elastic–plastic materials, in order to characterize the growth rate of fatigue cracks. The rationale was to apply the concept of configurational forces (e.g. Maugin 1995, Gurtin 2000), from the field of mechanics, and the *J*-integral concept from the regime of non-linear fracture mechanics.

The conventional *J*-integral (Rice 1968a,b) is commonly applied to describe crack growth when the material exhibits in general a nonlinear behavior, e.g. if crack growth is accompanied by significant plastic deformation (see e.g. Anderson 1995). It is well known that two fundamental conceptual difficulties appear when the conventional *J*-integral is applied to elastic–plastic materials:

- *J* does not provide a real thermodynamic driving force term in elastic–plastic materials (Rice 1968a,b),
- *J* is not applicable under non-proportional loading conditions, e.g. if unloading processes occur in the material, such as during crack extension and for cyclic loading (Rice 1968a,b; Anderson 1995).

The reason for these restrictions is that the conventional *J*-integral relies on the assumption of deformation theory of plasticity, i.e. the elastic–plastic material is idealized to behave nonlinear elastic. Despite these restrictions for the *J*-integral, an experimental cyclic *J*-integral ΔJ^{exp} is often used as crack driving force parameter to describe fatigue crack growth in cases where linear elastic fracture mechanics and the conventional stress intensity range ΔK are not applicable. But, this appears highly questionable (e.g. Anderson 1995, Suresh 1998).

The concept of configurational forces enables the derivation of the *J*-integral without restrictions regarding constitutive assumptions of the material (e.g. Simha et al. 2003). Using this concept, Simha et al. (2008) have derived the *J*-integral for elastic–plastic materials with incremental theory of plasticity. This new type of *J*-integral, called J^{ep}, overcomes the restrictions of the conventional *J*-integral:

- J^{ep} has the physical meaning of a true driving force term in elastic–plastic materials,
- J^{ep} is applicable even for strongly non-proportional loading conditions, which are inevitable during fatigue crack growth.

However, one has to bear in mind that J^{ep} is, in general, path dependent. Therefore, analyses on the path dependence of J^{ep} are required in order to find the appropriate integration path for the description of the crack driving force in elastic–plastic materials.

In a preceding PhD thesis, Schöngrundner (2011) studied the path dependence of J^{ep} for stationary and growing cracks in monotonically loaded elastic–plastic materials. Based on this work, Kolednik et al. (2014) demonstrated the usefulness of J^{ep} for the assessment of crack growth and fracture. Moreover, Kolednik et al. (2014) have shown that the J^{ep}-integral enables us to shed new light on the fundamental problems of the conventional J-integral for elastic–plastic materials: It has been demonstrated that the conventional J-integral J and the J^{ep}-integral complement each other, so that J remains useful if certain conditions are fulfilled.

The current thesis presents comprehensive case studies for cyclic loading in order to elucidate how J^{ep} shall be used for the evaluation of a cyclic J-integral ΔJ^{ep}, which characterizes the fatigue crack growth rate. The differences to and the usefulness of the conventional J-integral for fatigue will be also discussed.

The main questions the thesis will address in detail are:

1) How does J^{ep} change during a load cycle?
2) How should the cyclic J-integral ΔJ^{ep} be evaluated and can it be used for the characterization of fatigue crack growth when the conventional stress intensity range ΔK is not applicable?
3) Is the application of the experimental cyclic J-integral ΔJ^{exp} correct?

In practice, materials and structural components are often subjected to variable cyclic loading. Therefore, another main question of the thesis is:

4) Is the new parameter ΔJ^{ep} able to characterize crack growth retardation after a single tensile overload?

Questions 1) – 3) will be worked out first for *stationary* cracks, then for *growing* cracks that are cyclically loaded. Question 4) can be answered only in the context of growing fatigue cracks.

The thesis is structured in two parts: In Part I, first some fundamentals on continuum mechanics, fracture mechanics and configurational forces are presented (Sections 2–4). Subsequently, Section 5 presents the application of the incremental plasticity J-integral J^{ep} for the description of the crack driving force in elastic–plastic materials under monotonic loading. In Part II, first the answers to questions 1) – 4) are worked out, Sections 6–8. Each of these sections contains a peer reviewed journal article: Paper I and Paper II have already appeared in *International Journal of Fracture*; Paper III was sent to *International Journal of Fatigue* and has received excellent reviews. Preliminary remarks to these papers provide a brief description, which questions are answered in the following paper. The numbers of the equations, figures and tables have been changed according to the section number in the thesis.

The individual reference section of each paper has been removed and included into the reference section of this thesis. Section 9 discusses open questions that arise from the papers and provides proposals for ongoing work. Section 10 provides a summary of the main conclusions of the thesis.

Part I

Theoretical basis and review of the application of configurational forces in fracture mechanics

2 Fundamentals of continuum mechanics

Before we deal with fracture mechanics and configurational forces it is necessary to set a common continuum mechanical basis. For the sake of brevity detailed calculations are omitted and the reader is referred to the cited literature. Comprehensive treatments on continuum mechanics can be found in classical textbooks, e.g., by Truesdell and Noll (1965), Malvern (1969), Gurtin (1982), Marsden and Hughes (1983), Chadwick (1999), or Bonet and Wood (2008). Direct (coordinate-free) notation is used for the mathematical expressions in this thesis. The notation is briefly specified in Gurtin (2000) and the section titled "Nomenclature" of the current thesis.

2.1 Large strain theory

Continuum mechanics deals with the deformation of bodies under stress. For the description of deforming bodies the notion of *reference-* and *current* (or *actual*) *configuration* is essential. Assume an unloaded, homogeneous body $\mathcal{B}_0$ at initial time $t_0 = 0$ (Fig. 2.1). $\mathcal{B}_0$ is considered to be an assemblage of material points characterized by their coordinates $\mathbf{X}$, with respect to a global coordinate basis.[1] If $\mathcal{B}_0$ is subjected to external or internal stresses, it will deform accordingly into $\mathcal{B}$, at time $t \neq 0$. In $\mathcal{B}$, the material points are described by their current position $\mathbf{x}$. The unloaded and deformed configurations, $\mathcal{B}_0$ and $\mathcal{B}$, are denoted as reference (also *Lagrangian*) and current (also *Eulerian*) configuration (e.g. Bonet and Wood 2008).

The family of configurations that change with time t is called *motion* (Chadwick 1999). The motion is described by a nonlinear one-to-one mapping between reference and current material point positions (e.g. Bonet and Wood),

$$\mathbf{x} = \mathbf{x}\left(\mathbf{X}, t\right). \tag{2.1}$$

If t is held fixed, Eq. (2.1) represents a mapping between reference- and current configuration. For a fixed material point with position $\mathbf{X}$, Eq. (2.1) describes the motion or trajectory against time of the respective material point, see dashed line in Fig. 2.1 (Bonet and Wood 2008).

The velocity $\mathbf{w}$ of a material point is defined as the rate of change with time of the position $\mathbf{x}$, also designated by a superposed dot,

$$\mathbf{w} = \dot{\mathbf{x}} = \frac{\partial \mathbf{x}}{\partial t}; \tag{2.2}$$

the velocity of the same material point in the reference configuration is $\mathbf{v} = \dot{\mathbf{X}} = \partial \mathbf{X} / \partial t$.

[1] In this thesis, rectangular Cartesian coordinates are used.

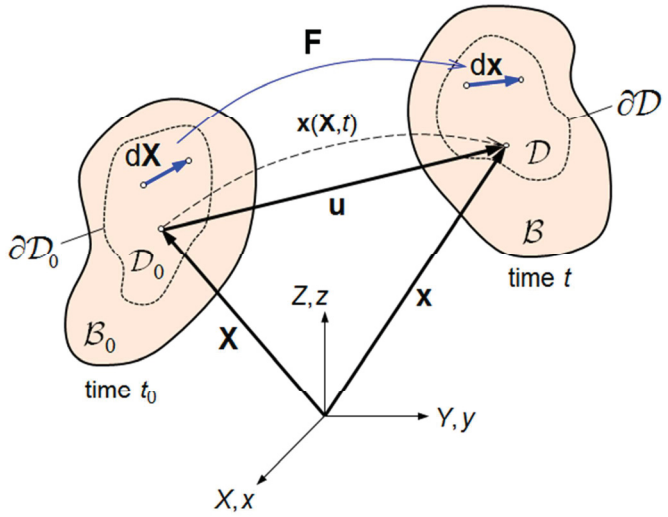

Fig. 2.1 Reference configuration $\mathcal{B}_0$ at time t_0 and current configuration $\mathcal{B}$ at time t of a deformable body. The nonlinear deformation map $\mathbf{x}=\mathbf{x}(\mathbf{X},t)$ maps at time t a material point position $\mathbf{X}$ of $\mathcal{B}_0$ onto the current position $\mathbf{x}$ on $\mathcal{B}$. Accordingly, the deformation gradient tensor $\mathbf{F}$ maps line elements of $\mathcal{B}_0$ on tangent vectors of $\mathcal{B}$ via $\mathrm{d}\mathbf{x} = \mathbf{F}\,\mathrm{d}\mathbf{X}$.

Analogously to the mapping of $\mathbf{X}$ onto $\mathbf{x}$, it is possible to describe the relative position of two neighboring material points after deformation, $\mathrm{d}\mathbf{x}$, with respect to their position before deformation, $\mathrm{d}\mathbf{X}$ (Fig. 2.1). The line segments $\mathrm{d}\mathbf{x}$ and $\mathrm{d}\mathbf{X}$ are related by the deformation gradient tensor $\mathbf{F}$ (e.g. Bonet and Wood 2008),

$$\mathbf{F} = \frac{\partial \mathbf{x}}{\partial \mathbf{X}} = \mathbf{1} + \nabla \mathbf{u}\,. \tag{2.3}$$

The parameter $\mathbf{F}$ enables a mapping of line elements from the reference into the current configuration and is the key quantity for the description of large deformations (*large strain theory*) and hence *strain*. For frequently used strain measures see, for example, Truesdell and Noll (1965) or Bonet and Wood (2008). In Eq. (2.3), the symbol ∇ is the Lagrangian gradient operator and $\nabla\mathbf{u}$ denotes the gradient of the displacement $\mathbf{u} = \mathbf{x} - \mathbf{X}$ (Fig. 2.1).

In large strain theory, no assumptions are made about the magnitude of the displacement $\mathbf{u}$. This means that $\mathbf{u}$ can be large in comparison to the dimensions of the body. Large strain theory is used in the current work, since the crack tip region undergoes large deformations during the loading process.

2.2 Stress

External forces acting on a body produce internal forces so that each part of the body is in a state of static equilibrium (Bonet and Wood 2008). Consider a cut-off part of body $\mathcal{B}$, Fig. 2.1, and a point located on a small area element $\mathrm{d}a$ on the cut surface (Fig. 2.2a); $\mathbf{n}$ designates the

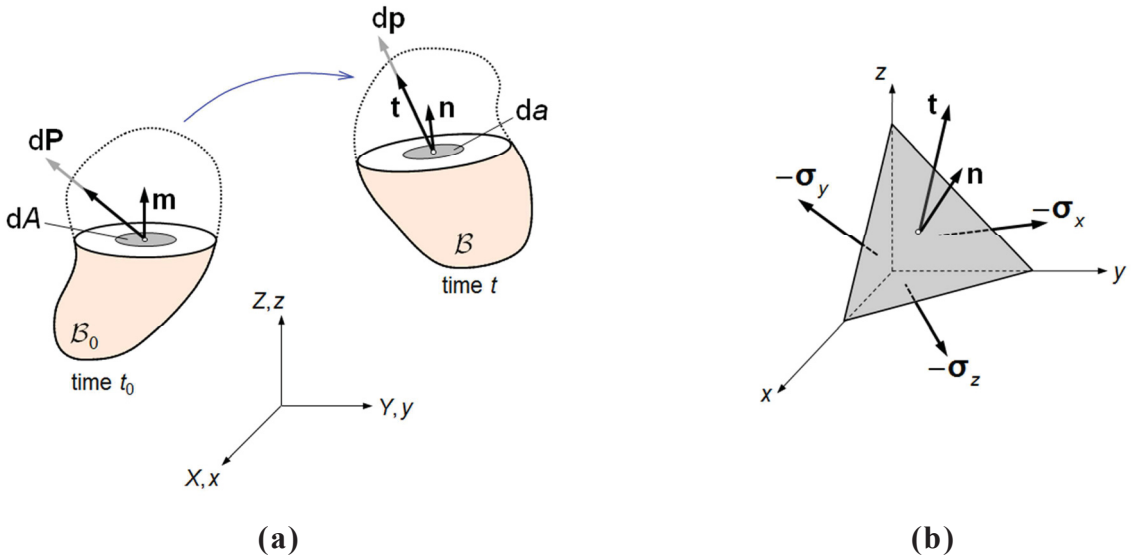

(a) **(b)**

Fig. 2.2 **(a)** Cut-off parts of $\mathcal{B}_0$ and $\mathcal{B}$. Reaction forces d**P** and d**p** act on the cut surface in order to fulfill the state of static equilibrium. **(b)** Cauchy tetrahedron with surface traction **t** acting on the cut surface. The existence of a bulk stress tensor $\boldsymbol{\sigma}$ becomes clear from the force balance.

outward unit normal vector to da. The surface traction **t** is given by the limit of the ratio $\mathrm{d}\mathbf{p}/\mathrm{d}a$ as da tends to zero; d**p** is the reaction force corresponding to da, see Bonet and Wood (2008). The existence of a bulk stress tensor arises from the balance of deformational forces on the Cauchy tetrahedron (Fig. 2.2b). The idea is to do three linearly independent cuts around a material point whereby **t** acts on the surface (e.g. Bonet and Wood 2008). From this balance the relationship between the Cauchy stress tensor $\boldsymbol{\sigma}$ and the surface traction vector **t** can be derived,

$$\mathbf{t} = \boldsymbol{\sigma}\,\mathbf{n}\,. \tag{2.4}$$

The Cauchy stress tensor $\boldsymbol{\sigma}$ completely defines the stress state of a material point in the current configuration. It is the stress that arises in response to deformation and relates, loosely speaking, the current element of force d**p** to the currently deformed area element, $\mathrm{d}\mathbf{a} = \mathbf{n}\,\mathrm{d}a$ (Fig. 2.2a). Therefore, $\boldsymbol{\sigma}$ is also called the *true stress* (Bonet and Wood 2008).

It is possible to define different stress measures with respect to the configuration. The first Piola–Kirchhoff stress, **S**, relates the element force vector d**p** in the current configuration to the undeformed area element of the reference configuration, d**A** (Fig. 2.2a). The traction is obtained by $\mathbf{t} = \mathbf{S}\,\mathbf{m}$, with **m** as the unit normal vector to the area element dA in the reference configuration. The first Piola–Kirchhoff stress and the Cauchy stress tensor are related by (Bonet and Wood 2008),

$$\mathbf{S} = J\,\boldsymbol{\sigma}\,\mathbf{F}^{-\mathrm{T}}\,; \tag{2.5}$$

J denotes the determinant of the Jacobian, $J = \det(\mathbf{F})$, and $\mathbf{F}^{-\mathrm{T}}$ the transposed of the inverse of $\mathbf{F}$.

The second Piola–Kirchhoff stress, $\mathbf{T}$, relates forces in the reference configuration, d$\mathbf{P}$, to areas in the reference configuration, d$\mathbf{A}$. Note that $\mathbf{T}$ has no real physical meaning, however, it is useful for the formulation of constitutive models; see Bonet and Wood (2008) for details.

For the description of crack growth with configurational forces, a description of the stresses in reference configuration, i.e. with first Piola–Kirchhoff stress, is necessary, see Section 4.

2.3 Balance laws

Balance laws are essential for the understanding of the theory of configurational forces. The five balance laws in continuum mechanics are: the balance of mass, of linear and angular momentum, the first and the second law of thermodynamics.

Since the transformation between first Piola–Kirchhoff stress and Cauchy stress, Eq. (2.5), lead to equivalent relations for the reference- and current configuration, the balance laws are only presented for upcoming reference configuration. For detailed derivations see e.g. Malvern (1969) or Bonet and Wood (2008).

It should be noted that, in contrast to constitutive relations (Section 2.5), balance laws are *universal* and not restricted to certain classes of materials.

Balance of mass

The balance, or conservation of mass postulates that the mass of a closed system cannot change if there is no transfer of mass (or energy) over the system boundary (Malvern 1969).

Balance of linear momentum

Consider an arbitrary *part* $\mathcal{D}_0$ of a deformable body $\mathcal{B}_0$ (Fig. 2.1). In a free-body diagram, one can imagine that traction forces $\mathbf{t}$ act on the boundary $\partial\mathcal{D}_0$ of $\mathcal{D}_0$, like in Fig. 2.2b; for simplicity, inertia and body forces are ignored in the following. The *global* (or integral) form for translational equilibrium (for statics) requires that the sum of all forces acting on $\mathcal{D}_0$ vanishes, leading to (e.g. Bonet and Wood 2008)

$$\int_{\partial\mathcal{D}_0} \mathbf{S}\,\mathbf{m}\,\mathrm{d}A = \mathbf{0} \qquad \text{for all parts } \mathcal{D}_0 \subset \mathcal{B}_0. \tag{2.6}$$

Here, dA denotes an area increment of the surface $\partial\mathcal{D}_0$. Application of the *divergence theorem* yields the *local* (or pointwise) form,

$$\nabla \cdot \mathbf{S} = \mathbf{0} \qquad \text{at each point in the body } \mathcal{D}_0 \subset \mathcal{B}_0; \tag{2.7}$$

$\nabla\cdot$ denotes the divergence.

Balance of angular momentum

The rotational equilibrium of $\mathcal{D}_0$ implies that the total moment of traction forces about an arbitrary point must vanish. This renders the Cauchy stress to be symmetric, $\boldsymbol{\sigma} = \boldsymbol{\sigma}^{\mathrm{T}}$. On the contrary, the first Piola–Kirchhoff stress is, in general, not symmetric, since $\mathbf{S}\mathbf{F}^{\mathrm{T}} = \mathbf{F}\mathbf{S}^{\mathrm{T}}$ (see e.g. Bonet and Wood 2008).

First law of thermodynamics – conservation of energy

This law postulates that the total energy of an isolated system is constant (Malvern 1969):

$$\frac{\mathrm{d}\mathcal{E}}{\mathrm{d}t} = \frac{\mathrm{d}\mathcal{A}}{\mathrm{d}t} + \frac{\mathrm{d}\mathcal{Q}}{\mathrm{d}t} \qquad \text{for all parts } \mathcal{D}_0 \subset \mathcal{B}_0; \tag{2.8}$$

$\mathcal{E}$ reflects the *stored* energy in the system and can be additively split up into external energy, like kinetic energy, and internal energy, like strain energy $\mathcal{U}$. The quantities $\mathcal{A}$ and $\mathcal{Q}$ represent *transported* energies over the system boundary; $\mathcal{A}$ denotes the mechanical energy or work of the applied forces, $\mathcal{Q}$ is the inserted or removed energy by heat. For the local form of Eq. (2.8) see Malvern (1969).

The energy balance, Eq. (2.8), will be used in Section 3.1 to define the criteria for crack growth and the crack driving force.

Second law of thermodynamics – dissipation inequality

The second law of thermodynamics identifies the direction of thermomechanical processes. A fundamental version of this law for continuum mechanics is the "Clausius–Duhem inequality" (e.g. Malvern 1969), which postulates the dissipation Ψ to be equal or larger than zero for every part $\mathcal{D}_0$ of a body $\mathcal{B}_0$. Hence, this law is also called *dissipation inequality*. The dissipation Ψ is a measure of reversibility of mechanical processes and can be expressed in global form by the relation (Malvern 1969, Gurtin 2000),

$$\Psi(\mathcal{D}_0) = \mathcal{W} - \frac{\mathrm{d}\mathcal{E}}{\mathrm{d}t} \geq 0 \qquad \text{for all parts } \mathcal{D}_0 \subset \mathcal{B}_0, \tag{2.9}$$

i.e. the difference between the working rate $\mathcal{W}$ and the rate of change of energy $\mathcal{E}$; in our cases the strain energy $\mathcal{U}$ reflects $\mathcal{E}$.

It should be mentioned that heat is not considered in our cases, thus, the dissipation arises mainly from plastic deformation. Under consideration of isothermal state changes, the local form of the dissipation inequality is given by (Malvern 1969, Gurtin 2000)

$$\psi_{\mathrm{bulk}} = \mathbf{S} \cdot \dot{\mathbf{F}} - \dot{\phi} \geq 0 \qquad \text{at each point in the body } \mathcal{D}_0 \subset \mathcal{B}_0. \tag{2.10}$$

The relation, Eq. (2.10), is also termed "bulk dissipation per unit volume" (e.g. Simha et al. 2003) and will be derived in Section 4.2.2. The parameter ϕ denotes the (Helmholtz) free energy per volume in the reference configuration and is in our cases identical to the *strain energy density*, see Section 2.5.1; $\dot{\phi}$ denotes the time derivative of ϕ.

If ϕ is a single valued function of deformation, i.e. ϕ exhibits the properties of a potential, $\psi_{\text{bulk}} = 0$. This means that mechanical processes are fully reversible in the material, and Eq. (2.10) serves for calculating the stresses (e.g. Simha et al. 2003),

$$\mathbf{S} = \frac{\mathrm{d}\phi(\mathbf{F})}{\mathrm{d}\mathbf{F}}. \tag{2.11}$$

On the contrary, if dissipative processes occur in the material, $\psi_{\text{bulk}} > 0$ applies, and ϕ is not a single valued function of deformation. As a consequence, Eq. (2.11) is not valid any more (e.g. Simha et al. 2003).

From this section it should be kept in mind that the dissipation inequality, Eq. (2.10), considers thermodynamically admissible processes for specific constitutive relations of a material, and Eq. (2.11) is only valid under certain conditions; constitutive relations are discussed in Section 2.5.

2.4 Small strain theory

Though the concept of configurational forces will be derived for large strain theory, it is in many cases useful, for an easier understanding, to apply formulations under assumptions of small deformations. In small strain theory the displacement **u** is assumed to be infinitesimally small. This means that reference- and current configurations are (approximately) the same, which implies that material points can be characterized only by **x** (e.g. Bonet and Wood 2008).

In small strain theory all strain and stress measures coincide. The linearized strain tensor $\boldsymbol{\varepsilon}$ is defined by

$$\boldsymbol{\varepsilon} = \frac{1}{2}\left(\nabla\mathbf{u} + (\nabla\mathbf{u})^{\mathrm{T}}\right); \tag{2.12}$$

see e.g. Bonet and Wood (2008) for details. Hence, the displacement **u** is the essential kinematic descriptor for small deformations. The stress tensor is given by the Cauchy stress tensor $\boldsymbol{\sigma}$ (Section 2.2).

For the linear equilibrium equation, **S** is substituted by $\boldsymbol{\sigma}$ in Eqs. (2.6) and (2.7). The dissipation inequality, Eq. (2.10), follows with

$$\psi_{\text{bulk}} = \boldsymbol{\sigma} \cdot \dot{\boldsymbol{\varepsilon}} - \dot{\phi} \geq 0 \qquad \text{at each point in the body } \mathcal{D}_0 \subset \mathcal{B}_0. \tag{2.13}$$

This leads to

$$\boldsymbol{\sigma} = \frac{\mathrm{d}\phi(\boldsymbol{\varepsilon})}{\mathrm{d}\boldsymbol{\varepsilon}}, \tag{2.14}$$

provided that $\phi = \phi(\boldsymbol{\varepsilon})$ applies, i.e. for specific constitutive assumptions, see next section.

2.5 Constitutive relations

A constitutive relation (also *material law*) specifies the stress–strain relationship for a certain material. Basically, the mechanics of solids distinguishes between *elastic* and *plastic* materials. Their constitutive behavior is defined after making assumptions about the strain energy density ϕ, Section 2.5.1.

The *Hooke's law* gives the stress–strain relationship in linear elasticity. For homogeneous, isotropic, elastic materials, two material constants uniquely define the material properties, i.e. Young's Modulus E and Poisson's ratio ν. For elastic–plastic materials, the description of the material law is more complex. In Section 2.5.2, two theories, which are crucial for this thesis, will be introduced.

For simplicity, small strain theory is considered in the following. Details on material theory can be found, e.g., in Truesdell and Noll (1965), Malvern (1969), Marsden and Hughes (1983).

2.5.1 Strain energy density

A body deforms elastically if the deformation is fully reversible. This implies that the stress state $\boldsymbol{\sigma}$ depends only on the current deformation $\boldsymbol{\varepsilon}$, but not on the deformation history (e.g. Malvern 1969). Figure 2.3 shows the stress–strain ($\sigma-\varepsilon$) behavior in a nonlinear elastic material: Point A is reached independently of the previous stress state B or 0.

The work done per unit volume during deformation is related to the strain energy density, which is given by

$$\phi(\boldsymbol{\varepsilon}) = \int_{\mathbf{0}}^{\boldsymbol{\varepsilon}} \boldsymbol{\sigma} \cdot \mathrm{d}\boldsymbol{\varepsilon} \,, \tag{2.15}$$

i.e. the area below the $\sigma-\varepsilon$-curve (Fig. 2.3a). The requirement for the validity of Eq. (2.15) is that ϕ is a single valued function of strain, $\phi = \phi(\boldsymbol{\varepsilon})$, i.e. ϕ exhibits the properties of a potential. Then, ψ_{bulk} = 0, Eq. (2.13), and the stresses $\boldsymbol{\sigma}$ can be derived after Eq. (2.14). This assumption applies for homogeneous, (linear or nonlinear) elastic materials. In Fig, 2.3, it does not matter how A is reached, the magnitude of strain energy density ϕ is always the same. On the contrary, this is not the case in dissipative materials, like elastic–plastic materials.

2.5.2 Deformation plasticity versus incremental theory of plasticity

If an elastic–plastic material is loaded beyond the yield stress σ_{y}, it will deform plastically. Such deformations are not reversible anymore. For small strain theory, the total strain $\boldsymbol{\varepsilon}$ can be split into elastic and plastic parts, $\boldsymbol{\varepsilon} = \boldsymbol{\varepsilon}_{\mathrm{e}} + \boldsymbol{\varepsilon}_{\mathrm{p}}$ (Fig. 2.3b). Two theories can be applied for

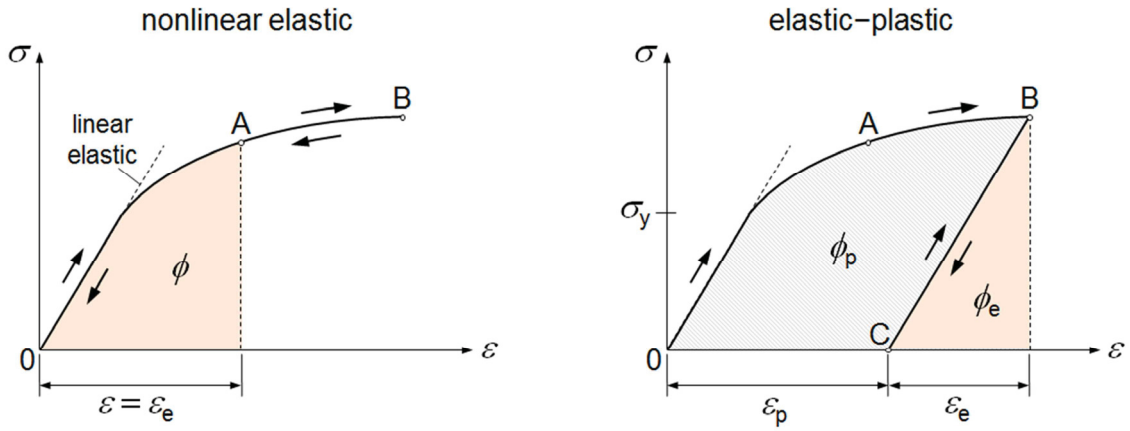

Fig. 2.3 Stress–strain ($\sigma - \varepsilon$) curves of a material point in **(a)** a nonlinear elastic material and **(b)** an elastic–plastic material. Deformation plasticity treats the elastic–plastic material to be nonlinear elastic. This means that the total strain energy density ϕ is assumed to be fully recoverable. On the contrary, only the elastic part ϕ_e of the total strain energy density $\phi = \phi_e + \phi_p$ is reversible in a *real* elastic–plastic material with incremental theory of plasticity.

the description of the relationship between the stresses $\boldsymbol{\sigma}$ and total strains $\boldsymbol{\varepsilon}$: *Deformation-* and *incremental theory of plasticity*.[2]

Deformation theory of plasticity

This theory presumes the plastic strain as a function of the deviatoric stresses, $\boldsymbol{\varepsilon}_p \sim \mathbf{s}$, or of the equivalent stress, $\boldsymbol{\varepsilon}_p \sim \sigma_{eq}$ (e.g. Chakrabarty 2006).[3]

Application of deformation theory of plasticity means that the elastic–plastic material behavior is idealized to be nonlinear elastic.[4] This is possible as long as the conditions of *proportional* loading are fulfilled, that is, if no unloading processes occur in the material. Then, a material point in an elastic–plastic and a comparable nonlinear elastic material exhibits the same stress–strain-curve; compare Figs. 2.3a,b. However, an error appears since only the elastic part of the total strain energy ϕ_e is reversible and not the total strain energy density $\phi = \phi_e + \phi_p$, which is composed of the elastic and plastic part (Fig. 2.3b); the plastic part ϕ_p has been dissipated during plastic deformation.

---

[2] For any theory in plasticity, a *yield condition*, a *hardening rule*, and a *flow rule* is needed, which shall not be discussed here. In this thesis, *von Mises* plasticity will be used. For details on plasticity theory see e.g. Kachanov (2004) and Chakrabarty (2006), respectively.

[3] Stresses can be decomposed into hydrostatic and deviatoric parts. The hydrostatic stress is related to the volume change, whereas the deviatoric stress is related to the shape change. Since plastic deformation is considered to be isochoric, only deviatoric stresses are crucial for plastic deformation. Note that the equivalent stress σ_{eq} is only a function of the deviatoric stresses, see e.g. Kachanov (2004) or Chakrabarty (2006) for details.

[4] The nonlinear stress–strain-curve for elastic–plastic materials is frequently approximated by the Ramberg-Osgood equation; see, for example, Anderson (1995).

This has important consequences for the application of the conventional *J*-integral as crack driving force parameter in elastic–plastic materials, as outlined in the Introduction and in Section 3.2.1 in detail.

Incremental theory of plasticity

This theory is required for the correct description of elastic–plastic materials. Here, the *increment* of plastic strain $\mathrm{d}\boldsymbol{\varepsilon}_\mathrm{p}$ is considered to evolve proportional to the *deviatoric* stresses, $\mathrm{d}\boldsymbol{\varepsilon}_\mathrm{p} \sim \mathbf{s}$, or the equivalent stress, $\mathrm{d}\boldsymbol{\varepsilon}_\mathrm{p} \sim \sigma_\mathrm{eq}$. The elastic strain increment $\mathrm{d}\boldsymbol{\varepsilon}_\mathrm{e}$ is related to the stresses by the Hooke's law. The total strain increment is given by $\mathrm{d}\boldsymbol{\varepsilon} = \mathrm{d}\boldsymbol{\varepsilon}_\mathrm{e} + \mathrm{d}\boldsymbol{\varepsilon}_\mathrm{p}$, which is referred to as *Prandtl–Reuss equation*, see Kachanov (2004).

Figure 2.3b shows the stress–strain relationship in an elastic–plastic material. After loading to point B the total strain energy density $\phi = \phi_\mathrm{e} + \phi_\mathrm{p}$ is not fully reversible any more, but only the elastic part ϕ_e. Therefore, point C is reached after unloading from B.

In a homogeneous, elastic–plastic material with incremental plasticity, the strain energy density is given by (Simha et al. 2003)

$$\phi\left(\boldsymbol{\varepsilon}_\mathrm{e}, \mathbf{x}\right) = \phi_\mathrm{e}\left(\boldsymbol{\varepsilon}_\mathrm{e}\right) + \phi_\mathrm{p}\left(\mathbf{x}\right), \tag{2.16}$$

where $\phi_\mathrm{e}\left(\boldsymbol{\varepsilon}_\mathrm{e}\right)$ is the reversible part of ϕ, evaluated analogously to Eq. (2.15), and $\phi_\mathrm{p}\left(\mathbf{x}\right)$ depends on the deformation history of a material point, defined by $\mathbf{x}$. Since ϕ, Eq. (2.16), does not exhibit the properties of a potential, Eq. (2.14) is not valid for elastic–plastic materials. The implications for the *J*-integral will be explained in Sections 3.2.1 and 4.3.2, respectively.

3 Fundamentals of fracture mechanics

Fracture mechanics is a continuum mechanics-based tool that enables the description of the behavior of cracks in materials and structural components. For a comprehensive overview about fracture mechanics much literature is available, e.g., Broek (1982), Anderson (1995), Gross and Seelig (2007), Kuna (2008). The article by Kolednik (2012) gives a compact review about this topic. For fatigue crack propagation, the book by Suresh (1998) is the standard reference.

The purpose of this section is to introduce relevant fracture mechanics terms and concepts, needed for this thesis. Emphasis is placed on the *J*-integral concept and the fundamental conceptual difficulties that appear when *J* is applied to elastic–plastic materials.

It should be mentioned that only long cracks under Mode I loading, i.e. the crack opening mode, are treated in this thesis, since it is the most critical loading mode (Anderson 1995). Moreover, Mode I commonly occurs during fatigue crack propagation, and other mode cracks (Mode II and III) often turn into Mode I, see Suresh (1998) for details on this topic.

3.1 Crack driving force and regimes of fracture mechanics

The major goal in fracture mechanics is to determine the criteria for the growth of cracks (Kolednik 2012). Crack extension is driven by a force, referred to as the *crack driving force*, and hindered by the *crack growth resistance*. The crack extends if the crack driving force becomes equal or larger than the crack growth resistance (e.g. Anderson 1995, Kolednik 2012). For the former case, "equilibrium crack growth" prevails. For the latter case, we have "unstable crack growth".

The definition of the crack driving force and the crack growth resistance originates from the balance of energy, Eq. (2.8). Assume a *monotonically* loaded, elastic–plastic body of thickness B with a crack during an increment of equilibrium crack extension $\mathrm{d}a$ (Fig. 3.1a). The balance of energy can be expressed as (e.g. Kolednik 2012)

$$\mathrm{d}\mathcal{A} = \mathrm{d}\mathcal{U}_{\mathrm{e}} + \mathrm{d}\mathcal{U}_{\text{non-rev}} + \mathrm{d}\Gamma_{\mathrm{s}} \,. \tag{3.1}$$

Here, $\mathcal{U}_{\mathrm{e}}$ and $\mathcal{U}_{\text{non-rev}}$ denote the reversible- (elastic) and the non-reversible strain energy. Γ_{s} is the surface energy, which reflects the work required to create new fracture surface (Anderson 1995, Kolednik 2012). For an elastic–plastic material $\mathcal{U}_{\text{non-rev}}$ contains mainly the plastic strain energy $\mathcal{U}_{\mathrm{p}}$. Rearrangement of Eq. (3.1) and division by the increased crack area, $B\,\mathrm{d}a$, leads to

$$\underbrace{-\frac{1}{B}\frac{\mathrm{d}\mathcal{U}_{\mathrm{e}} - \mathrm{d}\mathcal{A}}{\mathrm{d}a}}_{\text{crack driving force}} = \underbrace{-\frac{1}{B}\frac{\mathrm{d}\mathcal{P}}{\mathrm{d}a}}_{\text{crack driving force}} = \underbrace{-\frac{1}{B}\frac{\mathrm{d}\mathcal{U}_{\text{non-rev}} + \mathrm{d}\Gamma_{\mathrm{s}}}{\mathrm{d}a}}_{\text{crack growth resistance}} \,. \tag{3.2}$$

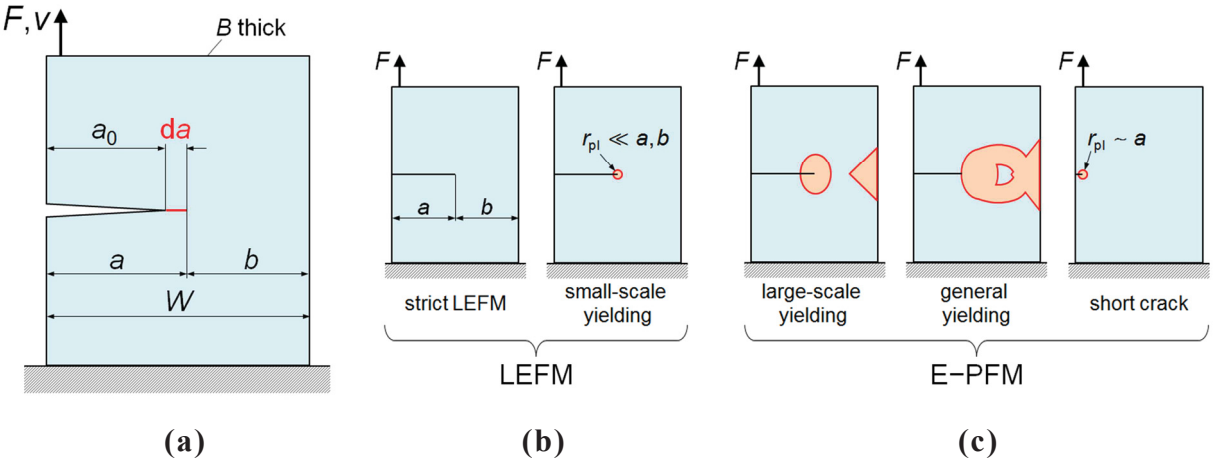

Fig. 3.1 **(a)** Loaded body with a crack of initial length a_0 after incremental crack extension da; the total crack length is $a = a_0 + \mathrm{d}a$. **(b) (c)** Regimes of fracture mechanics: **(b)** linear elastic fracture mechanics (LEFM) applies if linear elastic (strict LEFM) or small-scale yielding conditions prevail; **(c)** elastic–plastic fracture mechanics (E–PFM) applies under large-scale- or general yielding conditions, and during the growth of short cracks.

In Eq. (3.2), $\mathcal{P}$ denotes the potential energy that is supplied by the internal elastic strain energy and the work of the external force F; $\mathcal{P} = \mathcal{U}_e - \mathcal{A}$. For crack extension under constant displacement $v = const$, $\mathcal{P} = \mathcal{U}_e$ (e.g. Rice 1968a,b; Anderson 1995).

The left term in Eq. (3.2) is denominated as the crack driving force, i.e. the potential energy released per unit crack extension. The right term of Eq. (3.2) is conform to the crack growth resistance, i.e. the non-reversible energy required to produce a unit crack extension, see e.g. Griffith (1920), Eftis and Liebowitz (1975), Kolednik (1991), Turner and Kolednik (1994).

A major problem in fracture mechanics is that different parameters are used for the description of the crack driving force and the crack growth resistance (Kolednik 2012). For the current thesis the crack driving force is of major interest. For details about the crack growth resistance the reader is referred, e.g., to Anderson (1995).

Fracture mechanics can be divided into linear elastic fracture mechanics (LEFM) and elastic–plastic- or non-linear fracture mechanics (E–PFM, NLFM), see e.g. Kolednik (2012). LEFM is applied when crack growth is accompanied by zero or limited plastic deformation, i.e. the radius of the plastic zone r_{pl} is very small compared to the crack length a and the ligament length b, $r_{pl} \ll a,b$, so that *small-scale yielding* (ssy) conditions prevail, see Fig. 3.1b. E–PFM is used in presence of significant plastic deformation, $r_{pl} \gg a,b$, that is, if *large-scale yielding* (lsy) or *general yielding* (gy) conditions prevail (Fig. 3.1c), or when the material exhibits, in general, nonlinear behavior (Kolednik 2012). Lsy-conditions start with the onset of plastic deformation at the back face of the body. Gy-conditions prevail when the crack tip plastic zone and back face plasticity region merge, i.e. plasticity spreads over the whole ligament. Note that, in spite of a small crack tip plastic zone, $r_{pl} \ll a,b$ is not

guaranteed for short cracks (see *last image* in Fig. 3.1c), and therefore E–PFM must be applied.

In the regime of LEFM, the *elastic energy release rate G* (Griffith 1920) characterizes the thermodynamic crack driving force. Alternatively, the stress intensity factor *K* (Irwin 1957) can be used: the crack grows if a critical stress intensity of the crack tip field is reached. The parameters *G* and *K* are related for linear elasticity, hence, both concepts are in principle equivalent (e.g. Anderson 1995, Kolednik 2012).

The common approaches in the regime of E–PFM are the crack tip opening displacement δ_t (Wells 1963) and the *J*-integral (Rice 1968a,b). Similar to *K*, the parameters δ_t and *J* describe the intensity of the near-tip field; crack growth occurs if the corresponding critical values are reached. The *J*-integral also describes the thermodynamic crack driving force for nonlinear elastic bodies (Rice 1968a,b); see next section. For linear elastic bodies, Rice (1968a,b) showed that *J* is identical to the elastic energy release rate *G*. Since *K* (or *G*) is uniquely related to δ_t for ssy-conditions, a relation between *J* and δ_t can be obtained that holds even in the E–PFM regime, see Anderson (1995), Kolednik (2012) and Section 6.5.2 of the current thesis.

While crack growth can be readily described in LEFM, it is somewhat problematic in the E–PFM regime: the determination of accurate δ_t -values is, in general, difficult (e.g. Kolednik and Stüwe 1985, Siegmund et al. 1990); the application of the *J*-integral to elastic–plastic materials is connected with fundamental conceptual difficulties (e.g. Rice 1976).

The main focus of this thesis lies on the *J*-integral concept. Therefore, the most important aspects about the *J*-integral shall be presented in the following.

3.2 The conventional J-integral – definition and properties

Assume a homogeneous, nonlinear elastic body $\mathcal{B}$ as illustrated in Fig. 3.2a. The change in potential energy $\mathrm{d}\mathcal{P}$ released during an incremental crack extension d*a* can be expressed by the *J*-integral (Rice 1968a,b),

$$-\frac{1}{B}\frac{\mathrm{d}\mathcal{P}}{\mathrm{d}a}=\int_{\Gamma}\left(\phi\,\mathrm{d}y-\mathbf{t}\cdot\frac{\partial\mathbf{u}}{\partial x}\mathrm{d}s\right)\equiv J\,. \tag{3.3}$$

This implies that *J* reflects the magnitude of the crack driving force in nonlinear elastic materials, compare Eq. (3.2). The quantities of the integral term in Eq. (3.3) have been already explained in Section 2; d*s* denotes an increment of the integration path Γ, drawn from the lower to the upper crack flank in counterclockwise direction around a crack (Fig. 3.2a). The *J*-integral can be calculated when the stresses and strains along Γ are given, for example, after a conventional finite element (FE) analysis (Kolednik 2012).

The big advantage of the *J*-integral is its *path independence* in the context of homogeneous, nonlinear elastic materials (Rice 1968a,b). This path dependence is very important: a direct evaluation of the energy released at the crack tip, characterized by the near-tip *J*-integral J_{tip}, is very difficult. However, since $J_{\mathrm{tip}}=J_{\Gamma}=J_{\mathrm{far}}$, the magnitude of J_{tip} can readily be determined by the *J*-integral on a far-field contour, J_{far} (Fig. 3.2a).

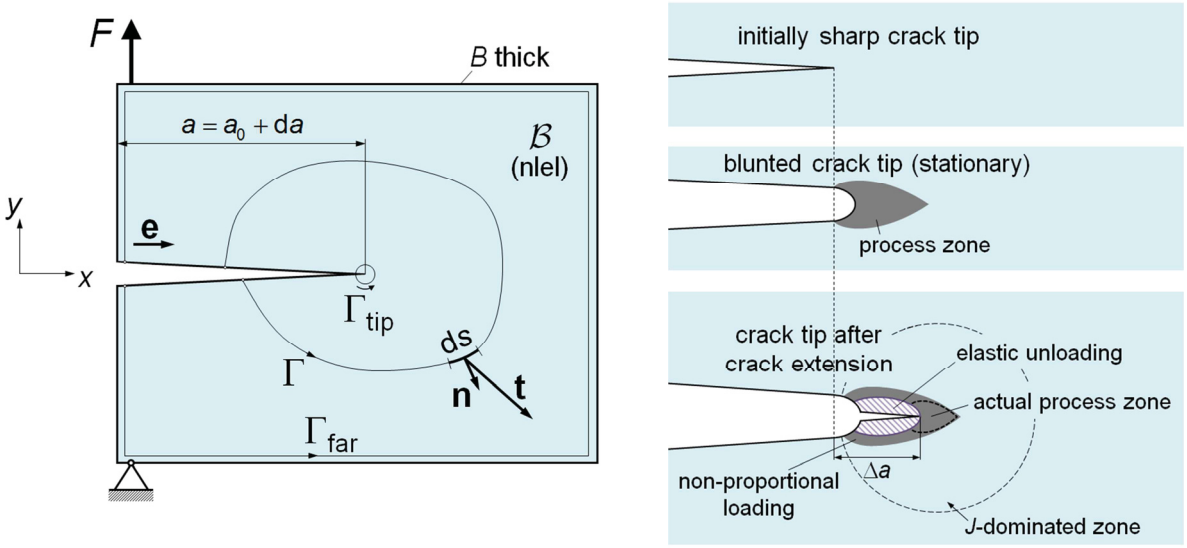

Fig. 3.2 **(a)** Homogeneous, nonlinear elastic (nlel) body $\mathcal{B}$ with a crack after one increment of crack extension; crack length $a = a_0 + \mathrm{d}a$. In nlel materials, the magnitude of the *J*-integral is independent of the integration path Γ. **(b)** Zones of non-proportional loading: process zone after crack-tip blunting (*second image*) and after crack extension Δa (*lower image*). "*J*-controlled crack growth" means that a *J*-dominated zone exists around a blunted crack tip even after crack extension.

Hutchinson (1968) and Rice and Rosengren (1968) showed that *J* provides a measure of the intensity of the crack tip field (called HRR field) for nonlinear elastic materials, similar to *K* for linear elasticity.

It should be emphasized that the meaning of a crack driving force term, Eq. (3.3), and the path independence of *J* can be shown only if the strain energy density ϕ exhibits the properties of a potential, so that Eq. (3.14) is valid; see e.g. Anderson (1995). Therefore, it is required that the material is characterized by nonlinear elastic behavior, i.e. deformation plasticity (Section 2.5).

3.2.1 Problems of J-integral in elastic–plastic materials

The application of the *J*-integral for elastic–plastic materials with incremental plasticity rests on the assumption that deformation theory of plasticity can be used. This is possible as long as the conditions of *proportional loading* are fulfilled, that is, if no unloading occurs in the material (Kolednik 2012).

Figure 2.3 shows that nonlinear elastic and elastic–plastic materials exhibit the same stress–strain-curves as long as no unloading occurs. But, even if proportional loading conditions prevail the *J*-integral does not reflect the thermodynamic driving force of a crack in elastic–plastic materials (Rice 1968a,b). The reason is that deformation plasticity presumes

the total strain energy density ϕ to be fully reversible, which applies in a nonlinear elastic material. In an elastic–plastic material, however, only the elastic part ϕ_e can be recovered and is available for driving crack extension, see Section 2.5.2. Moreover, Eq. (3.3) cannot be derived for incremental plasticity, since ϕ is not a thermodynamic potential, hence, Eq. (2.14) is invalid (e.g. Anderson 1995). Nevertheless, the *J*-integral still characterizes the intensity of the crack tip field (Hutchinson 1968, Rice and Rosengren 1968, McMeeking and Parks 1979).

Additional problems arise under assumption of deformation plasticity when proportional loading is violated, e.g. for cyclic loading and crack extension, due to the unloading behind the moving crack tip. Fig. 2.3 shows that wrong total strains are predicted. In reality, however, even when a crack remains stationary under monotonic loading, non-proportional loading occurs in a small region in front of the *blunted* crack tip.[5] This region is referred to as the *process zone*, Fig. 3.2b (*second image*), i.e. the region within which micromechanical damage processes occur, e.g. void initiation and void growth (Anderson 1995, Kolednik 2012). In numerical simulations with incremental plasticity and large strain theory, the intensely deformed zone in front of a blunted crack tip can be connected to the process zone. The length of the process zone is proportional to the crack tip opening displacement, $l_{\mathrm{proc.z}} \approx \kappa\delta_t$; the pre-factor κ is often assumed to be 3 (Rice and Johnson 1970; McMeeking 1977). The process zone provides a disturbance of the HRR field, like the plastic zone for the *K*-field. The *J*-integral is only meaningful as long as the process zone remains small, so that a so-called "*J*-dominated zone" exists, where *J* still characterizes the intensity of the crack tip field. The size requirement for the validity of *J* is due to $l_{\mathrm{proc.z}} \approx \kappa\delta_t$ related to the crack tip opening displacement and can be found in Anderson (1995) and Kolednik (2012), respectively.

As a consequence of all these restrictions when deformation theory of plasticity is presumed, incremental theory of plasticity is desired for a realistic description of the elastic–plastic material.

In incremental theory of plasticity, however, the *J*-integral becomes path dependent. Finite element analyses with incremental plasticity and large strain theory showed that the *J*-integral varies in the process zone, within which non-proportional loading occurs. For a stationary crack, *J* reaches a saturation value outside the process zone, which remains useful (e.g. McMeeking 1977, Brocks et al. 2003); see next section. For a growing crack, the path dependence of *J* is more pronounced due to the larger zone of non-proportional loading around the growing crack tip (Fig. 3.2b, *lower image*).

It should be remarked that, although such FE-analyses are performed with incremental plasticity, deformation plasticity is implicitly assumed in the evaluation of the *J*-integral, see e.g. Parks (1977). Therefore, the physical meaning of the near-tip *J*-integral J_{tip} as crack driving force parameter remains unclear for incremental plasticity (Simha et al. 2008).

---

[5] During loading of an elastic–plastic material, plastic deformation at the crack tip leads to crack-tip blunting; see Anderson (1995), Kolednik (2012) and Fig. 2.2b, for example.

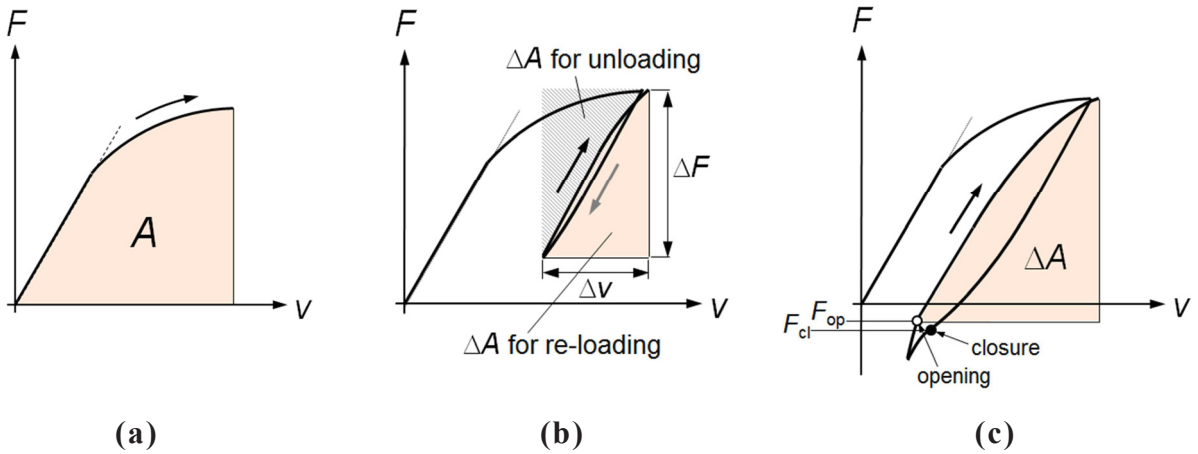

Fig. 3.3 **(a)** Determination of area A from the load–displacement (F–v) record for the evaluation of the evaluation of the experimental J-integral J^{exp}. **(b)** Determination of ΔA from a single loading branch for the experimental cyclic J-integral ΔJ^{exp}. **(c)** Determination of ΔA in the presence of crack closure. The *open dot* indicates the point where the crack fully opens during re-loading. The *full dot* indicates the beginning of crack closure during unloading.

On a more general level, it is also not clarified whether J_{tip} alone controls crack growth in elastic–plastic materials (Simha et al. 2008, Kolednik et al. 2014). The reason is that J strongly reduces for shrinking contours in the process zone to the very tip, leading finally to $J_{\text{tip}} = 0$. This appears independently whether deformation- or incremental theory of plasticity is applied, see e.g. Rice and Johnson (1970), McMeeking (1977), McMeeking and Parks (1979), Brocks et al. (2003), Kfouri and Miller (1976), Kfouri and Rice (1977), Kolednik et al. (2014). Immediately the question arises, how can a crack in an elastic–plastic material extend despite zero crack driving force? This is referred to as the "paradox of elastic–plastic fracture mechanics" (Rice 1979). The paradox has been extensively investigated in the thesis by Schöngrundner (2011) and Kolednik et al. (2014); see also Section 5 herein.

3.2.2 Experimental J-integral

The magnitude of the J-integral, Eq. (3.3), can be determined in fracture mechanics experiments from the area A below the load–displacement (F–v) curve of a single specimen (Fig. 3.3a); before crack extension, A is identical to the total strain energy $\mathcal{U} = \mathcal{U}_{\text{e}} + \mathcal{U}_{\text{p}}$ (Section 3.1). The experimental J-integral J^{exp} is evaluated, for deeply notched bend-type specimens, like Compact Tension (CT) or Single-Edge Notched Bend (SENB) specimens, by the relation (Rice et al. 1973),

$$J^{\text{exp}} = \frac{\eta A}{bB}; \tag{3.4}$$

b is the ligament length $W - a$, with W and a as the width of the specimen and the crack length, respectively (Fig. 3.1a). The dimensionless geometry factor $\eta(a/W)$ takes into

account the type of the specimen; see fracture mechanics standard testing procedures ESIS P2-92 (1992) or ASTM E1820 (2005).

Further estimations for $J^{\exp}$ exist, similar to Eq. (3.4), for other specimen types with different definitions of A (Rice et al. 1973), or where $J^{\exp}$ is split additively into elastic and plastic parts (e.g. ASTM E1820, 2005). Note that the assumption of deformation plasticity has been adopted for the experimental J-integral, therefore, its validity for elastic–plastic materials is unclear (e.g. Anderson 1995, Kolednik 2012).

It can be shown that Eq. (3.4) and Eq. (3.3) yield identical J-values, $J^{\exp} = J$, for a monotonically loaded, stationary crack in an elastic–plastic material with incremental plasticity (Rice et al. 1973, Kolednik 1991). This applies in numerical simulations with large strain theory, if the J-integral, Eq. (3.3), has been evaluated for a contour Γ outside the process zone (McMeeking 1977, Brocks et al. 2003). For growing cracks, $J^{\exp} \neq J$ (Kolednik 1991, 1993; Kolednik and Turner 1994). However, the J-integral remains applicable for a *limited* crack extension in form of an engineering approach, if the conditions of "J-controlled crack growth" are fulfilled (Hutchinson and Paris 1979). With crack extension, the non-proportional region around the crack tip extends, but the J-integral remains meaningful if this region remains small so that a "J-dominated zone" still exists in the surrounding whithin which J describes the intensity of the crack tip field (Fig. 3.2b, *lower image*); see Anderson (1995) and Kolednik (2012) for details.

3.3 Characterization of fatigue crack propagation

3.3.1 Paris regime of fatigue crack growth

A crack in a cyclically loaded material can extend even if the crack driving force lies significantly below the crack growth resistance. Thus, the meaning of the crack driving force for cyclic loading differs from that for monotonic loading. The "crack driving force" for cyclic loading characterizes the change in length of a fatigue crack per load cycle, i.e. the fatigue crack growth rate da/dN (e.g. Suresh 1998); a is the actual crack length after N load cycles.

When (cyclic) plastic deformation around the crack tip is small compared to the fatigue crack, LEFM is valid and the stress intensity range ΔK (Paris et al. 1961, Paris and Erdogan 1963) can be used for the prediction of the fatigue crack growth rate da/dN; ΔK is the difference between the stress intensity factors at maximum and minimum load of a load cycle, $K_{\max} - K_{\min}$. For fatigue, the regime where LEFM applies is also denominated as high cycle fatigue (HCF) regime (Suresh 1998).

For fatigue cracks that grow in elastic–plastic materials under *constant* cyclic loading, Paris et al. (1961) and Paris and Erdogan (1963) postulated the following power law relationship, known as *Paris law*,

$$\frac{\mathrm{d}a}{\mathrm{d}N} = C\left(\Delta K\right)^m . \tag{3.5}$$

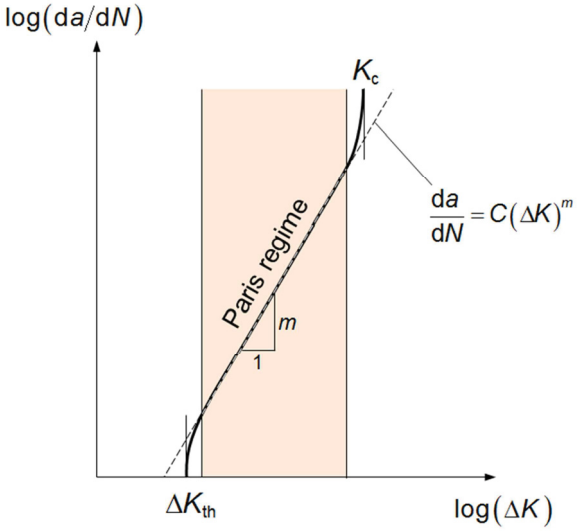

Fig. 3.4 Schematic diagram for different regimes of fatigue crack growth. Stable fatigue crack growth prevails in the Paris regime, whereas unstable crack growth occurs at high ΔK-levels; da/dN approaches zero at low ΔK-levels (e.g. Suresh 1998).

The terms C and m are empirical scaling constants; for most metals, m ranges between $2-4$ (Anderson 1995, Suresh 1998). In a double logarithmic diagram, Eq. (3.5) shows a linear relationship between $\log(\mathrm{d}a/\mathrm{d}N)$ and $\log(\Delta K)$. In reality, most metals and alloys exhibit a sigmoidal variation in the $\log(\mathrm{d}a/\mathrm{d}N)-\log(\Delta K)$-diagram, see Fig. 3.4. The linear regime, where Eq. (3.5) characterizes fatigue crack growth, is referred to as the "Paris regime". In the lower regime, da/dN approaches zero when ΔK tends to a certain non-zero ΔK-value, denominated as the *threshold* stress intensity factor range ΔK_{th}. In the upper regime, da/dN increases rapidly with increasing ΔK, up to the point where $K_{\max}$ reaches the critical stress intensity factor K_{c}, causing final failure; see Anderson (1995) or Suresh (1998) for details.

The validity of Eq. (3.5) originates from the relation between ΔK and the cyclic crack tip opening displacement $\Delta\delta_{\mathrm{t}}$, i.e. the difference in the crack tip opening displacement between maximum and minimum load, $\delta_{\mathrm{t,max}}-\delta_{\mathrm{t,min}}$; see Suresh (1998) and Section 6.5.2. The parameter $\Delta\delta_{\mathrm{t}}$ is proportional to da/dN, since fatigue crack growth in ductile metals and alloys is driven by cyclic plastic deformation at the crack tip. Figure 3.5a schematically illustrates the mechanism of fatigue crack growth: In the loading phase, plastic blunting of the crack tip occurs, followed by re-sharpening during unloading (Laird 1967, 1979). This two-step mechanism is also confirmed by experimental observations: striation markings form on the fracture surface (Zappfe and Worden 1951), whose spacing corresponds to the crack extension increments (Forsyth and Ryder 1960), see Fig. 3.5a. These spacings are proportional to the values of $\Delta\delta_{\mathrm{t}}$ (e.g. Tanaka 1989, Krupp et al. 2002, Pippan et al. 2010, Suresh 1998).

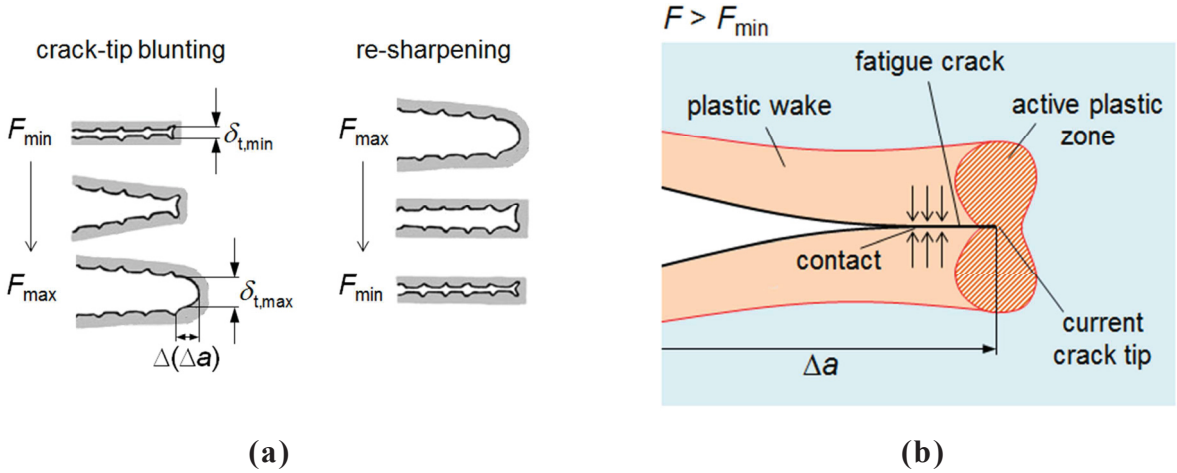

Fig. 3.5 **(a)** Fatigue crack growth model after Laird (1967, 1979); see also Anderson (1995) or Suresh (1998). *Blunting* (at F_{max}) and *re-sharpening* (at F_{min}) of the crack tip leads to crack propagation during cyclic loading; $\Delta(\Delta a)$ denotes an increment of crack extension during one load cycle. **(b)** Plasticity-induced crack closure: During fatigue crack growth, the movement of the active plastic zone, i.e. the crack tip plastic zone of the current crack tip, produces a plastic wake with residual stresses (indicated as *vertical arrows*), which cause premature crack flank contact.

It should be mentioned that Eq. (3.5) characterizes the behavior of *long* fatigue cracks during equilibrium crack growth, also called "stage II crack growth" (Suresh 1998). Short fatigue cracks show a different behavior as illustrated in Fig. 3.4. Modifications of Eq. (3.5) for short fatigue cracks exist, e.g., in Anderson (1995), Suresh (1998), Maierhofer et al. (2014, 2015). The current thesis, however, deals only with long fatigue cracks. An important phenomenon that must be considered, especially, during the growth of long cracks is *crack closure.*

3.3.2 Crack closure during fatigue

Elber (1970, 1971) showed in his experiments that fatigue cracks can close, i.e. crack flank contact occurs, before the minimum load is reached in a load cycle. There are many forms of *crack closure*, e.g. plasticity-, roughness- and oxide-induced crack closure; see Ritchie et al. (1980), Suresh and Ritchie (1982, 1984), Suresh (1998). Among those, plasticity-induced crack closure is most common in ductile metals (Fig. 3.5b). Hereby, crack flank contact is caused by residual compressive stresses in the plastic wake of the growing fatigue crack (Elber 1970, 1971).

According to Elber (1970, 1971), crack flank contact significantly influences the driving force for fatigue crack growth, since crack growth can only occur during that portion of the load cycle where the crack flanks are separated. Therefore, Elber (1970, 1971) proposed a modification of Eq. (3.5) by using the effective stress intensity range $\Delta K_{eff} = K_{max} - K_{op}$ in order to account for crack closure; K_{op} is the stress intensity at the load F_{op} where the crack fully opens during re-loading. The crack opening load F_{op} is commonly determined from the

compliance changes in the load–displacement (F–v) curve, which are visible as kinks (e.g. Elber 1970, 1971; Suresh 1998); Fig. 3.3c provides an example. It should be mentioned that there is no straightforward approach for the determination of F_{op} since crack opening occurs, under constant fatigue loads, continuously forward to the current crack tip; similar to the peel away of a tape. During unloading, the crack flanks close continuously backward from the crack tip (Suresh 1998). So it can happen that the crack tip is still closed when detecting crack opening from far-field displacement measurements; see "local crack closure" in Riddell et al. (1999).

The modification of Eq. (3.5) by using ΔK_{eff} has been very successful in correlating da/dN for many metals under various cyclic loading conditions (e.g. in Anderson 1995 and Suresh 1998). Furthermore, the crack closure phenomenon provides an explanation for the strong influence of the fatigue crack growth rate on the load ratio R, i.e. the ratio between minimum and maximum load during cyclic loading, $R = F_{min} / F_{max}$: Since crack flank contact is less pronounced for higher values of R, fatigue cracks grow faster with increasing load ratio at ΔK = *constant* (Suresh 1998). Other well-known influence factors on the fatigue crack growth behavior, e.g. microstructure and environment, can be explained with roughness- and oxide-induced crack closure; see Suresh (1998) for details on this topic. The reason for the different crack growth behavior of short fatigue cracks is also attributed to crack closure (e.g. Maierhofer et al. 2014, 2015; Suresh 1998).

In the current thesis, plasticity-induced crack closure will be of major importance.

3.3.3 The cyclic J-integral – theory and experiment

For the regime of elastic–plastic fracture mechanics, also referred to as the low-cycle fatigue (LCF) regime, the cyclic J-integral ΔJ or the cyclic crack tip opening displacement $\Delta \delta_t$ is commonly used instead of ΔK. Since, $\Delta \delta_t$ is connected to expensive experimental or numerical effort (e.g. Kolednik and Stüwe 1985, Siegmund et al. 1990, Solanki et al. 2003, 2004), a global parameter like the J-integral seems to be more favourable.

The parameter ΔJ is a contour integral for cyclic loading, analogously to the J-integral for monotonic loading, Eq. (3.3), (Lamba 1975; Wüthrich 1982; Tanaka 1983)

$$\Delta J = \int_{\Gamma} \left(\phi(\Delta\boldsymbol{\varepsilon})\,\mathrm{d}y - \Delta\mathbf{t} \cdot \frac{\partial(\Delta\mathbf{u})}{\partial x}\,\mathrm{d}s \right). \tag{3.6}$$

In Eq. (3.6), the symbol Δ refers to the relative change of the parameters between two loading stages. The quantity $\phi(\Delta\boldsymbol{\varepsilon})$ denotes the cyclic strain energy density,

$$\phi(\Delta\boldsymbol{\varepsilon}) = \int_{0}^{\Delta\boldsymbol{\varepsilon}} \Delta\boldsymbol{\sigma} \cdot \mathrm{d}(\Delta\boldsymbol{\varepsilon}); \tag{3.7}$$

The "Appendix" in Section 6 presents details on the *correct* calculation of Eq. (3.7). It is important to point out that, due to the definition of Eq. (3.7), ΔJ cannot be interpreted as the difference between the J-values at maximum and minimum load of a load cycle, $\Delta J \neq J_{max} - J_{min}$ (e.g. Anderson 1995). This can be also shown from the relation between

$\Delta\delta_t$ and ΔK, after substitution of $J = K^2/E$; see Section 6.5.2. At the moment it is not clear how ΔJ should be expressed with J_{max} and J_{min}, see Introduction.

Since the cyclic *J*-integral ΔJ relies on the assumption of deformation theory of plasticity, ΔJ exhibtis the same properties and limitations as outlined in Section 3.2 for the *J*-integral. However, since cyclic loading and crack extension seriously violate the basic assumptions leading to the *J*-integral and only incremental theory of plasticity correctly describes the real elastic–plastic material behavior, ΔJ is a questionable parameter for the description of the fatigue crack propagation rate in elastic–plastic materials (e.g. Anderson 1995).

Despite these doubts, Dowling and Begley (1976) proposed the experimental cyclic *J*-integral ΔJ^{exp} as driving force parameter for characterizing the growth rate of fatigue cracks in the regime of LCF. The parameter ΔJ^{exp} can be determined for deeply notched bending type specimens, similar to the experimental *J*-integral J^{exp}, Eq. (3.4), from the relation

$$\Delta J^{exp} = \frac{\eta \Delta A}{bB}. \tag{3.8}$$

For re-loading, the quantity ΔA denotes the area between a horizontal line at minimum load and the loading branch of the load–displacement (*F*–*v*) record (Fig. 3.3b). For unloading phases, ΔA is determined between the unloading brach of the *F*–*v*-curve and the horizontal line at maximum load.

Analogously to ΔK_{eff}, it is possible to determine an effective value of the experimental cyclic *J*-integral, ΔJ_{eff}^{exp}, in order to account for crack closure (Dowling and Begley 1976). In this case, ΔA is determined from the load F_{op} where the crack fully opens during re-loading (Fig. 3.3c). On the contrary, ΔA is determined to the load F_{cl} where crack flank contact appears during unloading.

Note that Eq. (3.8) is used for *long* fatigue cracks. Dowling (1977) presents a different formula for the evaluation of ΔJ^{exp} for short fatigue cracks.

Despite the theoretical restrictions of the *J*-integral for cyclic loading, Section 3.2.1, Dowling and Begley (1976) found a power law characterization similar to Eq. (3.5) based on ΔJ^{exp}. In many subsequent experimental and numerical studies, it has been confirmed that ΔJ^{exp} correlates to d*a*/d*N* for specific elastic–plastic materials under certain cyclic loading conditions, see e.g. Dowling (1976), Lambert et al. (1988), Banks-Sills and Volpert (1991); Section 6.2.2 provides details about these studies. Moreover, it has been confirmed by Lambert et al. (1988) and Banks-Sills and Volpert (1991), that Eq. (3.6) and Eq. (3.8) are in principle equivalent, $\Delta J = \Delta J^{exp}$. Recent finite element studies present the ability of ΔJ, Eq. (3.6), for the assessment of the fatigue lifetime of some elastic–plastic components under specific cyclic loading conditions (e.g. Vormwald 2014, 2015; Metzger et al. 2015). However, they do *not* provide new insights about the real physical meaning of the conventional cyclic *J*-integral.

Therefore, it can be concluded that there are lingering doubts of whether ΔJ and ΔJ^{exp} are physically appropriate to assess fatigue crack propagation in elastic–plastic materials due to the assumption of deformation plasticity (Anderson 1995, Suresh 1998).

“All life is problem solving.”

Sir Karl R. Popper, 1902–1994

4 Concept of configurational forces

The configurational force concept provides a convenient framework for studying fracture mechanics problems, see e.g. Maugin and Trimarco (1992), Gurtin and Podio-Guidugli (1996), Honein and Hermann (1997), Simha et al. (2003, 2005, 2008), Kolednik et al. (2009, 2010, 2014), Fischer et al. (2007; 2012a,b; 2014), Sistaninia and Kolednik (2014). A big advantage of this concept is that it enables the derivation of *J*-integrals without making any assumptions about the constitutive nature of the material; in contrast to the classical *J*-integral by Rice (1968a,b).

The configurational force concept is explained in books and articles, e.g., by Maugin (1995, 2011), Gurtin (1995, 2000), Kienzler and Herrmann (2000). Kolednik et al. (2014) provide a summary of the state of the art for the application of configurational forces in fracture mechanics, and an extensive review about the derivation of *J*-integrals, based on Simha et. al (2003, 2005, 2008).

The purpose of this chapter is to present the configurational force framework by Gurtin (1995, 2000), to show the relations between *J*-integrals and configurational forces (e.g. Simha et al. 2003), and to elucidate how the *J*-integral for elastic–plastic materials with incremental plasticity, J^{ep}, has been derived by Simha et al. (2008).

Before, it might be necessary to answer the questions: What are configurational forces, and why are they necessary?

4.1 Idea of configurational forces

Configurational forces are thermodynamic driving forces which are appropriate for the quantitative description of the behavior of various types of defects in materials, such as voids, dislocations, cracks, interfaces or phase boundaries (Eshelby 1951, 1970). A configurational force at a defect appears, if the total potential energy of the system varies for different positions of the defect in the material. The driving force tries to move a defect in such a way that the total potential energy of the system decreases; this is a consequence of the second law of thermodynamics.

Crack growth corresponds to the movement of the crack tip from one material point to another in the *reference configuration* (Fig. 4.1, *lower row*). This movement cannot be described only by the classical *deformational* (or *Newtonian*) forces that act in the current configuration (*upper row* in Fig. 4.1). A new force system must be introduced which enables the description of the thermodynamic driving force on the crack tip, i.e. *configurational forces* (Gurtin 1995, 2000). Nevertheless, crack growth requires energy that is provided by deformation: zero deformation means zero potential energy and no crack driving force, see Eq. (3.1).

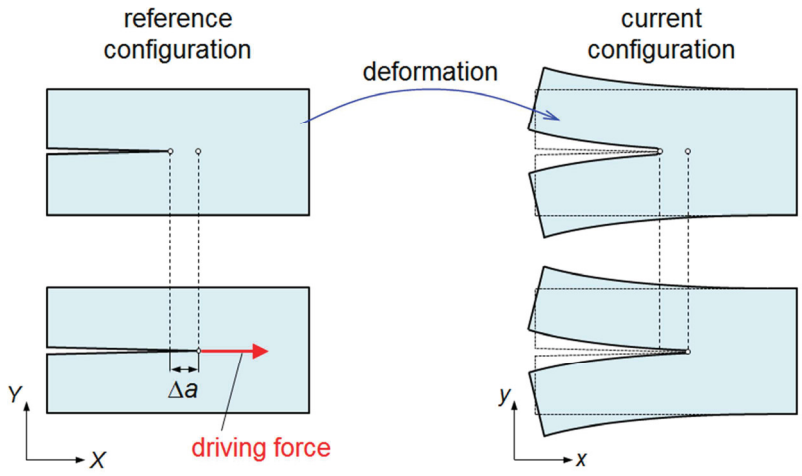

Fig. 4.1 Crack extension Δa is considered as a motion in the reference configuration, driven by a configurational force (*lower row*). Classic deformational forces cannot describe the movement of the crack tip between two material points (*upper row*).

4.2 Configurational framework

There are three main steps in the derivation of the configurational framework: formulation of (i) balance of deformational forces, (ii) balance of configurational forces, and (iii) dissipation inequality for the body under consideration (Simha et al. 2003).

4.2.1 Balance of deformational- and configurational forces

In Gurtin's (1995, 2000) approach configurational forces can be interpreted as separate force system that drives kinematic changes in the reference configuration and satisfies, parallel to deformational forces, their own balance laws (e.g. Simha et al. 2003). These balance laws can be obtained, e.g., by using free body diagrams in the reference configuration.

In the following we apply a simple two-dimensional setting in absence of inertia, heating and body forces. Figure 4.2a shows a homogeneous body $\mathcal{B}$ containing a crack in the reference configuration; the subscript "0", Section 2.1, is omitted henceforth. Note that *no* assumptions about the constitutive relations of the body are made.

Figures 4.2b,c show deformational and configurational forces acting on an arbitrary cut-out region $\mathcal{D}$ containing the crack tip. Figure 4.2b shows that only the contact force due to the bulk stress $\mathbf{S}$, i.e. the surface traction $\mathbf{t} = \mathbf{S}\,\mathbf{m}$ (Section 2.2), acts on the boundary $\partial\mathcal{D}$. Thus, the global balance of the deformational forces reads,

$$\int_{\partial\mathcal{D}} \mathbf{S}\,\mathbf{m}\,\mathrm{d}s = \mathbf{0} \qquad \text{for every subregion } \mathcal{D} \subset \mathcal{B}\,, \tag{4.1}$$

compare Eq. (2.6); $\mathrm{d}s$ denotes an increment along and $\mathbf{m}$ the unit normal to $\partial\mathcal{D}$.

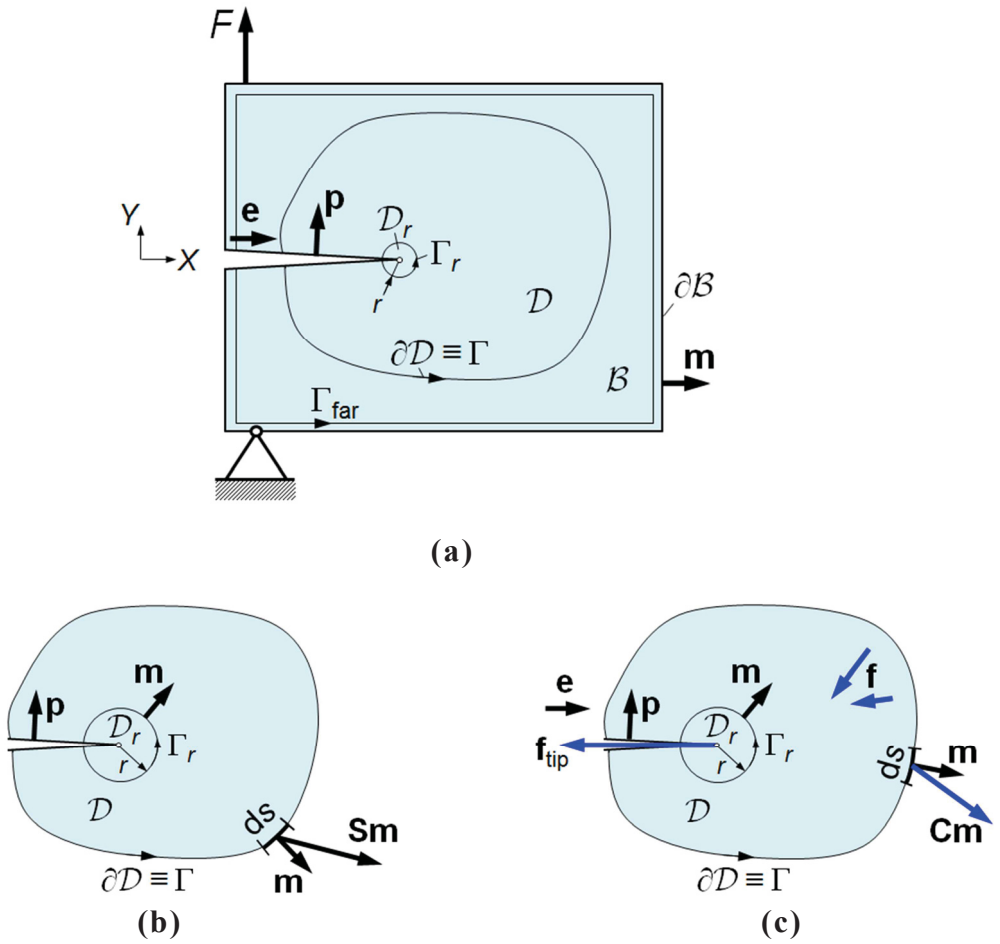

Fig. 4.2 **(a)** Two-dimensional, homogeneous body $\mathcal{B}$ with a sharp crack in the reference configuration; the direction of crack growth is **e**. The area $\mathcal{D}$ is a subregion of $\mathcal{B}$ containing the crack tip. Region $\mathcal{D}_r$ of radius r is centered at the crack tip. **(b) (c)** show free body diagrams for the deformational- and configurational force system, respectively. The configurational force system **(c)** considers internal body forces **f** and a driving force $\mathbf{f}_{\text{tip}}$ emanating from the crack tip.

Gurtin (1995, 2000) postulates the existence of a (global) configurational force balance (e.g. Simha et al. 2003)

$$\int_{\partial\mathcal{D}} \mathbf{C}\mathbf{m}\,\mathrm{d}s + \int_{\mathcal{D}} \mathbf{f}\,\mathrm{d}A + \mathbf{f}_{\text{tip}} = \mathbf{0} \qquad \text{for every subregion } \mathcal{D} \subset \mathcal{B}\,. \tag{4.2}$$

Here, $\mathbf{C}$ denotes the *bulk configurational stress,* and the configurational traction $\mathbf{C}\mathbf{m}$ acts on $\partial\mathcal{D}$, analogously to the traction stress in the deformational force system. Furthermore, bulk configurational forces $\mathbf{f}$ act within $\mathcal{D}$ and a single configurational force emerges at the crack tip $\mathbf{f}_{\text{tip}}$; see next section. It should be mentioned that the validity of Eq. (4.2) has been verified, e.g., in Maugin (1995) using an alternative method to Gurtin (1995, 2000).

For the local forms of the balances we have to consider that $\mathcal{D}$ intersects the crack flanks and contains the crack tip. Therefore, the divergence theorem must be modified in order to

account for singular stresses at the crack tip: a disk $\mathcal{D}_r$ of radius r centered at the crack tip is removed—as in *classical potential theory*—and the divergence theorem is applied for $\mathcal{D} \setminus \mathcal{D}_r$ where r tends to zero (Fig. 4.2a); the appendix in Simha et al. (2003) presents mathematical details about the modified divergence theorem. Localizing of Eq. (4.1) leads to (Simha et al. 2003):

$$\nabla \cdot \mathbf{S} = \mathbf{0} \qquad \text{at each point in } \mathcal{D} \subset \mathcal{B}, \tag{4.3}$$

$$[\![\mathbf{S}]\!]\mathbf{p} = \mathbf{0} \qquad \text{on the crack flanks,} \tag{4.4}$$

$$\lim_{r \to 0} \int_{\Gamma_r} \mathbf{S}\mathbf{m} \, \mathrm{d}s = \mathbf{0} \qquad \text{at the crack tip.} \tag{4.5}$$

Equation (4.3) is the translational equilibrium condition of continuum mechanics, see Eq. (2.7) in Sect. 2.3. Equation (4.4) states stress continuity along the traction free crack flanks; $[\![\cdot]\!]$ denotes the jump of a quantity, $\mathbf{p}$ is the unit normal to the crack flank. Equation (4.5) describes the limit value of the singular stress field at the crack tip; Γ_r designates a contour at distance r around the crack tip. It should be mentioned that Eqs. (4.3) – (4.5) are satisfied by the stress intensity (K-) field of LEFM (Simha et al. 2003).

Accordingly, we obtain from Eq. (4.2) for the configurational force system (e.g. Simha et al. 2003):

$$\nabla \cdot \mathbf{C} + \mathbf{f} = \mathbf{0} \qquad \text{at each point in } \mathcal{D} \subset \mathcal{B}, \tag{4.6}$$

$$[\![\mathbf{C}]\!]\mathbf{p} = \mathbf{0} \qquad \text{on the crack flanks,} \tag{4.7}$$

$$\lim_{r \to 0} \int_{\Gamma_r} \mathbf{C}\mathbf{m} \, \mathrm{d}s + \mathbf{f}_{\mathrm{tip}} = \mathbf{0} \qquad \text{at the crack tip.} \tag{4.8}$$

From Eqs. (4.6) and (4.8) we can define the configurational forces in the bulk and at the crack tip, $\mathbf{f}$ and $\mathbf{f}_{\mathrm{tip}}$. Remains only the definition of the bulk configurational stress tensor $\mathbf{C}$, also called *Eshelby tensor*, which is the central quantity in the theory of configurational forces (Eshelby 1951, 1970; Gurtin 1995, 2000).

4.2.2 Dissipation inequality and derivation of Eshelby's tensor

In this section we will elucidate how the configurational force tensor $\mathbf{C}$ has been derived by Gurtin (1995, 2000) from the *dissipation inequality*, Eq. (2.9); see also Simha et al. (2003).

Deformational forces act in the current configuration, hence, they perform work over positional changes in (*Euclidean*) space. Configurational forces act and perform work over positional changes in the reference configuration (Gurtin 2000).

In order to formulate a "configurational work", Gurtin (1995, 2000) introduces a *control volume* $\mathcal{D}(t)$ that *migrates* in an undeformed, three-dimensional body $\mathcal{B}$ (Fig. 4.3a).[6]

[6] Note that the *part* $\mathcal{D}_0$ in Fig. 2.1a designates a fixed subregion in the reference body $\mathcal{B}_0$, and the time t refers to the motion of $\mathcal{D}_0$ into the deformed part $\mathcal{D}$ (Gurtin 2000).

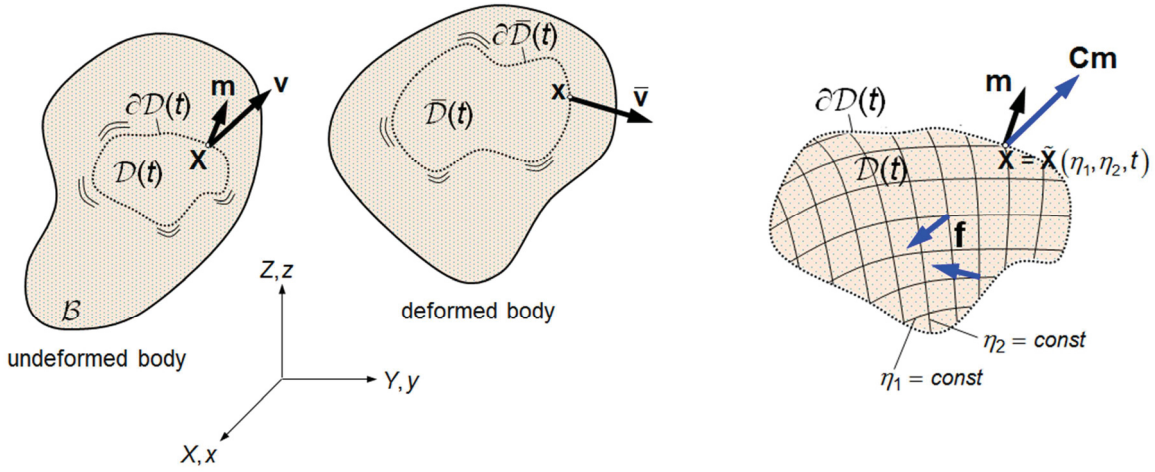

(a) **(b)**

Fig. 4.3 **(a)** Time-dependent control volume $\mathcal{D}(t)$ that migrates in the reference body $\mathcal{B}$ with a velocity field $\mathbf{v}$ of the boundary $\partial\mathcal{D}(t)$. After motion, $\mathcal{D}(t)$ deforms into $\bar{\mathcal{D}}(t)$ with a corresponding velocity $\bar{\mathbf{v}}$ of $\partial\bar{\mathcal{D}}(t)$ (see Gurtin 1995, 2000). **(b)** Cut-out volume $\mathcal{D}(t)$ with parameterized surface $\partial\mathcal{D}(t)$: the configurational traction force **Cm** acts on $\partial\mathcal{D}(t)$; configurational body forces **f** act inside $\mathcal{D}(t)$.

Migration means that $\mathcal{D}(t)$ evolves in the reference configuration with time t, while material transfer occurs across the boundary $\partial\mathcal{D}(t)$. Hereby, *material points* remain fixed and the material transfer occurs only due to the motion of $\mathcal{D}(t)$; see Gurtin (2000) for details.

Configurational forces perform work in conjunction with this material transfer. In order to define the work associated with the change of shape and volume of $\mathcal{D}(t)$, the velocity of $\partial\mathcal{D}(t)$ is required. The boundary $\partial\mathcal{D}(t)$ can be described by local parametrization by (e.g. Gurtin 1995),

$$\partial\mathcal{D}(t)=\left\{\mathbf{X}\in\mathcal{B}:\mathbf{X}=\tilde{\mathbf{X}}(\eta_1,\eta_2,t)\right\}, \tag{4.9}$$

where η_1 and η_2 denote scalar parameters (Fig. 4.3b). The time derivative of Eq. (4.9) yields the velocity $\mathbf{v}$ of $\partial\mathcal{D}(t)$,

$$\mathbf{v}=\frac{\partial\mathbf{X}}{\partial t}=\left.\frac{\partial\tilde{\mathbf{X}}(\eta_1,\eta_2,t)}{\partial t}\right|_{\eta_1,\eta_2}, \tag{4.10}$$

for fixed values of η_1 and η_2; see Gurtin (1995).

After motion of $\mathcal{B}$, Eq. (2.1), the local parametrization Eq. (4.9) results a corresponding local parametrization of the boundary $\partial\bar{\mathcal{D}}(t)$ of the migrating control volume $\bar{\mathcal{D}}(t)$ in the deformed body (Gurtin 1995). The velocity $\bar{\mathbf{v}}$ for the evolution of $\partial\bar{\mathcal{D}}(t)$ is given after application of the chain rule by (e.g. Gurtin 1995),

$$\bar{\mathbf{v}}=\frac{\partial\mathbf{x}}{\partial t}=\left.\frac{\partial\mathbf{x}\left(\tilde{\mathbf{X}}(\eta_1,\eta_2,t)\right)}{\partial t}\right|_{\eta_1,\eta_2}=\frac{\partial\mathbf{x}}{\partial t}+\frac{\partial\mathbf{x}}{\partial\mathbf{X}}\frac{\partial\tilde{\mathbf{X}}}{\partial t},$$

$$\overline{\mathbf{v}} = \dot{\mathbf{x}} + \mathbf{F}\,\mathbf{v}\,. \tag{4.11}$$

The velocity $\overline{\mathbf{v}}$ is composed of the "motion velocity" $\dot{\mathbf{x}}$, compare $\mathbf{w}$ in Eq. (2.2), and "the velocity $\mathbf{F}\,\mathbf{v}$ at which deformed material is being transferred to $\partial\overline{\mathcal{D}}(t)$"; see Gurtin (2000), p. 31.

Now, the working rate $\mathcal{W}\big(\mathcal{D}(t)\big)$, Eq. (2.9), can be formulated. The rate at which work is performed on $\mathcal{D}(t)$ consists of the *deformational-* and *configurational working*: deformational forces perform work over velocities conjugate to the deformed configuration; configurational forces perform work over reference velocities (e.g. Gurtin 1995, Simha et al. 2003). Consequently, the working rate reads (Gurtin 1995),

$$\mathcal{W}\big(\mathcal{D}(t)\big) = \int_{\partial\mathcal{D}(t)} \big(\mathbf{S}\mathbf{m}\cdot\big(\dot{\mathbf{x}}+\mathbf{F}\,\mathbf{v}\big)+\mathbf{C}\mathbf{m}\cdot\mathbf{v}\big)\,\mathrm{d}A\,. \tag{4.12}$$

The term $\mathbf{S}\mathbf{m}\cdot\dot{\mathbf{x}}$ is the classical deformational working per unit area, if $\mathcal{D}(t)$ is not a migrating volume but stationary. $\mathbf{S}\mathbf{m}\cdot\big(\mathbf{F}\,\mathbf{v}\big)$ accounts for the additional deformation due to the material transfer over $\partial\mathcal{D}(t)$. The term $\mathbf{C}\mathbf{m}\cdot\mathbf{v}$ represents the working per unit area due to the material entering or leaving the evolving control volume $\mathcal{D}(t)$, see Gurtin (1995, 2000). Note that bulk configurational forces $\mathbf{f}$ perform no work since material points inside $\mathcal{D}(t)$ do not move (Simha et al. 2003).

The internal energy $\mathcal{E}$ of region $\mathcal{D}(t)$ is given by,

$$\mathcal{E}\big(\mathcal{D}(t)\big) = \int_{\mathcal{D}(t)} \phi\,\mathrm{d}V\,, \tag{4.13}$$

with ϕ as the (Helmholtz) free energy per unit volume, see Sections 2.3 and 2.5.1. Application of *Reynolds' transport theorem* leads to (e.g. Simha et al. 2003),

$$\frac{\mathrm{d}\mathcal{E}\big(\mathcal{D}(t)\big)}{\mathrm{d}t} = \int_{\mathcal{D}(t)} \dot{\phi}\,\mathrm{d}V + \int_{\partial\mathcal{D}(t)} \phi\mathbf{v}\cdot\mathbf{m}\,\mathrm{d}A\,. \tag{4.14}$$

With Eq. (4.12) and Eq. (4.14), we are able to express the dissipation of $\mathcal{D}(t)$, e.g. Simha et al. (2003),

$$\Psi\big(\mathcal{D}(t)\big) = \int_{\partial\mathcal{D}(t)} \big(\mathbf{S}\mathbf{m}\cdot\big(\dot{\mathbf{x}}+\mathbf{F}\,\mathbf{v}\big)+\mathbf{C}\mathbf{m}\cdot\mathbf{v}-\phi\mathbf{v}\cdot\mathbf{m}\big)\,\mathrm{d}A - \int_{\mathcal{D}(t)} \dot{\phi}\,\mathrm{d}V \geq 0\,. \tag{4.15}$$

The expression for the configurational stress tensor $\mathbf{C}$ follows from the requirement that Eq. (4.15) must be independent of changes in the parametrization for $\partial\mathcal{D}(t)$ and $\mathbf{v}$, respectively. This is equivalent to invariance of the working (Gurtin 1995). Rearrangement of Eq. (4.15) gives

$$\Psi\big(\mathcal{D}(t)\big) = \int_{\partial\mathcal{D}(t)} \Big(\mathbf{S}\mathbf{m}\cdot\dot{\mathbf{x}}+\big(\mathbf{F}^{\mathrm{T}}\mathbf{S}\mathbf{m}+\mathbf{C}\mathbf{m}\big)\cdot\mathbf{v}-\phi\mathbf{v}\cdot\mathbf{m}\Big)\,\mathrm{d}A - \int_{\mathcal{D}(t)} \dot{\phi}\,\mathrm{d}V \geq 0\,. \tag{4.16}$$

Since only the normal component of the velocity, $\mathbf{v}\cdot\mathbf{m}$, is not affected by reparametrization, the term $\left(\mathbf{F}^{\mathrm{T}}\mathbf{S}\mathbf{m}+\mathbf{C}\mathbf{m}\right)$ must be parallel to $\mathbf{m}$ for all lengths α of $\mathbf{m}$, hence, $\left(\mathbf{F}^{\mathrm{T}}\mathbf{S}+\mathbf{C}\right)\mathbf{m}=\alpha\mathbf{m}$. This leads to (Gurtin 1995)

$$\mathbf{C}=\alpha\mathbf{I}-\mathbf{F}^{\mathrm{T}}\mathbf{S}, \tag{4.17}$$

where $\mathbf{I}$ denotes the identity tensor. Substitution of Eq. (4.17) into Eq. (4.16) and transformation gives (Simha et al. 2003)

$$\Psi\left(\mathcal{D}(t)\right)=\int_{\partial\mathcal{D}(t)}\left(\phi-\alpha\right)\mathbf{v}\cdot\mathbf{m}\,\mathrm{d}A+\int_{\mathcal{D}(t)}\left(\mathbf{S}\cdot\dot{\mathbf{F}}-\dot{\phi}\right)\mathrm{d}V\geq 0\,. \tag{4.18}$$

In Eq. (4.18), $\dot{\mathbf{F}}$ denotes the Lagrangian time derivative of $\mathbf{F}$. The scalar α is denominated as "bulk tension" in Gurtin (1995); it works to increase the volume of $\mathcal{D}(t)$ through the accumulation of material across the boundary $\partial\mathcal{D}(t)$.

Now, it can be shown that α is equal to the free energy ϕ; see Gurtin (1995) or Simha et al. (2003). Consider a second subregion $\mathcal{D}'(t)\subset\mathcal{B}$ that matches with $\mathcal{D}(t)$ at initial time, but the boundary $\partial\mathcal{D}'(t)$ has a different velocity $\mathbf{v}'\neq\mathbf{v}$. The dissipation $\Psi\left(\mathcal{D}'(t)\right)$ is similar to Eq. (4.15) or Eq. (4.18); only $\mathbf{v}'$ appears instead of $\mathbf{v}$. In order to ensure a non-negative dissipation in any part of $\mathcal{B}$, the bulk tension α must be identical to the bulk free energy ϕ; an analogon is the coincidence of surface tension and surface free energy (Gurtin 1995). This gives the expression of the configurational stress tensor (Gurtin 1995)

$$\mathbf{C}=\phi\mathbf{I}-\mathbf{F}^{\mathrm{T}}\mathbf{S}, \tag{4.19}$$

which is equal to Eshelby's "energy momentum tensor" (Eshelby 1970). Inserting $\alpha=\phi$ into Eq. (4.18) gives the dissipation inequality of the sub-volume $\mathcal{D}(t)$,

$$\Psi\left(\mathcal{D}(t)\right)=\int_{\mathcal{D}(t)}\left(\mathbf{S}\cdot\dot{\mathbf{F}}-\dot{\phi}\right)\mathrm{d}V\geq 0\,; \tag{4.20}$$

compare Eq. (2.10).

Now, since the configurational stress $\mathbf{C}$ is known, the configurational forces in the bulk and at the crack tip, $\mathbf{f}$ and $\mathbf{f}_{\mathrm{tip}}$, can be expressed after rearrangement of the balance equations (3.6) and (3.8), see Simha et al. (2003):

$$\mathbf{f}=-\nabla\cdot\mathbf{C}=-\nabla\cdot\left(\phi\mathbf{I}-\mathbf{F}^{\mathrm{T}}\mathbf{S}\right), \tag{4.21}$$

$$\mathbf{f}_{\mathrm{tip}}=-\lim_{r\to 0}\int_{\Gamma_r}\left(\phi\mathbf{I}-\mathbf{F}^{\mathrm{T}}\mathbf{S}\right)\mathbf{m}\,\mathrm{d}s\,. \tag{4.22}$$

Equation (4.21) implies that a configurational force $\mathbf{f}$ appears on those positions in the body where the divergence of the configurational stress tensor $\mathbf{C}$ does not vanish, which is at the position of a defect (e.g. Kolednik et al. 2014). The vector $\mathbf{f}$ determines magnitude and

direction of the thermodynamic driving force on a defect, such as, for example, $\mathbf{f}_{\text{tip}}$ for the crack tip.

At this point it should be noted that the derivation of **C,** and consequently of $\mathbf{f}$ and $\mathbf{f}_{\text{tip}}$, has been done *independent* of any assumptions about ϕ. So the derivations of Eqs. (4.19), (4.21), and (4.22) are valid for dissipative materials, like elastic–plastic materials (Gurtin 1995, Simha et al. 2003).

4.3 Configurational forces and J-integrals

4.3.1 General relations

The dissipation inequality for a cracked body leads to the definition of the crack driving force (e.g. Simha et al. 2003). We consider again our two-dimensional setting of Fig. 4.2. The total dissipation in a subregion $\mathcal{D} \subset \mathcal{B}$ containing the crack tip is given by (Gurtin and Podio-Guidugli 1996)

$$\Psi(\mathcal{D}) = \Psi_{\text{bulk}} + \Psi_{\text{tip}} = \int_{\mathcal{D}} \left(\mathbf{S} \cdot \dot{\mathbf{F}} - \dot{\phi} \right) \mathrm{d}A + \left(-\mathbf{f}_{\text{tip}} \right) \cdot \mathbf{v}_{\text{tip}} \geq 0 \,, \tag{4.23}$$

i.e. the dissipation in the bulk, including plastic dissipation, plus the dissipation due to the crack tip propagation (in the reference configuration) with a velocity $\mathbf{v}_{\text{tip}}$. Note that there is no working of the deformational forces at the crack tip due to Eq. (4.5), see Simha et al. (2003). Localizing Eq. (4.23) yields the bulk dissipation at each material point, Eq. (2.10), and due to the movement of the crack tip (Simha et al. 2003),

$$\psi_{\text{tip}} = \left(-\mathbf{f}_{\text{tip}} \right) \cdot \mathbf{v}_{\text{tip}} \geq 0 \,. \tag{4.24}$$

In fracture mechanics, the energy dissipated per unit crack extension is equal to the crack driving force (Section 3.1). Since $\left(-\mathbf{f}_{\text{tip}} \right)$ is the force term conjugate to the crack tip velocity $\mathbf{v}_{\text{tip}}$, the negative configurational force at the crack tip $\left(-\mathbf{f}_{\text{tip}} \right)$ can be identified as the thermodynamic crack driving force, which is characterized, e.g., by the near-tip *J*-integral vector $\mathbf{J}_{\text{tip}} = \left(-\mathbf{f}_{\text{tip}} \right)$, see e.g. Simha et al. (2003). In order to get the common scalar *J*-integral, the *J*-integral vector must be projected into the nominal crack growth direction $\mathbf{e} = \mathbf{v}_{\text{tip}} \big/ \left| \mathbf{v}_{\text{tip}} \right|$. The near-tip *J*-integral J_{tip} by Rice (1968a,b), Sect. 3.2, is expressed by the relation (Simha et al. 2003)

$$J_{\text{tip}} = \mathbf{e} \cdot \left(-\mathbf{f}_{\text{tip}} \right) = \mathbf{e} \cdot \mathbf{J}_{\text{tip}} = \mathbf{e} \cdot \lim_{r \to 0} \int_{\Gamma_r} \left(\phi \mathbf{I} - \mathbf{F}^{\mathrm{T}} \mathbf{S} \right) \mathbf{m} \, \mathrm{d}s \,. \tag{4.25}$$

The *J*-integral for a specific contour Γ and the far-field *J*-integral, J_{far}, are derived from the configurational force balance for a region $\mathcal{D} \setminus \mathcal{D}_r$, i.e. without the circle containing the crack tip, Fig. 4.2c, (Simha et al. 2003)

$$\int_{\mathcal{D} \setminus \mathcal{D}_r} \mathbf{f} \, \mathrm{d}A + \int_{\partial \mathcal{D}} \mathbf{C}\mathbf{m} \, \mathrm{d}s + \int_{\Gamma_r} \mathbf{C}\left(-\mathbf{m} \right) \mathrm{d}s = \mathbf{0} \,. \tag{4.26}$$

If r tends to zero, so that the crack tip contour vanishes, the balance can be written in the form

$$\lim_{r\to 0}\int_{\Gamma_r}\mathbf{C}\mathbf{m}\,\mathrm{d}s-\int_{\partial\mathcal{D}}\mathbf{C}\mathbf{m}\,\mathrm{d}s=\int_{\mathcal{D}\setminus\mathrm{tip}}\mathbf{f}\,\mathrm{d}A\,, \tag{4.27}$$

The scalar product of this equation with $\mathbf{e}$ yields (Simha et al. 2003)

$$J_{\mathrm{tip}}-J_{\Gamma}=\mathbf{e}\cdot\int_{\mathcal{D}\setminus\mathrm{tip}}\mathbf{f}\,\mathrm{d}A\,, \tag{4.28}$$

where J_{Γ} is the scalar J-integral for any desired contour Γ,

$$J_{\Gamma}=\mathbf{e}\cdot\mathbf{J}_{\Gamma}=\mathbf{e}\cdot\int_{\Gamma}\left(\phi\mathbf{I}-\mathbf{F}^{\mathrm{T}}\mathbf{S}\right)\mathbf{m}\,\mathrm{d}s=J_{\mathrm{tip}}-\mathbf{e}\cdot\int_{\mathcal{D}\setminus\mathrm{tip}}\mathbf{f}\,\mathrm{d}A\,; \tag{4.29}$$

$\mathbf{J}_{\Gamma}$ is the J-integral vector. The far-field J-integral J_{far} on contour Γ_{far}, is obtained for letting Γ become a contour adjacent to the external boundary $\partial\mathcal{B}$ of the body, Fig. 4.2a,

$$J_{\mathrm{far}}=\mathbf{e}\cdot\mathbf{J}_{\mathrm{far}}=\mathbf{e}\cdot\int_{\Gamma_{\mathrm{far}}}\left(\phi\mathbf{I}-\mathbf{F}^{\mathrm{T}}\mathbf{S}\right)\mathbf{m}\,\mathrm{d}s=J_{\mathrm{tip}}-\mathbf{e}\cdot\int_{\mathcal{B}\setminus\mathrm{tip}}\mathbf{f}\,\mathrm{d}A\,. \tag{4.30}$$

The physical meaning of J_{far} is that of the driving force inserted into the body by the applied load (Kolednik et al. 2014). Equation (4.30) gives also the relation between J_{tip} and J_{far} (Simha et al. 2003),

$$J_{\mathrm{tip}}-J_{\mathrm{far}}=\mathbf{e}\cdot\int_{\mathcal{B}\setminus\mathrm{tip}}\mathbf{f}\,\mathrm{d}A\,; \tag{4.31}$$

the integral is taken over the entire body excluding the crack tip, $\mathcal{B}\setminus\mathrm{tip}$ (and the boundary $\partial\mathcal{B}$). The right term in Eq. (4.31) can be used to describe the influence of plasticity on the crack driving force, see Simha et al. (2008). This will be discussed in Section 4.3.3.

It is important to reiterate that no assumptions have been made about the constitutive relations of the body. Thus, the J-integrals derived via configurational force concept are, in contrast to the classical J-integral, physically appropriate to describe true driving force terms for elastic–plastic materials with incremental theory of plasticity (Simha et al. 2008).

Configurational forces have been proven to be useful to analyze the behavior of cracks in inhomogeneous materials. The configurational force concept treats material transitions (interfaces) also like defects. For *inhomogeneous* materials, configurational forces $\mathbf{f}_{\Sigma}$ are induced along the interface Σ where the material properties exhibit a change. These configurational forces $\mathbf{f}_{\Sigma}$ can be used to evaluate a "material inhomogeneity term" which enables an explanation of the effect of inhomogeneities on the crack driving force; see, e.g., Simha et al. (2003), Kolednik et al. (2009, 2010), Fischer et al. (2007; 2012a,b; 2014), Sistaninia and Kolednik (2014).

For a *homogeneous* body, the external boundary $\partial\mathcal{B}$ (Fig. 4.2a) acts like an interface between material and air. Consequently, *surface* configurational forces $\mathbf{f}_{\mathrm{S}}$ appear on $\partial\mathcal{B}$, induced by the applied load. The value of J_{far} can be also evaluated by integration of all

surface configurational forces on the external boundary $\partial\mathcal{B}$, see Fischer et al. (2012a), Kolednik et al. (2014). The integration over all configurational forces in $\mathcal{B}$ and along $\partial\mathcal{B}$ yields zero, due to translational equilibrium.

4.3.2 J-integral for elastic–plastic materials with incremental plasticity

In this section we will make assumptions about ϕ for a nonlinear elastic and an elastic–plastic material. Since the reversible part of ϕ is different for such materials, Section 2.5, differences will appear already in the evaluation of the configurational stress $\mathbf{C}$, Eq. (4.19). Consequently, the configurational forces and the *J*-integrals will be different.

First, assume that body $\mathcal{B}$, Fig. 4.4a, consists of *nonlinear elastic* material. The *total* strain energy density ϕ is reversible in nonlinear elastic materials. Substitution of ϕ into Eq. (4.21) and Eq. (4.29) yields the nonlinear elastic configurational force $\mathbf{f}^{\mathrm{nlel}}$ and nonlinear elastic *J*-integral J^{nlel},

$$J_{\Gamma}^{\mathrm{nlel}} = J_{\mathrm{tip}}^{\mathrm{nlel}} + \mathbf{e}\cdot\int_{\mathcal{D}\setminus\mathrm{tip}} \nabla\cdot\left(\phi\mathbf{I}-\mathbf{F}^{\mathrm{T}}\mathbf{S}\right)\mathrm{d}A = J_{\mathrm{tip}}^{\mathrm{nlel}} - \mathbf{e}\cdot\int_{\mathcal{D}\setminus\mathrm{tip}} \mathbf{f}^{\mathrm{nlel}}\,\mathrm{d}A\,. \tag{4.32}$$

The J^{nlel}-integral is identical to the conventional *J*-integral by Rice, Eq. (3.3), Section 3.2.

Since the crack tip is the single source of dissipation and $\mathcal{B}$ is homogeneous, bulk configurational forces do not exist, $\mathbf{f}^{\mathrm{nlel}}=\mathbf{0}$. Only a single configurational force emerges from the crack tip $\mathbf{f}_{\mathrm{tip}}^{\mathrm{nlel}}$ (Fig. 4.4a). This implies according to Eq. (4.32) that $J_{\mathrm{tip}}^{\mathrm{nlel}} = J_{\Gamma}^{\mathrm{nlel}} = J_{\mathrm{far}}^{\mathrm{nlel}}$, if Γ becomes Γ_{far}, hence, the nonlinear elastic *J*-integral is path independent (Kolednik et al. 2014). Equation (4.29) shows that the magnitude of the *J*-integral J_{Γ} and its path (in-) dependence are intimately connected to the configurational force distribution in the body (Simha et al. 2008), see below.

Next, assume that $\mathcal{B}$ consists of *elastic–plastic* material, but it is described with *deformation theory of plasticity* (Fig. 4.4b), i.e. the elastic–plastic material is treated to be nonlinear elastic (Section 2.5.2). Therefore, the *total* ϕ is also inserted into Eq. (4.21) and Eq. (4.29). The "deformation plasticity" configurational force for elastic–plastic materials shall be termed $\mathbf{f}^{\mathrm{def.pl}}$. The deformation plasticity *J*-integral for elastic–plastic materials is identical to the commonly applied conventional *J*-integral from elastic–plastic fracture mechanics, Sect. 3.2, and shall be designated accordingly,

$$J_{\Gamma}^{\mathrm{conv}} = J_{\mathrm{tip}}^{\mathrm{conv}} + \mathbf{e}\cdot\int_{\mathcal{D}\setminus\mathrm{tip}} \nabla\cdot\left(\phi\mathbf{I}-\mathbf{F}^{\mathrm{T}}\mathbf{S}\right)\mathrm{d}A = J_{\mathrm{tip}}^{\mathrm{conv}} - \mathbf{e}\cdot\int_{\mathcal{D}\setminus\mathrm{tip}} \mathbf{f}^{\mathrm{def.pl}}\,\mathrm{d}A\,. \tag{4.33}$$

The difficulties that appear for this *J*-integral have been already outlined in Section 3.2.1.

As long as the conditions of proportional are fulfilled in the elastic–plastic material, configurational forces do not appear in the body $\mathbf{f}^{\mathrm{def.pl}}=\mathbf{0}$. Therefore, J^{conv}, Eq. (4.33), is path independent. As soon as the conditions of proportional loading are disturbed, e.g. in the process zone, "artificial" bulk configurational forces $\mathbf{f}^{\mathrm{def.pl}}$ occur, which do not have any

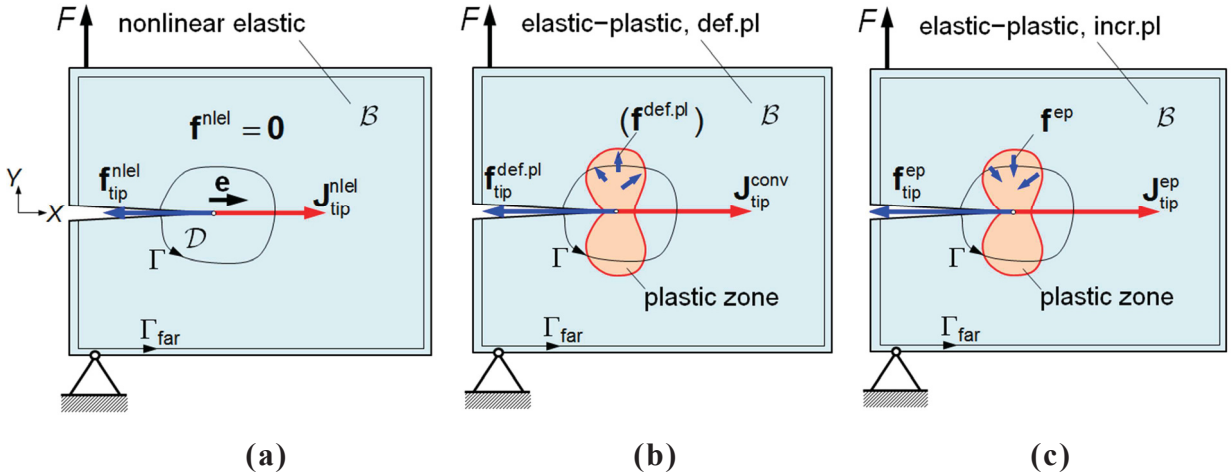

Fig. 4.4 Homogeneous body made of **(a)** nonlinear elastic material, **(b)** elastic–plastic material derscribed with deformation plasticity (*def.pl*) and **(c)** incremental plasticity (*incr.pl*). The path (in-) dependence of the *J*-integrals, J^{nlel}, J^{conv} and J^{ep}, is connected to the appearance of configurational forces in the body: if the integration contour Γ increases from the crack tip, more and more configurational forces become included, so that the magnitude of the *J*-integral changes, see Eq. (4.29). For simplicity, surface configurational forces on the external boundary are omitted.

physical background and cause J^{conv} to become path dependent (Fig. 4.4b). Kolednik et al. (2014) demonstrated in a numerical cyclic tensile test that $\mathbf{f}^{\mathrm{def.pl}}$-vectors emerge on positions with a gradient in plastic strain as soon as non-proportional loading occurs; this is also shown for crack extension under monotonic loading in Kolednik et al. (2014).

Now, assume that $\mathcal{B}$ consists of *elastic–plastic* material, correctly described by *incremental theory of plasticity* (Fig. 4.4c). Only the elastic part of the total strain energy density ϕ_{e} is recoverable. Substitution of ϕ_{e} into Eq. (4.21) and Eq. (4.29) gives the relation for the bulk configurational force $\mathbf{f}^{\mathrm{ep}}$ and the *J*-integral J^{ep} for incremental plasticity (Simha et al. 2008),

$$J^{\mathrm{ep}}_{\Gamma} = J^{\mathrm{ep}}_{\mathrm{tip}} + \mathbf{e}\cdot\int\limits_{\mathcal{D}\setminus\mathrm{tip}} \nabla\cdot\left(\phi_{\mathrm{e}}\mathbf{I} - \mathbf{F}^{\mathrm{T}}\mathbf{S}\right)\mathrm{d}A = J^{\mathrm{ep}}_{\mathrm{tip}} - \mathbf{e}\cdot\int\limits_{\mathcal{D}\setminus\mathrm{tip}} \mathbf{f}^{\mathrm{ep}}\,\mathrm{d}A\,. \tag{4.34}$$

The great advantage of the J^{ep}-integral is that it provides a *real* thermodynamic driving force term in elastic–plastic materials with incremental theory of plasticity, since the second law of thermodynamics has been invoked in the derivation (Simha et al. 2008); see Sect. 4.3.1. A further advantage is that J^{ep} is potentially applicable for the description of a growing crack under monotonic or cyclic loading. However, J^{ep} is, in general, path dependent, since bulk configurational forces $\mathbf{f}^{\mathrm{ep}}$ are induced in *plastically* deformed regions of the material, given by the relation (Simha et al. 2008)

$$\mathbf{f}^{\mathrm{ep}} = \left(\mathbf{F}^{\mathrm{e}}\right)^{\mathrm{T}}\mathbf{S} : \frac{\partial \mathbf{F}^{\mathrm{p}}}{\partial \mathbf{X}}; \tag{4.35}$$

$\mathbf{F}^{\mathrm{e}}$ and $\mathbf{F}^{\mathrm{p}}$ denote the elastic and plastic components of the deformation gradient $\mathbf{F}=\mathbf{F}^{\mathrm{e}}\mathbf{F}^{\mathrm{p}}$. Note that the matrix product $\left(\mathbf{F}^{\mathrm{e}}\right)^{\mathrm{T}}\mathbf{S}$ gives a second-order tensor, and the gradient of $\mathbf{F}^{\mathrm{p}}$, $\partial\mathbf{F}^{\mathrm{p}}/\partial\mathbf{X}$, gives a third-order tensor. Thus, we obtain a *vector* after operation ":" (see section titled "Nomenclature"). In this thesis, third-order tensors appear only in the equations for $\mathbf{f}^{\mathrm{ep}}$; see also Eq. (4.36) and Eq. (4.39). Equation (4.35) shows that $\mathbf{f}^{\mathrm{ep}}$ evolves proportional to the gradient of $\mathbf{F}^{\mathrm{p}}$. Simha et al. (2008) have derived also the expression of $\mathbf{f}^{\mathrm{ep}}$ for small-strain theory,

$$\mathbf{f}^{\mathrm{ep}}=\boldsymbol{\sigma}:\frac{\partial\boldsymbol{\varepsilon}^{\mathrm{p}}}{\partial\mathbf{x}}. \tag{4.36}$$

This equation shows that the behavior of $\mathbf{f}^{\mathrm{ep}}$ can be understood by analyzing the stress and the gradient of the plastic strain. For an easier understanding, Eq. (4.36) will be used in Sections 5–8 of this thesis for the explanation of the variations of the J^{ep}-integral.

If the body deforms only *elastically*, it is evident that configurational forces $\mathbf{f}^{\mathrm{ep}}$ do not appear in the body. Moreover, since ϕ consists only of ϕ_{e}, deformation- and incremental plasticity are equivalent, thus, J^{ep} becomes identical to the conventional J-integral J^{conv}. In Section 5.1 and Section 6, we will see that this fact plays an important role for the usefulness of J^{conv} as crack driving force parameter in elastic–plastic materials.

4.3.3 Plasticity influence term

The plastic dissipation in the bulk material can be written in the form (Simha et al. 2008)

$$\psi_{\mathrm{bulk}}=\left(\mathbf{F}^{\mathrm{e}}\right)^{\mathrm{T}}\mathbf{S}\cdot\dot{\mathbf{F}}^{\mathrm{p}}\geq 0; \tag{4.37}$$

$\dot{\mathbf{F}}^{\mathrm{p}}$ denotes the rate of $\mathbf{F}^{\mathrm{p}}$. The total dissipation in the body $\mathcal{B}$, Fig. 4.4c, can be expressed by (Simha et al. 2008)

$$\Psi\left(\mathcal{B}\right)=\Psi_{\mathrm{bulk}}+\Psi_{\mathrm{tip}}=\int_{\mathcal{B}}\left(\mathbf{F}^{\mathrm{e}}\right)^{\mathrm{T}}\mathbf{S}\cdot\dot{\mathbf{F}}^{\mathrm{p}}\,\mathrm{d}A+\left(-\mathbf{f}_{\mathrm{tip}}\right)\cdot\mathbf{v}_{\mathrm{tip}}\geq 0. \tag{4.38}$$

There are two sources of dissipation in $\mathcal{B}$: plastic deformation and crack tip propagation. The force term conjugate to the crack tip velocity is $\mathbf{J}_{\mathrm{tip}}=\left(-\mathbf{f}_{\mathrm{tip}}\right)$, Section 4.3.1. The external boundary $\partial\mathcal{B}$ does not induce dissipation since it has no velocity in the reference configuration. Thus, there is no dissipation term related explicitly to the far-field J-integral (Simha et al. 2008, Kolednik et al. 2014). The effect of plastic deformation in $\mathcal{B}$ is obtained by integrating the bulk configurational force $\mathbf{f}^{\mathrm{ep}}$, Eq. (4.35), over the whole body, but without the crack tip (Simha et al. 2008),

$$C_{\mathrm{p}}=\mathbf{e}\cdot\mathbf{C}_{\mathrm{p}}=\mathbf{e}\cdot\int_{\mathcal{B}\setminus\mathrm{tip}}\mathbf{f}^{\mathrm{ep}}\,\mathrm{d}A=\mathbf{e}\cdot\int_{\mathcal{B}\setminus\mathrm{tip}}\left(\mathbf{F}^{\mathrm{e}}\right)^{\mathrm{T}}\mathbf{S}:\frac{\partial\mathbf{F}^{\mathrm{p}}}{\partial\mathbf{X}}\,\mathrm{d}A. \tag{4.39}$$

The quantity C_{p} is denominated as *plasticity influence term*. It can be interpreted as the scalar driving force that is induced by plasticity in the body (Simha et al. 2008). In equivalence to

the scalar *J*-integral, C_p is the component of the corresponding driving force vector, $\mathbf{C}_\mathrm{p}$, in crack growth direction **e**. After substitution of Eq. (4.39) into Eq. (4.31), the difference between the near-tip and far-field *J*-integral can be written in the form (Simha et al. 2008),

$$J_{\mathrm{tip}}^{\mathrm{ep}} - J_{\mathrm{far}}^{\mathrm{ep}} = C_\mathrm{p} \,. \tag{4.40}$$

The plasticity influence term C_p, Eq. (4.40), has proven to be very useful for the theoretical analysis and the understanding of plasticity effects on the driving force of the crack tip, $J_{\mathrm{tip}}^{\mathrm{ep}}$. For example, Simha et al. (2008) showed that $C_\mathrm{p} = 0$ for nonlinear elastic materials, or deformation plasticity as long as the conditions of proportional loading remain undisturbed. This implies $J_{\mathrm{tip}}^{\mathrm{nlel}} = J_{\mathrm{far}}^{\mathrm{nlel}}$. On the contrary, due to the appearance of bulk configurational forces in elastic–plastic materials, C_p is non-zero and $J_{\mathrm{tip}}^{\mathrm{ep}} \neq J_{\mathrm{far}}^{\mathrm{ep}}$. If $C_\mathrm{p} < 0$, plasticity around the crack tip provides a *shielding effect* since the crack driving force is smaller than the driving force inserted by the applied load system, $J_{\mathrm{tip}}^{\mathrm{ep}} < J_{\mathrm{far}}^{\mathrm{ep}}$, Eq. (4.40). Crack tip *anti-shielding* occurs vice-versa. For rigid-plastic, elastic-ideal plastic and elastic–plastic materials that exhibit a linear hardening behavior, Simha et al. (2008) showed $C_\mathrm{p} = -J_{\mathrm{far}}^{\mathrm{ep}}$, which implies a *zero* crack driving force. This means that the whole driving force induced into the body by the applied load, $J_{\mathrm{far}}^{\mathrm{ep}}$, is consumed by plasticity in the bulk, so that there is no sufficient energy available to drive the crack tip. This problem has been already identified by Rice (1979), see "paradox of elastic–plastic fracture mechanics" (Section 3.2.1).

It should be mentioned that Simha et al. (2008) performed a short numerical case study to investigate the *J*-integrals J^{conv} and J^{ep} for a C(T)-specimen, made of elastic–plastic material with incremental plasticity and containing a stationary crack. They showed that the *J*-integrals on a path enclosing the process zone, are approximately equal in magnitude, $J_{\mathrm{proc.z}}^{\mathrm{ep}} \approx J_{\mathrm{proc.z}}^{\mathrm{conv}} = J_{\mathrm{far}}^{\mathrm{conv}} = J^{\mathrm{exp}}$, and they reflect the value of the experimental *J*-integral, Eq. (3.4). The near-tip *J*-integrals have been investigated extensively in Kolednik et al. (2014), see Section 5.

4.4 Numerical computation of configurational forces and J-integrals

The configurational forces and *J*-integrals are computed by a post-processing routine after a conventional finite element (FE) stress and strain analysis. For the FE program, the commercial software ABAQUS/Standard (see http://www.simulia.com/products/abaqus_fea.html) is used. The post-processing routine is written in Python, i.e. the scripting language of ABAQUS, based on Müller et al. (2002, 2004) and Denzer et al. (2003). The idea is to implement Eq. (4.21) for the computation of configurational forces **f** that are consistent with the finite element discretization.[7] A detailed description of the routine is provided in the internal manual by Shan (2005), which is available at the institute, and in Schöngrundner (2011). Therefore, only the basic steps are described in the following.

[7] Alternatively to Eq. (4.21), it is possible to implement Eq. (4.35) or Eq. (4.36) for the evaluation of **f**-vectors; see Özenç et al. (2014) for details.

Once the stresses and displacements are known from the FE analysis, the configurational stress tensor **C**, Eq. (4.19), can readily be computed for each integration point in the FE-mesh (Fig. 4.5). It should be remarked that the deformation gradient tensor **F** needs to be calculated from Eq. (2.3), since **F** is not provided by ABAQUS, and the Cauchy stresses **σ** from ABAQUS have to be transformed according to Eq. (2.5) into the first Piola–Kirchhoff stresses **S**. The *nodal* configurational force **f**-vector can be evaluated for a single element *e* by the relation (Müller et al. 2002),

$$\mathbf{f}^{(e)} = \int_{V^{(e)}} \left(\mathbf{D}^{(e)}\right)^{\mathrm{T}} \cdot \mathbf{C}\, \mathrm{d}V \,; \tag{4.41}$$

see Fig. 4.5a. In Eq. (4.41), $\mathbf{D}^{(e)}$ denotes the derivative of the element shape functions after node coordinates, see e.g. Zienkiewicz and Taylor (2005) and Bathe (2007), respectively. The integration is performed numerically using a Gauß quadrature, under consideration of $\mathrm{d}V = B\,\mathrm{d}A$. Finally, the configurational forces $\mathbf{f}^{(e)}$ of all elements adjacent to one node *n* need to be summed up (*assembled*) to get the resulting **f**-vector at this node (Müller et al. 2002),

$$\mathbf{f}^{(n)} = \sum_{n \in e} \mathbf{f}^{(e)} \,; \tag{4.42}$$

see Fig. 4.5b.

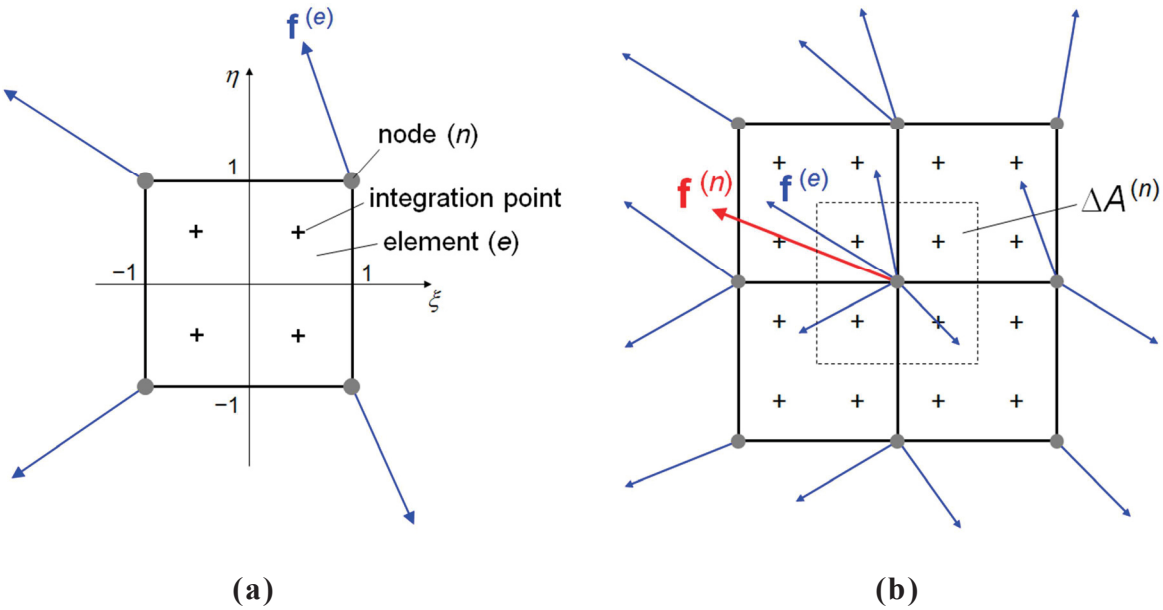

(a) **(b)**

Fig. 4.5 **(a)** 4-node element (*e*) with integration points (+) and natural (local) coordinate system (η, ξ). The vector $\mathbf{f}^{(e)}$ denotes the configurational force at one node (*n*) of a single element (*e*). **(b)** The resulting configurational force vector $\mathbf{f}^{(n)}$ in one node (*n*) is the sum of the $\mathbf{f}^{(e)}$-vectors of all elements adjacent to this node.

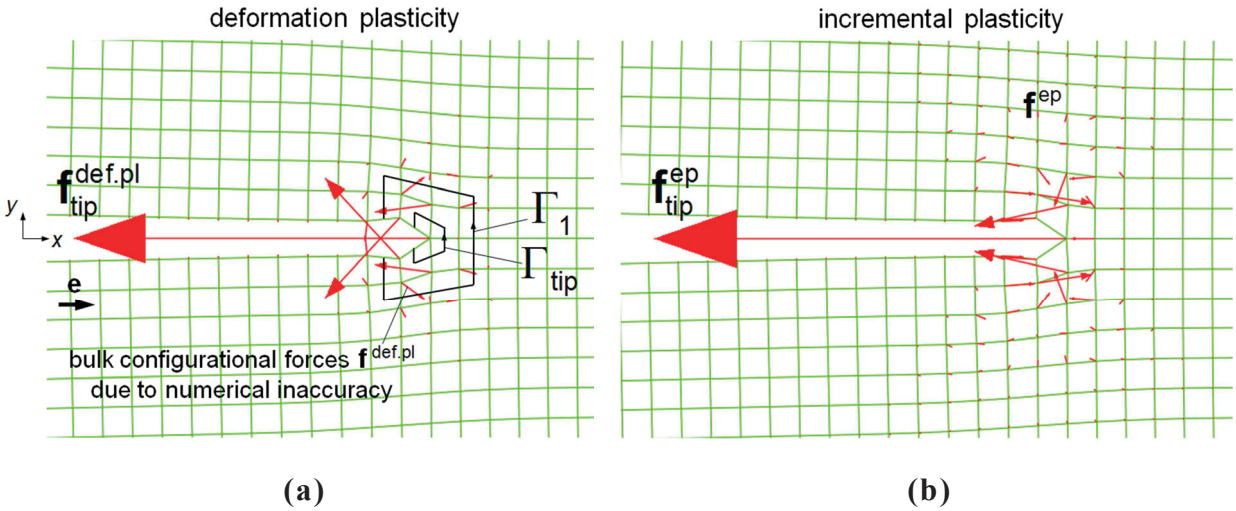

Fig. 4.6 Near-tip region of a stationary crack in an elastic–plastic material after loading to a maximum load. **(a)** Distribution of the configurational forces for deformation plasticity $\mathbf{f}^{\text{def.pl}}$ and for **(b)** incremental plasticity $\mathbf{f}^{\text{ep}}$. **(a)** includes also the first two *J*-integral contours; mesh size $m = 0.2$ mm.

In the post-processing the configurational forces are computed for deformation plasticity $\mathbf{f}^{\text{def.pl}}$ and for incremental plasticity $\mathbf{f}^{\text{ep}}$ (Section 4.3.2). The FE stress and strain analysis is always performed with *incremental plasticity*.

The scalar *J*-integrals J^{conv} for deformation plasticity and J^{ep} for incremental plasticity are evaluated on specific contours Γ around the crack tip, by a summation of configurational forces emanating from all nodes that lie within the area $\mathcal{D}$ bounded by Γ, compare Eqs. (4.33) and (4.34), e.g. Kolednik et al. (2014),

$$J_{\Gamma}^{\text{conv}} = \sum_{n \in \mathcal{D}} -\left(\mathbf{e} \cdot \mathbf{f}^{\text{def.pl}}\right) \Delta A_n \,, \tag{4.43}$$

$$J_{\Gamma}^{\text{ep}} = \sum_{n \in \mathcal{D}} -\left(\mathbf{e} \cdot \mathbf{f}^{\text{ep}}\right) \Delta A_n \,. \tag{4.44}$$

In Eqs. (4.43) and (4.44), the quantity ΔA_n is the element area corresponding to a certain node n. Since the magnitude of the $\mathbf{f}$-vector at one node is influenced by the adjacent elements, the integration contour Γ always crosses the *middle* of the elements (Fig. 4.5b and Fig. 4.6a); see Kolednik et al. (2014). The nomenclature of interesting *J*-integral contours will be specified in Sections 6.3, 7.3, and 8.3, where details about the FE-modeling for the case studies are presented.

For comparison, the values of the *J*-integral J^{VCE}, implemented in ABAQUS adopting the virtual crack extension method by Parks (1977), are computed. Note that deformation plasticity is implicitly assumed in this method.

At this point, an important remark should be made about the accuracy of near-tip configurational forces and near-tip *J*-integrals. Figure 4.6 shows, for example, the distribution

of the configurational forces $\mathbf{f}^{\text{def.pl}}$ and $\mathbf{f}^{\text{ep}}$ around a stationary crack tip in an elastic–plastic material with incremental plasticity after monotonic loading to a maximum load; the mesh size is m = 0.2 mm.[8] Directly at the crack tip a big configurational force, $\mathbf{f}_{\text{tip}}^{\text{def.pl}}$ and $\mathbf{f}_{\text{tip}}^{\text{ep}}$, appears. According to theory, *no* bulk configurational forces $\mathbf{f}^{\text{def.pl}}$ should not appear for deformation plasticity, see Section 4.3.2. Figure 4.6a, however, shows $\mathbf{f}^{\text{def.pl}}$-vectors in the surrounding of the crack tip. They appear due to numerical inaccuracies, since the 4-node isoparametric elements cannot reflect the singularity at the crack tip (e.g. Simha et al. 2008, Kolednik et al. 2014). For the numerical computation of the near-tip J-integral $J_{\text{tip}}^{\text{conv}}$ the component of $\mathbf{f}_{\text{tip}}^{\text{def.pl}}$ into the crack growth direction $\mathbf{e}$ and the area ΔA_{tip} of Γ_{tip}, Fig. 4.6a, must be considered, $J_{\text{tip}}^{\text{conv}} = -\left(\mathbf{e}\cdot\mathbf{f}_{\text{tip}}^{\text{def.pl}}\right)\Delta A_{\text{tip}}$ (Simha et al. 2008). Due to the discretization problem the magnitude of $J_{\text{tip}}^{\text{conv}}$ is usually about 30% lower than the far-field J-integral value, $J_{\text{far}}^{\text{conv}}$. In order to receive the magnitude of $J_{\text{far}}^{\text{conv}}$, the discretization-induced configurational forces around the crack tip must be included, see e.g. Simha et al. (2008), Kolednik et al. (2014).

Figure 4.6b presents the distribution of configurational forces $\mathbf{f}^{\text{ep}}$ for incremental plasticity. The discretization problem appears also here: Parts of the bulk configurational forces $\mathbf{f}^{\text{ep}}$ within a small region around the crack tip are induced by discretization and not only by the plastic strain gradients (Simha et al. 2008, Kolednik et al. 2014). As a consequence, the "true" magnitude of $\mathbf{f}_{\text{tip}}^{\text{ep}}$ and $J_{\text{tip}}^{\text{ep}} = -\left(\mathbf{e}\cdot\mathbf{f}_{\text{tip}}^{\text{ep}}\right)\Delta A_{\text{tip}}$ cannot be easily determined. Simha et al. (2008) considered the *second* contour Γ_2 around the crack tip as an approximation of $J_{\text{tip}}^{\text{ep}}$, and showed that $J_{\text{tip}}^{\text{ep}} \approx J_{\Gamma 2}^{\text{ep}} \approx J_{\text{far}}^{\text{conv}}$.

According to Rice (1979), the near-tip J-integral J_{tip} vanishes in an elastic–plastic material. It should be noted that finite values of $\mathbf{f}_{\text{tip}}^{\text{def.pl}}$ and $\mathbf{f}_{\text{tip}}^{\text{ep}}$, or $J_{\text{tip}}^{\text{conv}}$ and $J_{\text{tip}}^{\text{ep}}$, only occur due to numerical reasons and depend on the used FE-mesh size. A mesh refinement yields a reduction in the magnitude of $\mathbf{f}_{\text{tip}}^{\text{def.pl}}$ and $\mathbf{f}_{\text{tip}}^{\text{ep}}$ and the corresponding J-integrals, suggesting finally $J_{\text{tip}}^{\text{conv}} = J_{\text{tip}}^{\text{ep}} = 0$ (see e.g. McMeeking 1977, Brocks et al. 2003, Kolednik et al. 2014). This will be discussed in the next section.

In contrast to near-tip J-integrals, the magnitude of J-integrals evaluated for contour radii disctintively larger, e.g., than the length of the process zone $l_{\text{proc.z}} \approx 3\delta_{\text{t}}$, Section 3.2.1, is almost independent of the FE-mesh size; Section 7.5.1 presents an example.

[8] For generating Fig. 4.6, the case study presented in Section 6.4.1 was taken.

5 Crack driving force in elastic–plastic materials under monotonic loading

In the previous section the incremental plasticity *J*-integral J^{ep} has been introduced, which has the physical meaning of a true driving force term in elastic–plastic materials, in contrast to the conventional *J*-integral J^{conv}. However, bulk configurational forces cause J^{ep} to become path dependent and it had to be shown how J^{ep} should be used in order to characterize the crack driving force. Moreover, the role of $J_{\mathrm{tip}}^{\mathrm{ep}}$ for the assessment of crack extension was not clear since its magnitude vanishes in an elastic–plastic material, as does the conventional *J*-integral (Rice 1975).

Schöngrunder (2011) and Kolednik et al. (2014) analyzed the path dependence of the incremental plasticity *J*-integral J^{ep} for long, stationary and continuously growing cracks that are subjected to *monotonic* loading and showed how the crack driving force should be correctly evaluated. The results provide also an answer to Rice' paradox of zero crack driving force and demonstrate the usefulness of the conventional *J*-integral as crack driving force parameter for elastic–plastic materials despite its theoretical restrictions.

The methodological approach in Schöngrunder (2011) and Kolednik et al. (2014) consists of numerical case studies for Compact Tension specimens made of homogeneous, isotropic, elastic–plastic material with incremental theory of plasticity. The material data is taken from an annealed steel St37; see also Section 6.5.4. Plane strain conditions and large-strain theory are applied. The specimen is subjected to monotonic loading. The crack remains first stationary and grows then at constant load-line displacement $v_{\mathrm{LL}} = const$. Various maximum load-line displacements $v_{\mathrm{LL,max}}$ are prescribed, so that small-scale, large-scale and general yielding conditions prevail in the specimen, in order to study the role of plasticity for the configurational force distribution and the behavior of the J^{ep}-integral. Since the path dependence of J^{ep} on contours very close to the crack tip was especially of interest, specific numerical parameters have been varied systematically to separate numerical from physical effects.

Section 5 presents the central findings of Kolednik et al. (2014). For a better understanding of the path dependence of J^{ep}, schematic figures of the specimen with directions and magnitudes of bulk configurational forces $\mathbf{f}^{\mathrm{ep}}$ have been created.

5.1 Stationary cracks under monotonic loading

5.1.1 Path dependence of J-integrals for stationary cracks

Figure 5.1a presents, for example, the spatial distribution of plasticity for the C(T)-specimen of Kolednik et al. (2014) with a stationary crack after loading to a load-line displacement

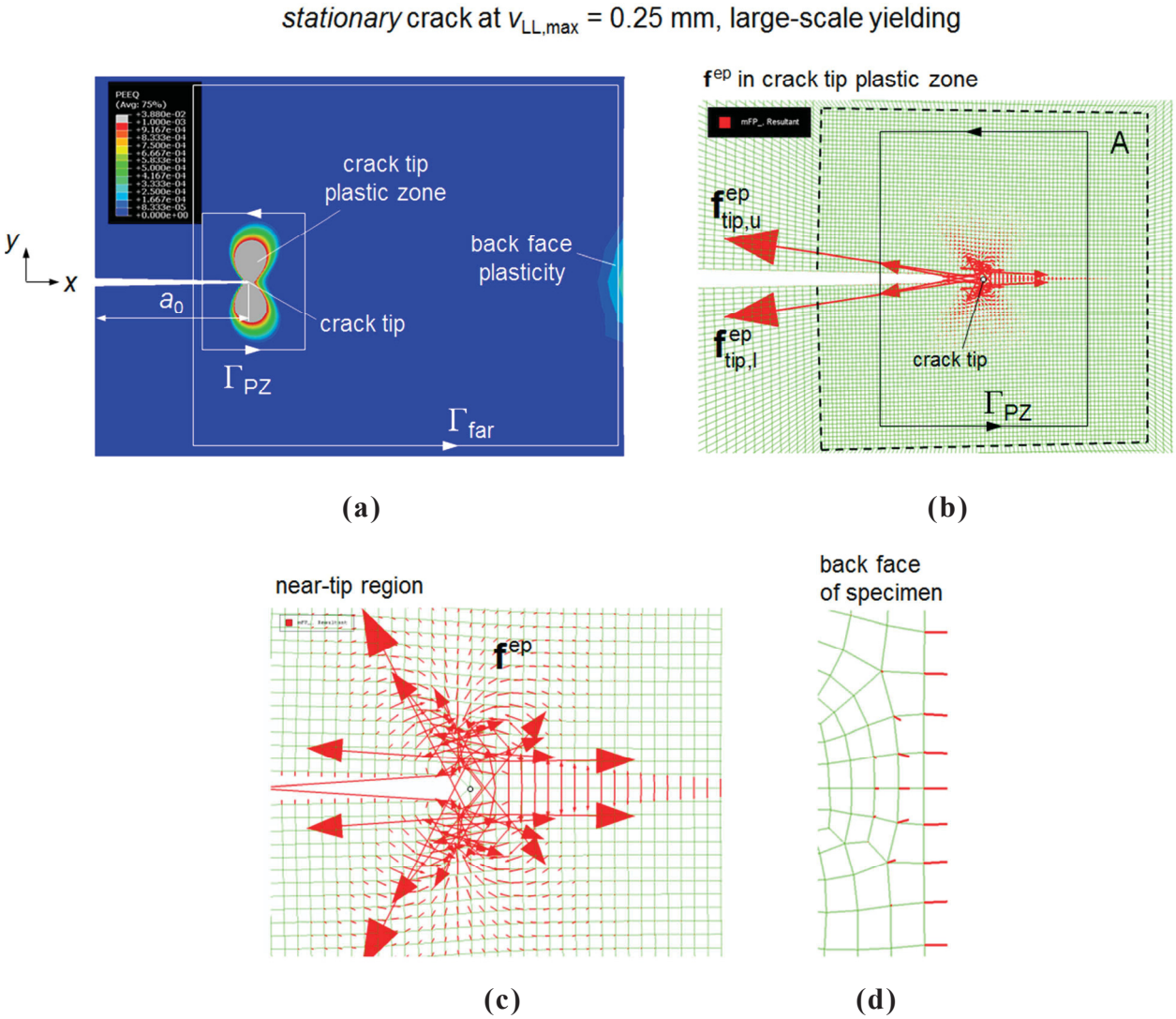

Fig. 5.1 Details of the C(T)-specimen with a stationary crack, initial crack length a_0 = 27 mm; compare Figs. 6b, 8d–f in Kolednik et al. (2014). **(a)** Distribution of the accumulated plastic strain PEEQ at v_{LL} = 0.25 mm (large-scale yielding). The *grey color* corresponds to regions with PEEQ ≥ 0.001. Γ_{PZ} and Γ_{far} denote the crack tip plastic zone and far-field *J*-integral contours. **(b)** Distribution of the incremental plasticity configurational forces $\mathbf{f}^{ep}$ in the crack tip plastic zone. The configurational force at the crack tip $\mathbf{f}^{ep}_{tip}$ is the vector sum of the two partial configurational forces $\mathbf{f}^{ep}_{tip,u}$ and $\mathbf{f}^{ep}_{tip,l}$ of the *upper* and *lower* specimen half. Mesh size in region A, m = 0.15 mm. **(b)** Detail of the near-tip region without large configurational forces of the crack tip. **(c)** Back face region of the specimen.

v_{LL} = 0.25 mm (lsy prevails). Figure 5.1b shows the distribution of incremental plasticity configurational forces $\mathbf{f}^{ep}$ in the crack tip plastic zone; the mesh size in region A is m = 0.15 mm. Figures 5.1c,d show a detail of the crack tip and the back face region. Note that in Fig. 5.1c two inclined partial configurational forces appear on nodes along the ligament due to

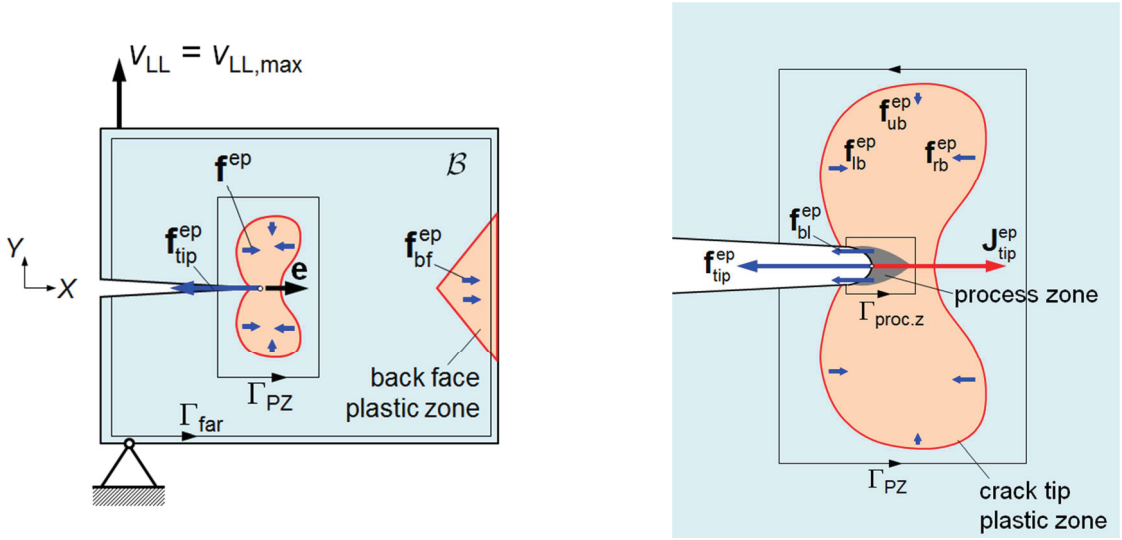

Fig. 5.2 *J*-integral contours and schematic distribution of incremental plasticity configurational forces $\mathbf{f}^{ep}$ in plastically deformed regions of an elastic–plastic body $\mathcal{B}$ with a stationary crack at maximum load-line displacement $v_{LL} = v_{LL,max}$. **(a)** entire body **(b)** detail of the crack tip plastic zone with blunted crack tip and process zone. The integration contour Γ_{PZ} encloses the crack tip plastic zone. $\Gamma_{proc.z}$ surrounds the process zone.

the coinciding master and slave nodes of the lower and upper specimen half for the subsequent crack growth simulation. The resulting configurational force vector at one node on the ligament is the sum of the two partial configurational forces and has only a *x*-component. This applies also for the $\mathbf{f}^{ep}_{tip}$-vector; compare Fig. 4.6 and Fig. 5.1b. In Fig. 5.2, the directions and magnitudes of the incremental plasticity configurational forces, $\mathbf{f}^{ep}_{i}$, are *schematically* indicated in various regions *i*. Note that only the *x*-component of the configurational force vectors, i.e. the components into crack growth direction **e**, contribute to the scalar *J*-integral, see Eq. (4.44).

First, we concentrate on configurational forces that appear in the crack tip plastic zone (Fig. 5.1b,c and 5.2b). According to Eq. (4.36), $\mathbf{f}^{ep}$-vectors appear only in plastically deformed regions of the material, and they point into the direction of the plastic strain gradient (Simha et al. 2008). It is seen from Fig. 5.1c that a configurational force on the left boundary "lb" of the crack tip plastic zone, $\mathbf{f}^{ep}_{lb}$, points, at tensile (positive) load, into positive *x*-direction, whereas $\mathbf{f}^{ep}_{rb}$ on the right boundary "rb" points into the negative *x*-direction; on the upper boundary "up", $\mathbf{f}^{ep}_{ub}$ has only a negative *y*-component, hence, it is not relevant for the magnitude of J^{ep}. Bulk configurational forces induced by crack tip blunting point into both negative and positive *x*-direction (e.g. Kolednik et al. 2014), but the resulting $\mathbf{f}^{ep}$-vector, $\mathbf{f}^{ep}_{bl}$, points into the negative *x*-direction, like the configurational force emanating from the crack tip, $\mathbf{f}^{ep}_{tip}$ (Fig. 5.2b).

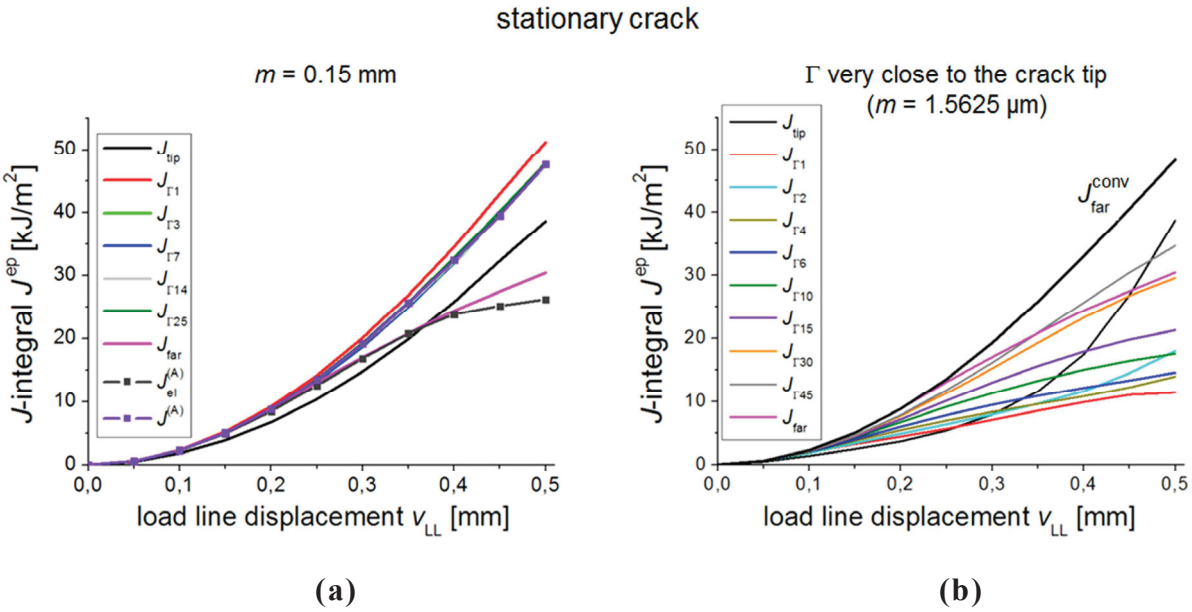

Fig. 5.3 Variations of J^{ep}-integrals with increasing load-line displacement v_{LL} for a stationary crack; see Fig. 11c and Fig. 13 in Kolednik et al. (2014). Different integration contours Γ are centered at the crack tip, for a mesh size **(a)** m = 0.15 mm, and **(b)** m = 1.5625 µm, i.e. Γ is very close to the crack tip. The curves of the experimental J-integral J^{exp}, Eq. (3.4), i.e. denominated as $J^{(\mathrm{A})}$ in Kolednik et al. (2014), and the conventional far-field J-integral $J_{\mathrm{far}}^{\mathrm{conv}} \cong J_{\mathrm{PZ}}^{\mathrm{ep}}$ are drawn for comparison.

Near-tip $\mathbf{f}^{\mathrm{ep}}$-vectors have the largest magnitude, since stresses and plastic strain gradients are largest, see Eq. (4.36). With increasing distance from the crack tip, the magnitudes of the $\mathbf{f}^{\mathrm{ep}}$-vectors descrease significantly, i.e. up to 10^4 orders of magnitude. Fig. 5.1c and Fig. 5.2b show that $\left|\mathbf{f}_{\mathrm{lb}}^{\mathrm{ep}}\right|$ and $\left|\mathbf{f}_{\mathrm{rb}}^{\mathrm{ep}}\right|$ are distinctively smaller than $\left|\mathbf{f}_{\mathrm{tip}}^{\mathrm{ep}}\right|$, respectively.

Rice (1979) and subsequent authors (e.g. McMeeking 1977, Brocks et al. 2003) reported that the conventional near-tip J-integral $J_{\mathrm{tip}}^{\mathrm{conv}}$ is zero in an elastic–plastic material if large strain theory is applied, i.e. the crack tip blunts. The computations by Kolednik et al. (2014) showed that the magnitude of $\mathbf{f}_{\mathrm{tip}}^{\mathrm{ep}}$ depends strongly on the used FE-mesh size: with decreasing mesh size, parts of $\mathbf{f}_{\mathrm{tip}}^{\mathrm{ep}}$ become distributed onto the neighboring nodes within the process zone so that $\mathbf{f}_{\mathrm{tip}}^{\mathrm{ep}}$ decreases with mesh refinement. This implies, finally, a zero driving force at the very crack tip, $J_{\mathrm{tip}}^{\mathrm{ep}} = -\left(\mathbf{e}\cdot\mathbf{f}_{\mathrm{tip}}^{\mathrm{ep}}\right)\Delta A_{\mathrm{tip}} = 0$; see also Schöngrunder (2011). Note that this is a "physical" effect and *not* connected to a vanishing element area ΔA_n, Eq. (4.45), since the value of J^{ep} tends to zero even if many elements are included in the integration contour; see Fig. 14 in Kolednik et al. (2014). The reason for this effect is explaned in the next section.

Figure 5.3 presents the variations of the J^{ep}-integral with increasing load-line displacement v_{LL}. Figure 5.3a shows J^{ep}-curves for various integration contours around the crack tip and a mesh size in A, Fig. 5.1b, of m = 0.15 mm. Figure 5.3b shows J^{ep}-curves for contours *very close* to the crack tip, i.e. within the process zone; mesh size m = 1.5625 µm. Small-scale yielding prevails at low v_{LL}; large-scale yielding starts with the onset of plasticity

at the backface of the specimen at $v_{LL} \approx 0.20$ mm, and general yielding starts at $v_{LL} \approx 0.35$ mm.

The path dependence of the J^{ep}-integral inside the crack tip plastic zone can be understood from Fig. 5.2b and Eqs. (4.34) and (4.44). Note that the path dependence close to the crack tip is both *physically* caused due to the plastic strain gradients and *numerically* caused due to the discretization problem, see Section 4.4. For contours inside the process zone, $\Gamma_{tip} < \Gamma < \Gamma_{proc.z}$, J^{ep} exhibits a very strong path dependence (Fig. 5.3b): With decreasing mesh size parts of the big crack tip configurational force vector $\mathbf{f}^{ep}_{tip}$, Fig. 5.2b, become distributed within the small process zone (see Kolednik et al. 2014). If the size of Γ decreases from $\Gamma_{proc.z}$, more and more $\mathbf{f}^{ep}$-vectors with negative x-component lie outside the contour and cause that J^{ep} decreases, see Eq. (4.44). On the contrary, J^{ep} exhibits only a slight path dependence between a contour that includes the process zone with the blunting region, $\Gamma_{proc.z} \approx \Gamma_3$, and a contour surrounding the crack tip plastic zone, $\Gamma_{PZ} \approx \Gamma_{25}$ (Fig. 5.2b and Fig. 5.3a). The reason is that $\mathbf{f}^{ep}$-vectors on the left and right boundary of the plastic zone, $\mathbf{f}^{ep}_{lb}$ and $\mathbf{f}^{ep}_{rb}$, almost cancel out each other (Fig. 5.2b). Kolednik et al. (2014) showed that J^{ep} evaluated for a contour radius of $l_{proc.z} \approx 3\delta_t$ lies approximately 10% below the value of J^{ep}_{PZ}.

For a further increase of Γ outside the crack tip plastic zone, $\Gamma > \Gamma_{PZ}$, the J^{ep}-integral remains constant, since *no* bulk configurational forces appear in *elastically* deformed regions of the material. For ssy-conditions, $\mathbf{f}^{ep} = \mathbf{0}$ up to the path Γ_{far}, hence, $J^{ep}_{PZ} = J^{ep}_{far}$. For lsy, the J^{ep}-integral becomes again path dependent if Γ crosses the back face "bf" plasticity region (Fig. 5.2a). Here, bulk configurational forces $\mathbf{f}^{ep}_{bf}$ appear with positive x-components, Fig. 5.1d, and provide an anti-shielding effect, $C_p > 0$, Eq. (4.39), see Simha et al. (2008). This causes a slight reduction of the J^{ep}-integral and is the reason why the far-field J-integral becomes smaller, e.g. about 4% for v_{LL} = 0.25 mm, than the J-integral around the crack tip plastic zone, $J^{ep}_{far} < J^{ep}_{PZ}$ (Fig. 5.3a). For gy-conditions, Fig. 3.1c, J^{ep} is always path dependent from Γ_{tip} up to Γ_{far}. For v_{LL} = 0.50 mm, the value of J^{ep}_{far} is about 37% lower than the conventional far-field J-integral $J^{conv}_{far} \cong J^{ep}_{PZ}$ (Fig. 5.3a); see also Section 9.1.

Next, the properties of the conventional J-integral J^{conv}, Eqs. (4.33) and (4.43), shall be discussed. The strong path dependence of J^{conv} for contours within the process zone (see McMeeking 1977, Brocks et al. 2003), and $J^{conv}_{tip} = 0$ has been confirmed by Kolednik et al. (2014). The path dependence can be explained by the occurrence of "artificial" bulk configurational forces $\mathbf{f}^{def.pl}$ due to the discretization problem, Section 4.4, and non-proportional loading in the process zone; in contrast to $\mathbf{f}^{ep}$, such $\mathbf{f}^{def.pl}$-vectors are not physically sound, see Section 4.3.2. Since proportional loading is not violated in remote regions of the crack tip, artificial $\mathbf{f}^{def.pl}$ do not appear and J^{conv} remains constant for contour radii increasing from the magnitude of the process zone to the far-field contour, $J^{conv}_{proc.z} = J^{conv}_{PZ} = J^{conv}_{far}$ (Simha et al. 2008, Kolednik et al. 2014).

The largest differences between the magnitude of J^{ep} and J^{conv} is seen in the far-field J-integral after onset of back face plasticity: $J^{ep}_{far} < J^{conv}_{far}$ for lsy- and gy-conditions, see Fig. 5.3a

under consideration that $J^{ep}_{\Gamma 25} \approx J^{conv}_{far}$; $J^{ep}_{far} = J^{conv}_{far}$ as long as no back face plasticity occurs (ssy-conditions).

An important finding of Kolednik et al. (2014) is the equivalence of J^{ep} and J^{conv} for contours surrounding the entire crack tip plastic zone Γ_{PZ}, Fig. 5.2,

$$J^{ep}_{PZ} = J^{conv}_{PZ} = J^{conv}_{far} = J^{exp}, \tag{5.1}$$

see Fig. 5.3a. The right hand equality in Eq. (5.1) has been already discussed in Section 3.2.2. The equality $J^{ep}_{PZ} = J^{conv}_{PZ}$ becomes evident from the middle term of Eq. (4.29) and Fig. 5.2a: Since Γ_{PZ} goes only through *elastically* deformed material, the total strain energy density consists only of an elastic component, $\phi = \phi_e$. Therefore, no difference exists between a formulation via incremental- and deformation plasticity. Note that $J^{ep}_{PZ} \neq J^{conv}_{PZ}$ for gy-conditions, since there is no elastic corridor between the crack tip plastic zone and the plastic zone at the back face.

Finally, it should be remarked that the values of the ABAQUS *J*-integral J^{VCE} give, with very high accuracy, the magitudes of J^{conv} computed via configurational force approach; except for very small contour radii, $\Gamma \ll \Gamma_{proc.z}$; see Kolednik et al. (2014) for details.

5.1.2 Plasticity and crack driving force

Kolednik et al. (2014) provide an explanation to the seeming paradox of crack extension in elastic–plastic materials in spite of zero crack driving force, $J^{ep}_{tip} = 0$.

The physical meaning of the *J*-integral is that it describes the driving force for the simultaneous translational movement of all defects enclosed by the integration contour Γ (Kolednik et al. 2014). This means that the physical meaning of the near-tip *J*-integral J^{ep}_{tip} is that of the driving force for the *exclusive* movement of the crack tip (Fig. 5.4a). However, in an elastic–plastic material, it is impossible that crack extension occurs without simultaneous movement of the surrounding process zone and the plastic zone of the crack tip (Fig. 5.4b). Therefore, the magnitude of J^{ep}_{tip} becomes meaningless. The physical meaning of the *J*-integral J^{ep}_{PZ} is that of the driving force for the joint movement of the crack tip plus the crack tip plastic zone. Thus, J^{ep}_{PZ} is the appropriate driving force parameter for a stationary crack in a monotonically loaded elastic–plastic material (Kolednik et al. 2014).

An important finding is that the conventional *J*-integral $J^{conv}_{PZ} = J^{conv}_{far}$ (or $J^{VCE}_{PZ} = J^{VCE}_{far}$), and the experimental *J*-integral, J^{exp}, are physically appropriate to assess crack growth initiation, despite the restrictions of deformation plasticity for elastic–plastic materials (Section 3.2.1). Due to the validity of Eq. (5.1), they reflect the magnitude of J^{ep}_{PZ}.

Note that Eq. (5.1) strictly applies unless general yielding conditions appear where no "elastic corridor" separates the crack tip plastic zone and the back face plasticity region (Fig. 3.1c). Kolednik et al. (2014) showed that Eq. (5.1) remains approximately valid shortly after onset of gy, but the difference might increase significantly with further increasing load; the evaluation of J^{ep}_{PZ}-values under gy-conditions will be discussed in detail in Section 9.1.

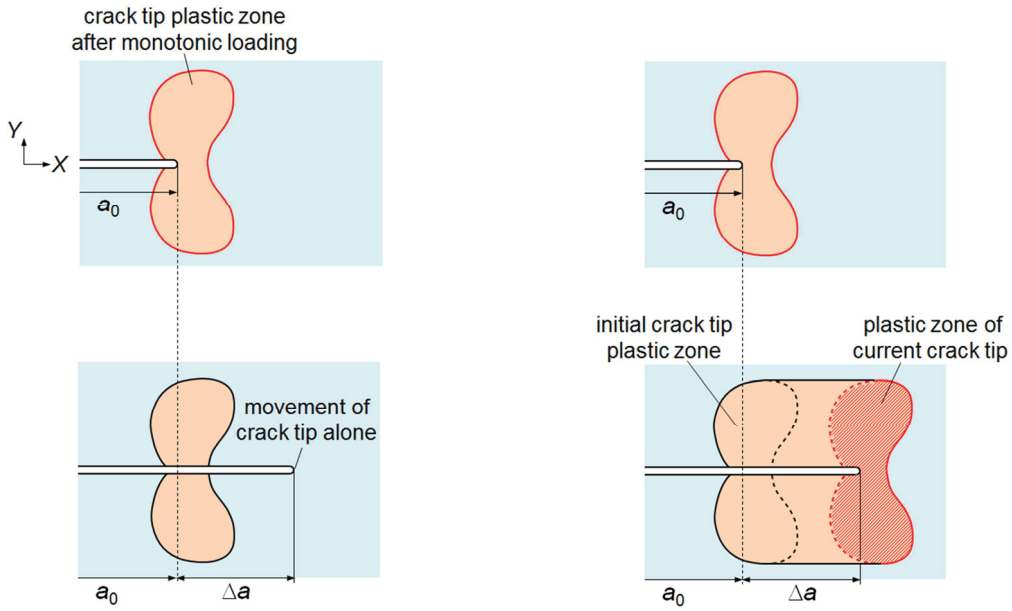

Fig. 5.4 On the explanation of crack extension in an elastic–plastic material; see also Fig. 16b,c in Kolednik et al. (2014). **(a)** A translational propagation of the crack tip alone, while the crack tip plastic zone remains stationary, is impossible in an elastic–plastic material. **(b)** Crack growth always occurs combined with the movement of the plastic zone surrounding the current crack tip.

Alternatively, the *J*-integral around the process zone, $J^{ep}_{proc.z}$, can be used as an approximation, since $J^{ep}_{proc.z}$ only slightly underestimates the magnitude of J^{conv}_{far} (Kolednik et al. 2014). Therefore, at the moment it is not clear how long J^{conv}_{far} can be used beyond onset of general yielding as a driving force parameter; but J^{conv}_{far} remains useful as a parameter that describes the intensity of the crack tip field if the process zone is sufficiently small so that a "*J*-dominated zone" exists, see Section 3.2.1.

5.2 Growing cracks under monotonic loading

5.2.1 Relevant J-integral contours for growing cracks

Figure 5.5a presents how the crack tip plastic zone in Fig. 5.1a changes after a crack extension of Δa = 2.7 mm under constant load-line displacement $v_{LL,max}$ = 0.25 mm (lsy): After crack extension, the entire crack tip plastic zone consists of the initial plastic zone of the stationary crack, the plastic wake and the *active* plastic zone, which travels with the moving crack tip and produces the plastic wake. The corresponding field of configurational forces $\mathbf{f}^{ep}$ is shown in Fig. 5.5b. The directions and magnitudes of the $\mathbf{f}^{ep}$-vectors in various regions of the crack tip plastic zone are schematically indicated in Fig. 5.6.

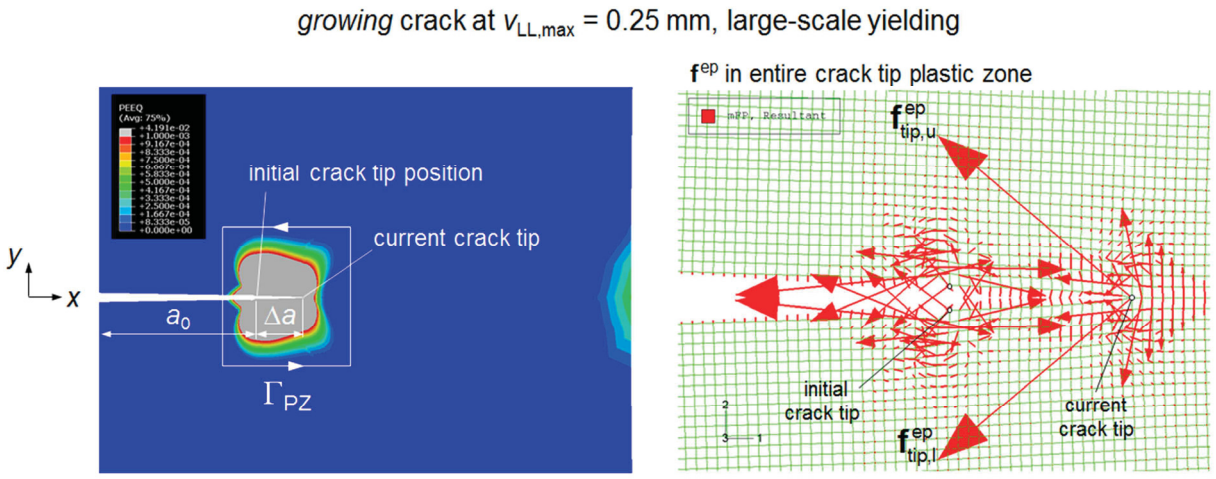

Fig. 5.5 Details of the C(T)-specimen after crack extension Δa = 2.7 mm at constant load-line displacement $v_{LL,max}$ = 0.25 mm; compare Figs. 6d and 10b in Koledník et al. (2014). **(a)** Distribution of the accumulated plastic strain PEEQ; large-scale yielding prevails. **(b)** Arrow plot of the incremental plasticity configurational forces $\mathbf{f}^{ep}$ in the crack tip plastic zone. The resulting $\mathbf{f}^{ep}_{tip}$-vector at the current crack tip is the vector sum of $\mathbf{f}^{ep}_{tip,u}$ and $\mathbf{f}^{ep}_{tip,l}$; compare Fig. 5.1b. Mesh size m = 0.15 mm.

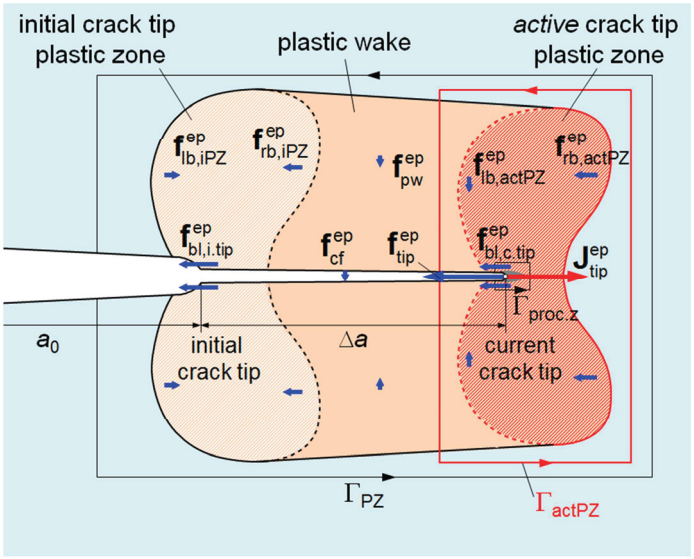

Fig. 5.6 Schematic distribution of incremental plasticity configurational forces $\mathbf{f}^{ep}$ in the entire crack tip plastic zone after crack extension Δa at fixed displacement, $v_{LL} = v_{LL,max}$. The magnitude of $\mathbf{f}^{ep}$-vectors located in the initial crack tip plastic zone has been slightly decreased during unloading. The integration contour Γ_{PZ} encloses the plastic zone of the initial crack tip, the plastic wake and the active plastic zone of the current crack tip. Γ_{actPZ} surrounds only the active plastic zone.

It is seen from Fig. 5.5 that the distribution of configurational forces $\mathbf{f}^{\mathrm{ep}}$ is dominated by the gradients of the plastic strain field of the initial crack tip plastic zone and the *right* boundary of the active plastic zone (Kolednik et al. 2014). The $\mathbf{f}^{\mathrm{ep}}$-vectors on the left boundary of the active plastic zone "actPZ" and in the plastic wake "pw" have only a *y*-component, see $\mathbf{f}^{\mathrm{ep}}_{\mathrm{lb,actPZ}}$ and $\mathbf{f}^{\mathrm{ep}}_{\mathrm{pw}}$ in Fig. 5.6. Vertical surface configurational forces that appear along the newly crated crack flanks, $\mathbf{f}^{\mathrm{ep}}_{\mathrm{cf}}$, are not important; they cancel out each other (Fig. 5.5b).

The basic differences to the stationary crack are: (i) The magnitudes of $\mathbf{f}^{\mathrm{ep}}$-vectors in the initial crack tip plastic zone decrease due to the unloading during crack extension at $v_{\mathrm{LL}} = const$. (ii) The configurational force at the *current* crack tip, $\mathbf{f}^{\mathrm{ep}}_{\mathrm{tip}}$, and the $\mathbf{f}^{\mathrm{ep}}$-vectors in the surrounding blunting region are significantly smaller compared to the stationary crack (Fig. 5.5b and Fig. 5.1b,c). The reason might be connected to the weaker singularity of a growing crack (Rice et al. 1980). Moreover, Fig. 5.5b presents a smaller crack tip opening displacement δ_{t}; thus, the length of the process zone, $l_{\mathrm{proc.z}} \approx \kappa\delta_{\mathrm{t}}$, is also smaller compared to the stationary crack.

As for the stationary crack, a mesh refinement of the crack tip region results in a reduction of the magnitude of $\mathbf{f}^{\mathrm{ep}}_{\mathrm{tip}}$ also for a growing crack tip, leading finally to a zero crack driving force, $J^{\mathrm{ep}}_{\mathrm{tip}} = 0$, see Kolednik et al. (2014).

Figure 5.7 presents the path dependence of the J^{ep}-integral during crack extension up to Δa = 2.7 mm at fixed $v_{\mathrm{LL,max}}$ = 0.25 mm. Shown is the evolution of J^{ep} against (step-) time: $t = 0 \div 1$ corresponds to monotonic loading of the stationary crack (Fig. 5.3a); crack growth corresponds to $t > 1$. In comparison to the stationary crack, the path dependence of J^{ep} is more pronounced even for contours fully enclosing the process zone, $\Gamma > \Gamma_{\mathrm{proc.z}}$; see contours larger than Γ_1 in Fig. 5.7. The value of J^{ep} increases stronger with increasing contour size since the *x*-components of $\mathbf{f}^{\mathrm{ep}}_{\mathrm{lb,actPZ}}$ and $\mathbf{f}^{\mathrm{ep}}_{\mathrm{rb,actPZ}}$ do not compensate (Fig. 5.5b and Fig. 5.6). Thus, the J^{ep}-integral evaluated for a contour around the process zone, including the $\mathbf{f}^{\mathrm{ep}}$-vectors induced by crack tip blunting of the current crack tip "c.tip", $\mathbf{f}^{\mathrm{ep}}_{\mathrm{bl,c.tip}}$, is distictively smaller than the *J*-integral $J^{\mathrm{ep}}_{\mathrm{actPZ}}$ for a contour around the active plastic zone Γ_{actPZ} (Fig. 5.6). The path dependence of J^{ep} becomes more pronounced with higher applied load; see Kolednik et al. (2014) where figures similar to Fig. 5.7 are provided for ssy- and gy-conditions.

If the integration contour Γ surrounds the active plastic zone, and further increases through the plastic wake, $J^{\mathrm{ep}}_{\mathrm{actPZ}}$ remains constant, since the vertical $\mathbf{f}^{\mathrm{ep}}$-vectors do not deliver a contribution to the magnitude of J^{ep}, see Eq. (4.44). The value of J^{ep} varies again when bulk configurational forces of the initial plastic zone become included (Fig. 5.5b). The magnitude of $J^{\mathrm{ep}}_{\mathrm{PZ}}$ is reached when $\mathbf{f}^{\mathrm{ep}}_{\mathrm{rb,iPZ}}$ and $\mathbf{f}^{\mathrm{ep}}_{\mathrm{lb,iPZ}}$ of the initial plastic zone "iPZ" and $\mathbf{f}^{\mathrm{ep}}_{\mathrm{bl,i.tip}}$, of the initial crack tip "i.tip", are included in Γ (Fig. 5.6).

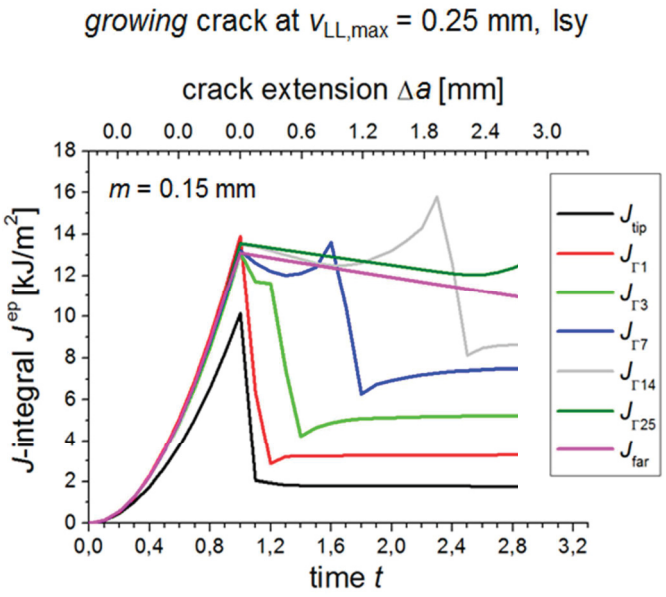

Fig. 5.7 Path dependence of J^{ep}-integral for different integration contours around a growing crack tip; compare Fig. 12b in Kolednik et al. (2014). During time $t = 0 \div 1$, the crack remains stationary, the specimen is loaded to $v_{LL,max} = 0.25$ mm (lsy prevails); compare Fig. 5.3a. After $t = 1$, crack growth occurs at fixed $v_{LL,max}$. The mesh size is $m = 0.15$ mm.

Interesting is the characteristic variation of J^{ep}_{actPZ} with crack extension, compared to the variation of J^{ep}_{PZ}. Figure 5.8 presents *schematically* the evolution of the incremental plasticity J-integrals, J^{ep}_{actPZ} and J^{ep}_{PZ}, versus time t during crack extension.[9] For the stationary crack, time $t = 0 \div 1$, the active and the initial crack tip plastic zone coincide, $\Gamma_{actPZ} = \Gamma_{PZ}$ (Fig. 5.4b), and therefore $J^{ep}_{actPZ} = J^{ep}_{PZ}$. During crack extension, $t = 1 \div 2$, J^{ep}_{PZ} exhibits a slight, linear decrease since the applied load decreases with increasing crack extension while the displacement $v_{LL} = v_{LL,max}$ remains constant (Kolednik et al. 2014). On the contrary, J^{ep}_{actPZ} exhibits the following characteristic variations as marked in Fig. 5.8:

a) J^{ep}_{actPZ} increases when the contour Γ_{actPZ} is shifted to the right during crack extension since $\mathbf{f}^{ep}_{lb,iPZ}$ becomes exluded (compare Fig. 5.6).
b) The negative parts of the configurational forces induced by initial crack tip blunting, $\mathbf{f}^{ep}_{bl,i.tip}$, Fig. 5.5b, drop out of Γ_{actPZ}, Fig. 5.6, leading to the steep drop of J^{ep}_{actPZ}, compare Eq. (4.44).
c) J^{ep}_{actPZ} slightly increases, in general, due to the positive parts of $\mathbf{f}^{ep}_{bl,i.tip}$ in front of the crack tip; they are in sum larger than the magnitude of $\mathbf{f}^{ep}_{rb,iPZ}$ (compare Fig. 5.5b).
d) J^{ep}_{actPZ} decreases parallel to J^{ep}_{PZ}.

[9] It should be remarked that for generating Figure 5.8, the results for cyclic loading with crack extension (Section 7) were used.

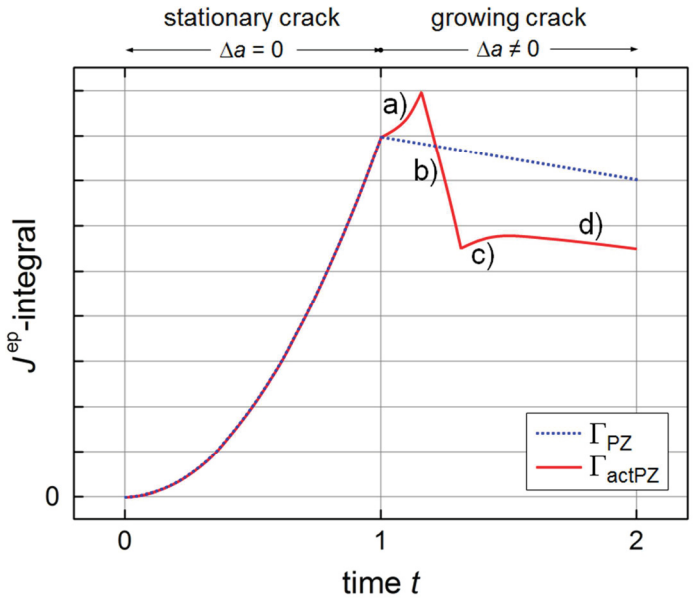

Fig. 5.8 Schematic curves of incremental plasticity J-integrals around the entire crack tip plastic zone, J^{ep}_{PZ}, and around the active plastic zone, J^{ep}_{actPZ}, versus time t during loading to $v_{LL} = v_{LL,max}$ and subsequent crack extension Δa at fixed displacement. For a stationary crack, $t = 0 \div 1$, $J^{ep}_{PZ} = J^{ep}_{actPZ}$ since the entire crack tip plastic zone consists only of the active plastic zone, see Fig. 4.2b.

It should be noted that, provided that the active plastic zone has completely left the plastic zone of the initial crack tip, the magnitude of J^{ep}_{actPZ} is barely affected by the used FE-mesh size and the exact shape of the contour Γ_{actPZ}, since vertically oriented $\mathbf{f}^{ep}$-vectors in the plastic wake do not deliver a contribution to the value of J^{ep}_{actPZ}. However, before the active plastic zone exludes the blunting region of the initial crack tip, the FE-mesh size significantly influences the position and magnitude of the peak value of J^{ep}_{actPZ}, Fig. 5.8; see Section 7.7 for an example. The extent of the characteristic variations in the J^{ep}_{actPZ}-curve, a) – c) in Fig. 5.8, depends on the magnitude of the applied load: The higher the applied load, the larger the initial crack tip blunting region, and, consequently, the larger the resulting $\mathbf{f}^{ep}$-vectors in this region that become excluded from the moving contour Γ_{actPZ}.

From the analysis of the configurational force distribution, it becomes clear that the difference between J^{ep}_{actPZ} and J^{ep}_{PZ} for larger crack extension is attributed to the positive net contribution of $\mathbf{f}^{ep}$-vectors in the initial blunting region (Figs. 5.6 and 5.8), see Kolednik et al. (2014).

The zero-value of J^{conv}_{tip} for a growing crack (e.g. by Kfouri and Miller 1976, Kfouri and Rice 1977) is also confirmed by Kolednik et al. (2014). After onset of crack extension, the conventional J-integral J^{conv} shows even negative values for small contours around the current crack tip; the reason lies in the radial distribution of $\mathbf{f}^{def.pl}$-vectors from the crack tip, whereby $\mathbf{f}^{def.pl}$-vectors with positive x-component are located inside the moving integration contours centered around the current crack tip, see Eq. (4.43). The values of the J^{conv}-integral

around the active plastic zone, J^{conv}_{actPZ}, lie distinctively lower and decrease slightly stronger than J^{ep}_{actPZ} with increasing crack extension.

As for the stationary crack, $J^{conv}_{PZ} = J^{ep}_{PZ}$ is also valid for a growing crack, if the contour passes only elastically deformed regions of the material, see Fig. 5.5a. However, the experimental *J*-integral J^{exp} does not measure the magnitude of J^{conv}_{PZ}, see Kolednik (1991, 1993) and Turner and Kolednik (1994) for details.

5.2.2 Assessment of the crack driving force for crack growth under constant loading

For a growing crack, the incremental plasticity *J*-integral around the *entire* crack tip plastic zone, J^{ep}_{PZ}, has the physical meaning of the driving force for the simultaneous translational movement of the current crack tip and the *entire* crack tip plastic zone. However, during crack extension only the *active* plastic zone moves with the current crack tip, see Fig. 5.6 or Fig. 5.4b. The initial crack tip plastic zone and the plastic wake remain stationary. Therefore, J^{ep}_{PZ} is not the appropriate driving force parameter for a growing crack. Instead, the incremental plasticity *J*-integral computed on a contour completely enclosing the *active* plastic zone, J^{ep}_{actPZ}, is the correct parameter to assess crack extension and fracture (Kolednik et al. 2014); J^{ep}_{actPZ} reflects the driving force for the joint movement of the current crack tip and the surrounding active plastic zone.

Note that $J^{conv}_{actPZ} \neq J^{ep}_{actPZ}$, since Γ_{actPZ} crosses the plastic wake (Fig. 5.6). The experimental *J*-integral J^{exp} also does not reflect the value of J^{ep}_{actPZ}; see Kolednik (1991; 1993) and Turner and Kolednik (1994). This implies that both the conventional and the experimental *J*-integrals are not appropriate to quantify the physically correct driving force of a *growing* crack under monotonic loading. For a stationary crack, however, the active plastic zone and the initial crack tip plastic zone coincide, $\Gamma_{actPZ} = \Gamma_{PZ}$, hence, $J^{ep}_{actPZ} = J^{ep}_{PZ} = J^{conv}_{PZ} = J^{exp}$, Eq. (5.1).

As summary of Section 5, it can be stated that configurational forces can help us to explain and understand the properties of *J*-integrals in a better way, and lead to a physically appropriate determination of the crack driving force in elastic–plastic materials.

“Engineering is the art of modelling materials we do not wholly understand, into shapes we cannot precisely analyse so as to withstand forces we cannot properly assess, in such a way that the public has no reason to suspect the extent of our ignorance.”

Dr. AR Dykes,
Institution of Structural Engineers, 1976

Part II

Driving force of cyclically loaded cracks in elastic–plastic materials

6 Stationary fatigue cracks

Part I has explained the application of the configurational force concept in fracture mechanics, introduced the incremental plasticity J-integral J^{ep} for elastic–plastic materials, and presented how J^{ep} should be used to assess the crack driving force under *monotonic* loading.

Now it is investigated how J^{ep} can be used to evaluate the crack driving force for *cyclically* loaded elastic–plastic materials. This is first shown in the context of *stationary* fatigue cracks in Paper I, which is presented on the following pages.

During fatigue, the crack driving force is disctinctively smaller than the crack growth resistance (Section 3.1), so that the fatigue crack cannot grow at constant maximum load. Therefore, the meaning of the crack driving force for cyclic loading differs from that for monotonic loading. A "crack driving force" term for cyclic loading is *per se* not a real driving force term in the thermodynamic sense. The main purpose of a crack driving force term for cyclic loading is that it should allow the characterization of the crack growth rate da/dN during fatigue, see e.g. Suresh (1998) and Sect. 3.3.1. The stress intensity range ΔK-concept is such a term and can be used if LEFM is applicable. For the regime of low-cycle fatigue there exists no physically appropriate crack driving force parameter, since the experimental cyclic J-integral ΔJ^{exp} (Dowling and Begley 1976) is questionable due to its lack of theoretical basis, see Section 3.3.3.

This leads to the two main questions to be answered in Paper I:

(i) Does a cyclic J-integral ΔJ^{ep} provide a correct fatigue crack driving force term for the regime of LCF?
(ii) Is the application of the experimental cyclic J-integral ΔJ^{exp} correct?

In Paper I, a set of numerical simulations is performed for a two-dimensional Compact Tension specimen with a long, *stationary* crack under cyclic Mode I loading for different load ratios $R = F_{min}/F_{max}$ and *large-scale yielding* conditions. The most important results of this paper are:

- The J^{ep}-integral can be applied for cyclic loading when LEFM is not valid any more. An analysis of the behavior of the bulk configurational forces $\mathbf{f}^{ep}$ during cyclic loading enables an explanation of the path dependence of J^{ep} for various load ratios. It is shown that negative values of J^{ep}, for integration contours close around the crack tip, are physically sound, since they originate from compressive residual stresses within the crack tip plastic zone during unloading.
- As for monotonic loading it is shown that deformation plasticity and incremental plasticity give identical J-integral values for cyclic loading if the integration contour Γ

goes only through *elastically* deformed regions of the elastic–plastic material, such as for a path Γ_{PZ} around the crack tip plastic zone, $J_{PZ}^{ep} = J_{PZ}^{conv}$ (Tables 6.1–6.3).

- A path Γ_{PZ} should be used in order to evaluate a cyclic *J*-integral ΔJ_{PZ}^{ep} for the description of the driving force of *stationary* fatigue cracks in elastic–plastic materials; the back face plasticity region should be excluded since it is not relevant for cyclic plastic deformation at the crack tip which drives a fatigue crack.
- Theoretical considerations and a comparison with the cyclic crack tip opening displacement $\Delta\delta_t$, Fig. 6.11b, show that the cyclic *J*-integral ΔJ_{PZ}^{ep} is not the range between the maximum and minimum *J*-values, $\Delta J_{PZ}^{ep} \neq J_{PZ,max}^{ep} - J_{PZ,min}^{ep}$. Instead, ΔJ_{PZ}^{ep} should be evaluated by Eq. (6.19) so that ΔJ_{PZ}^{ep} is proportional to d*a*/d*N*. For negative load ratios $R < 0$, J_{PZ}^{ep} reaches exactly a minimum value of zero, $J_{PZ,min}^{ep} = 0$, so that $\Delta J_{PZ}^{ep} = J_{PZ.max}^{ep}$.
- It is shown that the experimental cyclic *J*-integral ΔJ^{exp} reflects the magnitude of ΔJ_{PZ}^{ep}, see Tables 6.1–6.3. This implies that ΔJ^{exp} is physically appropriate to characterize *stationary* fatigue cracks. The equality $\Delta J^{exp} = \Delta J_{PZ}^{ep}$ rest on the equivalence of ΔJ_{PZ}^{ep} and the conventional cyclic *J*-integral around the crack tip plastic zone, ΔJ_{PZ}^{conv}, Eq. (6.22).
- The conventional determination of the area ΔA via compliance changes for the value of ΔJ^{exp} in the presence of crack flank contact leads to an overestimation of the magnitude of ΔJ_{PZ}^{ep} by about 10%, see Table 6.3. Instead, the load where J_{PZ}^{ep} reaches a minimum of zero should be considered in order to get the correct crack driving force value.
- The ABAQUS *J*-integral J^{VCE}, which implicitly relies on deformation plasticity, can be also used to evaluate the driving force of a stationary fatigue crack, since in all cases the *J*-integral for deformation plasticity J^{conv} equals J^{VCE}, hence, $J_{PZ}^{ep} = J_{PZ}^{conv} = J_{PZ}^{VCE}$. Note that ΔJ_{PZ}^{VCE} can be easily computed after Eq. (6.22). A numerically expensive implementation based on Eq. (6.3) like, e.g., in Vormwald (2014, 2015) or Metzger et al. (2015) is not necessary since Eq. (6.22) and Eq. (6.3) are equivalent; see "Appendix" in Paper I.

Paper I:

A new basis for the application of the *J*-integral for cyclically loaded cracks in elastic–plastic materials

W. Ochensberger and O. Kolednik

published in

International Journal of Fracture (2014) 189:77–101

Abstract

Fatigue crack propagation is by far the most important failure mechanism. Often cracks under low-cycle fatigue conditions and, especially, short fatigue cracks cannot be treated with the conventional stress intensity range ΔK-concept, since linear elastic fracture mechanics is not valid. For such cases, Dowling and Begley, *ASTM STP 590 (1976) 82*, proposed to use the experimental cyclic *J*-integral ΔJ^{exp} for the assessment of the fatigue crack growth rate. However, severe doubts exist concerning the application of ΔJ^{exp}. The reason is that, like the conventional *J*-integral, ΔJ^{exp} presumes deformation theory of plasticity and, therefore, problems appear due to the strongly non-proportional loading conditions during cyclic loading. The theory of configurational forces enables the derivation of the *J*-integral independent of the constitutive relations of the material. The *J*-integral for incremental theory of plasticity, J^{ep}, has the physical meaning of a true driving force term and is potentially applicable for the description of cyclically loaded cracks, however, it is path dependent. The current paper aims to investigate the application of J^{ep} for the assessment of the crack driving force in cyclically loaded elastic–plastic materials. The properties of J^{ep} are worked out for a stationary crack in a compact tension specimen under cyclic Mode I loading and large-scale yielding conditions. Different load ratios, between pure tension- and tension-compression loading, are considered. The results provide a new basis for the application of the *J*-integral concept for cyclic loading conditions in cases where linear elastic fracture mechanics is not applicable. It is shown that the application of the experimental cyclic *J*-integral ΔJ^{exp} is physically appropriate, if certain conditions are observed.

Keywords: Configurational force concept; Crack driving force; Cyclic *J*-integral; Incremental theory of plasticity; Low-cycle fatigue

6.1 Introduction

The crack extension per load cycle of a fatigue crack $\mathrm{d}a/\mathrm{d}N$ can be in many cases related to the stress intensity range ΔK (Paris et al. 1961; Paris and Erdogan 1963) or the effective stress intensity range ΔK_{eff} (Elber 1970, 1971). This is possible, if the conditions of small-scale yielding are fulfilled and linear elastic fracture mechanics (LEFM) is applicable. If conditions of large-scale yielding or general yielding prevail, LEFM is not applicable and ΔK is not a valid parameter. This also applies in the case of short fatigue cracks where the size of the plastic zone is often large compared to the crack length. Therefore, elastic–plastic fracture mechanics (E-PFM) with the *J*-integral concept is required. However, the conventional *J*-integral, which is based on deformation theory of plasticity (Rice 1968a,b), is formally not applicable due to the appearance of non-proportional loading during fatigue (e.g. Anderson 1995; Suresh 1998). Incremental theory of plasticity is a core requirement to describe real elastic–plastic material behavior in such cases. Nevertheless, Dowling and Begley (1976) proposed that the crack growth rate in the E-PFM regime is a function of an experimental cyclic *J*-integral ΔJ^{exp}, which can be determined experimentally from the area below a single loading branch of the load–displacement (*F*–*v*) curve. Experimental data (e.g. Dowling and Begley 1976; Dowling 1976; Lambert et al. 1988; Banks-Sills and Volpert 1991) show that ΔJ^{exp} correlates to $\mathrm{d}a/\mathrm{d}N$ for some elastic–plastic materials under certain cyclic loading conditions. In spite of these empirical results, the general applicability of ΔJ^{exp} remains doubtful due to the lack of its theoretical basis (Suresh 1998).

The concept of configurational forces enables the derivation of the *J*-integral for elastic–plastic materials with incremental theory of plasticity, called J^{ep}, which is able to overcome the restrictions of the conventional *J*-integral (Simha et al. 2008). Advantageous features of J^{ep} are its physical meaning as a true driving force term in elastic–plastic materials and the extended field of potential application, e.g. during crack extension or for cyclic loading. However, it should be taken into account that the incremental plasticity *J*-integral J^{ep} is not path independent. Simha et al. (2008) investigated the path dependence of J^{ep} due to the gradient of plastic strain and the appearance of bulk configurational forces for monotonically loaded specimens with stationary cracks. They defined a plasticity influence term C_{p}, which describes the shielding or anti-shielding effect of the plastic zone. Kolednik et al. (2014) investigated the properties of J^{ep} for growing cracks in elastic–plastic materials under monotonic loading and demonstrated how J^{ep} and the conventional *J*-integral concept complement each other.

The purpose of the current paper is twofold: (i) we investigate in form of a numerical case study, whether the incremental plasticity *J*-integral J^{ep} can be used for predicting the crack growth rate in cyclically loaded elastic–plastic materials; (ii) we clarify whether the application of the experimental cyclic *J*-integral ΔJ^{exp} is correct.

The paper is structured as follows: Section 6.2 gives a short literature review on the conventional *J*-integral, the experimental cyclic *J*-integral ΔJ^{exp}, and the incremental plasticity *J*-integral J^{ep}. Section 6.3 presents the details of the numerical modeling. Section 6.4 deals with the properties of J^{ep} for a cyclically loaded elastic–plastic material under

large-scale yielding conditions and discusses the influence of various load ratios $R = F_{\min} / F_{\max}$. Section 6.5 describes how the driving force of a cyclically loaded crack can be expressed via J^{ep}, followed by a comparison to the experimental cyclic *J*-integral ΔJ^{exp}.

6.2 Theoretical background

The notation of the mathematical expressions in this paper follows that used by Gurtin (2000). Scalars are denoted by lightface letters, vectors by lowercase boldface letters (with the exceptions of the reference coordinate $\mathbf{X}$ and the *J*-integral vector $\mathbf{J}$), and tensors by uppercase boldface letters (with the exceptions of the Cauchy stress tensor $\boldsymbol{\sigma}$ and the linear strain tensor $\boldsymbol{\varepsilon}$). A dot, as in $\mathbf{a} \cdot \mathbf{b} = a_i b_i$, with summation of repeated indices, designates the scalar, inner product of vectors; a dot, as in $\mathbf{A} \cdot \mathbf{B} = A_{ij} B_{ij}$ designates the scalar, inner product of tensors. The expressions $(\mathbf{A}\mathbf{a})_i = A_{ij} a_j$ and $(\mathbf{A}\mathbf{B})_{ij} = A_{ik} B_{kj}$ denote matrix products. The expression $\mathbf{A} : \boldsymbol{\Lambda}$, with $\mathbf{A}$ as second-order and $\boldsymbol{\Lambda}$ as third-order tensor, gives a vector defined by $(\mathbf{A} : \boldsymbol{\Lambda})_k = A_{ij} \Lambda_{ijk}$.

6.2.1 The J-integral concept

Assume a homogeneous body $\mathcal{B}$ as illustrated in Fig. 6.1a (without plastic zone), consisting of (nonlinear) elastic material. The *J*-integral is a line integral along an integration path Γ drawn from the lower to the upper crack flank in counterclockwise direction around a crack (Rice 1968a,b),

$$J = \int_{\Gamma} \left(\phi \, \mathrm{d}y - \mathbf{t} \cdot \frac{\partial \mathbf{u}}{\partial x} \mathrm{d}s \right), \tag{6.1}$$

where ϕ denotes the strain energy density, $\mathbf{t}$ is the traction vector, $\mathbf{u}$ is the displacement vector, and d*s* is an increment of the integration path Γ. It can be proven that *J* is independent of the integration path Γ if the strain energy density ϕ exhibits the properties of a potential (Rice 1968a,b). This assumption holds for (linear or nonlinear) elastic materials.

Rice (1968a,b) also showed that the *J*-integral describes the crack driving force for elastic bodies. Hutchinson (1968) and Rice and Rosengren (1968) found that *J* characterizes the intensity of the crack tip field (also called HRR crack tip field), similar to the stress intensity factor *K* for linear elasticity.

Application of the classical *J*-integral for elastic–plastic materials rests on the assumption of deformation plasticity, which treats elastic–plastic materials as if they were nonlinear elastic. Since only the elastic part of the strain energy density ϕ_{e} is recoverable in elastic–plastic materials and not the total strain energy density ϕ, Fig. 6.1b, the conventional *J*-integral does not characterize the crack driving force any more (Rice 1968a,b). But *J* is still a measure of the intensity of the crack tip field (Hutchinson 1968; Rice and Rosengren 1968; McMeeking and Parks 1979). Deformation plasticity is applicable only as long as the conditions of proportional loading are fulfilled. Therefore, problems appear if unloading processes occur in the material. If the unloading processes are small and confined, such as for

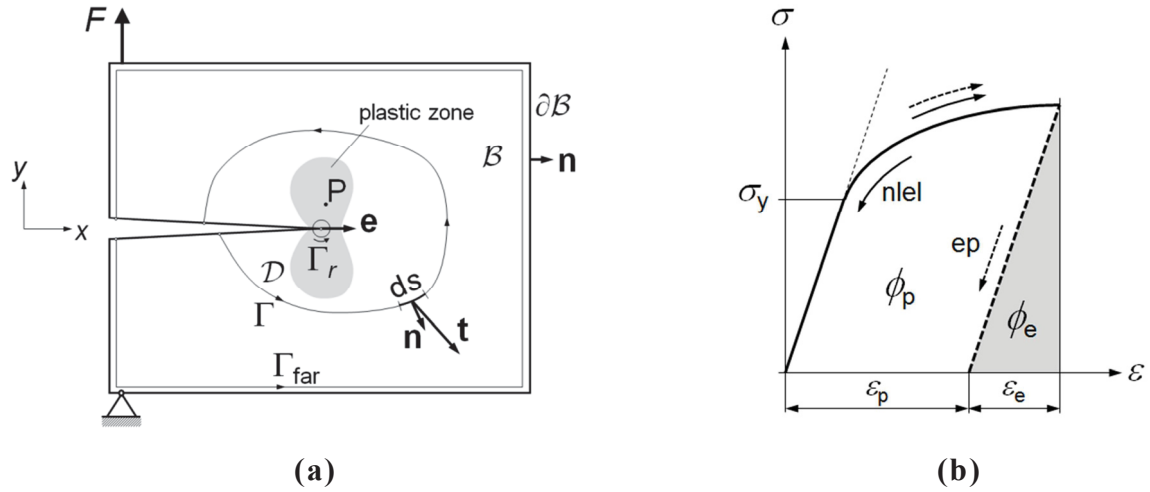

Fig. 6.1 **(a)** Homogeneous elastic–plastic body $\mathcal{B}$ containing a sharp crack and a plastic zone. Γ is an arbitrary contour for the evaluation of the *J*-integral, **n** denotes the unit normal vector on the contour, **t** the traction vector. **(b)** Stress–strain curve for point P. For deformation theory of plasticity, i.e. nonlinear elastic materials, the total strain energy density, $\phi = \phi_e + \phi_p$, is recoverable; for incremental theory of plasticity, only the elastic part ϕ_e is recoverable.

a limited crack extension, *J* can still be applied in the form of an engineering approach, as long as the conditions of "*J*-controlled crack growth" are fulfilled (Hutchinson and Paris 1979). This is, however, not the case for global unloading of the specimen, such as during cyclic loading. Here incremental theory of plasticity is required for a realistic description, and the conventional *J*-integral loses its physical meaning.

In fracture mechanics experiments, the experimental *J*-integral $J^{\exp}$ is determined from the load–displacement (F–v) records. For deeply notched bending type specimens, i.e. Compact Tension or Single-Edge Notched Bend specimens, $J^{\exp}$ is evaluated from the relation (Rice et al. 1973)

$$J^{\exp} = \frac{\eta A}{bB}. \tag{6.2}$$

The parameter A is the area below the F–v-curve (Fig. 6.2a), the ligament length is $b = W - a$, where W and a are the width of the specimen and the crack length, respectively. The dimensionless factor $\eta(a/W)$ depends on specimen type and geometry, see the fracture mechanics standard testing procedures ESIS P2-92 (1992) or ASTM E1820 (2005), where also modifications of Eq. (6.2) are given. Equations similar to Eq. (6.2), but with different definitions of the parameter A, exist for other specimen types, such as the Center Cracked Tension and the Single- or Double-Edge Notched Tension specimen, see Rice et al. (1973). Equations (6.1) and (6.2) yield identical *J*-values for a monotonically loaded elastic–plastic material as long as the crack remains stationary. This is not so for a growing crack (Kolednik 1991, 1993).

6.2.2 The cyclic J-integral

The cyclic *J*-integral ΔJ is a contour integral for cyclic loading, analogous to the *J*-integral for monotonic loading, and is defined by the relation (Lamba 1975; Wüthrich 1982; Tanaka 1983),

$$\Delta J = \int_{\Gamma} \left(\phi(\Delta\boldsymbol{\varepsilon})\,\mathrm{d}y - \Delta\mathbf{t} \cdot \frac{\partial(\Delta\mathbf{u})}{\partial x}\,\mathrm{d}s \right). \tag{6.3}$$

ΔJ has been termed "*Z*-integral" in Wüthrich (1982). The symbol Δ in Eq. (6.3) refers to the relative change of the parameters between two states. The quantity $\phi(\Delta\boldsymbol{\varepsilon})$ is analogously to the strain energy density defined as

$$\phi(\Delta\boldsymbol{\varepsilon}) = \int_{0}^{\Delta\varepsilon} \Delta\boldsymbol{\sigma} \cdot \mathrm{d}(\Delta\boldsymbol{\varepsilon}), \tag{6.4}$$

see the example presented in Appendix A. For the determination of the cyclic stresses and strains, a $\Delta\boldsymbol{\sigma} - \Delta\boldsymbol{\varepsilon}$-diagram is drawn with origin reset to the beginning of a new loading phase in a stress–strain hysteresis loop (Fig. 6.2b). The axes point into the direction of variation, i.e. into positive directions for a loading sequence. The expression $\phi(\Delta\boldsymbol{\varepsilon})$ corresponds to the strain energy density achieved during a single loading branch. Lamba (1975) and Tanaka (1983) showed that ΔJ is path independent if $\phi(\Delta\boldsymbol{\varepsilon})$ exhibits the properties of a potential, i.e. if the stress range $\Delta\boldsymbol{\sigma}$ is a unique function of $\Delta\boldsymbol{\varepsilon}$ (see also Anderson 1995).

The validity of the cyclic *J*-integral for elastic–plastic materials is dubious, since deformation plasticity does not describe the real elastic–plastic material behavior (see Section 6.2.1). This makes the application of ΔJ for the characterization of fatigue crack growth in elastic–plastic materials questionable (Anderson 1995).

Dowling and Begley (1976) proposed that the crack growth rate in low-cycle fatigue (LCF) is a function of the experimental cyclic *J*-integral. This experimental cyclic *J*-integral ΔJ^{exp} is determined from the area ΔA below the load–displacement record of a single loading (or unloading) branch (Fig. 6.2c). For deeply notched bending type specimens, ΔJ^{exp} is evaluated, analogously to Eq. (6.2), from the relation,

$$\Delta J^{\mathrm{exp}} = \frac{\eta \Delta A}{bB}. \tag{6.5}$$

Dowling and Begley (1976) propose to determine an effective value of the experimental cyclic *J*-integral $\Delta J_{\mathrm{eff}}^{\mathrm{exp}}$, if crack closure occurs: For the evaluation from the loading branch of the *F*–*v*-curve, the area ΔA should be taken from the point where crack flank contact fully disappears (point "op" in Fig. 6.2d); for evaluation from the unloading branch, ΔA should be taken only to the point when crack closure starts to become significant (point "cl" in Fig. 6.2d).

Dowling and Begley (1976) conducted fatigue tests using Compact Tension (C(T)-) specimens manufactured from A533B steel. Hereby the loading (mainly zero-to-maximum

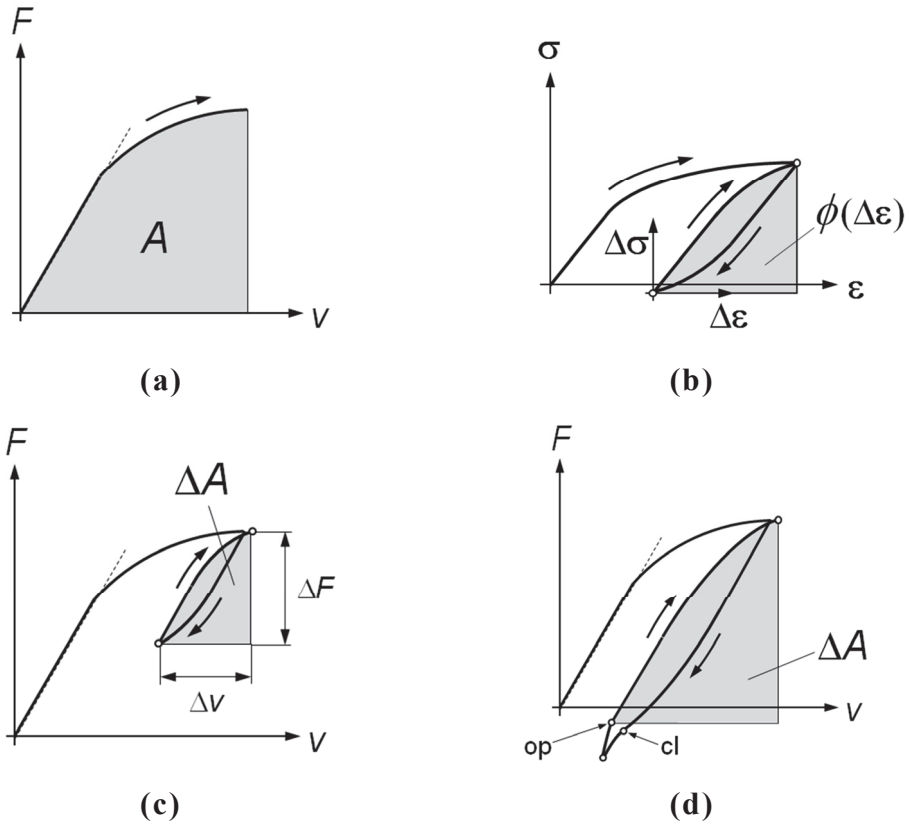

Fig. 6.2 **(a)** Determination of the experimental *J*-integral $J^{\exp}$ for a deeply notched bending type specimen from the area A under the load–displacement record. **(b)** Evaluation of cyclic stresses and strains for the evaluation of $\phi(\Delta\boldsymbol{\varepsilon})$, Eq. (5.4), by resetting the origin of a $\Delta\boldsymbol{\sigma}-\Delta\boldsymbol{\varepsilon}$-diagram. **(c)** Determination of ΔA for a re-loading sequence to calculate the experimental cyclic *J*-integral $\Delta J^{\exp}$, Eq. (5.5). **(d)** Determination of ΔA for a re-loading sequence in presence of crack closure from the point of crack opening "op" which yields $\Delta J_{\text{eff}}^{\exp}$; for an unloading sequence, ΔA should be determined only to the point "cl" where crack closure starts.

displacement control) was chosen so that general yielding conditions occurred, i.e. plasticity spreads from the crack tip to the back face of the specimen. The major finding in Dowling and Begley (1976) was that there exists a Paris-law type correlation between crack propagation rate $\mathrm{d}a/\mathrm{d}N$ and $\Delta J^{\exp}$ if no ratcheting effect appears, i.e. that stable stress and strain hysteresis loops are formed during cyclic loading. In a subsequent study, Dowling (1976) found a similar correlation for fatigue cracks in Center Cracked Tension specimens. Lambert et al. (1988) and Banks-Sills and Volpert (1991) combined experimental and numerical (finite element) studies of the cyclic *J*-integral. Lambert et al. (1988) performed displacement controlled tests on compact tension specimens made of AISI 316 stainless steel. Banks-Sills and Volpert (1991) conducted load controlled fatigue tests on compact tension specimens made of Al 2024-T351 with load ratios $R = 0.05$ and $R = 0.5$. In both papers, correlations between $\Delta J^{\exp}$ and $\mathrm{d}a/\mathrm{d}N$ were observed. In their numerical tests, cyclic *J*-integral values were evaluated from numerical *F*–*v* data, Eq. (6.5), and by applying Eq. (6.3) with

substitution of stresses and displacements determined from the numerical analysis. Close agreement between experimental and numerical results was found and, furthermore, the equivalence between Eq. (6.5) and Eq. (6.3) was numerically demonstrated.

Several other researchers have demonstrated via fatigue experiments that a functional relationship exists between ΔJ^{exp} and the fatigue crack growth rate, but this relationship has not been conclusively proven (Anderson 1995). "At this point, experimental documentation of a reasonably good characterization of fatigue crack growth under some elastic–plastic conditions is the main justification that can be provided for the application of *J*-integral to cyclic loading" (Suresh 1998, p. 315).

It should be noted here that Dowling (1977) derived a formula different from Eq. (6.5) for determining the experimental cyclic *J*-integral for *short* fatigue cracks, e.g. semi-circular surface cracks. It was found that the correlation between $\mathrm{d}a/\mathrm{d}N$ and ΔJ^{exp} for short cracks, in general, coincides with the correlation earlier found for long cracks (Dowling and Begley 1976; Dowling 1976). McClung et al. (1997) extended the ΔJ^{exp}-evaluation procedure to other surface crack geometries and to combined and multiaxial loading conditions. These and similar procedures have been applied successfully in fatigue life prediction models, e.g., in Döring et al. (2006). Such short fatigue cracks do not lie within the scope of the current paper.

6.2.3 The configurational force concept and the incremental plasticity J-integral J^{ep}

An extensive review on the relation between configurational forces and *J*-integrals has been given recently in Kolednik et al. (2014). Therefore, only essential relations are repeated in this section.

Configurational forces are thermodynamic forces that describe the driving force on defects in materials, such as dislocations, cracks, or interfaces (Maugin 1995; Gurtin 1995, 2000; Kienzler and Herrmann 2000). The notion of configurational forces, also called material forces, goes back to the works of Eshelby (1951, 1970), who introduced the configurational stress tensor **C** as "energy momentum tensor". A configurational force **f** appears at those positions in the body where the divergence of the configurational stress **C** does not vanish,

$$\mathbf{f} = -\nabla \cdot \mathbf{C} = -\nabla \cdot \left(\phi \mathbf{I} - \mathbf{F}^{\mathrm{T}} \mathbf{S} \right). \tag{6.6}$$

In Eq. (6.6) the symbol $\nabla \cdot$ denotes the divergence, **I** the identity tensor, $\mathbf{F}^{\mathrm{T}}$ the transposed of the deformation gradient, and **S** the 1st Piola-Kirchhoff stress. The configurational force **f** describes magnitude and direction of the driving force acting on the defect.

Consider a homogeneous body $\mathcal{B}$ with a sharp crack as illustrated in Fig. 6.1a. The scalar, near-tip *J*-integral can be derived from the concept of configurational forces in the form (Simha et al. 2003),

$$J_{\mathrm{tip}} = \mathbf{e} \cdot \mathbf{J}_{\mathrm{tip}} = \mathbf{e} \cdot \left(-\mathbf{f}_{\mathrm{tip}} \right) = \mathbf{e} \cdot \lim_{r \to 0} \int_{\Gamma_r} \mathbf{C}\,\mathbf{n}\, \mathrm{d}s\,, \tag{6.7}$$

where $\mathbf{f}_{\text{tip}}$ designates the configurational force vector emanating from the crack tip, and Γ_r is a contour drawn around the crack tip at a distance r; $\mathbf{n}$ is the outward unit normal vector to the contour. The scalar near-tip J-integral J_{tip} is the projection of the near-tip J-integral vector $\mathbf{J}_{\text{tip}}$ into the direction of the unit nominal vector in crack growth direction $\mathbf{e}$. The scalar J-integral along an arbitrary contour Γ is given by the relation,

$$J = \mathbf{e} \cdot \mathbf{J} = \mathbf{e} \cdot \int_{\Gamma} \mathbf{C}\mathbf{n}\,\mathrm{d}s = \mathbf{e} \cdot \int_{\Gamma} \left(\phi \mathbf{I} - \mathbf{F}^{\mathrm{T}}\mathbf{S}\right)\mathbf{n}\,\mathrm{d}s = J_{\text{tip}} - \mathbf{e} \cdot \int_{\mathcal{D}} \mathbf{f}\,\mathrm{d}A\,. \tag{6.8}$$

Here, $\mathcal{D}$ is the area enclosed by the contour Γ, but excludes the crack tip. The scalar J-integral J for an arbitrary contour Γ is the projection of the J-integral vector $\mathbf{J}$ into the direction $\mathbf{e}$.

The benefit of derivation of the J-integral via the configurational force concept is that Eq. (6.7) and Eq. (6.8) are independent of the constitutive relations of the material. For nonlinear elastic materials or elastic–plastic materials described by deformation plasticity, the total strain energy density ϕ is recoverable, whereas for incremental plasticity only the elastic part of the strain energy density ϕ_{e} is recoverable (Fig. 6.1b). Therefore, we distinguish in the following between the nonlinear elastic configurational force $\mathbf{f}^{\text{nlel}}$, if the total strain energy density ϕ is inserted into Eq. (6.6), and the elastic–plastic configurational force $\mathbf{f}^{\text{ep}}$, if the elastic part of the strain energy density ϕ_{e} is inserted.

Substitution of the total strain energy density ϕ into the configurational stress $\mathbf{C}$, Eq. (6.6), and into Eq. (6.8) yields the nonlinear elastic J-integral,

$$J^{\text{nlel}} = J_{\text{tip}}^{\text{nlel}} + \mathbf{e} \cdot \int_{\mathcal{D}} \nabla \cdot \left(\phi \mathbf{I} - \mathbf{F}^{\mathrm{T}}\mathbf{S}\right)\mathrm{d}A = J_{\text{tip}}^{\text{nlel}} - \mathbf{e} \cdot \int_{\mathcal{D}} \mathbf{f}^{\text{nlel}}\,\mathrm{d}A\,, \tag{6.9}$$

which is identical to the classical J-integral, Eq. (6.1). In homogeneous, nonlinear elastic materials, bulk configurational forces do not exist. Only a single configurational force $\mathbf{f}_{\text{tip}}^{\text{nlel}}$ appears at the crack tip, and the J-integral is path-independent.

In elastic–plastic fracture mechanics, the nonlinear elastic J-integral J^{nlel} is commonly applied to elastic–plastic materials. This application rests on the assumption of deformation theory of plasticity, see Introduction. However in such cases, J^{nlel} does not characterize the crack driving force any more (Rice 1968a,b). Another problem is that this approach is limited due to the occurrence of non-proportional loading, i.e. if unloading processes occur due to crack extension or unloading of the whole body, e.g. McMeeking (1977) or Anderson (1995). For the nonlinear elastic J-integral applied to elastic–plastic materials, based on deformation plasticity, we introduce the term "conventional J-integral" J^{conv}; the corresponding nonlinear elastic configurational force for elastic–plastic materials, based on deformation plasticity, is designated $\mathbf{f}^{\text{def.pl}}$.

It is well known from literature that the conventional J-integral, when applied to real elastic–plastic materials, i.e. materials modelled with incremental theory of plasticity, is path independent as long as proportional loading conditions prevail. If non-proportional loading occurs, J^{conv} becomes path dependent, see e.g. Brocks et al. (2003). Within the concept of

configurational forces, path dependence of J^{conv} means that (artificial) bulk configurational forces $\mathbf{f}^{\text{def.pl}}$ are induced, compare Eq. (6.9). This fact was demonstrated exemplarily by a numerical cyclic tensile test and then shown for crack extension under monotonic loading in Kolednik et al. (2014).

Substitution of the elastic part of the strain energy density ϕ_{e} into the configurational stress $\mathbf{C}$, Eq. (6.6), and into Eq. (6.8) yields the *J*-integral for elastic–plastic materials with incremental theory of plasticity (Simha et al. 2008),

$$J^{\text{ep}} = J^{\text{ep}}_{\text{tip}} + \mathbf{e} \cdot \int_{\mathcal{D}} \nabla \cdot \left(\phi_{\text{e}} \mathbf{I} - \mathbf{F}^{\text{T}} \mathbf{S} \right) \mathrm{d}A = J^{\text{ep}}_{\text{tip}} - \mathbf{e} \cdot \int_{\mathcal{D}} \mathbf{f}^{\text{ep}} \, \mathrm{d}A \,. \tag{6.10}$$

The main advantage of the elastic–plastic *J*-integral J^{ep} is that it has the physical meaning of a true driving force term in elastic–plastic materials.

In elastic–plastic materials bulk configurational forces $\mathbf{f}^{\text{ep}}$ appear in plastically deformed regions and they evolve proportional to the gradient of the plastic component of the deformation gradient (Simha et al. 2008),

$$\mathbf{f}^{\text{ep}} = \left(\mathbf{F}^{\text{e}} \right)^{\text{T}} \mathbf{S} : \frac{\partial \mathbf{F}^{\text{p}}}{\partial \mathbf{X}} \,. \tag{6.11}$$

Note that $\left(\mathbf{F}^{\text{e}} \right)^{\text{T}} \mathbf{S}$ gives a second order tensor, $\partial \mathbf{F}^{\text{p}} / \partial \mathbf{X}$ is a third-order tensor, see Section 6.2. Due to these bulk configurational forces, the elastic–plastic *J*-integral J^{ep} becomes path-dependent. Equation (6.11) holds for large strain theory with $\mathbf{F}^{\text{e}}$ and $\mathbf{F}^{\text{p}}$ as the elastic and plastic components of the deformation gradient.

The properties of J^{ep} (and J^{conv}) for monotonic loading, with and without crack extension and under various yielding conditions, have been studied extensively in Kolednik et al. (2014). It has been found that for stationary cracks and contours within the crack tip plastic zone, J^{ep} does not vary significantly for contour radii larger than the process zone. Hereby the process zone characterizes the intensely deformed region around the blunted crack tip, Rice and Johnson (1970). The length of the process zone $l_{\text{proc.z}}$ is proportional to the crack tip opening displacement δ_{t}, $l_{\text{proc.z}} = \kappa \delta_{\text{t}}$, with a pre-factor often assumed as $\kappa \approx 3$ (Rice and Johnson 1970; McMeeking 1977). A further decrease of the contour radius leads to a sharp decrease of J^{ep} and yields finally $J^{\text{ep}}_{\text{tip}} = 0$. This means that the driving force becomes zero, if the contour shrinks to the very tip, a fact first discovered by Rice (1979). The implications have been discussed in Kolednik et al. (2014), see also Section 6.5.1. When increasing the contour radius from a value $l_{\text{proc.z}}$, the incremental plasticity *J*-integral J^{ep} first remains approximately constant (inside the crack tip plastic zone), then remains exactly constant (for contours outside the crack tip plastic zone). Path dependence again starts, if the contours intersect the region of back-face plasticity.

For cracks continuously growing at a constant load, pronounced path dependence of J^{ep} occurs even for contours fully enclosing the region of the process zone, i.e. integration contour radius larger than $l_{\text{proc.z}}$, around the current crack tip (Kolednik et al. 2014). J^{ep} increases with increasing contour radius up to the point where the active plastic zone around

the current crack tip is surrounded. Again, a decrease of the contour radius to the current crack tip yields finally $J_{\mathrm{tip}}^{\mathrm{ep}} = 0$.

An important finding of Kolednik et al. (2014) is the following: For a stationary crack under monotonic loading, the appropriate parameter describing the crack driving force is the incremental plasticity *J*-integral $J_{\mathrm{PZ}}^{\mathrm{ep}}$ for an integration path, which encloses completely the crack tip plastic zone. If small- and large-scale yielding conditions prevail, $J_{\mathrm{PZ}}^{\mathrm{ep}}$ equals both the deformation plasticity *J*-integral around the crack tip plastic zone $J_{\mathrm{PZ}}^{\mathrm{conv}}$ and the experimental *J*-integral J^{exp},

$$J_{\mathrm{PZ}}^{\mathrm{ep}} = J_{\mathrm{PZ}}^{\mathrm{conv}} = J^{\mathrm{exp}} \tag{6.12}$$

The basic reason for the validity of Eq. (6.12) is that the condition $J_{\Gamma}^{\mathrm{ep}} = J_{\Gamma}^{\mathrm{conv}}$ holds, if the integration contour Γ goes only through elastically deformed regions. This can be seen from the middle terms of Eq. (6.8): If the contour Γ passes elastically deformed region only, there will appear no difference between the descriptions of deformation plasticity and incremental plasticity. Note that for monotonically loaded cracks $J_{\mathrm{PZ}}^{\mathrm{conv}}$ equals the far-field *J*-integral $J_{\mathrm{far}}^{\mathrm{conv}}$; this is not so for cyclically loaded cracks, since the conditions of proportional loading are disturbed in the unloading cycle. The reason for the equality at the right hand side of Eq. (6.12) has been discussed at the end of Section 6.2.1.

The appropriate crack driving force parameter for a continuously growing crack at constant load is the incremental plasticity *J*-integral $J_{\mathrm{actPZ}}^{\mathrm{ep}}$ for an integration path, which encloses completely the *active* plastic zone. The left side of Eq. (6.12) applies also for a growing crack, if the contour surrounds the complete plastic zone. It should be stressed that the right side of Eq. (6.12) does not apply, since $J_{\mathrm{PZ}}^{\mathrm{conv}} \neq J^{\mathrm{exp}}$ for a growing crack, see Kolednik (1991, 1993), Turner and Kolednik (1994).

The characteristic properties of J^{ep} for a stationary crack under cyclic loading conditions shall be worked out in the following by a numerical case study.

6.3 Finite element modeling and post processing

All simulations are performed using the commercially available finite element (FE) program ABAQUS/Standard 6.12 (see http://www.simulia.com/products/abaqus_fea.html), and a self-written post processing code developed in Python. The numerical case studies are conducted for a cyclically loaded C(T)-specimen (ASTM E1820, 2005) with a straight crack in horizontal *x*-direction (Fig. 6.3a). A stationary crack is considered, since the crack extension per load cycle is usually small in fatigue. Note that the doubts about the application of the *J*-integral in fatigue are caused by the strongly non-proportional loading conditions and not by the small crack extension per load cycle, which is similar to that during the blunting of a stationary crack. A possible influence of a small crack extension per load cycle will be investigated in a later study by adopting the numerical procedure of Newman (1976). The specimen dimensions are: crack length a = 25 mm, width W = 50 mm, height H = 60 mm, and

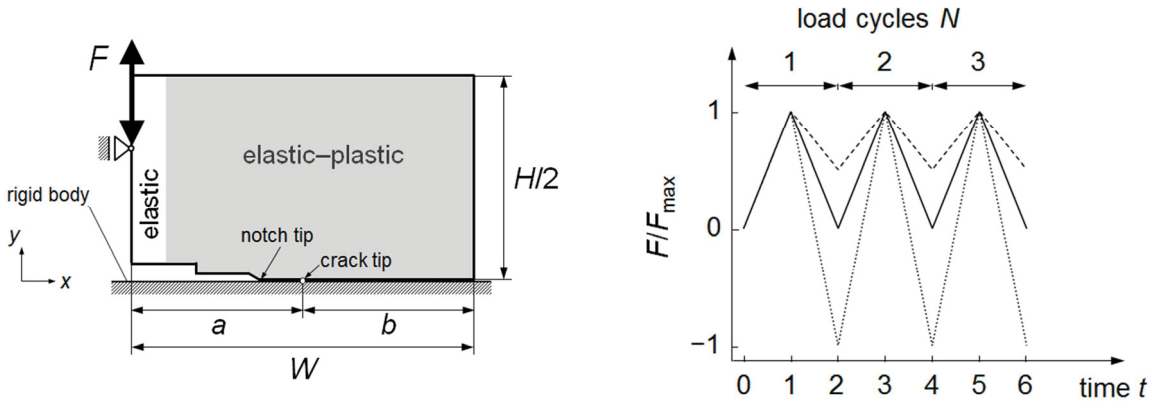

(a) **(b)**

Fig. 6.3 **(a)** FE model of the upper half of a C(T)-specimen. **(b)** Variation of the load F in time for constant maximum load F_{max} and various load ratios, $R = 0$ (*solid line*), $R = 0.5$ (*dashed line*), $R = -1$ (*dotted line*).

nominal thickness $B = 25$ mm. The crack is cyclically loaded under Mode I by prescribing the load F at the load application point.

The material is homogeneous, isotropic, elastic−ideally plastic. The material behavior is modeled using the incremental plasticity model provided by ABAQUS. The Young's modulus is $E = 200$ GPa, Poisson's ratio $\nu = 0.3$, and yield strength $\sigma_y = 270$ MPa. To avoid large plastic deformations at the load application point, a small strip is modeled consisting of linear elastic elements with $E = 200$ GPa (Fig. 6.3a). This does not pose any problems, since the plastic zone does not come close to the elastic strip.

Half of the two-dimensional C(T)-specimen is discretized. The FE mesh consists of bilinear 4-node continuum elements, under assumption of plane strain. The mesh size around the crack tip region is held constant for all simulations ($m = 0.2$ mm). Geometric nonlinearity is taken into account, since elements in the near-tip region undergo large deformations during the loading process. To consider crack flank contact, the counterpart to the upper geometry is modeled as rigid surface. No friction between the rigid body and the upper crack flank is applied. The displacements of all nodes on the plane $y = 0$ are fixed in y-direction but unlocked in x-direction, except the nodes on the crack flank.

The maximum number of applied load cycles is set to $N = 200$. The maximum load is set to $F_{max} = 35$ kN. Figure 6.4a shows the distribution of the accumulated plastic strain PEEQ for the load F_{max}. Large-scale yielding conditions are assumed to prevail, since plastic deformation appears at the back face of the specimen. The load ratio $R = F_{min}/F_{max}$, i.e. the ratio between minimum and maximum applied load, is set to $R = 0$ (zero-tension), $R = 0.5$ (pure tension), and $R = -1$ (tension-compression loading), see Fig. 6.3b.

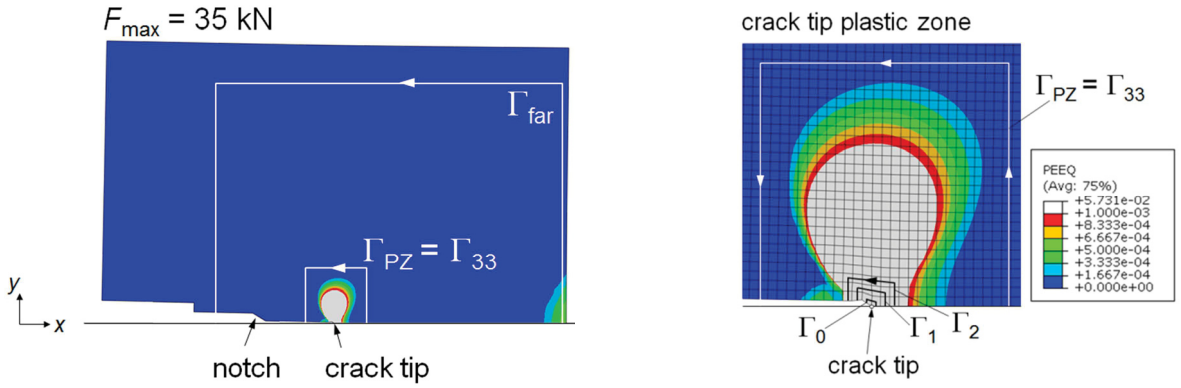

(a) **(b)**

Fig. 6.4 **(a)** Contour plots of the accumulated plastic strain PEEQ at $F_{max} = 35$ kN, which corresponds to large-scale yielding conditions. The back face plasticity region is also visible. **(b)** Nomenclature for *J*-integral contours. The *color code* of PEEQ is the same for both graphs. The *grey color* corresponds to regions with an equivalent plastic strain $\varepsilon_{eq}^{p} \geq 0.001$.

The finite element stress and strain analysis is in all cases performed with incremental theory of plasticity. The configurational force is calculated at each node following Eq. (6.6), using a self-written post processor based on the papers of Müller et al. (2002, 2004) and Denzer et al. (2003). Both types of configurational force, $\mathbf{f}^{\text{def.pl}}$ for deformation plasticity and $\mathbf{f}^{\text{ep}}$ for incremental plasticity, are computed. The *J*-integrals for deformation plasticity J^{conv} and incremental plasticity J^{ep} are calculated by a summation of all configurational forces lying within the area $\mathcal{D}$ bounded by the contour Γ,

$$J_{\Gamma}^{\text{conv}} = \sum_{n \in \mathcal{D} \cup \text{tip}} -\left(\mathbf{e} \cdot \mathbf{f}^{\text{def.pl}}\right) \Delta A_n , \tag{6.13}$$

$$J_{\Gamma}^{\text{ep}} = \sum_{n \in \mathcal{D} \cup \text{tip}} -\left(\mathbf{e} \cdot \mathbf{f}^{\text{ep}}\right) \Delta A_n . \tag{6.14}$$

The quantity ΔA_n designates the element area corresponding to a specific node n. Note that the crack tip node must be included in the summation. The summation of the configurational forces within a certain contour Γ is also performed by our post processing routine.

In addition to the *J*-integrals derived from the configurational forces, J^{conv} and J^{ep}, the computational *J*-integral values J^{VCE} are calculated for comparison, using the virtual crack extension method of ABAQUS (Parks 1977). Note that deformation plasticity is implicitly assumed in the calculation of J^{VCE}, when applying to elastic–plastic materials.

Figure 6.4b explains the nomenclature for various *J*-integral contours. The index i denotes the distance of an arbitrary contour Γ_i from its center, i.e. the crack tip, in units of element rings. For example, Γ_2 means that the integration area includes the nodes of two entire element rings; the corresponding *J*-integral is denoted J_2. From Eq. (6.13) and Eq. (6.14) it is clear that the integration contours go through the middle of the elements. The near-tip *J*-integral around the crack tip node $\Gamma_{\text{tip}} = \Gamma_0$ is denoted J_{tip}. The contour Γ_{PZ} designates a

path surrounding the crack tip plastic zone; the corresponding *J*-integral is denoted J_{PZ}. The far-field *J*-integral along the path Γ_{far} is termed J_{far}.

6.4 Application of the incremental plasticity J-integral J^{ep} for cyclic loading

This section deals with the characteristic properties of the incremental plasticity *J*-integral J^{ep} for a cyclically loaded specimen under large-scale yielding conditions. The conventional *J*-integral based on deformation plasticity, J^{conv}, and the computational *J*-integral J^{VCE} are studied for comparison. The load ratio *R* is varied to examine its possible influence on J^{ep}.

6.4.1 Load ratio R = 0

Figure 6.5 shows the evolution of the conventional *J*-integral J^{conv} for different integration contours Γ_i centered at the crack tip. In Fig. 6.5a, J^{conv} is plotted against time *t* for the first three load cycles, $N = 1 \div 3$. Figure 6.5b shows curves connecting the J^{conv}-values at maximum and minimum load, $F_{\max}$ and $F_{\min}$, respectively. Time $t = 2N - 1$, with $N \in \mathbb{N}$, corresponds to the state at maximum load $F_{\max}$, time $t = 2N$ corresponds to the state at minimum load $F_{\min}$ in the N^{th} load cycle.

It is seen from Fig. 6.5a that the J^{conv}-curves oscillate between certain maximum and minimum values, roughly corresponding to the variation of the prescribed load. Hereby a strong path dependence is observed. A slight path dependence appears already during monotonic loading in the first load cycle. The value directly at the crack tip, $J_{\mathrm{tip}}^{\mathrm{conv}}$, is significantly smaller than higher contour values, but this effect is mainly caused due to the discretization problem; configurational forces are induced onto the neighboring nodes, which usually belong to the crack tip (Kolednik et al. 2014). The path dependence of J^{conv} becomes especially strong during unloading from $F_{\max}$. Also in all the following load cycles, path dependence becomes more and more pronounced during the unloading sequence and decreases during the loading sequence.

Note that path dependence of J^{conv} is in contradiction to theory, since no bulk configurational forces should appear in a material with deformation plasticity, see Section 6.2.3. Hence, the question arises whether the computed J^{conv}-values are physically sound. Performing a numerical cyclic tensile test, Kolednik et al. (2014) exemplified the difficulties in applying deformation plasticity for the description of elastic–plastic materials. The reason is that artificial bulk configurational forces $\mathbf{f}^{\mathrm{def.pl}}$ are induced in regions with a plastic strain gradient, as soon as the conditions of proportional loading are violated. Due to these artificial bulk configurational forces, which do not have any physical meaning, J^{conv} becomes path dependent under cyclic loading, within plastically deformed regions.

Since the plastic strain gradient decreases with increasing distance from the crack tip, path dependence becomes weaker with increasing contour radius. For contours outside the crack tip plastic zone, J^{conv} becomes path-independent, $J_{\Gamma}^{\mathrm{conv}} = J_{\mathrm{PZ}}^{\mathrm{conv}}$, as long as the contour Γ does not intersect the region of remote plasticity. Note that the contour $\Gamma_{33} = \Gamma_{\mathrm{PZ}}$ encloses completely the crack tip plastic zone (Fig. 6.4a). Once the integration path crosses the back-

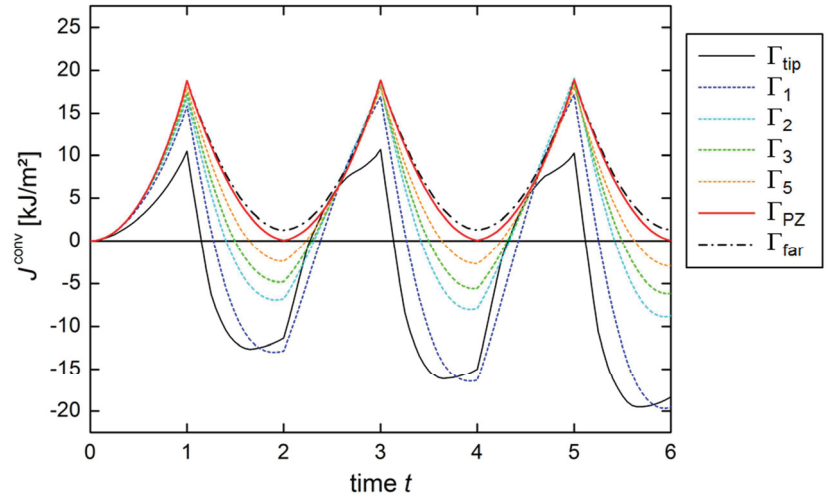

(a)

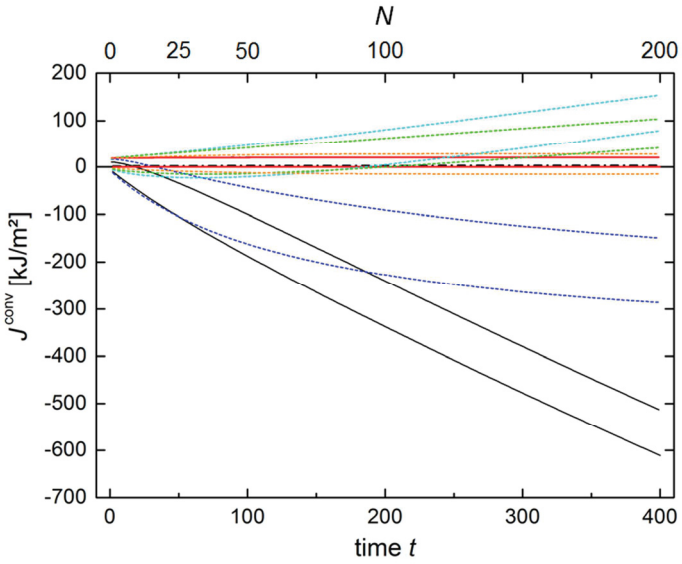

(b)

Fig. 6.5 **(a)** Conventional, deformation plasticity *J*-integral J^{conv} plotted against time t for various contours Γ_i around the crack tip. The first three load cycles are depicted. The load ratio is $R = 0$ (zero-tension cyclic loading). **(b)** Development of J^{conv} for high load cycle numbers N; the curves connect the *J*-values, J^{conv}_{min} and J^{conv}_{max}, at maximum and minimum load, respectively. The J^{conv}-values for contours near the tip do not exhibit saturation; J^{conv}_{PZ} and J^{conv}_{far} show saturated values for high N.

face plastic zone, J^{conv} starts to become path dependent again and reaches finally the far-field value, J^{conv}_{far}. For the second load cycle, $N = 2$, J^{conv}_{PZ} varies between $J^{conv}_{PZ,max} = 18.86$ kJ/m² at F_{max} and $J^{conv}_{PZ,min} = 0.053$ kJ/m² at F_{min}, whereas the far-field *J*-integral varies between the values $J^{conv}_{far,max} = 18.87$ kJ/m² and $J^{conv}_{far,min} = 1.286$ kJ/m². In general, $J^{conv}_{far,max}$ is almost equal to $J^{conv}_{PZ,max}$, and $J^{conv}_{far,min}$ is somewhat larger than $J^{conv}_{PZ,min}$.

Table 6.1 Values of the incremental plasticity *J*-integrals, $J_{\mathrm{PZ}}^{\mathrm{ep}}$ and $J_{\mathrm{far}}^{\mathrm{ep}}$, and the conventional, deformation plasticity *J*-integral $J_{\mathrm{PZ}}^{\mathrm{conv}}$ for load ratio $R = 0$ during various load cycles *N*.

N	$J_{\mathrm{PZ,max}}^{\mathrm{ep}}$	$J_{\mathrm{PZ,min}}^{\mathrm{ep}}$	$J_{\mathrm{far,max}}^{\mathrm{ep}}$	$J_{\mathrm{far,min}}^{\mathrm{ep}}$	$J_{\mathrm{PZ,max}}^{\mathrm{conv}}$	$J_{\mathrm{PZ,min}}^{\mathrm{conv}}$	$\Delta J_{\mathrm{PZ}}^{\mathrm{ep}}$	$\Delta J_{\mathrm{PZ}}^{\mathrm{conv}}$	ΔJ^{exp}
-	[kJ/m²]						[kJ/m²]		
1	18.80	0.050	17.56	0.028	18.80	0.050	-	-	18.42
2	18.86	0.053	17.61	0.028	18.86	0.053	16.97	16.97	16.72
25	19.54	0.086	18.02	0.036	19.54	0.086	17.03	17.03	16.69
50	19.84	0.105	18.19	0.039	19.84	0.105	17.06	17.06	16.70
100	20.09	0.124	18.31	0.040	20.09	0.124	17.06	17.06	16.72
200	20.15	0.135	18.30	0.037	20.15	0.135	17.00	17.00	16.74

The indices "max" and "min" denote values at maximum and minimum load. The cyclic *J*-integral values $\Delta J_{\mathrm{PZ}}^{\mathrm{ep}}$ and $\Delta J_{\mathrm{PZ}}^{\mathrm{conv}}$ are calculated for re-loading sequences following Eq. (6.19) and Eq. (6.22). The values of the experimental cyclic *J*-integral ΔJ^{exp} are evaluated from Eq. (6.5). For the first load cycle, the value listed under column ΔJ^{exp} denotes the experimental *J*-integral after loading to the maximum load.

Figure 6.5b shows the development of $J_{i,\mathrm{max}}^{\mathrm{conv}}$ - and $J_{i,\mathrm{min}}^{\mathrm{conv}}$ -values for load cycle numbers up to $N = 200$. For contours at and very close to the crack tip, $i = 0$ (tip) and $i = 1$, the $J_{i,\mathrm{max}}^{\mathrm{conv}}$ - and $J_{i,\mathrm{min}}^{\mathrm{conv}}$ -curves continuously decrease with increasing *N*, whereas the curves for $i = 2$ and $i = 3$ continuously increase. The curves for $J_{\mathrm{PZ}}^{\mathrm{conv}}$ and $J_{\mathrm{far}}^{\mathrm{conv}}$ increase only slightly and seem to reach stationary values for high load cycle numbers. For example, $J_{\mathrm{PZ,max}}^{\mathrm{conv}} = 20.15\ \mathrm{kJ/m^2}$ and $J_{\mathrm{far,max}}^{\mathrm{conv}} = 20.36\ \mathrm{kJ/m^2}$ at maximum load of the 200th load cycle; the values at minimum load are $J_{\mathrm{PZ,min}}^{\mathrm{conv}} = 0.135\ \mathrm{kJ/m^2}$ and $J_{\mathrm{far,min}}^{\mathrm{conv}} = 2.094\ \mathrm{kJ/m^2}$. Table 6.1 lists additional $J_{\mathrm{PZ}}^{\mathrm{conv}}$ - values for various load cycles.

The computation of the standard ABAQUS J^{VCE}- values leads, with high accuracy, to the same results as J^{conv}. In spite of the problems that occur when deformation plasticity is used to describe elastic–plastic material behavior, the application of $J_{\mathrm{PZ}}^{\mathrm{conv}}$ or $J_{\mathrm{PZ}}^{\mathrm{VCE}}$, which varies always between a certain maximum and a value close to zero, might be still useful for cyclic loading; the reason will be explained below.

Next, the behavior of the *J*-integral for elastic–plastic materials with incremental plasticity J^{ep} is discussed for zero-tension cyclic loading, Fig. 6.6. The J^{ep}-curves for the first three load cycles, Fig. 6.6a, appear similar to the J^{conv}-curves shown in Fig. 6.5a. Some important details are different, however.

The basic difference is that the depicted path dependence of J^{ep} is physically correct; the reason is the appearance of bulk configurational forces $\mathbf{f}^{\mathrm{ep}}$ within the plastically deformed regions, see Section 6.2.3. With increasing radius of the integration contour, starting from $\Gamma_0 = \Gamma_{\mathrm{tip}}$, more and more $\mathbf{f}^{\mathrm{ep}}$-vectors are included and cause a variation of J^{ep}, compare Eq. (6.14). The behavior will be explained in more detail in Section 6.4.2. When for a contour

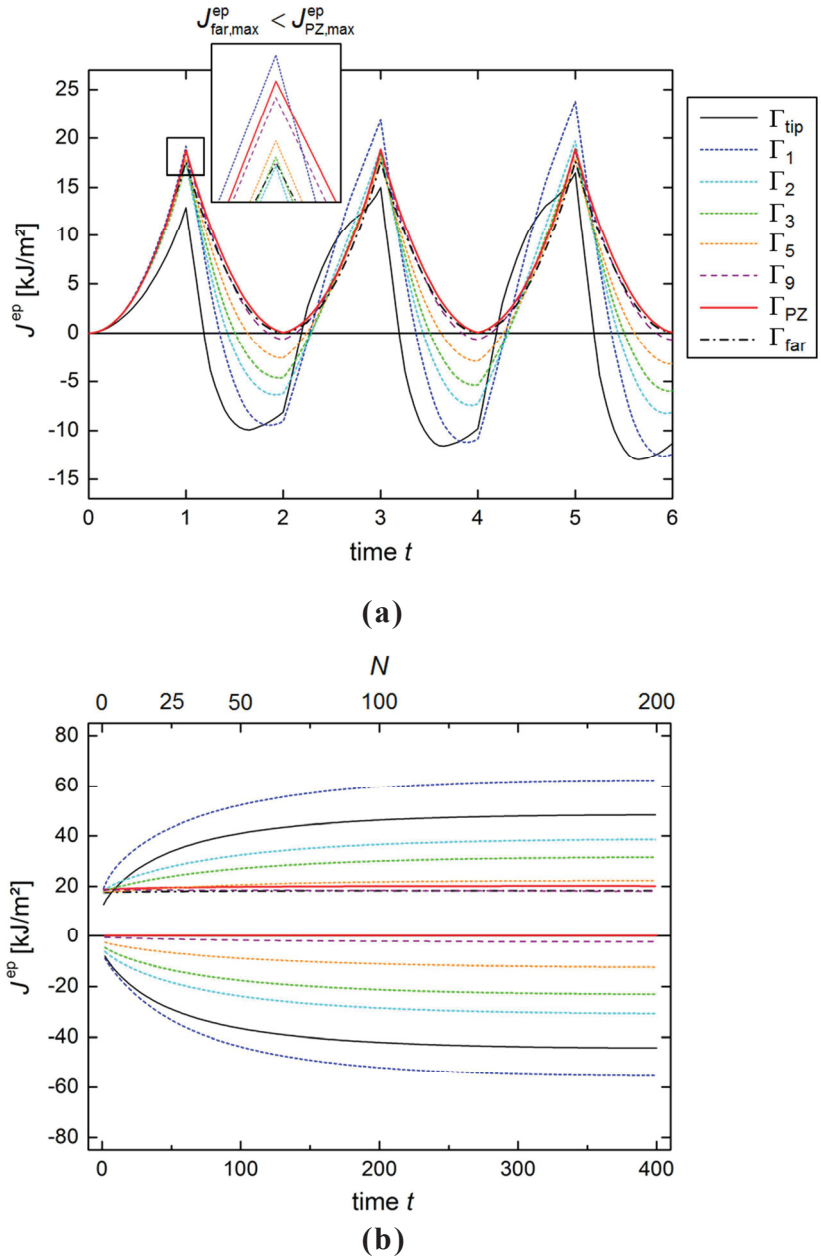

Fig. 6.6 **(a)** Incremental plasticity J-integral J^{ep} plotted against time t for various contours Γ_i around the crack tip. The first three load cycles are depicted. The load ratio is $R = 0$ (zero-tension cyclic loading). A lower J^{ep}_{far}-curve compared to J^{ep}_{PZ} appears due to the anti-shielding effect of the back-face plastic zone. **b** Behavior of J^{ep} for high load cycle numbers N. Saturation is visible for all J^{ep}-curves.

$\Gamma_{33} = \Gamma_{PZ}$ the crack tip plastic zone is completely enclosed, $J^{ep}_{\Gamma} = J^{ep}_{PZ}$ remains constant for further increasing contour radius. The reason is that the integration contour then proceeds only through elastically deformed regions where no bulk configurational forces appear. Path dependence again starts when Γ intersects the remote plastic zone at the back face of the specimen, and J^{ep} reaches finally the value of J^{ep}_{far} on the far-field contour.

A few examples for the values of $J_{\mathrm{PZ}}^{\mathrm{ep}}$ and $J_{\mathrm{far}}^{\mathrm{ep}}$ shall be given: For the second load cycle, $N = 2$, $J_{\mathrm{PZ}}^{\mathrm{ep}}$ varies between $J_{\mathrm{PZ,max}}^{\mathrm{ep}} = 18.86$ kJ/m² and $J_{\mathrm{PZ,min}}^{\mathrm{ep}} = 0.053$ kJ/m², whereas $J_{\mathrm{far}}^{\mathrm{ep}}$ varies between $J_{\mathrm{far,max}}^{\mathrm{ep}} = 17.61$ kJ/m² and $J_{\mathrm{far,min}}^{\mathrm{ep}} = 0.028$ kJ/m². Whereas the difference between $J_{\mathrm{PZ}}^{\mathrm{ep}}$ and $J_{\mathrm{far}}^{\mathrm{ep}}$ is negligible at the minimum load, this is not so at the maximum load. The reason will be explained in Section 4.2. Irreversible elastic strain energy, which is stored around the crack tip (Atkins and Mai 1986), is probably the reason why $J_{\mathrm{PZ,min}}^{\mathrm{ep}}$ and $J_{\mathrm{far,min}}^{\mathrm{ep}}$ are not exactly zero after full unloading of the specimen.

Figure 6.6b shows the development of the incremental plasticity *J*-integral values at maximum and minimum load, $J_{i,\mathrm{max}}^{\mathrm{ep}}$ and $J_{i,\mathrm{min}}^{\mathrm{ep}}$, with increasing load cycle number, up to $N = 200$. The J_i^{ep}-amplitudes increase and, on the contrary to J_i^{conv}, all curves seem to reach saturation values. The values of $J_{\mathrm{PZ}}^{\mathrm{ep}}$ and $J_{\mathrm{far}}^{\mathrm{ep}}$ exhibit only little variation with increasing *N*, see Table 6.1. For example, for $N = 200$ we get $J_{\mathrm{PZ,max}}^{\mathrm{ep}} = 20.15$ kJ/m² and $J_{\mathrm{PZ,min}}^{\mathrm{ep}} = 0.135$ kJ/m², and $J_{\mathrm{far,max}}^{\mathrm{ep}} = 18.30$ kJ/m² and $J_{\mathrm{far,min}}^{\mathrm{ep}} = 0.037$ kJ/m², respectively.

A comparison of Fig. 6.5 with Fig. 6.6 and the data listed in Table 6.1 demonstrate that, for contours surrounding the crack tip plastic zone Γ_{PZ}, the deformation plasticity *J*-integral J^{conv} has exactly the same value as the incremental plasticity *J*-integral J^{ep}. This is so, independent of the considered time step *t*. For example, at the maximum load during the second load cycle, $t = 3$, we get $J_{\mathrm{PZ,max}}^{\mathrm{ep}} = J_{\mathrm{PZ,max}}^{\mathrm{conv}} = 18.86$ kJ/m²; at the maximum load during the 200th load cycle, $t = 399$, we get $J_{\mathrm{PZ,max}}^{\mathrm{ep}} = J_{\mathrm{PZ,max}}^{\mathrm{conv}} = 20.15$ kJ/m². The same applies for larger contour radii, as long as the back-face plasticity region is not touched. The reason lies in the left-hand side equality of Eq. (6.12): The incremental- and deformation plasticity *J*-integrals are equal, $J_{\Gamma}^{\mathrm{ep}} = J_{\Gamma}^{\mathrm{conv}}$, if the integration contour Γ goes through elastically deformed regions only, see Kolednik et al. (2014). This is valid also for cyclic loading conditions.

6.4.2 Variations of bulk configurational forces during unloading

In order to find out why J^{ep} achieves so different—and even negative—values for various contours and different loading stages, it is reasonable to examine the distribution of the incremental plasticity configurational forces $\mathbf{f}^{\mathrm{ep}}$.

First, we concentrate on the configurational forces that appear in the region of back-face plasticity. Fig. 6.7a shows the field of $\mathbf{f}^{\mathrm{ep}}$-vectors at maximum load F_{max} of the first load cycle, Fig. 6.7b shows the $\mathbf{f}^{\mathrm{ep}}$-vectors at F_{min}. At maximum load, all $\mathbf{f}^{\mathrm{ep}}$-vectors point into positive *x*-direction (Fig. 6.7a). Consideration of Eq. (6.10) reveals that these $\mathbf{f}^{\mathrm{ep}}$-vectors diminish the magnitude of the *J*-integral J^{ep} as soon as the integration contour Γ crosses the back-face plastic zone. Back-face plasticity provides an anti-shielding effect and, consequently, $J_{\mathrm{far}}^{\mathrm{ep}} < J_{\mathrm{PZ}}^{\mathrm{ep}}$ at maximum load; this is also seen in the inlay diagram in Fig. 6.6a. During unloading, the bulk configurational forces decrease and, finally, they almost vanish at $F_{\mathrm{min}} = 0$ (Fig. 6.7b). This is the reason why $J_{\mathrm{far,min}}^{\mathrm{ep}}$ is almost equal to $J_{\mathrm{PZ,min}}^{\mathrm{ep}}$.

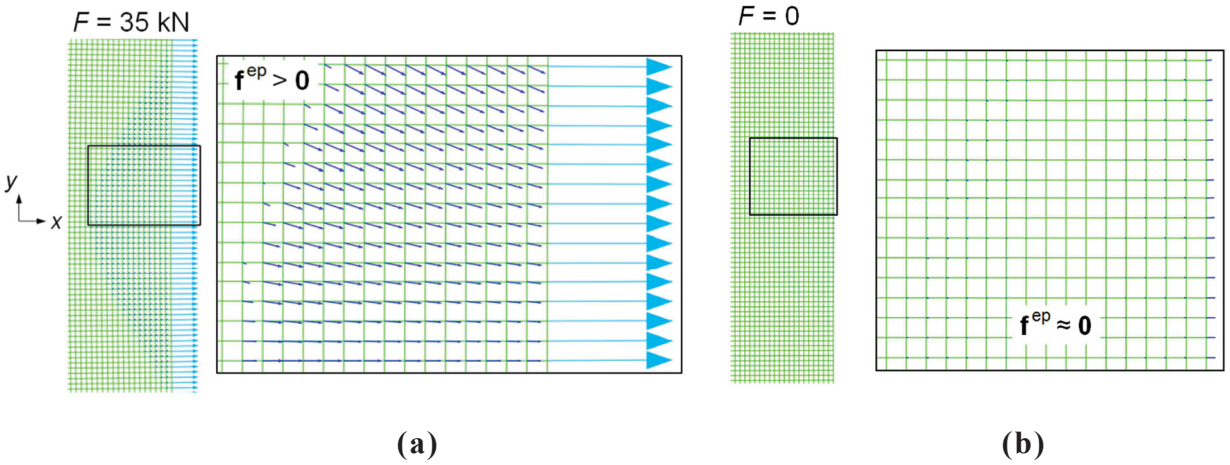

Fig. 6.7 Distribution of incremental plasticity bulk configurational forces $\mathbf{f}^{\mathrm{ep}}$. Detailed view of the back-face region **(a)** at time $t = 1$, maximum load, and **(b)** at $t = 2$ after unloading to zero. After fully unloading the $\mathbf{f}^{\mathrm{ep}}$-field nearly vanishes.

Notice that in the case of post-processing with deformation plasticity, artificial bulk configurational force vectors $\mathbf{f}^{\mathrm{def.pl}}$ are present due to non-proportional loading in the back-face plasticity region. However, the behavior of the $\mathbf{f}^{\mathrm{def.pl}}$-vectors is opposite to that of the $\mathbf{f}^{\mathrm{ep}}$-vectors: At maximum load $F_{\max}$ the $\mathbf{f}^{\mathrm{def.pl}}$-vectors are very small and this is the reason why the values of $J^{\mathrm{conv}}_{\mathrm{PZ,max}}$ and $J^{\mathrm{conv}}_{\mathrm{far,max}}$ barely differ, see Section 6.4.1 and Fig. 6.5a. The conditions of proportional loading are violated during unloading and a field of $\mathbf{f}^{\mathrm{def.pl}}$-vectors is induced. These $\mathbf{f}^{\mathrm{def.pl}}$-vectors have negative x-components. Therefore, at $F_{\min} = 0$ the value of $J^{\mathrm{conv}}_{\mathrm{far,min}}$ becomes larger than $J^{\mathrm{conv}}_{\mathrm{PZ,min}}$, compare Eq. (6.9) and Fig. 6.5a.

Next we want to clarify the questions why negative J^{ep}-values appear during unloading within the crack tip plastic zone and whether these negative J^{ep}-values are physically sound. Therefore, the behavior of the configurational forces near the crack tip is studied during the first unloading step.

Figure 6.8 presents arrow plots of the bulk configurational forces $\mathbf{f}^{\mathrm{ep}}$ within the crack tip plastic zone at different time steps. Figure 6.8a shows the $\mathbf{f}^{\mathrm{ep}}$-field at $t = 1$, maximum load. The configurational force $\mathbf{f}^{\mathrm{ep}}_{\mathrm{tip}}$, emanating from the tip node, points into the negative x-direction, i.e. the near-tip J-integral $J^{\mathrm{ep}}_{\mathrm{tip}} = \mathbf{e} \cdot \left(- \mathbf{f}^{\mathrm{ep}}_{\mathrm{tip}} \right)$ is positive, Eq. (6.7).[10] Note that the unit nominal vector in crack growth direction $\mathbf{e}$ points into the positive x-direction (Fig. 6.1a). If the specimen is unloaded, we observe that the magnitude of the $\mathbf{f}^{\mathrm{ep}}_{\mathrm{tip}}$-vector decreases, Fig 6.8b. At $t = 1.17$ and $F = 28.4\,\mathrm{kN}$, $\left| \mathbf{f}^{\mathrm{ep}}_{\mathrm{tip}} \right|$ becomes zero and, hence, $J^{\mathrm{ep}}_{\mathrm{tip}}$ vanishes (Fig. 6.8c). After further unloading, the $\mathbf{f}^{\mathrm{ep}}_{\mathrm{tip}}$-vector points into positive x-direction (Fig. 6.8d), which implies that $J^{\mathrm{ep}}_{\mathrm{tip}}$ is negative. The magnitude of the $\mathbf{f}^{\mathrm{ep}}_{\mathrm{tip}}$-vector increases with further decreasing load (Fig. 6.8e), until $F = 0$ (Fig. 6.8f).

[10] For numerical reasons, the magnitude of $J^{\mathrm{ep}}_{\mathrm{tip}}$ depends on the mesh size, see Kolednik et al. (2014).

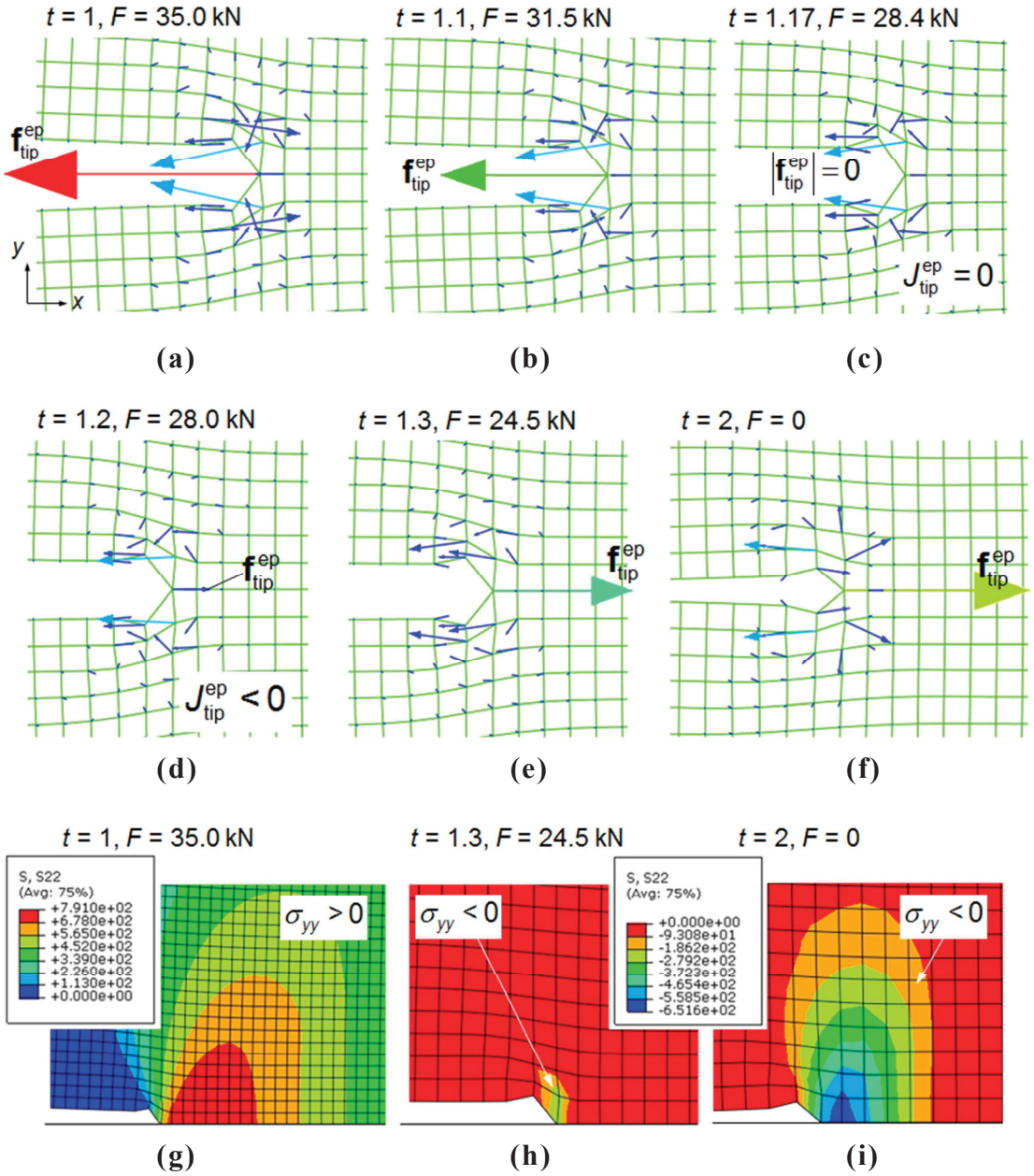

Fig. 6.8 Arrow plots of incremental plasticity bulk configurational forces $\mathbf{f}^{\mathrm{ep}}$ at different time steps during unloading: **(a)** time $t = 1$, maximum load; **(b)** $t = 1.1$; **(c)** $t = 1.17$, where $\left|\mathbf{f}_{\mathrm{tip}}^{\mathrm{ep}}\right|$ and, hence, $J_{\mathrm{tip}}^{\mathrm{ep}}$ vanish; **(d)** $t = 1.2$, where $\mathbf{f}_{\mathrm{tip}}^{\mathrm{ep}}$ and $J_{\mathrm{tip}}^{\mathrm{ep}}$ have turned in sign; **(e)** $t = 1.3$; **(f)** $t = 2$, after full unloading. The lower row shows contour plots of the principal stress σ_{yy}: **(g)** tensile stress field near the crack tip at $F_{\max}$, $t = 1$; **(h)** compressive stresses appear in front of the crack tip already after small unloading, $t = 1.3$; **(i)** final compressive stress field at $F_{\min}$, $t = 2$.

Configurational forces emanating from nodes near the crack tip rotate during unloading (Fig. 6.8b–f). A comparison of Fig. 6.8a, f shows that most of the near-tip bulk configurational forces have rotated so that their *x*-components have changed signs. Consequently, it becomes clear why the scalar J^{ep}-integrals for contours near the crack tip also changed from positive to negative values, compare Eq. (6.14).

Now to the question, why do the *x*-components of the near-tip $\mathbf{f}^{\mathrm{ep}}$-vectors change sign during unloading? The bulk configurational force of Eq. (6.11) can be expressed for small strain plasticity as (Simha et al. 2008),

$$\mathbf{f}^{\mathrm{ep}} = \boldsymbol{\sigma} : \frac{\partial \dot{\boldsymbol{\varepsilon}}^{\mathrm{p}}}{\partial \mathbf{x}}, \tag{6.15}$$

where $\boldsymbol{\sigma}$ denotes the Cauchy stress tensor and $\boldsymbol{\varepsilon}^{\mathrm{p}}$ the plastic part of the linear strain tensor $\boldsymbol{\varepsilon}$. Hence, $\mathbf{f}^{\mathrm{ep}}$ depends on the stress and the gradient of the plastic strain. Only the *x*-component f_x^{ep} contributes to the scalar *J*-integral,

$$f_x^{\mathrm{ep}} = \sigma_{xx} \frac{\partial \dot{\varepsilon}_{xx}^{\mathrm{p}}}{\partial x} + 2\sigma_{xy} \frac{\partial \dot{\varepsilon}_{xy}^{\mathrm{p}}}{\partial x} + \sigma_{yy} \frac{\partial \dot{\varepsilon}_{yy}^{\mathrm{p}}}{\partial x}. \tag{6.16}$$

At maximum load $F_{\max}$, the stress components in *y*-direction σ_{yy} near the crack tip are tensile stresses (Fig. 6.8g); also the stress components in *x*-direction σ_{xx} are positive. Both normal stress components become negative during unloading, which is shown for the component σ_{yy} in Fig. 6.8h, i. While compressive stresses appear near the crack tip already after small unloading, the components of the plastic strain only slightly change. From Eq. (6.16) it is evident that changes in sign of the stresses σ_{xx} and σ_{yy} lead to a change in sign of the *x*-component of the bulk configurational force f_x^{ep}.

Thus, we can conclude that the negative values of the incremental plasticity *J*-integral J^{ep} during the unloading stage for contours near to the crack tip are correct. Remains the question, how far does the zone extend where negative J^{ep}-values may occur? Since negative J^{ep}-values are connected with the appearance of compressive stresses, the cyclic plastic zone is a probable candidate. The radius of the cyclic plastic zone can be estimated by inserting twice the yield stress σ_{y} into Irwin's estimate of the plastic zone (Rice 1967) and using the relation between *J*-integral and stress intensity factor *K* in the form $J = K^2/E$ where the term $\left(1-\nu^2\right)$ for plane strain conditions is neglected. The radius of the plastic zone for monotonic and cyclic loading is given by

$$r_{\mathrm{pl}} = \beta \frac{JE}{\left(\sigma_{\mathrm{y}}\right)^2} \qquad \text{and} \qquad r_{\mathrm{pl,cyc}} = \beta \frac{\Delta J\, E}{\left(2\sigma_{\mathrm{y}}\right)^2}, \tag{6.17}$$

respectively, where β is a constant with the magnitude $\beta \cong 0.1$. Note that Eq. (6.28) must be applied for evaluating the cyclic *J*-integral ΔJ, see Appendix and Section 6.5.2.

For the maximum load $F_{\max} = 35$ kN, the extension of the monotonic plastic zone (in *y*-direction) is determined from the numerical analysis, $r_{\mathrm{pl}} = 6.6$ mm, i.e. 33 elements counted from the crack tip (this can be seen if the equivalent plastic strain is plotted in Fig. 6.4b with

an upper limit value $\varepsilon_{eq}^{p} \geq 10^{-10}$); the extension of the cyclic plastic zone is $r_{pl,cyc} = 1.8$ mm, i.e. 9 elements. This relation between r_{pl} and $r_{pl,cyc}$ is roughly in agreement with Eq. (6.17).

The size of the cyclic plastic zone roughly corresponds to the field of compressive negative σ_{yy} in Fig. 6.8i. The depicted compressive stress zone is the region where the x-components of the bulk configurational forces reverse their signs during unloading. The J^{ep}-value is given by the sum of the x-components of all $\mathbf{f}^{ep}$-vectors lying inside the contour, Eq. (6.14). Therefore, for a contour surrounding the cyclic plastic zone, the J^{ep}-value at F_{min} is negative; for example, after the first load cycle, at $t = 2$, we get $J_{9,min}^{ep} = -0.871$ kJ/m², see also Fig. 6.6a. This means that at minimum load the driving force for the combined movement of the crack tip plus the cyclic plastic zone is negative. For larger contours, the configurational forces with reversed sign are more and more compensated: at $t = 2$, we get $J_{18,min}^{ep} = -0.018$ kJ/m², $J_{19,min}^{ep} = 0.005$ kJ/m², and finally, for a contour surrounding the entire crack tip plastic zone, $J_{PZ,min}^{ep} = 0.053$ kJ/m².

6.4.3 Load ratio R = 0.5

In this section, the properties of the incremental plasticity J-integral J^{ep} are explained for a load ratio $R = 0.5$ (pure tension cyclic loading). Figure 6.9 shows the evolution of J^{ep} versus time t for different integration paths Γ_i during the first three load cycles. In comparison to the case with $R = 0$, the J^{ep}-curves for $R = 0.5$ are more similar to the corresponding zigzag shape of the prescribed load. Only for the inner three contours, $i = 0$ (tip), $i = 1$, and $i = 2$, J_i^{ep} becomes negative at the minimum load, $F_{min} = 17.5$ kN. This corresponds to a smaller extension of the cyclic plastic zone, $r_{pl,cyc} = 0.6$ mm, which should be, in agreement with Eq. (6.17), approximately one-sixteenth of the monotonic plastic zone size, $r_{pl} = 6.6$ mm. The magnitude of $J_{i,min}^{ep}$ increases with increasing contour radius and reaches finally the value of $J_{PZ,min}^{ep}$, which is distinctly larger than zero.

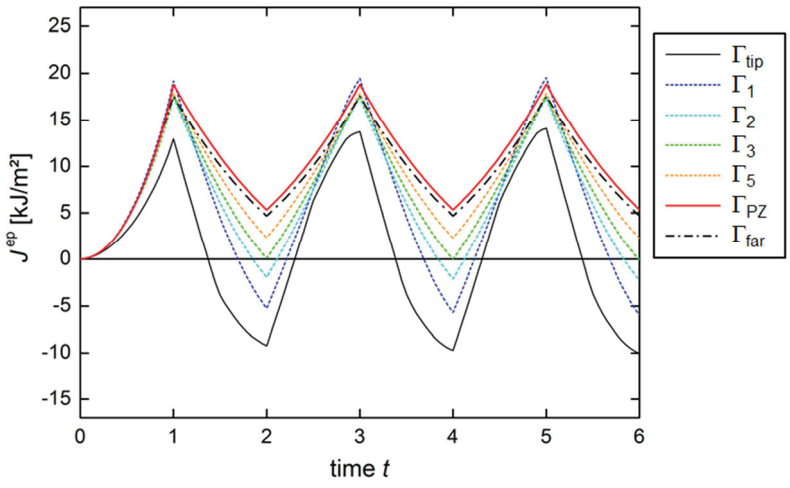

Fig. 6.9 Incremental plasticity J-integral J^{ep} plotted against time t for various contours Γ_i centered the crack tip. The first three load cycles, $N = 1 \div 3$, are plotted. The load ratio is $R = 0.5$.

Table 6.2 Values of the incremental plasticity *J*-integrals, $J_{\mathrm{PZ}}^{\mathrm{ep}}$ and $J_{\mathrm{far}}^{\mathrm{ep}}$, and the conventional, deformation plasticity *J*-integral $J_{\mathrm{PZ}}^{\mathrm{conv}}$ for load ratio $R = 0.5$ during various load cycles *N*.

N	$J_{\mathrm{PZ,max}}^{\mathrm{ep}}$	$J_{\mathrm{PZ,min}}^{\mathrm{ep}}$	$J_{\mathrm{far,max}}^{\mathrm{ep}}$	$J_{\mathrm{far,min}}^{\mathrm{ep}}$	$J_{\mathrm{PZ,max}}^{\mathrm{conv}}$	$J_{\mathrm{PZ,min}}^{\mathrm{conv}}$	$\Delta J_{\mathrm{PZ}}^{\mathrm{ep}}$	$\Delta J_{\mathrm{PZ}}^{\mathrm{conv}}$	ΔJ^{exp}
-	[kJ/m²]						[kJ/m²]		
1	18.80	5.321	17.56	4.681	18.80	5.321	-	-	18.42
2	18.82	5.334	17.58	4.688	18.82	5.334	4.127	4.127	4.054
25	18.96	5.407	17.66	4.727	18.96	5.407	4.117	4.117	4.040
50	19.01	5.433	17.68	4.740	19.01	5.433	4.117	4.117	4.038
100	19.05	5.455	17.70	4.749	19.05	5.455	4.117	4.117	4.038
200	18.80	5.321	17.56	4.681	18.80	5.321	-	-	18.42

The cyclic *J*-integral values $\Delta J_{\mathrm{PZ}}^{\mathrm{ep}}$ and $\Delta J_{\mathrm{PZ}}^{\mathrm{conv}}$ are calculated for re-loading sequences following Eq. (6.19) and Eq. (6.22). The values of the experimental cyclic *J*-integral ΔJ^{exp} are evaluated from Eq. (6.5).

Due to the anti-shielding effect of the bulk configurational forces emanating from the region of back-face plasticity, the far-field *J*-integral $J_{\mathrm{far}}^{\mathrm{ep}}$ is always lower than $J_{\mathrm{PZ}}^{\mathrm{ep}}$, see Section 6.4.2. For example, $J_{\mathrm{PZ}}^{\mathrm{ep}}$ varies for the second load cycle between $J_{\mathrm{PZ,max}}^{\mathrm{ep}} = 18.82\ \mathrm{kJ/m^2}$ and $J_{\mathrm{PZ,min}}^{\mathrm{ep}} = 5.334\ \mathrm{kJ/m^2}$, whereas $J_{\mathrm{far}}^{\mathrm{ep}}$ varies between $J_{\mathrm{far,max}}^{\mathrm{ep}} = 17.58\ \mathrm{kJ/m^2}$ and $J_{\mathrm{far,min}}^{\mathrm{ep}} = 4.688\ \mathrm{kJ/m^2}$. Table 6.2 lists the values for increasing load cycle numbers, together with the values of the conventional *J*-integral around the crack tip plastic zone $J_{\mathrm{PZ}}^{\mathrm{conv}}$. Again it is seen that $J_{\mathrm{PZ}}^{\mathrm{ep}} = J_{\mathrm{PZ}}^{\mathrm{conv}}$. The values of $J_{\mathrm{far}}^{\mathrm{conv}}$ shall be given here for comparison, during $N = 2$, $J_{\mathrm{far,max}}^{\mathrm{conv}} = 18.82\ \mathrm{kJ/m^2}$ and $J_{\mathrm{far,min}}^{\mathrm{conv}} = 5.929\ \mathrm{kJ/m^2}$.

6.4.4 Load ratio $R = -1$

Next, the case for tension-compression loading, $R = -1$, is considered. Such a case is especially interesting, since crack closure appears and must be adequately taken into account for the determination of the driving force for a cyclically loaded crack, see Section 6.5.2. Fig. 6.10a presents curves J_i^{ep} against time t for the first three load cycles. The same integration contours Γ_i are plotted as previously for $R = 0$ and $R = 0.5$.

The J_i^{ep}-values decrease rapidly during unloading from $J_{i,\mathrm{max}}^{\mathrm{ep}}$ and reach a negative minimum value, termed $\min\left(J_{i,\mathrm{max}}^{\mathrm{ep}}\right)$, distinctly before or at the point where $F = 0$ is reached, i.e. at $t \le 1.5$ for the first load cycle. Subsequently, the magnitude of J_i^{ep} remains almost stationary, while the specimen is further unloaded to $F = F_{\mathrm{min}} = -35\ \mathrm{kN}$ and re-loaded to $F = 0$ in the compression regime; a slight increase is just visible for contours at and very close to the crack tip. With increasing contour radius, this stationary value increases until $J_{\mathrm{PZ}}^{\mathrm{ep}} \approx 0$ is reached for a contour surrounding the crack tip plastic zone. The incremental plasticity far-field *J*-integral $J_{\mathrm{far}}^{\mathrm{ep}}$ decreases to a value very close to zero at $t = 1.5$, but then increases again and reaches a peak value at F_{min}, $t = 2$. This peak value is rather high, e.g. $J_{\mathrm{far,min}}^{\mathrm{ep}} = 4.973\ \mathrm{kJ/m^2}$ for $N = 2$.

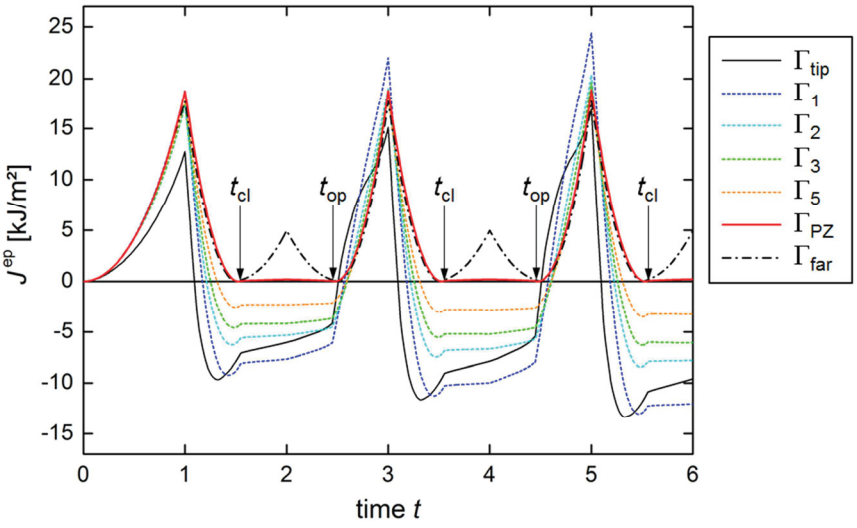
J^{ep} [kJ/m²]
time t
t_{cl}
t_{op}
Γ_{tip}
Γ_1
Γ_2
Γ_3
Γ_5
Γ_{PZ}
Γ_{far}

(a)

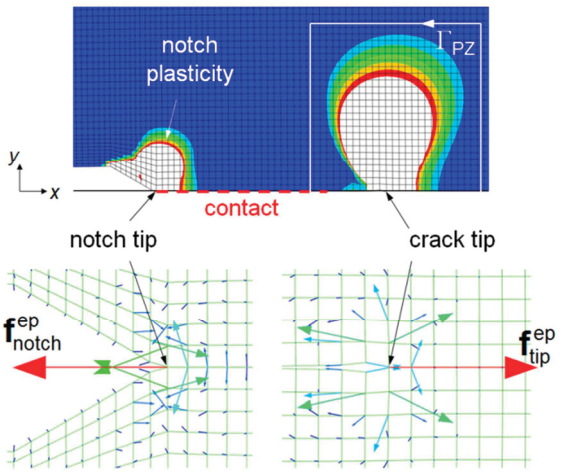
notch plasticity
Γ_{PZ}
contact
notch tip
crack tip
$\mathbf{f}^{ep}_{notch}$
$\mathbf{f}^{ep}_{tip}$

(b)

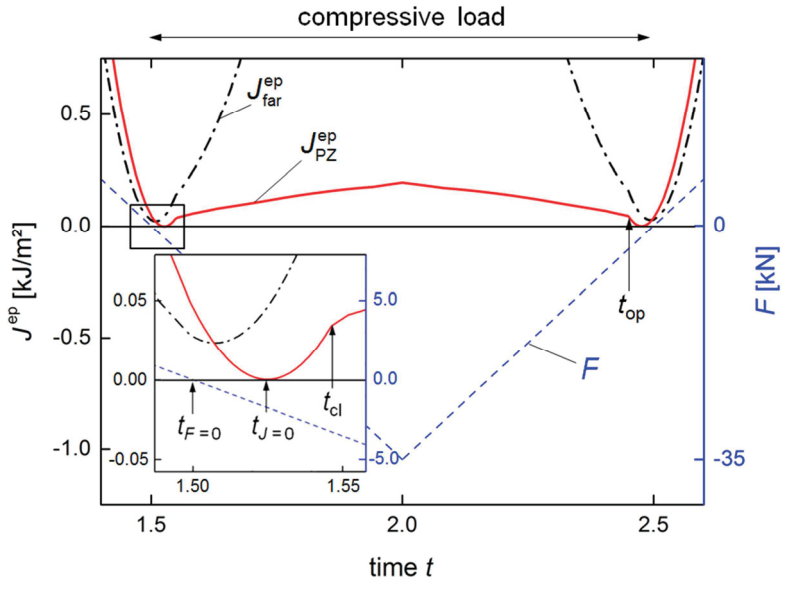
compressive load
J^{ep}_{far}
J^{ep}_{PZ}
J^{ep} [kJ/m²]
F [kN]
t_{op}
t_{cl}
$t_{F=0}$
$t_{J=0}$
time t

(c)

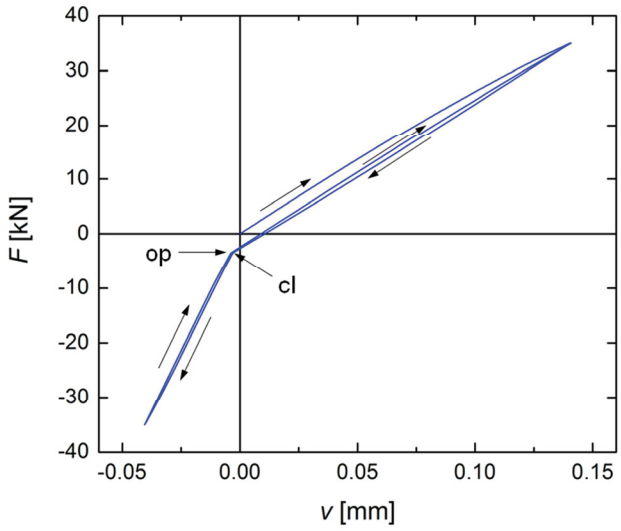

(d)

Fig. 6.10 (a) Incremental plasticity *J*-integral J^{ep} plotted against time t for various contours Γ_i around the crack tip. The first three load cycles are depicted. The load ratio is $R=-1$ (tension-compression loading). The crack closure and opening times t_{cl} and t_{op} are indicated. **(b)** PEEQ plot at $F_{\mathrm{min}}=-F_{\mathrm{max}}$ (the legend is the same as in Fig. 4b): $J^{\mathrm{ep}}_{\mathrm{far}}$ exhibits a peak during negative loads due to the appearance of notch plasticity when crack flank contact occurs. The contact surface at $F_{\mathrm{min}}=-F_{\mathrm{max}}$ is shown as dashed line in the upper image. The lower images show the distribution of incremental plasticity bulk configurational forces $\mathbf{f}^{\mathrm{ep}}$ in the notch- and crack tip regions. **(c)** $J^{\mathrm{ep}}_{\mathrm{PZ}}$ (solid line), $J^{\mathrm{ep}}_{\mathrm{far}}$ (dash-dot line), and applied load F (dashed line) in the time interval $t \approx 1.5 \div 2.5$, i.e. during the compressive loading stage. $J^{\mathrm{ep}}_{\mathrm{PZ}}$ has a minimum value equal to zero at a time $t_{J=0}$. **(d)** F–v curve during the time interval $t = 0 \div 3$. Kinks are clearly visible when at the times t_{cl} and t_{op} crack flank contact appears (closure "cl") or disappears (opening "op").

The reason for this peak value of $J^{\mathrm{ep}}_{\mathrm{far}}$ and the roughly stationary values of J^{ep}_i lies in the appearance of crack flank contact. We detect the beginning of crack flank contact as the time when the first point lying on the crack flank reaches during the unloading stage a displacement in y-direction, $u_y=0$; the corresponding time is denoted as t_{cl} (closure time). Analogously, the crack flank opening time t_{op} can be determined when u_y becomes again non-zero during the following re-loading stage (Newman 1976). Exactly at these times, t_{cl} and t_{op}, kinks occur in the $J^{\mathrm{ep}}_i - t$-curves; for example, at $t_{\mathrm{cl}} = 1.55$ during the first unloading stage, and $t_{\mathrm{op}} = 2.45$ for the subsequent loading stage. The first crack flank contact occurs at the notch tip, located 7 mm behind the crack tip, see Fig. 6.4a and Fig. 6.10b. The near-tip stresses barely change in the time interval between closure and opening and, therefore, the J^{ep}_i - values remain almost stationary.

The peak value $J^{\mathrm{ep}}_{\mathrm{far,min}}$ at F_{min} occurs, since a big configurational force $\mathbf{f}^{\mathrm{ep}}_{\mathrm{notch}}$ appears at the notch tip pointing into the negative x-direction which more than compensates the sum of

Table 6.3 Values of the incremental plasticity *J*-integrals, $J_{\mathrm{PZ}}^{\mathrm{ep}}$ and $J_{\mathrm{far}}^{\mathrm{ep}}$, and the conventional, deformation plasticity *J*-integral $J_{\mathrm{PZ}}^{\mathrm{conv}}$ for load ratio $R = -1$ during various load cycles *N*.

N	$J_{\mathrm{PZ,max}}^{\mathrm{ep}}$	$\min(J_{\mathrm{PZ}}^{\mathrm{ep}})$	$J_{\mathrm{far,max}}^{\mathrm{ep}}$	$\min(J_{\mathrm{far}}^{\mathrm{ep}})$	$J_{\mathrm{PZ,max}}^{\mathrm{conv}}$	$\min(J_{\mathrm{PZ}}^{\mathrm{conv}})$	$\Delta J_{\mathrm{PZ}}^{\mathrm{ep}}$	$\Delta J_{\mathrm{PZ}}^{\mathrm{conv}}$	$\Delta J_{F_{\mathrm{op}}}^{\mathrm{exp}}$	$\Delta J_{F_{J=0}}^{\mathrm{exp}}$
-	[kJ/m²]						[kJ/m²]			
1	18.80	0.000	17.56	0.022	18.80	0.000	-	-	18.42	18.42
2	18.87	0.000	17.70	0.028	18.87	0.000	18.87	18.87	20.45	18.59
25	19.64	0.000	18.13	0.032	19.64	0.000	19.64	19.64	21.01	19.30
50	19.96	0.000	18.29	0.032	19.96	0.000	19.96	19.96	21.76	19.58
100	20.10	0.000	18.32	0.031	20.10	0.000	20.10	20.10	22.19	19.77
200	20.02	0.000	18.09	0.024	20.02	0.000	20.02	20.02	22.19	19.59

The cyclic *J*-integral values $\Delta J_{\mathrm{PZ}}^{\mathrm{ep}}$ and $\Delta J_{\mathrm{PZ}}^{\mathrm{conv}}$ are calculated for re-loading sequences following Eq. (6.19) and Eq. (6.22). The values of the experimental cyclic *J*-integral ΔJ^{exp} are evaluated from Eq. (6.5). The term $\Delta J_{F_{\mathrm{op}}}^{\mathrm{exp}}$ considers the conventional crack opening load, F_{op}, whereas the term $\Delta J_{F_{J=0}}^{\mathrm{exp}}$ uses the correct opening load, $F_{J=0}$, compare Fig. 6.10.

the configurational forces around the crack tip, see Fig. 6.10b and compare Section 6.4.2. Note that compressive stresses appear during unloading at the notch and at the crack tip. However, the components of the plastic strains around the notch have a different sign as those around the crack tip. This is the reason why $\mathbf{f}_{\mathrm{notch}}^{\mathrm{ep}}$ and the configurational force emanating from the crack tip node $\mathbf{f}_{\mathrm{tip}}^{\mathrm{ep}}$ point into opposite directions.

Figure 6.10c shows a detail of Fig. 6.10a for the time interval between $t \approx 1.5$ and $t \approx 2.5$, i.e. during the compression stage. It is seen that the minimum value of $J_{\mathrm{PZ}}^{\mathrm{ep}}$ is exactly zero, $\min\left(J_{\mathrm{PZ}}^{\mathrm{ep}}\right) = 0$. The term "exactly" means here that the deviation is smaller than 10^{-4} kJ/m^2.

The minimum value of $J_{\mathrm{far}}^{\mathrm{ep}}$ is small, but not exactly zero; e.g. for the second load cycle $\min\left(J_{\mathrm{far}}^{\mathrm{ep}}\right) = 0.028$ kJ/m². The variation of the load *F* is also plotted in Fig. 6.10c. It is seen that $J_{\mathrm{PZ}}^{\mathrm{ep}}$ reaches its minimum value during unloading at a time $t_{J=0}$ when the load is already negative, but before crack flank closure occurs, i.e. $t_{J=0} < t_{\mathrm{cl}}$ for the unloading stage. On the contrary, $t_{J=0} > t_{\mathrm{op}}$ for the loading stage.

The cyclic plastic zone has a magnitude of $r_{\mathrm{pl,cyc}} = 2.0$ mm, which comes close to the theoretically quarter of the size of the monotonic plastic zone. Table 6.3 lists the *J*-integral values for different load cycles *N*. It is seen that $J_{\mathrm{PZ,\,max}}^{\mathrm{ep}}$ and $J_{\mathrm{far,max}}^{\mathrm{ep}}$ increase with increasing load cycle numbers, but seem to reach saturation values. The minimum values of $J_{\mathrm{PZ}}^{\mathrm{ep}}$ are always zero. Table 6.3 collects also values for $J_{\mathrm{PZ}}^{\mathrm{conv}}$; Eq. (6.12) is again confirmed.

We can conclude Sect. 6.4 by stating that deformation plasticity is not appropriate for cyclic loading conditions, since bulk configurational forces appear during unloading which are not physically sound and cause the artificial path-dependence of J^{conv}. The incremental plasticity *J*-integral J^{ep} is also path dependent. This is physically appropriate, since bulk configurational forces are induced in the plastically deformed regions. Even negative J^{ep}-

values, which appear during unloading for integration contours close to the crack tip, are correct, since they originate due to compressive residual stresses caused by reverse plasticity within the crack tip plastic zone. This means that the incremental plasticity *J*-integral leads to reasonable results for cyclic loading. Furthermore, our numerical case study confirms the relation $J_\Gamma^{\mathrm{ep}} = J_\Gamma^{\mathrm{conv}}$, if the integration paths Γ go only through elastically deformed regions, such as around the entire crack tip plastic zone Γ_{PZ}.

6.5 Plasticity and driving force under cyclic loading

This section discusses the use of the incremental plasticity *J*-integral J^{ep} as a measure of the crack driving force for cyclically loaded elastic–plastic materials, the application and evaluation of the cyclic *J*-integral ΔJ^{ep} for characterizing the crack growth rate in fatigue, and the correctness of the experimental cyclic *J*-integral ΔJ^{exp} of Dowling and Begley (1976).

6.5.1 Crack driving force for monotonic and cyclic loading

An essential property of the incremental plasticity *J*-integral J^{ep} is its path dependence within plastically deformed regions. Therefore, the question arises, which integration path Γ should be considered for calculating J^{ep} in order to predict the crack driving force for cyclic loading. Before solving this question, it is useful to clarify the physical meaning of the critical driving force.

We consider first a monotonically loaded body with a crack (Fig. 1a). The crack will extend if the crack driving force equals or exceeds the crack growth resistance R_{cg} of the material. The crack driving force reflects the energy that becomes available during a unit crack extension. The crack growth resistance R_{cg} is the non-reversible energy required to produce a unit crack extension, see e.g. Griffith (1920), Eftis and Liebowitz (1975), Kolednik (1991), Turner and Kolednik (1994). If the material is non-linear elastic, the *J*-integral is path independent and characterizes the crack driving force. Therefore, the condition for crack extension reads $J \geq R_{\mathrm{cg}}$. For elastic–plastic materials under small- and large-scale yielding conditions, the crack driving force is characterized by the incremental plasticity *J*-integral for a contour completely enclosing the crack tip plastic zone, $J_{\mathrm{PZ}}^{\mathrm{ep}}$, see Kolednik et al. (2014), and the condition for crack extension becomes,

$$J_{\mathrm{PZ}}^{\mathrm{ep}} = J_{\mathrm{PZ}}^{\mathrm{conv}} = J^{\mathrm{exp}} \geq R_{\mathrm{cg}} \tag{6.18}$$

compare Eq. (6.12). The physical meaning of $J_{\mathrm{PZ}}^{\mathrm{ep}}$ is that of the driving force for the combined, translational movement of the crack tip and the crack tip plastic zone, including the process zone. The physical meaning of near-tip incremental plasticity *J*-integral $J_{\mathrm{tip}}^{\mathrm{ep}}$ is that of the crack driving force for the translational movement of the crack tip alone. For crack extension in an elastic–plastic material, the movement of the crack tip without simultaneous movement of the surrounding process zone and tip plastic zone does not make sense. Thus, $J_{\mathrm{tip}}^{\mathrm{ep}}$ is irrelevant for understanding whether a crack can propagate or not, apart from the fact

that $J_{\mathrm{tip}}^{\mathrm{ep}} = 0$, see Kolednik et al. (2014) and Rice (1979). It should be also mentioned that the incremental plasticity *J*-integral for a contour around the process zone, $J_{\mathrm{proc.z}}^{\mathrm{ep}}$, is approximately equal to $J_{\mathrm{PZ}}^{\mathrm{ep}}$ (Kolednik et al. 2014). Note that the condition $J_{\mathrm{PZ}}^{\mathrm{ep}} = J_{\mathrm{PZ}}^{\mathrm{conv}}$ still holds for monotonic loading after a cyclic pre-deformation, since the integration path Γ_{PZ} goes, for small- and large-scale yielding conditions, only through elastically deformed material, see Sect. 6.2.3.

Now we consider a cyclically loaded elastic–plastic body with a crack. As common in the fatigue of metals and alloys, the crack driving force is considerably smaller than the crack growth resistance, $J_{\mathrm{PZ,max}}^{\mathrm{ep}} < R_{\mathrm{cg}}$, and the crack cannot extend at maximum load, $F_{\max} = const$. A crack driving force term has been introduced for a cyclically loaded crack, whose meaning differs from that of monotonically loaded cracks (Paris et al. 1961; Paris and Erdogan 1963). The main purpose of this crack driving force term in fatigue is that it should allow the prediction of the crack propagation rate of a fatigue crack. Crack extension under cyclic loading in micro-ductile materials is caused by a two-step mechanism: blunting of the crack tip during each loading phase and the re-sharpening process during the subsequent unloading phase (Laird 1967, 1979; Pippan et al. 2010). For elastic−plastic materials, the crack growth rate per load cycle $\mathrm{d}a/\mathrm{d}N$ can be assumed as being proportional to the cyclic crack tip opening displacement, i.e. the difference of the crack tip opening displacement between minimum and maximum load, $\Delta\delta_{\mathrm{t}} = \delta_{\mathrm{t,max}} - \delta_{\mathrm{t,min}}$. The proportionality constant might depend, apart from several other factors, such as material properties, also on the magnitude of $\Delta\delta_{\mathrm{t}}$ (Tanaka 1989, Schweizer et al. 2010).

Since (cyclic) plasticity at the crack tip is responsible for fatigue crack propagation, it is reasonable to consider $J_{\mathrm{PZ}}^{\mathrm{ep}}$ and its variation during cyclic loading as possible candidate for the crack driving force for cyclic loading. The reason is that the contour Γ_{PZ} includes the whole plasticity within the crack tip plastic zone. At a first glance, it appears that $J_{\mathrm{proc.z}}^{\mathrm{ep}}$ might be also a possible candidate, since $\Gamma_{\mathrm{proc.z}}$ takes into account the plasticity within the process zone, which should be mainly responsible for the formation of cyclic crack tip blunting. However, it is seen from the results of Fig. 6.6, Fig. 6.9, and Fig. 6.10a that path dependence of the incremental plasticity *J*-integral J_i^{ep}, on contours Γ_i, extends during the unloading stages to much higher distances from the crack tip than the length of the process zone $l_{\mathrm{proc.z}}$. This path dependence would make a reliable determination of a driving force parameter very complicated.

Therefore, the conclusion of this section is that the incremental plasticity *J*-integral for a contour completely enclosing the crack tip plastic zone, $J_{\mathrm{PZ}}^{\mathrm{ep}}$, should be taken as parameter characterizing the crack growth rate in fatigue.

6.5.2 Evaluation of the cyclic J-integral $\Delta J_{\mathrm{PZ}}^{\mathrm{ep}}$

The parameter $J_{\mathrm{PZ}}^{\mathrm{ep}}$ varies during a considered load cycle between a minimum and a maximum value, $J_{\mathrm{PZ,min}}^{\mathrm{ep}}$ and $J_{\mathrm{PZ,max}}^{\mathrm{ep}}$. The cyclic *J*-integral $\Delta J_{\mathrm{PZ}}^{\mathrm{ep}}$ should be evaluated by the relation

$$\Delta J_{\mathrm{PZ}}^{\mathrm{ep}} = J_{\mathrm{PZ,max}}^{\mathrm{ep}} + J_{\mathrm{PZ,min}}^{\mathrm{ep}} - 2\sqrt{J_{\mathrm{PZ,max}}^{\mathrm{ep}} J_{\mathrm{PZ,min}}^{\mathrm{ep}}} \,. \tag{6.19}$$

The reason for the validity of Eq. (6.19) will be presented in the following, see also Appendix.

The cyclic crack tip opening displacement, $\Delta\delta_{\mathrm{t}} = \delta_{\mathrm{t,max}} - \delta_{\mathrm{t,min}}$, can be expressed in terms of the stress intensity range ΔK by inserting twice the yield stress σ_{y} into the standard relation between crack tip opening displacement and stress intensity (Rice 1967),

$$\Delta\delta_{\mathrm{t}} = \alpha \frac{(\Delta K)^2}{2E\sigma_{\mathrm{y}}}, \tag{6.20}$$

similar to the estimate of the cyclic plastic zone, Eq. (6.17). The parameter α is a constant, e.g. $\alpha \cong 0.5$ for plane stress and $\alpha \cong 1$ for plane strain conditions. The results of stereophotogrammetric measurements by Siegmund et al. (1990) support the validity of Eq. (6.20). By expanding the term $\Delta K = K_{\mathrm{max}} - K_{\mathrm{min}}$ and substituting the relation $J = K^2/E$, we get a relation between cyclic crack tip opening displacement and cyclic *J*-integral ΔJ in the form,

$$\Delta\delta_{\mathrm{t}} = \frac{\alpha}{2\sigma_{\mathrm{y}}}\left(J_{\mathrm{max}} + J_{\mathrm{min}} - 2\sqrt{J_{\mathrm{max}} J_{\mathrm{min}}}\right) = \frac{\alpha}{2\sigma_{\mathrm{y}}}\Delta J \,. \tag{6.21}$$

Eq. (6.19) then follows from the right-hand side equality of Eq. (6.21). Similarly, Eq. (6.19) could be derived just based on the empirical fact that the crack growth rate per load cycle in fatigue $\mathrm{d}a/\mathrm{d}N$ depends on the stress intensity range ΔK and by substituting the relation $J = K^2/E$ into $(\Delta K)^2$.

Use of Eq. (6.19) is especially important for load ratios $R > 0$, since $J_{\mathrm{PZ,min}}^{\mathrm{ep}} > 0$ for these cases. If $J_{\mathrm{PZ,min}}^{\mathrm{ep}} = 0$, Eq. (6.19) and the term $J_{\mathrm{PZ,max}}^{\mathrm{ep}} - J_{\mathrm{PZ,min}}^{\mathrm{ep}}$ lead to identical results.

In order to check the validity of Eq. (6.19), the variation of the crack tip opening displacement δ_{t} during cyclic loading is analyzed. The values of δ_{t} are determined one element length *m* behind the crack tip. Figure 6.11a shows for the load ratios R = 0, 0.5 and –1 the evolution of δ_{t} during the first three load cycles. It is seen that both the values at maximum and minimum load, $\delta_{\mathrm{t,max}}$ and $\delta_{\mathrm{t,min}}$, increase with increasing numbers of load cycles *N*. This increase is stronger for higher magnitudes of the applied load amplitude $\Delta F = F_{\mathrm{max}} - F_{\mathrm{min}}$. For high load cycle numbers *N*, $\delta_{\mathrm{t,max}}$ and $\delta_{\mathrm{t,min}}$ seem to reach saturation values, as already seen for various J^{ep}-curves depicted in Fig. 6.6b. The cyclic crack tip opening displacement $\Delta\delta_{\mathrm{t}} = \delta_{\mathrm{t,max}} - \delta_{\mathrm{t,min}}$ exhibits only little change with increasing load cycle number and reaches a saturation value for high *N*.

In Figure 6.11b, the cyclic *J*-integral values $\Delta J_{\mathrm{PZ}}^{\mathrm{ep}}$ according to Eq. (6.19) and the values of the term $J_{\mathrm{PZ,max}}^{\mathrm{ep}} - J_{\mathrm{PZ,min}}^{\mathrm{ep}}$ are plotted against the cyclic crack tip opening displacement $\Delta\delta_{\mathrm{t}}$. Hereby, the values of the second load cycle, N = 2, are taken. In order to have more data points, additional computations are made for various load ratios between R = −0.1 and R = 0.8. It is seen that $\Delta J_{\mathrm{PZ}}^{\mathrm{ep}}$ increases proportional to $\Delta\delta_{\mathrm{t}}$, as it should according to Eq. (6.21), whereas this is clearly not so for the values of the term $J_{\mathrm{PZ,max}}^{\mathrm{ep}} - J_{\mathrm{PZ,min}}^{\mathrm{ep}}$.

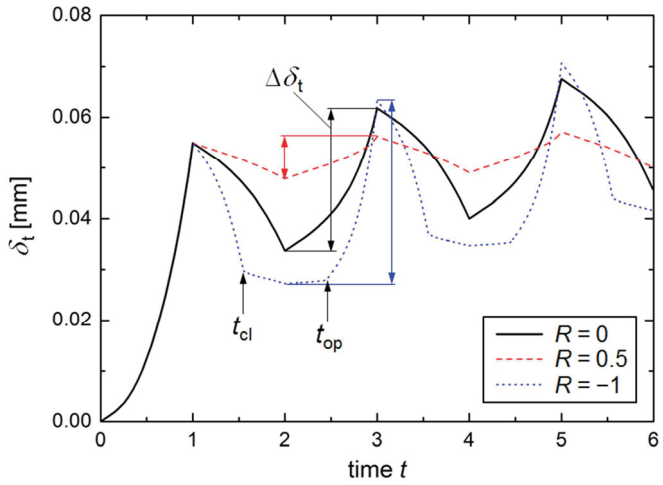

(a)

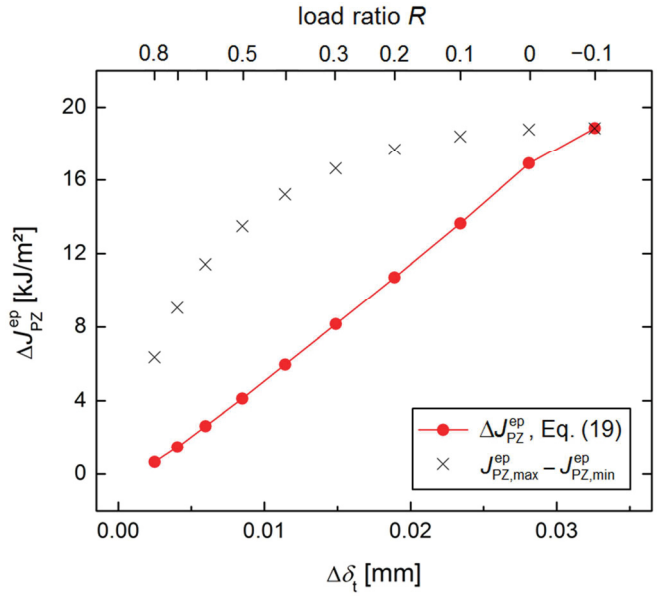

(b)

Fig. 6.11 (a) Evolution of the crack tip opening displacement δ_t during the first three load cycles for the load ratios R = 0, 0.5, and –1. For R = –1 the times t_{cl} and t_{op}, when crack closure appears and disappears, are indicated. **(b)** Incremental plasticity cyclic J-integral ΔJ_{PZ}^{ep}, Eq. (6.19), and values of the term $J_{PZ,max}^{ep} - J_{PZ,min}^{ep}$ plotted against the cyclic crack tip opening displacement $\Delta\delta_t$. Proportionality is clearly given between ΔJ_{PZ}^{ep} and $\Delta\delta_t$; results for additional values of the load ratio R confirm this finding.

It should be remarked that the determination of very accurate δ_t- or $\Delta\delta_t$-values would require a much finer mesh than we used in these FE-analyses. For R = 0, the crack tip opening displacement is at the second load cycle $\delta_{t,max} = 62.4\,\mu m$. Ideally, the magnitude of δ_t should be measured a distance behind the crack tip, which corresponds to the width of the stretched zone, i.e. approximately $0.4\,\delta_t \cong 25\,\mu m$ behind the blunted tip (Kolednik and Stüwe 1985; Siegmund et al. 1990). The mesh size is m = 0.2 mm, i.e. we are not able to determine δ_t at

the correct distance. Because of the larger measurement distance, the elastic component of δ_t will be overestimated. Change of this elastic component might be also the reason for the small variation of δ_t, which is seen for $R=-1$ between the times t_{cl} and t_{op} in Fig. 6.11a. Nevertheless, our analysis is accurate enough in order to be able to confirm Eq. (6.19) and to show that $\Delta J_{PZ}^{ep} \neq J_{PZ,max}^{ep} - J_{PZ,min}^{ep}$. It should be mentioned here that the cyclic crack tip opening displacement $\Delta\delta_t$ would be an ideal parameter for the estimation of the crack driving force during cyclic loading and the crack propagation rate in fatigue (Pippan and Grosinger 2014). However, its accurate determination would be numerically very expensive and, therefore, a global parameter, such as J_{PZ}^{ep}, which is barely affected by the mesh size, is much more suitable in practice.

In Fig. 6.11b, two ΔJ_{PZ}^{ep}-values are drawn for load ratio R = 0: For the theoretical value, $J_{PZ,min}^{ep} = 0$, we would get $\Delta J_{PZ}^{ep} = J_{PZ,max}^{ep} = 18.86$ kJ/m²; the FE-analysis gives $J_{PZ,min}^{ep} = 0.050$ kJ/m² and Eq. (6.19) yields $\Delta J_{PZ}^{ep} = 16.97$ kJ/m². These two ΔJ_{PZ}^{ep}-values differ by 10%. This example shows that the square root term in Eq. (6.19) makes the cyclic *J*-integral ΔJ_{PZ}^{ep} sensitive to small variations of the J_{min}^{ep}-values. A slightly negative load ratio, R = −0.1, is required so that really $J_{PZ,min}^{ep} = 0$.

Tables 6.1 and 6.2 lists values of $J_{PZ,max}^{ep}$, $J_{PZ,min}^{ep}$, and ΔJ_{PZ}^{ep} after re-loading following Eq. (6.19) for load ratios R = 0 and 0.5 during various load cycles. The incremental plasticity cyclic *J*-integral around the crack tip plastic zone ΔJ_{PZ}^{ep} slightly increases with increasing load cycle number *N*, but the values seem to approach a saturation value. The corresponding values of the conventional, deformation plasticity cyclic *J*-integral around the crack tip plastic zone ΔJ_{PZ}^{conv} are listed for comparison. These values are evaluated analogously to Eq. (6.19),

$$\Delta J_{PZ}^{conv} = J_{PZ,max}^{conv} + J_{PZ,min}^{conv} - 2\sqrt{J_{PZ,max}^{conv} J_{PZ,min}^{conv}} \,. \tag{6.22}$$

From Eq. (6.12) it is clear that ΔJ_{PZ}^{ep} and ΔJ_{PZ}^{conv} are identical,

$$\Delta J_{PZ}^{ep} = \Delta J_{PZ}^{conv} = \Delta J^{exp} \,. \tag{6.23}$$

The right hand equality of Eq. (6.23) will be further discussed in Section 6.5.3.

Evaluation of the incremental plasticity cyclic *J*-integral ΔJ_{PZ}^{ep} for negative load ratios is simple in most cases, since J_{PZ}^{ep} reaches a minimum of zero, $\min\left(J_{PZ}^{ep}\right) = 0$, and ΔJ_{PZ}^{ep} is equal to the *J*-integral at maximum load, $\Delta J_{PZ}^{ep} = J_{PZ,max}^{ep}$. Table 6.3 lists the ΔJ_{PZ}^{ep}-values with increasing load cycle number *N* for tension-compression loading, R = –1. The results of ΔJ_{PZ}^{conv} are also listed for comparison.

It has been demonstrated in this section that the incremental plasticity cyclic *J*-integral evaluated along a contour around the crack tip plastic zone, ΔJ_{PZ}^{ep}, is an appropriate parameter for the characterization of the crack driving force for cyclic loading and the crack growth rate in fatigue. ΔJ_{PZ}^{ep} and the deformation plasticity cyclic *J*-integral around the crack tip plastic zone ΔJ_{PZ}^{conv} are identical as long as crack tip plastic zone and region of back face plasticity are separated by an elastic region. The quantities ΔJ_{PZ}^{ep} and ΔJ_{PZ}^{conv} must be evaluated from

Eq. (6.19) and Eq. (6.22), respectively. Equation (6.23) means that it is possible to apply the conventional *J*-integral for estimating the crack driving force for cyclic loading, if certain conditions are fulfilled.

This fact provides also the basis for the application of the experimental cyclic *J*-integral ΔJ^{exp}, proposed by Dowling and Begley (1976). The reasoning is that the conventional *J*-integral of Eq. (6.1) and the experimental *J*-integral J^{exp}, Eq. (6.2), yield identical results for a monotonically loaded elastic–plastic material with a stationary crack (Rice 1973; Kolednik 1991), and the fatigue crack during a single loading branch of a load cycle can be treated like a stable crack, since only crack tip blunting occurs. As shown in Tables 6.1, 6.2 and 6.3, the shape of the *F*−*v*-curve and the values of the *J*-integrals at maximum (and minimum) load vary with increasing load cycle number *N*. However, this fact does not influence the validity of Eq. (6.12) and Eq. (6.23) during a single branch of a considered load cycle.

The application of ΔJ^{exp} is investigated in the following section.

6.5.3 Determination of the experimental cyclic J-integral ΔJ^{exp}

The values of the experimental cyclic *J*-integral ΔJ^{exp} are evaluated from Eq. (6.5) and compared to the results presented in Section 6.5.2. The resulting ΔJ^{exp}-values for load ratios $R = 0$ and $R = 0.5$ are inserted into Table 6.1 and Table 6.2. It is seen that the ΔJ^{exp}-values are about 2% smaller than the values of $\Delta J_{\mathrm{PZ}}^{\mathrm{ep}}$ or $\Delta J_{\mathrm{PZ}}^{\mathrm{conv}}$ for all load cycles *N*. The same underestimate occurs already at the maximum load of the first load cycle. Therefore, it can be concluded that the deviation between ΔJ^{exp} and $\Delta J_{\mathrm{PZ}}^{\mathrm{ep}} = \Delta J_{\mathrm{PZ}}^{\mathrm{conv}}$ can be attributed to the geometry factor η from ASTM E1820 (2005). Taking this fact into account, we can state that ΔJ^{exp} gives very good approximations of $\Delta J_{\mathrm{PZ}}^{\mathrm{ep}}$ or $\Delta J_{\mathrm{PZ}}^{\mathrm{conv}}$.

Dowling and Begley (1976) propose that in presence of crack closure, the area ΔA for a loading branch should be taken as area above the load F_{op} where the crack fully opens (Fig. 6.2c and Fig. 6.10d). When analyzing the unloading branch, ΔA should be taken as area to the load F_{cl} when crack closure starts. Dowling and Begley (1976) propose to determine the crack opening (or closure) loads from the compliance changes, which are visible as kinks in the load–displacement (*F*−*v*) hysteresis loops.

Such kinks are also visible in the *F*−*v*-curves of our analyses for cyclic tension-compression loading with load ratio *R* = −1 (Fig. 6.10d). As already mentioned in Section 6.4.4, we determine from the numerical analysis the time t_{cl} of the first crack flank contact during an unloading cycle as the time when the first point lying on the crack flank reaches $u_y = 0$. The time for complete crack flank opening t_{op} is determined analogously. The times t_{cl} and t_{op} are indicated in the $J_{\mathrm{PZ}}^{\mathrm{ep}}$ versus time curve of Fig. 6.10a and 6.10c, as well as in the δ_{t} versus time plot of Fig. 6.11a.

Figures 6.10c, d show that for *R* = −1 crack flank closure and -opening do not occur at load $F = 0$, but the closure- and opening loads, F_{cl} and F_{op}, are both slightly negative. Figure 6.10c shows also that $J_{\mathrm{PZ}}^{\mathrm{ep}}$ reaches during the unloading sequence a minimum value, $\min\left(J_{\mathrm{PZ}}^{\mathrm{ep}}\right) = 0$ at a load $F_{J=0}$, which lies between $F = 0$ and F_{cl}, i.e. at a time $t_{J=0} < t_{\mathrm{cl}}$.

During the loading sequence $J_{\mathrm{PZ}}^{\mathrm{ep}}$ reaches the minimum value, $\min\left(J_{\mathrm{PZ}}^{\mathrm{ep}}\right)=0$, at a time $t_{J=0} > t_{\mathrm{op}}$.

Additional analyses are conducted for cyclic tension-compression loading with load ratios between $R=-0.1$ and $R=-2$. In all cases, the minimum value of the incremental plasticity cyclic *J*-integral evaluated along a contour around the crack tip plastic zone is exactly zero, $\min\left(J_{\mathrm{PZ}}^{\mathrm{ep}}\right)=0$. From these results, it can be concluded that

$$\Delta J_{\mathrm{PZ}}^{\mathrm{ep}} = J_{\mathrm{PZ,max}}^{\mathrm{ep}} = J_{\mathrm{PZ,max}}^{\mathrm{conv}} \qquad \text{for} \qquad R \le -0.1\,. \tag{6.24}$$

Note that the exact upper boundary and a possible lower boundary for the validity of Eq. (6.24) have not been determined.

It is clear that for $R<0$ the values of the experimental cyclic *J*-integral ΔJ^{exp} rely on the determination of the correct area ΔA, i.e. the correct crack opening or -closure load. The analysis above (Fig. 6.10c) has shown that the conventional determination via compliance changes leads to inaccurate results: Use of F_{op} for the determination of ΔA leads to values, $\Delta J_{F_{\mathrm{op}}}^{\mathrm{exp}}$, that are 10% too high, see Table 6.3; the same inaccuracy appears if F_{cl} is considered for the determination of ΔA during an unloading branch. If the correct opening or -closure loads $F_{J=0}$ are used where $\min\left(J_{\mathrm{PZ}}^{\mathrm{ep}}\right)=0$, the experimental cyclic *J*-integral comes very close to the correct value, $\Delta J_{F_{J=0}}^{\mathrm{exp}} \cong \Delta J_{\mathrm{PZ}}^{\mathrm{ep}}$.

The difference between $\Delta J_{F_{\mathrm{op}}}^{\mathrm{exp}}$ and $\Delta J_{F_{J=0}}^{\mathrm{exp}}$ can be interpreted as follows: An abrupt compliance change for negative load ratios appears, since crack closure at the load F_{cl} occurs during unloading first at a point lying significantly behind the crack tip, i.e. at the notch tip in Fig. 6.10b, so that the effective crack length significantly changes. The material around the crack tip becomes already fully unstressed at a somewhat higher load $F_{J=0}$, causing that $J_{\mathrm{PZ}}^{\mathrm{ep}}$ becomes zero. At the load F_{cl} where crack closure appears, the material around the crack tip is already re-stressed again, so that $J_{\mathrm{PZ}}^{\mathrm{ep}}$ increases (Fig. 6.10c). This interpretation can also explain the fact that the compliance dependent opening- or closure loads, F_{cl} and F_{op}, are influenced by the notch geometry (Fig. 6.4a). For example, the magnitudes of F_{cl} and F_{op} vary, if the length between crack tip and notch tip is changed. On the contrary, the correct opening load $F_{J=0}$ does not significantly vary.

This section can be concluded by stating that the experimental cyclic *J*-integral ΔJ^{exp} proposed by Dowling and Begley (1976) is correct, if the correct procedure is applied to determine the area ΔA in cases of crack closure. A problem for the practical application is that it is in the moment not able to propose an easily applicable procedure for the determination of the correct closure load $F_{J=0}$, apart from the computation of the incremental plasticity *J*-integral, $J_{\mathrm{PZ}}^{\mathrm{ep}}$.

6.5.4 Influences of strain hardening and other computational aspects

All the computational results presented so far have been generated for elastic–ideally plastic material. Additional numerical analyses have been conducted for a material with isotropic hardening. Young's modulus, Poisson's ratio, and yield strength are the same as introduced in

Section 6.3; the ultimate tensile strength is σ_u = 426 MPa and the average strain hardening exponent is n = 0.2. These material data have been taken from an annealed steel with German designation St37 and were previously used in Simha et al. (2008) and Kolednik et al. (2014).

In principle, the results do not change due to the isotropic hardening, and it is possible to draw the same conclusions as for an elastic–ideally plastic material. The conclusions drawn in this paper are valid also for materials with kinematic hardening, or for combinations of isotropic and kinematic hardening behavior, which is typical for metals subjected to low-cycle fatigue.

It should be stressed that the numerical analyses presented in this paper have been conducted for large-scale yielding (and not general yielding) conditions. The reason is that only then it is possible to show that Eq. (6.12) and, as a consequence, Eq. (6.23) are strictly correct. This does not apply if general yielding conditions prevail in the specimen, since the crack tip- and the back-face plastic zone are not separated by an "elastic corridor", see Sect. 6.4. The correctness of the experimental cyclic J-integral ΔJ^{exp} approach for general yielding conditions will be topic of a separate paper.

Furthermore it should be stressed that stationary cracks have been considered in this paper. The differences that occur by considering *growing* fatigue cracks will be discussed in a forthcoming paper (Ochensberger and Kolednik 2014).

6.6 Summary

The current paper provides the basis for the physically appropriate application of the J-integral for the assessment of fatigue cracks in elastic–plastic materials. A set of numerical simulations for a two-dimensional compact tension specimen with a stationary crack under cyclic Mode I loading conditions has led to the following findings:

- The incremental plasticity J-integral J^{ep} can be applied for cyclic loading when linear elastic fracture mechanics is not applicable anymore. J^{ep} has the physical meaning of a true driving force even in cases of non-proportional loading conditions, such as cyclic loading. J^{ep} is, in general, path dependent on contours intersecting plastically deformed regions. This is physically correct due to the appearance of bulk configurational forces within plastically deformed regions. Negative J^{ep}-values, which appear during unloading for integration contours close to the crack tip, are also correct, since they are caused by compressive residual stresses within the crack tip plastic zone.
- Deformation plasticity is usually not appropriate for cyclic loading conditions, since bulk configurational forces appear during unloading which are not physically sound and lead to an artificial path-dependence of the conventional deformation plasticity J-integral J^{conv}. However, the deformation- and incremental plasticity J-integrals are equal, $J_\Gamma^{\mathrm{ep}} = J_\Gamma^{\mathrm{conv}}$, if the integration contour Γ goes only through elastically deformed regions, such as a path around the crack tip plastic zone Γ_{PZ}. Consequently, the

conventional, deformation plasticity *J*-integral can be useful for cyclic loading conditions, if certain conditions are fulfilled.

- The incremental plasticity *J*-integral for a contour completely surrounding the crack tip plastic zone, J_{PZ}^{ep}, should be taken as parameter characterizing the driving force of a crack in an elastic−plastic material, which is monotonically loaded after a cyclic pre-deformation. Crack extension occurs, if J_{PZ}^{ep} is equal or larger than the crack growth resistance.
- It is physically appropriate to characterize the crack growth rate in fatigue by the incremental plasticity cyclic *J*-integral, computed along a contour around the crack tip plastic zone, ΔJ_{PZ}^{ep}. The parameter ΔJ_{PZ}^{ep} and the corresponding deformation plasticity cyclic *J*-integral ΔJ_{PZ}^{conv} are equal, as long as crack tip plastic zone and region of back face plasticity are separated by an elastic region. The quantities ΔJ_{PZ}^{ep} and ΔJ_{PZ}^{conv} must be, in general, evaluated from Eq. (6.19) and Eq. (6.22), respectively.
- The experimental cyclic *J*-integral ΔJ^{exp} proposed by Dowling and Begley (1976) is, in principle, physically appropriate. However, a correct procedure must be applied in cases of crack closure to determine the area below a single branch of the load−displacement record, ΔA. The conventionally applied procedure via the determination of the closure- or opening loads, F_{cl} and F_{op}, as proposed by Dowling and Begley (1976), can lead to inaccurate results.

Acknowledgements

The authors would like to express their gratitude to Prof. R. Pippan and Prof. F.D. Fischer for helpful discussions. Financial support by the Austrian Federal Government and the Styrian Provincial Government within the research activities of the K2 Competence Center on "Integrated Research in Materials, Processing and Product Engineering", under the frame of the Austrian COMET Competence Center Programme, is gratefully acknowledged (strategic projects A4.11-WP4 and A4.20-WP3).

Appendix: J-integral and cyclic J-integral

In this appendix, the difference between *J*-integral, Eq. (6.1), and cyclic *J*-integral, Eq. (6.3), shall be demonstrated, and Eq. (6.19) is derived for a simple specimen geometry.

Fig. 6.12a shows a double cantilever beam (DCB) specimen with height h and a long crack. The material is linear elastic. The specimen is clamped at the lower boundary and loaded at the upper boundary by prescribing the vertical displacement v. Rice (1968a) showed that the *J*-integral can be expressed as,

$$J = \phi_{rb} h = \frac{1}{2} E \varepsilon_{appl}^2 h \,. \tag{6.25}$$

The term ϕ_{rb} denotes the strain energy density at the right boundary, and the applied strain is given by $\varepsilon_{\mathrm{appl}} = v/h$. At a fixed displacement $v_{\min}$, the *J*-integral $J_{\min} = \phi_{\mathrm{rb,min}} h = 1/2\left(E\varepsilon^2_{\mathrm{appl,min}} h\right)$ corresponds to the area 0AE0 in Fig. 6.12b.

Now the specimen shall be loaded from the displacement $v_{\min}$ to $v_{\max}$, Fig. 6.12b. The increase in *J*-integral is then

$$J_{\max} - J_{\min} = \left(\phi_{\mathrm{rb,max}} - \phi_{\mathrm{rb,min}}\right) h = \frac{1}{2} E\left(\varepsilon^2_{\mathrm{appl,max}} - \varepsilon^2_{\mathrm{appl,min}}\right) h\,, \tag{6.26}$$

corresponding to the area ABDEA in Fig. 6.12b. During cyclic loading between the displacements $v_{\min}$ and $v_{\max}$, the *J*-integral varies between the values of $J_{\min}$ and $J_{\max} = \phi_{\mathrm{rb,max}} h = 1/2\left(E\varepsilon^2_{\mathrm{appl,max}} h\right)$.

For calculating the cyclic *J*-integral ΔJ as defined by Eq. (6.3), we should note that the cyclic stress $\Delta\sigma$ and cyclic strain $\Delta\varepsilon$ are taken from the minimum load, point A in Fig. 6.12b; the quantity $\phi(\Delta\varepsilon)$ of Eq. (6.4) corresponds to the area ABCA in Fig. 6.12b. The cyclic *J*-integral is then given by

$$\Delta J = \phi(\Delta\varepsilon) h = \frac{1}{2} E\left(\Delta\varepsilon\right)^2 h = \frac{1}{2} E\left(\varepsilon_{\mathrm{appl,max}} - \varepsilon_{\mathrm{appl,min}}\right)^2 h\,, \tag{6.27}$$

again corresponding to the area ABCA. The comparison of Eq. (6.26) and Eq. (6.27) shows that $\Delta J \neq J_{\max} - J_{\min}$ and that

$$\Delta J = J_{\max} + J_{\min} - 2\sqrt{J_{\max} J_{\min}}\,, \tag{6.28}$$

which is in form identical to Eq. (6.19) or Eq. (6.22).

The areas 0AEA and 0BD0 correspond to the areas $A_{\min}$ and $A_{\max}$ under the load−displacement (F−v) curve and, therefore, the magnitudes of the experimental *J*-integrals $J^{\mathrm{exp}}_{\min}$ and $J^{\mathrm{exp}}_{\max}$ can be evaluated from Eq. (6.2). By inserting the appropriate geometry factor η, we will find that $J^{\mathrm{exp}}_{\min} = J_{\min}$ and $J^{\mathrm{exp}}_{\max} = J_{\max}$. Similarly, the area ABCA in Fig. 6.12b corresponds to the area ΔA of a loading branch of the F−v-curve during a single load cycle, and we find that the experimental cyclic *J*-integral of Eq. (6.5) and the cyclic *J*-integral of Eq. (6.3) yield equal results, $\Delta J^{\mathrm{exp}} = \Delta J$.

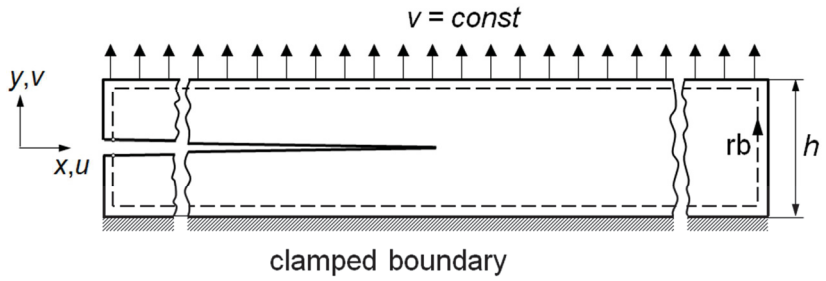

(a)

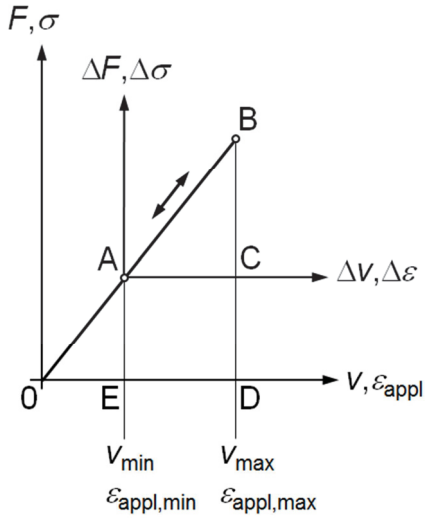

(b)

Fig. 6.12 (a) Double cantilever beam specimen with a long crack. The lower boundary is clamped. A constant displacement in y-direction, v, is prescribed on the upper boundary; the displacements u in x-direction are free. **(b)** Load−displacement (F−v) curve and stress−strain $(\sigma-\varepsilon)$ curve for a linear elastic material. For cyclic loading between the displacements $v_{\min}$ and $v_{\max}$, the origin of the coordinate system is reset into point A.

7 Growing fatigue cracks

Paper I has shown that the incremental plasticity cyclic *J*-integral $\Delta J_{\mathrm{PZ}}^{\mathrm{ep}}$, evaluated for a contour around the crack tip plastic zone, is physically appropriate to characterize the driving force of *stationary* fatigue cracks in elastic–plastic materials.

For a *growing* fatigue crack, the entire crack tip plastic zone consists of the initial plastic zone of the stationary crack tip, the plastic wake, and the active plastic zone of the moving crack tip (Fig. 7.1b). Since cyclic plasticity around the *current* crack tip drives a fatigue crack (e.g. Laird 1967, 1979), and from the results of Sect. 5.2, it can be guessed that the incremental plasticity cyclic *J*-integral around the *active* plastic zone of a propagating crack tip, $\Delta J_{\mathrm{actPZ}}^{\mathrm{ep}}$, Eq. (7.15), is the appropriate driving force parameter of *growing* fatigue cracks.

The main intention of Paper II is to check whether this is true. The same finite element model as in Paper I is applied. A basic difference is that a crack extension step occurs at minimum load after each load cycle. The maximum load is changed so that small- and large-scale yielding conditions prevail in the specimen.

A problem observed from these analyses is that $J_{\mathrm{actPZ}}^{\mathrm{ep}}$ becomes negative at minimum load, $J_{\mathrm{actPZ,min}}^{\mathrm{ep}} < 0$, due to compressive stresses during unloading, which yields a complex square root term in Eq. (7.15). However, comparisons of the variations of $J_{\mathrm{actPZ}}^{\mathrm{ep}}$ with the evolution of the crack tip opening displacement δ_{t} during a load cycle showed that the crack tip is closed, $\delta_{\mathrm{t}} = 0$, during the stages where $J_{\mathrm{actPZ}}^{\mathrm{ep}} < 0$, see Fig. 7. Consequently, negative values of $J_{\mathrm{actPZ}}^{\mathrm{ep}}$ do not deliver a contribution to the driving force for fatigue crack growth and $\Delta J_{\mathrm{actPZ}}^{\mathrm{ep}}$ is equal to the value of $J_{\mathrm{actPZ,max}}^{\mathrm{ep}}$ at maximum load of a load cycle, $\Delta J_{\mathrm{actPZ}}^{\mathrm{ep}} = J_{\mathrm{actPZ,max}}^{\mathrm{ep}}$, i.e. for load ratios $R \le 0$.

The conventional cyclic *J*-integral around the active plastic zone, calculated via configurational forces, $\Delta J_{\mathrm{actPZ}}^{\mathrm{conv}}$, or by ABAQUS, $\Delta J_{\mathrm{actPZ}}^{\mathrm{VCE}}$, analogously to Eq. (7.15), leads to erroneous results for growing fatigue cracks. They are only correct in the case of a stationary fatigue crack, where the active and the initial crack tip plastic zone coincide, so that $\Delta J_{\mathrm{actPZ}}^{\mathrm{ep}} = \Delta J_{\mathrm{PZ}}^{\mathrm{ep}} = \Delta J_{\mathrm{PZ}}^{\mathrm{conv}} = \Delta J_{\mathrm{PZ}}^{\mathrm{VCE}}$, Fig. 7.1a,b.

It is shown that the experimental cyclic *J*-integral ΔJ^{exp}, Eq. (3.8), corresponds to $\Delta J_{\mathrm{PZ}}^{\mathrm{ep}}$; see Fig. 7.8, Table 7.1 and Table 7.2. This implies that ΔJ^{exp} is only fully appropriate for *stationary* fatigue cracks, where $\Delta J_{\mathrm{actPZ}}^{\mathrm{ep}} = \Delta J_{\mathrm{PZ}}^{\mathrm{ep}}$. After crack extension, however, $\Delta J^{\mathrm{exp}} = \Delta J_{\mathrm{PZ}}^{\mathrm{ep}}$ is not equal to the magnitude of $\Delta J_{\mathrm{actPZ}}^{\mathrm{ep}}$, and, therefore, ΔJ^{exp} is not fully appropriate to measure the driving force for a *growing* fatigue crack. The difference between ΔJ^{exp} and $\Delta J_{\mathrm{actPZ}}^{\mathrm{ep}}$ can be small for *constant* fatigue loads under ssy-conditions, but it can reach 20% for lsy-conditions (Tables 7.1 and 7.2).

The ultimate check of $\Delta J_{\mathrm{actPZ}}^{\mathrm{ep}}$ as physically correct driving force parameter for fatigue crack growth is by conducting a numerical experiment where the constant fatigue load is superimposed by a single overload. The fatigue crack growth rate da/dN is proportional to the

cyclic crack tip opening displacement $\Delta\delta_t$ even after application of an overload (e.g. Bichler and Pippan 2007). Thereby, it is demonstrated that ΔJ^{ep}_{actPZ} correctly reflects crack growth retardation since it varies analogously to $\Delta\delta_t$ (Fig. 7.9). Moreover, the estimated maximum reduction in ΔJ^{ep}_{actPZ}, compared to a constant fatigue load, is in very good aggreement with the results reported for an experimental overload test conducted by Bichler and Pippan (2007).

On the contrary, the experimental cyclic *J*-integral ΔJ^{exp} (and ΔJ^{ep}_{PZ}), predict a continuously increasing crack growth rate after an overload, which confirms that ΔJ^{exp} is *not* strictly correct, if the fatigue crack grows.

Paper II:

Physically appropriate characterization of fatigue crack propagation rate in elastic–plastic materials using the *J*-integral concept

W. Ochensberger and O. Kolednik

published in

International Journal of Fracture (2015) 192:25–45

Abstract

The current paper discusses the physically correct evaluation of the driving force for fatigue crack propagation in elastic–plastic materials using the *J*-integral concept. This is important for low-cycle fatigue and for short fatigue cracks, where the conventional stress intensity range (ΔK) concept cannot be applied. Using the configurational force concept, Simha et al., *J. Mech. Phys. Solids 56 (2008) 2876*, have derived the *J*-integral for elastic–plastic materials with incremental theory of plasticity, J^{ep}, which is applicable for cyclic loading and/or for growing cracks, in contrast to the conventional *J*-integral. The variation of this incremental plasticity *J*-integral J^{ep} is studied in numerical investigations conducted on two-dimensional C(T)-specimens with long cracks under cyclic Mode I loading. The crack propagates by an increment after each load cycle. The maximum load is varied so that small- and large-scale yielding conditions prevail. Three different load ratios are considered, from pure tension to tension-compression loading. By theoretical considerations and comparisons with the variation of the crack tip opening displacement δ_t, it is demonstrated that the cyclic, incremental plasticity *J*-integral ΔJ^{ep}_{actPZ}, which is computed for a contour around the active plastic zone of the growing crack, is physically appropriate to characterize the growth rate of fatigue cracks. The validity of the experimental cyclic *J*-integral, ΔJ^{exp}, proposed by Dowling and Begley, *ASTM STP 590 (1976) 82*, is also investigated. The results show that ΔJ^{exp} is correct for the first load cycle, however, not fully appropriate for a growing fatigue crack.

Keywords: Configurational force concept; Crack driving force; Cyclic *J*-integral; Low-cycle fatigue; Fatigue crack growth; Overload effect

7.1 Introduction

This paper deals with the physically correct evaluation of the driving force of cyclically loaded, growing cracks in elastic–plastic materials for cases where linear elastic fracture mechanics is not applicable.

The conventional *J*-integral J^{conv} (Rice 1968a,b), which is commonly applied in the regime of nonlinear fracture mechanics, relies on deformation theory of plasticity, i.e. the elastic–plastic material is treated as being nonlinear elastic. For this reason, J^{conv} suffers from two fundamental problems when it is applied to elastic–plastic materials: (i) J^{conv} is formally not applicable for non-proportional loading conditions (Rice 1968a,b; Anderson 1995), (ii) J^{conv} does not describe the real driving force of a crack in elastic–plastic materials (Rice 1968a,b). In spite of these problems, Dowling and Begley (1976) proposed the experimental cyclic *J*-integral ΔJ^{exp} as a parameter characterizing the growth rate $\mathrm{d}a/\mathrm{d}N$ of fatigue cracks for cases where the stress intensity range ΔK is not applicable. Although supported for some materials by experimental data (e.g. Dowling and Begley 1976; Dowling 1976; Lambert et al. 1988; Banks-Sills and Volpert 1991), the applicability of ΔJ^{exp} has remained doubtful due to the lack of its theoretical basis (Suresh 1998).

New insight into this problem has been gained by adopting the concept of configurational forces, which enables the derivation of the *J*-integral for elastic–plastic materials with incremental theory of plasticity (Simha et al. 2008). This incremental plasticity *J*-integral J^{ep} has the physical meaning of a real driving force term of a crack in an elastic–plastic material even under strongly non-proportional loading conditions, however it is path dependent (Simha et al. 2008). Kolednik et al. (2014) studied this path dependence and demonstrated the usefulness of J^{ep} for stationary and growing cracks under monotonic loading conditions. In a very recent study, Ochensberger and Kolednik (2014) have investigated the application of J^{ep} for stationary cracks in elastic–plastic materials that are cyclically loaded, and it has been shown that the experimental cyclic *J*-integral ΔJ^{exp} is, in principle correct, if certain conditions are observed.

The current paper complements the study of Ochensberger and Kolednik (2014) by considering *growing* cracks in elastic–plastic, cyclically loaded materials. It will be demonstrated that important differences occur compared to the case of a stationary crack. The paper shall provide a new basis for the application of the *J*-integral concept for characterizing the crack growth rate in fatigue.

The next section briefly reviews the incremental plasticity *J*-integral J^{ep} and the findings of the papers by Kolednik et al. (2014) and Ochensberger and Kolednik (2014) that are necessary for the understanding of the current paper. Readers who are already familiar with the topic may continue reading at the last paragraph in Sect. 7.2.

7.2 Incremental plasticity J-integral J^{ep} and crack driving force

Configurational forces are thermodynamic driving forces on defects in materials (Maugin 1995; Gurtin 1995, 2000; Kienzler and Hermann 2000). The application of the configurational

force concept for studying fracture mechanics problems has gained increasing research interest, see e.g. Simha et al. (2003, 2005), Nguyen et al. (2005), Özenç et al. (2014), Sistaninia and Kolednik (2014), Kolednik et al. (2014) and the according references in Section 2 therein. The concept rests on the notion of the second-rank configurational stress tensor, which is defined in the form, $\mathbf{C} = \phi \mathbf{I} - \mathbf{F}^{\mathrm{T}}\mathbf{S}$ (Eshelby 1951, 1970). [11] The parameter ϕ denotes the strain energy density, $\mathbf{I}$ the identity tensor, $\mathbf{F}^{\mathrm{T}}$ the transposed of the deformation gradient tensor $\mathbf{F}$, and $\mathbf{S}$ the 1st Piola-Kirchhoff stress. A configurational force $\mathbf{f}$ in a body is associated with the divergence of the configurational stress tensor,

$$\mathbf{f} = -\nabla \cdot \mathbf{C} = -\nabla \cdot \left(\phi \mathbf{I} - \mathbf{F}^{\mathrm{T}}\mathbf{S} \right). \tag{7.1}$$

The vector $\mathbf{f}$ gives the magnitude and direction of the thermodynamic driving force acting on the defect.

7.2.1 Configurational forces and J-integrals for elastic–plastic materials

A literature review on the application of configurational force concept for the prediction of the behavior of cracks has been given in Kolednik et al. (2014) and shall not be repeated here. Figure 7.1a shows a sketch of a homogeneous body $\mathcal{B}$ containing a crack with length a_0 and a unit vector in the nominal crack growth direction $\mathbf{e}$. The configurational force concept allows the derivation of the *J*-integral. The scalar, near-tip *J*-integral J_{tip} is related to the configurational force vector emanating from the crack tip, $\mathbf{f}_{\mathrm{tip}}$, in the form (see e.g. Simha et al. 2003),

$$J_{\mathrm{tip}} = \mathbf{e} \cdot \mathbf{J}_{\mathrm{tip}} = \mathbf{e} \cdot \left(-\mathbf{f}_{\mathrm{tip}} \right) = \mathbf{e} \cdot \lim_{r \to 0} \int_{\Gamma_r} \mathbf{C}\mathbf{n} \, \mathrm{d}s \,, \tag{7.2}$$

where Γ_r is a contour drawn from the lower to the upper crack surface in counterclockwise direction at a distance r around the crack tip; $\mathbf{n}$ is the outward unit normal vector to the contour Γ, and ds is an increment of the integration path. The scalar *J*-integral J_{tip} of Eq. (7.2) is the projection of the near-tip *J*-integral vector $\mathbf{J}_{\mathrm{tip}}$ into the nominal crack growth direction $\mathbf{e}$. The *J*-integral along an arbitrary contour Γ can be evaluated from the relation,

$$J = \mathbf{e} \cdot \mathbf{J} = \mathbf{e} \cdot \int_{\Gamma} \mathbf{C}\mathbf{n} \, \mathrm{d}s = \mathbf{e} \cdot \int_{\Gamma} \left(\phi \mathbf{I} - \mathbf{F}^{\mathrm{T}}\mathbf{S} \right) \mathbf{n} \, \mathrm{d}s = J_{\mathrm{tip}} - \mathbf{e} \cdot \int_{\mathcal{D}} \mathbf{f} \, \mathrm{d}A \,, \tag{7.3}$$

where $\mathcal{D}$ denotes the area bounded by Γ, but excluding the crack tip. Note that Eq. (7.2) and Eq. (7.3) do not rely on constitutive equations of the material.

We assume that body $\mathcal{B}$ is homogeneous and consists of elastic–plastic material. Then we can distinguish between two different types of *J*-integral, the conventional *J*-integral J^{conv}, which presumes deformation theory of plasticity (see e.g. Simha et al. 2003), and the

[11] For the mathematical expressions in this paper the direct (coordinate-free) notation is used as in Gurtin (2000). The notation is specified in Ochensberger and Kolednik (2014).

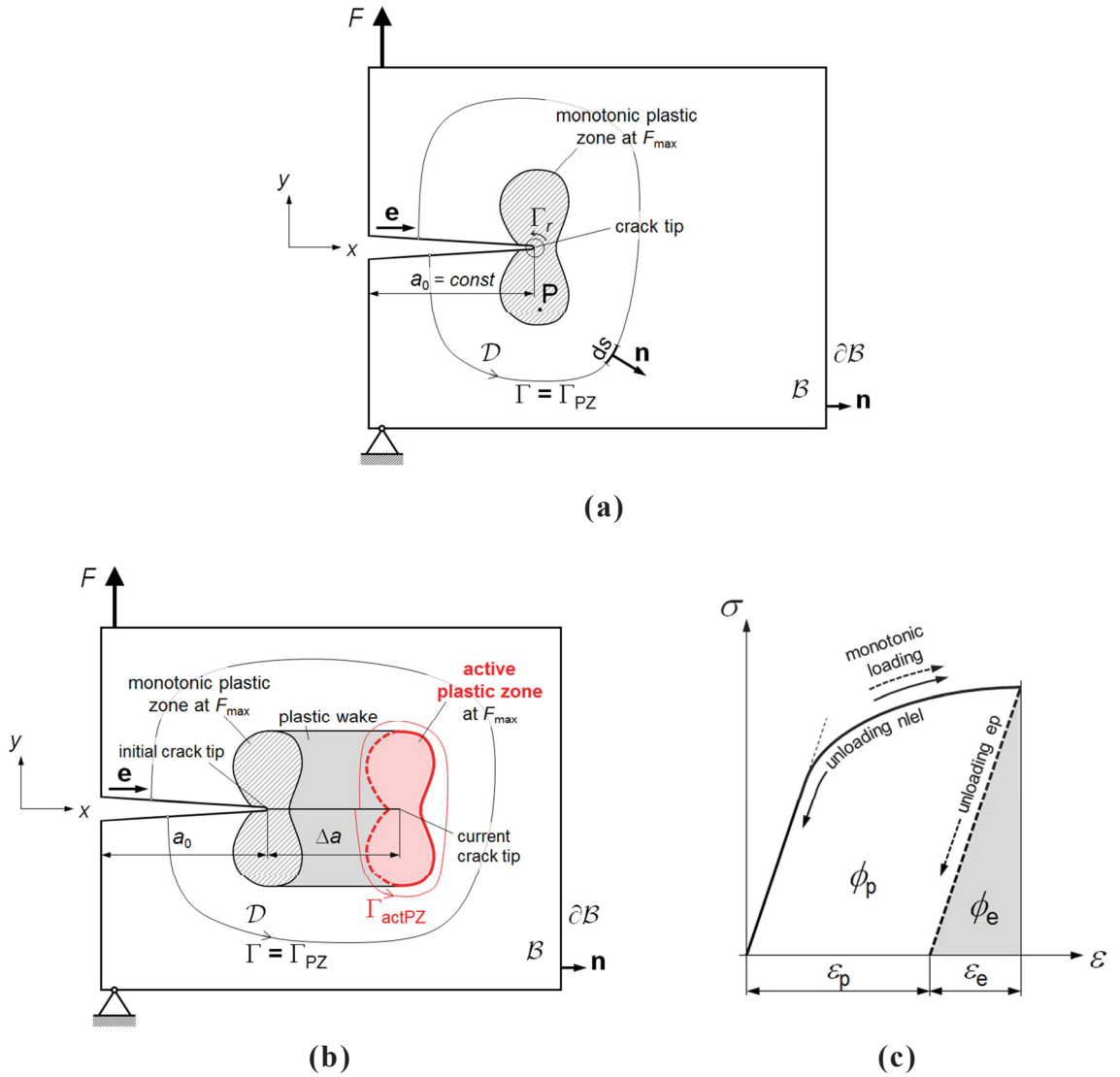

Fig. 7.1 **(a)** Homogeneous elastic–plastic body $\mathcal{B}$ with a long, stationary crack. The contour Γ_{PZ} encloses the crack tip plastic zone. **(b)** Body $\mathcal{B}$ after crack extension Δa. The contour Γ_{actPZ} encloses the active plastic zone of the current crack tip, whereas the contour Γ_{PZ} encloses the entire crack tip plastic zone, including the plastic wake. **(c)** Stress–strain ($\sigma - \varepsilon$) curve for point P in the plastic zone. Only the elastic part of the strain energy density ϕ_e is reversible. The total strain energy density $\phi = \phi_e + \phi_p$ would be recoverable in a comparable nonlinear elastic material with the identical $\sigma - \varepsilon$-curve.

incremental plasticity *J*-integral J^{ep} for materials with incremental theory of plasticity (Simha et al. 2008),

$$J^{conv} = J^{conv}_{tip} + \mathbf{e}\cdot\int_{\mathcal{D}} \nabla\cdot\left(\phi\mathbf{I} - \mathbf{F}^{T}\mathbf{S}\right)\mathrm{d}A = J^{conv}_{tip} - \mathbf{e}\cdot\int_{\mathcal{D}} \mathbf{f}^{def.pl}\,\mathrm{d}A\,, \tag{7.4}$$

$$J^{ep} = J^{ep}_{tip} + \mathbf{e}\cdot\int_{\mathcal{D}} \nabla\cdot\left(\phi_e\,\mathbf{I} - \mathbf{F}^{T}\mathbf{S}\right)\mathrm{d}A = J^{ep}_{tip} - \mathbf{e}\cdot\int_{\mathcal{D}} \mathbf{f}^{ep}\,\mathrm{d}A\,. \tag{7.5}$$

The difference between J^{conv} and J^{ep} appears in the substitution of the strain energy density ϕ. For deformation plasticity, the total strain energy density ϕ is inserted as for a nonlinear elastic material, whereas for incremental plasticity only the elastic part of the strain energy density ϕ_{e} is inserted, see Fig. 7.1c. From Eq. (7.4) and Eq. (7.5), or by inserting either ϕ or ϕ_{e} into Eq. (7.1), it is clear that also two different types of configurational force exist, the deformation plasticity configurational force $\mathbf{f}^{\mathrm{def.pl}}$ and the elastic–plastic configurational force $\mathbf{f}^{\mathrm{ep}}$.

If the body $\mathcal{B}$ deforms only elastically, there exists no difference between $\mathbf{f}^{\mathrm{def.pl}}$ and $\mathbf{f}^{\mathrm{ep}}$, or between J^{conv} and J^{ep}. The bulk configurational force $\mathbf{f}$ vanishes, and configurational forces appear only at the crack tip, $\mathbf{f}_{\mathrm{tip}}$, and at the external boundary $\partial\mathcal{B}$ (Fischer et al. 2012a). Therefore, the *J*-integral is path-independent, see the right-hand side extension of Eq. (7.4).

If body $\mathcal{B}$ is also plastically deformed, bulk configurational forces $\mathbf{f}^{\mathrm{ep}}$ are induced in the plastically deformed regions of the body and, according to the right-hand side extension of Eq. (7.5), the incremental plasticity *J*-integral J^{ep} becomes path-dependent. The bulk configurational force $\mathbf{f}^{\mathrm{ep}}$ at a material point in the elastic–plastic body evolves proportional to the gradient of the plastic component of the deformation gradient (Simha et al. 2008),

$$\mathbf{f}^{\mathrm{ep}} = \left(\mathbf{F}^{\mathrm{e}}\right)^{\mathrm{T}} \mathbf{S} : \frac{\partial \mathbf{F}^{\mathrm{p}}}{\partial \mathbf{X}} . \tag{7.6}$$

In Eq. (7.6), $\mathbf{F}^{\mathrm{e}}$ and $\mathbf{F}^{\mathrm{p}}$ are the elastic and plastic components of the deformation gradient tensor $\mathbf{F}$, and $\partial \mathbf{F}^{\mathrm{p}} / \partial \mathbf{X}$ is the gradient of $\mathbf{F}^{\mathrm{p}}$ with respect to the unloaded reference coordinate system.

Performing a numerical cyclic tensile test, Kolednik et al. (2014) have demonstrated the problem of idealizing elastic–plastic materials with deformation theory of plasticity: artificial bulk configurational forces $\mathbf{f}^{\mathrm{def.pl}}$ emerge on positions with a gradient in plastic strain as soon as non-proportional loading occurs. These bulk configurational forces do not have a physical background and lead to an artificial path dependence of J^{conv}, compare Eq. (7.4); see also Brocks et al. (2003) or, e.g., in Kuna (2008).

A big advantage of the incremental plasticity *J*-integral J^{ep} is that it has the physical meaning of a true driving force term in elastic–plastic materials even for non-proportional loading conditions, such as a growing crack or a cyclically loaded crack, while, on the contrary, the conventional *J*-integral J^{conv} possesses the well-known restrictions outlined in the Introduction.

7.2.2 Path dependence of J^{ep} and driving force for cracks under monotonic loading

The path dependence of the incremental plasticity *J*-integral J^{ep} for stationary and growing cracks in monotonically loaded elastic–plastic materials has been investigated in Kolednik et al. (2014). The investigation showed that for a stationary crack, the *J*-integral for a contour enclosing the entire crack tip plastic zone $J^{\mathrm{ep}}_{\mathrm{PZ}}$, Fig. 7.1a, should be taken as parameter

characterizing the driving force. Crack extension occurs, if $J_{\mathrm{PZ}}^{\mathrm{ep}}$ is equal or larger than the crack growth resistance.

The incremental plasticity *J*-integral for a contour enclosing the crack tip plastic zone $J_{\mathrm{PZ}}^{\mathrm{ep}}$ has the physical meaning of the driving force for the combined movement of the crack tip and the crack tip plastic zone. From a comparison of Fig. 7.1a and 7.1b it becomes clear that it is impossible for a crack to grow in an elastic–plastic material without the simultaneous movement of the surrounding plastic zone. Thus, the near-tip *J*-integral $J_{\mathrm{tip}}^{\mathrm{ep}}$, which is the driving force for the translational movement of the crack tip alone, is meaningless for the assessment of crack extension. The numerical results in Kolednik et al. (2014) suggest that the magnitude of the incremental plasticity near-tip *J*-integral is zero, $J_{\mathrm{tip}}^{\mathrm{ep}} = 0$, for both a stationary and a growing crack under monotonic loading. As noted already in classical papers, e.g. Rice and Johnson (1970) or Rice (1979), also the conventional, deformation plasticity near-tip *J*-integral is zero, $J_{\mathrm{tip}}^{\mathrm{conv}} = 0$, for stationary and growing cracks under monotonic loading.

For a contour around the crack tip plastic zone, the conventional *J*-integral $J_{\mathrm{PZ}}^{\mathrm{conv}}$ is identical to the incremental plasticity *J*-integral $J_{\mathrm{PZ}}^{\mathrm{ep}}$,

$$J_{\mathrm{PZ}}^{\mathrm{ep}} = J_{\mathrm{PZ}}^{\mathrm{conv}} . \tag{7.7}$$

The requirement for this equality is that the crack tip plastic zone is completely surrounded by material that is only elastically deformed. In this case there is no difference in the formulation between deformation- and incremental plasticity, see middle term in Eq. (7.3).

Notice that a relation similar to Eq. (7.7) for the far-field *J*-integrals, $J_{\mathrm{far}}^{\mathrm{ep}} = J_{\mathrm{far}}^{\mathrm{conv}}$, only exists, if no part of the outer boundary of the specimen is plastically deformed. A back-face plasticity region appears in case of large-scale yielding (lsy) conditions, compare Fig. 7.4b. Configurational forces $\mathbf{f}^{\mathrm{ep}}$ with a positive component in *x*-direction are induced in the back-face plasticity region so that J^{ep} decreases and $J_{\mathrm{far}}^{\mathrm{ep}} < J_{\mathrm{PZ}}^{\mathrm{ep}}$, compare Eq. (7.5). On the contrary, the conventional *J*-integral remains constant, $J_{\mathrm{far}}^{\mathrm{conv}} = J_{\mathrm{PZ}}^{\mathrm{conv}}$, since proportional loading conditions prevail. It is well known that for a stationary crack the conventional *J*-integral J^{conv} equals the experimental *J*-integral J^{exp}, which is determined from the load–displacement curve (Rice et al. 1973; Kolednik 1991). Therefore, the incremental plasticity *J*-integral for a contour around the crack tip plastic zone $J_{\mathrm{PZ}}^{\mathrm{ep}}$ equals the experimental *J*-integral for a stationary crack, $J_{\mathrm{PZ}}^{\mathrm{ep}} = J_{\mathrm{PZ}}^{\mathrm{conv}} = J_{\mathrm{far}}^{\mathrm{conv}} = J^{\mathrm{exp}}$. This means that both the conventional and the experimental *J*-integral give the correct driving force for the initiation of crack growth.

For a continuously growing crack at constant load, the *J*-integral $J_{\mathrm{actPZ}}^{\mathrm{ep}}$ for a contour Γ_{actPZ} around the *active* plastic zone of the moving crack tip, Fig. 7.1b, is the physically correct crack driving force parameter (Kolednik et al. 2014). Here, the contour Γ_{PZ} encloses the initial plastic zone of the stationary crack, the plastically deformed regions along the crack flanks (plastic wake), and the active plastic zone around the current crack tip. Since the contour Γ_{PZ} goes only through elastic deformed regions, Eq. (7.7) is still valid. However, note that $J_{\mathrm{actPZ}}^{\mathrm{ep}} \neq J_{\mathrm{actPZ}}^{\mathrm{conv}}$, since the contour Γ_{actPZ} crosses the plastic wake along the crack flanks

(Fig. 7.1b). It should be mentioned that the experimental *J*-integral J^{exp} does, in general, not reflect the driving force for a growing crack, $J^{\mathrm{ep}}_{\mathrm{actPZ}} \neq J^{\mathrm{exp}}$; see Kolednik (1991, 1993) and Turner and Kolednik (1994). This means that neither the conventional nor the experimental *J*-integral give the correct driving force for a continuously growing crack under monotonic loading.

7.2.3 Driving force for cyclically loaded, stationary cracks in elastic–plastic materials

The characteristic properties of the incremental plasticity *J*-integral J^{ep} under cyclic loading conditions, but for a *stationary* crack, have recently been presented in Ochensberger and Kolednik (2014). The path-dependence of J^{ep} was investigated for various, positive and negative, load ratios $R = F_{\min}/F_{\max}$ under lsy-conditions. It has been shown that negative J^{ep} -values can appear during the unloading stages on contours close to the crack tip; they originate from compressive residual stresses caused by reverse plasticity within the crack tip plastic zone.

The incremental plasticity *J*-integral for a contour enclosing the crack tip plastic zone $J^{\mathrm{ep}}_{\mathrm{PZ}}$ also characterizes the driving force of a crack in an elastic–plastic material, which is monotonically loaded after a cyclic pre-deformation. It is clear that $J^{\mathrm{ep}}_{\mathrm{PZ}} = J^{\mathrm{conv}}_{\mathrm{PZ}}$, since Eq. (7.7) is valid also for cyclic loading conditions, as long as the crack tip plastic zone is surrounded by elastically deformed material.

In the fatigue of metals and alloys, the magnitude of the crack driving force at the maximum load $J^{\mathrm{ep}}_{\mathrm{PZ,max}}$ is considerably smaller than the crack growth resistance, so that the crack cannot extend at $F_{\max} = \mathrm{constant}$. Driving force terms for fatigue crack growth have been introduced, which should allow the prediction of the crack propagation rate of a fatigue crack (e.g. see Suresh 1998). Note that these terms are not necessarily real driving force terms in the thermodynamic sense. The stress intensity range ΔK (Paris et al. 1961; Paris and Erdogan 1963) or the effective stress intensity range ΔK_{eff} (Elber 1970, 1971) are used, if linear elastic fracture mechanics is applicable. For the regime of elastic-plastic fracture mechanics, Dowling and Begley (1976) proposed the application of the experimental cyclic *J*-integral ΔJ^{exp}, which is determined from a single loading or unloading branch of the load–displacement (*F*–*v*) curve, similar to J^{exp} for monotonic loading. For deeply notched bend- and C(T)-specimens, ΔJ^{exp} is given by the relation

$$\Delta J^{\mathrm{exp}} = \frac{\eta \Delta A}{b B}, \tag{7.8}$$

where ΔA is the area below a single loading branch of the *F*–*v*-curve (Fig. 7.2a), $b = W - a$ is the ligament length, with *W* as the specimen width and *a* as the crack length, and *B* is the specimen thickness. The geometry factor $\eta(a/W)$ depends on the specimen type (see also ESIS P2-92, 1992 or ASTM E1820, 2005). In spite of empirical results showing that ΔJ^{exp} correlates to $\mathrm{d}a/\mathrm{d}N$ for specific materials under certain cyclic loading conditions (e.g.

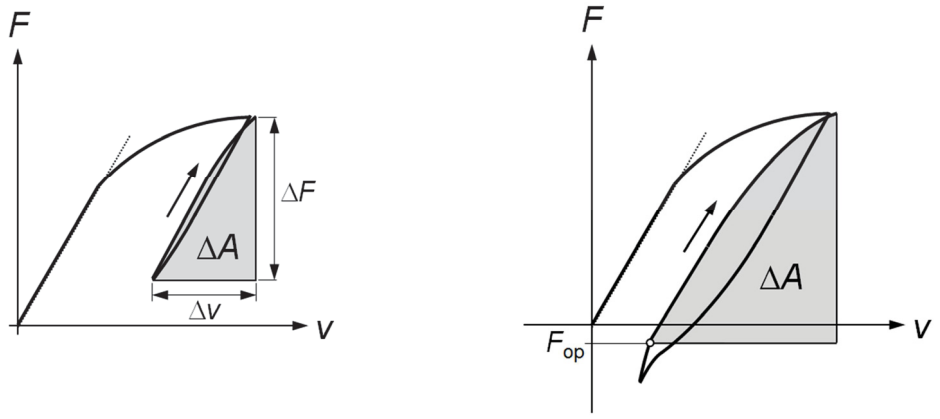

(a) **(b)**

Fig. 7.2 To the determination of the experimental cyclic *J*-integral ΔJ^{exp} for a C(T) or deeply notched bend specimen from the area ΔA below a single loading branch of the load–displacement (F–v) curve, **(a)** for load ratio $R > 0$ without crack closure, **(b)** for $R < 0$. The load F_{op} denotes the point of crack opening.

Dowling and Begley 1976; Dowling 1976; Lambert et al. 1988; Banks-Sills and Volpert 1991), the general applicability of ΔJ^{exp} remained doubtful due to the lack of theoretical basis (Anderson 1995; Suresh 1998).

Ochensberger and Kolednik (2014) have shown that the incremental plasticity cyclic *J*-integral for a contour around the crack tip plastic zone, $\Delta J^{\mathrm{ep}}_{\mathrm{PZ}}$, is a physically appropriate parameter for characterizing the driving force for a cyclically loaded, stationary crack. The parameter $\Delta J^{\mathrm{ep}}_{\mathrm{PZ}}$ should be evaluated by the relation,

$$\Delta J^{\mathrm{ep}}_{\mathrm{PZ}} = J^{\mathrm{ep}}_{\mathrm{PZ,max}} + J^{\mathrm{ep}}_{\mathrm{PZ,min}} - 2\sqrt{J^{\mathrm{ep}}_{\mathrm{PZ,max}} J^{\mathrm{ep}}_{\mathrm{PZ,min}}} \ . \tag{7.9}$$

Here, $J^{\mathrm{ep}}_{\mathrm{PZ,max}}$ and $J^{\mathrm{ep}}_{\mathrm{PZ,min}}$ denote the maximum and minimum $J^{\mathrm{ep}}_{\mathrm{PZ}}$-values achieved in a single load cycle. It should be mentioned that the magnitude of $\Delta J^{\mathrm{ep}}_{\mathrm{PZ}}$ is, due to the square root term in Eq. (7.9), very sensitive to small values of $J^{\mathrm{ep}}_{\mathrm{PZ,min}}$. This fact is especially important for small positive load ratios. For a stationary crack, negative load ratios gave minimum $J^{\mathrm{ep}}_{\mathrm{PZ}}$-values of exactly zero, $J^{\mathrm{ep}}_{\mathrm{PZ,min}} = 0$, leading to $\Delta J^{\mathrm{ep}}_{\mathrm{PZ}} = J^{\mathrm{ep}}_{\mathrm{PZ,max}}$ (Ochensberger and Kolednik 2014).

The application of Eq. (7.9) for the correct calculation of the cyclic *J*-integral can be demonstrated by comparison with the cyclic crack tip opening displacement $\Delta\delta_{\mathrm{t}}$ (Ochensberger and Kolednik 2014). In a very recent study, Metzger et al. (2014) demonstrated the correlation between the conventional cyclic *J*-integral (Lamba 1975; Wüthrich 1982; Tanaka 1983) and $\Delta\delta_{\mathrm{t}}$. Note that the conventional cyclic *J*-integral used in Metzger et al. (2014) is, in principle, equal to the expression in Eq. (7.9), see Appendix in Ochensberger and Kolednik (2014) for details.

If the crack tip plastic zone is completely surrounded by elastically deformed material, Eq. (7.7) applies for both the J^{ep}-values at maximum and minimum load. Therefore, the

incremental plasticity and deformation plasticity cyclic *J*-integrals for a contour around the crack tip plastic zone must be equal,

$$\Delta J_{\mathrm{PZ}}^{\mathrm{ep}} = \Delta J_{\mathrm{PZ}}^{\mathrm{conv}} = \Delta J^{\mathrm{exp}} . \tag{7.10}$$

The right-hand side extension of Eq. (7.10) results from Ochensberger and Kolednik (2014), who have shown that the experimental cyclic *J*-integral ΔJ^{exp} reflects the magnitude of $\Delta J_{\mathrm{PZ}}^{\mathrm{ep}}$, provided that in cases of crack closure a correct procedure is applied for the determination of the area ΔA in Eq. (7.8). The conventionally applied procedure via the determination of the closure- or opening loads, F_{cl} and F_{op} (Fig. 7.2b), as proposed by Dowling and Begley (1976), can lead to inaccurate results, see also Section 7.5.2 below.

The results of Ochensberger and Kolednik (2014) demonstrate that the experimental cyclic *J*-integral ΔJ^{exp} proposed by Dowling and Begley (1976) is, in principle, a physically appropriate driving force parameter for a cyclically loaded specimen. It should be noted, however, that this investigation has been conducted for a stationary crack. Therefore, the question remains to be solved whether these findings are applicable also in the case where the crack grows under cyclic loading, as it occurs in fatigue crack growth.

We consider in the current paper cyclic loading *with* crack extension. It will be demonstrated in this paper that important differences appear between a stationary and a growing crack, although the crack growth rate per load cycle is small.

7.3 Numerical modeling and computational aspects

For the numerical investigations the same procedure is applied as in Ochensberger and Kolednik (2014). The simulations are performed using the finite element (FE) program ABAQUS (see http://www.simulia.com/products/abaqus_fea.html). A two-dimensional C(T)-specimen (ASTM E1820, 2005) is modeled with a straight crack in horizontal *x*-direction, Fig. 7.3a. The specimen dimensions are: width $W = 50\,\mathrm{mm}$, height H = 60 mm, nominal thickness B = 25 mm, and initial crack length a_0 = 25 mm. The specimen is subjected to cyclic Mode I loading by prescribing the load F at the load application point. Plane strain conditions are assumed.

The specimen consists of homogeneous, isotropic, elastic–ideally plastic material with Young's modulus E = 200 GPa, Poisson's ratio ν = 0.3, and yield strength σ_{y} = 270 MPa. A small strip near the left boundary of the specimen is adopted as linear elastic, with Young's modulus E = 200 GPa and Poisson's ratio ν = 0.3. This is done to prevent large plastic deformation at the load application point. Note that this does not cause any problems, since the plastic zone does not approach the elastic region.

Half of the specimen is discretized (Fig. 7.3a). The mesh consists of bilinear 4-node continuum elements. The inner region A, where the crack propagates, has a dimension of 13.5×3.0 mm²; it is filled with elements of equal size. If not specified otherwise, the element size is $m = 0.1\,\mathrm{mm}$. Geometric nonlinearity is applied to consider large deformations around

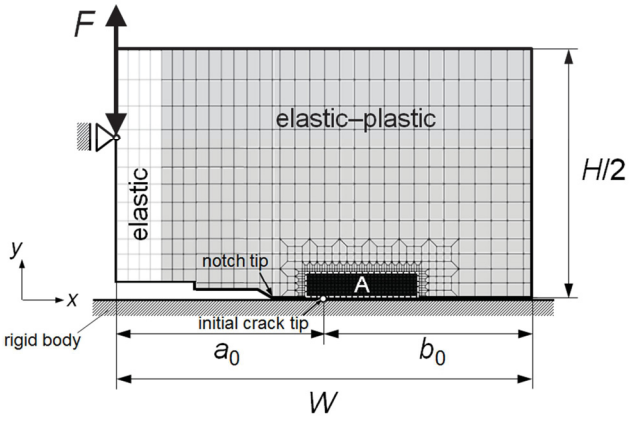

(a)

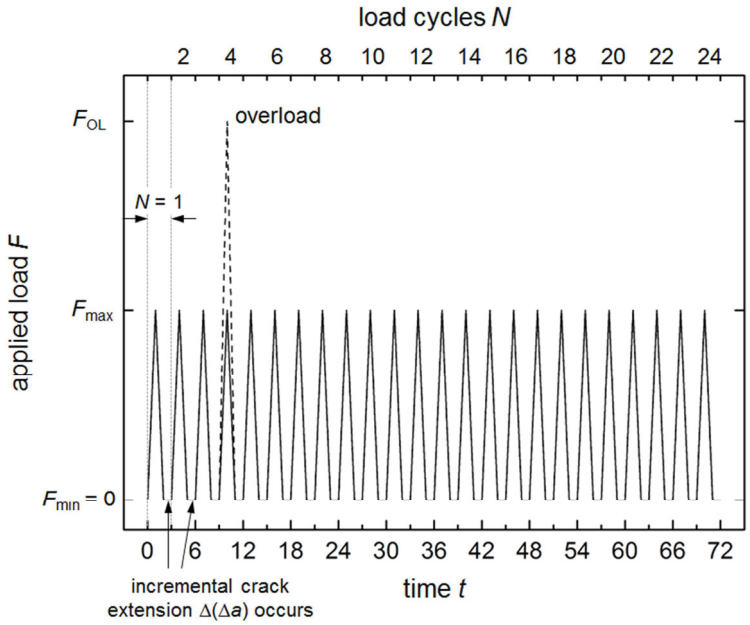

(b)

Fig. 7.3 **(a)** Model of the C(T)-specimen with boundary conditions. **(b)** Applied load F versus time t for a load ratio $R = 0$; the increment of crack extension per load cycle $\Delta(\Delta a)$ is two element lengths. Apart from the cases with constant loads, an additional study is conducted for a single tensile overload F_{OL}, applied during the fourth load cycle.

the crack tip. Crack flank contact without friction is modeled; a rigid body serves as counterpart to the upper half of the specimen. The nodes on the plane $y = 0$, except the nodes on the crack flank, are locked in y-direction, but unlocked in x-direction.

The loading steps are shown in Fig. 7.3b. Each load cycle N can be divided into three steps. In the first step, finished at time $t = 3N - 2$ with $N \in \mathbb{N}$, the specimen is loaded to maximum load F_{max}. In the second step, finished at $t = 3N - 1$, the specimen is unloaded to minimum load F_{min}. The crack length is held fixed during the loading and unloading stages.

In the third step, finished at $t = 3N$, the crack extends by an increment at the minimum load $F_{\min}$. We refer to Solanki et al. (2004) regarding the preferred load level for incremental crack extension. Incremental crack extension is modeled by adopting the node release technique (Ohji et al. 1975; Newman 1976). Hereby initially bonded nodes on the plane $y = 0$ are released according to a pre-defined crack length function of time (see also Kuna 2008). Two elements are chosen as crack extension increment per load cycle, $\Delta(\Delta a) = 2m$. The number of applied load cycles is $N = 24$; the total crack advance is $\Delta a = \sum_{i=1}^{N} \Delta(\Delta a)_i = 4.8$ mm.

The maximum load is varied so that we get small-scale yielding (ssy) and large-scale yielding (lsy) conditions at $F_{\max} = 12.5\,\text{kN}$ and $F_{\max} = 27$ kN, respectively (Fig. 7.4a and 7.4b). Large-scale yielding is assumed to start with the onset of plasticity at the back face of the specimen (Fig. 7.4b). Three load ratios are considered, $R = 0$ (zero-tension loading, Fig. 7.3b), $R = 0.5$ (pure tension), and $R = -1$ (tension-compression).

The FE stress and strain analyses are in all cases performed using the incremental plasticity model provided by ABAQUS. Subsequently, the configurational forces are evaluated by a self-written post-processing routine, which is based on the papers by Müller et al. (2002, 2004) and Denzer et al. (2003). Deformation plasticity and incremental plasticity are alternatively applied for this post-processing in order to calculate at each node the deformation- and incremental plasticity configurational force, $\mathbf{f}^{\text{def.pl}}$ and $\mathbf{f}^{\text{ep}}$, by inserting either ϕ and ϕ_{e} into Eq. (7.1).

The scalar J-integral for an arbitrary contour Γ is calculated by a summation of the configurational forces over all nodes within the area $\mathcal{D}$ bounded by Γ, including the crack tip node, compare Eq. (7.4) and Eq. (7.5). The J-integrals for deformation plasticity and incremental plasticity, J^{conv} and J^{ep}, are given by

$$J_{\Gamma}^{\text{conv}} = \sum_{n \in \mathcal{D} \cup \text{tip}} -\left(\mathbf{e} \cdot \mathbf{f}^{\text{def.pl}}\right) \Delta A_n \,, \tag{7.11}$$

$$J_{\Gamma}^{\text{ep}} = \sum_{n \in \mathcal{D} \cup \text{tip}} -\left(\mathbf{e} \cdot \mathbf{f}^{\text{ep}}\right) \Delta A_n \,. \tag{7.12}$$

The parameter ΔA_n denotes the element area corresponding to a specific node n.

Important are the computation of J-integrals around the crack tip plastic zone J_{PZ} and around the active plastic zone J_{actPZ}, see Fig. 7.1b. The shape of the active plastic zone is obtained by observation of currently yielding integration points, i.e. when the plastic strain $\boldsymbol{\varepsilon}^{\text{p}}$ changes during a loading sequence. An example is presented in Fig. 7.4a; currently yielding integration points are marked by x-symbols. The integration path Γ_{actPZ} is chosen so that it includes all marked integration points at maximum load $F_{\max}$. It should be noted that the magnitude of the integration path is held fixed for a specific loading and unloading sequence, i.e. Γ_{actPZ} does not vary with increasing or decreasing load.

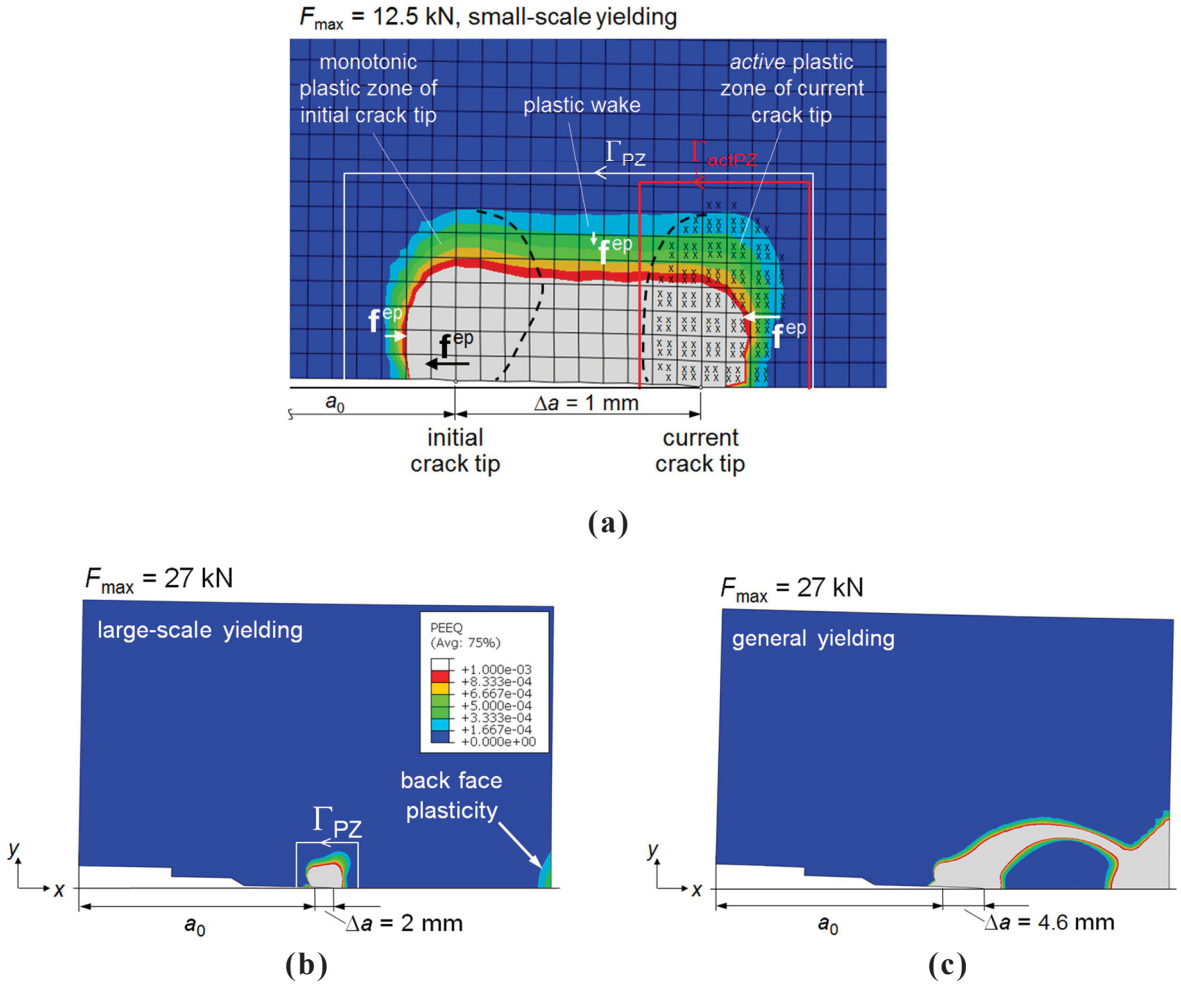

Fig. 7.4 Maps of the equivalent plastic strain ε_{eq}^{p} at an applied load of **(a)** $F_{max} = 12.5\,\text{kN}$ (small-scale yielding conditions), **(b)** $F_{max} = 27\,\text{kN}$ (large-scale yielding, i.e. after onset of back face plasticity), and **(c)** at $F_{max} = 27\,\text{kN}$ and $\Delta a = 4.6\,\text{mm}$ (general yielding). In **(a)** the configuration after $\Delta a = 1\,\text{mm}$ crack extension is depicted, when the active plastic zone has completely left the monotonic plastic zone of the initial crack tip; the *plastic zone shapes* are marked with *dashed lines*. Γ_{PZ} and Γ_{actPZ} denote the contours around the entire and the active plastic zone, respectively. Directions of the bulk configurational force $\mathbf{f}^{ep}$ are schematically indicated.

In addition to the *J*-integrals derived from configurational forces, J^{conv} and J^{ep}, the conventional computational *J*-integral of ABAQUS J^{VCE}, which is based on the virtual crack extension method developed by Parks (1977), is also computed. Note that J^{VCE} implicitly relies on deformation plasticity, when applied to elastic–plastic materials.

7.4 Incremental plasticity J-integral J^{ep} for crack extension under cyclic loading

7.4.1 Characteristic incremental plasticity J-integral terms, J^{ep}_{PZ} and J^{ep}_{actPZ}

Figures 7.5a and 7.5c present, for a load ratio $R = 0$, the variations of the incremental plasticity *J*-integrals around the crack tip plastic zone, J^{ep}_{PZ}, and around the active plastic zone, J^{ep}_{actPZ}, under ssy- and lsy-conditions, i.e. $F_{max} = 12.5\,\text{kN}$ and $F_{max} = 27\,\text{kN}$, respectively. Shown are $N = 24$ load cycles; Fig. 7.5b, d show in more detail the 11th load cycle. The J^{ep}-values reached at maximum load F_{max} are marked with full (for $J^{ep}_{PZ,max}$) and open (for $J^{ep}_{actPZ,max}$) dots.

It is seen from Fig. 7.5 that, due to the crack extension after each load cycle, the J^{ep}-values at maximum load, $J^{ep}_{PZ,max}$ and $J^{ep}_{actPZ,max}$, continuously increase, whereas the values taken at minimum load, $J^{ep}_{PZ,min}$ and $J^{ep}_{actPZ,min}$, remain approximately constant. While J^{ep}_{PZ} shows a regular behavior, with values very close to zero at F_{min}, the J^{ep}_{actPZ}-curve exhibits some irregularities during the first load cycles. The J^{ep}_{actPZ}-curve appears shifted downwards compared to the J^{ep}_{PZ}-curve.

The values of J^{ep}_{actPZ} and J^{ep}_{PZ} are equal for the first loading and unloading cycle, since crack extension has not occurred yet. With the first crack extension step, time $t > 2$, the active plastic zone starts to leave the plastic zone of the initial crack tip, and J^{ep}_{actPZ} differs from J^{ep}_{PZ}. The active plastic zone has completely left the initial plastic zone after a crack extension of $\Delta a = 0.6$ and 2 mm, $N = 4$ and 11, for ssy- and lsy-conditions, respectively. This is indicated by a vertical dashed line in Fig. 7.5a and 7.5c. It is seen that the irregularities of the J^{ep}_{actPZ}-curve occur before this line; e.g. especially high $J^{ep}_{actPZ,max}$-values appear during $N = 2$, followed by especially low $J^{ep}_{actPZ,min}$-values. This behavior will be discussed in more detail in the next section.

The *J*-integral values are collected in Tables 7.1 and 7.2. The values of $J^{ep}_{actPZ,max}$ lie approximately 6% lower than the values of $J^{ep}_{PZ,max}$; the difference decreases to approximately 4% with increasing crack extension. The difference almost disappears, if the active plastic zone merges with the back-face plasticity region so that general yielding (gy) conditions prevail. This happens for the values in Table 7.2 after $\Delta a = 4.6\,\text{mm}$, see also Fig. 7.4c and Fig. 7.5c. The values of $J^{ep}_{PZ,min}$ are very close to zero for ssy-conditions (Table 7.1), whereas they reach several tenths of kJ/m^2 for lsy-conditions (Table 7.2), probably caused by irreversible elastic strain energy stored around the crack tip (Atkins and Mai 1986). The $J^{ep}_{actPZ,min}$-values are, in general, negative.

The incremental plasticity far-field *J*-integral J^{ep}_{far} equals J^{ep}_{PZ} for ssy-conditions. Due to the appearance of back-face plasticity, J^{ep}_{far} is lower than J^{ep}_{PZ} for lsy- and gy-conditions. With increasing crack length the difference between $J^{ep}_{far,max}$ and $J^{ep}_{PZ,max}$ increases from 0.5% up to 33%, due to the increase of the back-face plasticity region.

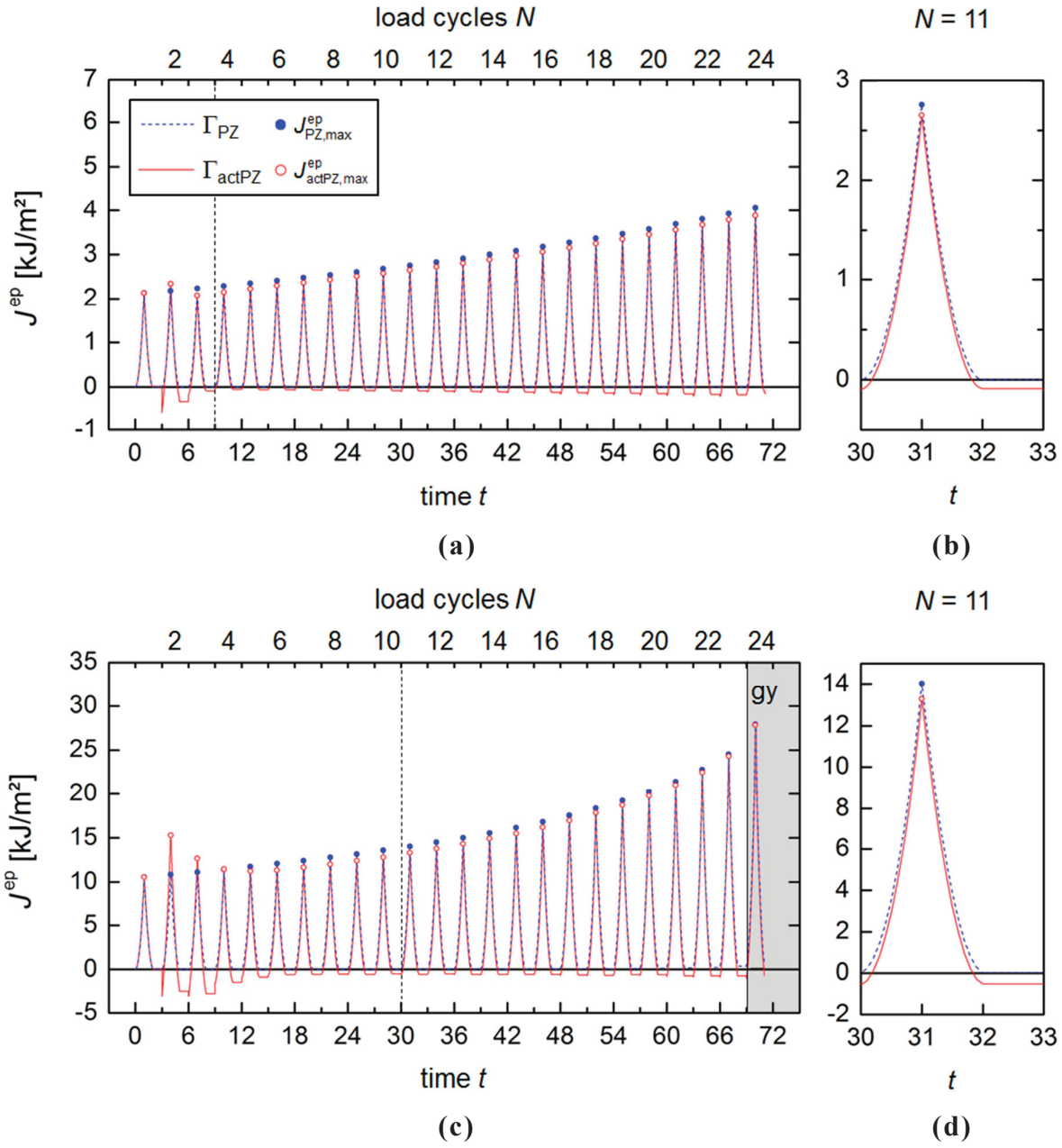

Fig. 7.5 Incremental plasticity *J*-integrals around the crack tip plastic zone, J^{ep}_{PZ}, and around the active plastic zone, J^{ep}_{actPZ}, versus time t for **(a)** small-scale yielding; **(c)** large-scale yielding, turning to general yielding after t = 69, $\Delta a = 4.6\,\text{mm}$. **(b)** and **(d)** show a detail of the 11th load cycle. The values reached at maximum load, $J^{ep}_{PZ,max}$ and $J^{ep}_{actPZ,max}$, are marked with full and open dots, respectively. The vertical dashed lines indicate when the active plastic zones leave the initial crack tip plastic zones.

Table 7.1 Values of the incremental plasticity *J*-integrals around the crack tip plastic zone, $J^{\mathrm{ep}}_{\mathrm{PZ}}$, and around the active plastic zone, $J^{\mathrm{ep}}_{\mathrm{actPZ}}$, for small-scale yielding conditions.

R	N	Δa	$J^{\mathrm{ep}}_{\mathrm{PZ,max}}$	$J^{\mathrm{ep}}_{\mathrm{PZ,min}}$	$J^{\mathrm{ep}}_{\mathrm{actPZ,max}}$	$J^{\mathrm{ep}}_{\mathrm{actPZ,min}}$	$\Delta^{J_{\mathrm{actPZ,max}}}_{J_{\mathrm{PZ,max}}}$	$\Delta J^{\mathrm{ep}}_{\mathrm{PZ}}$	$\Delta J^{\mathrm{ep}}_{\mathrm{actPZ}}$	ΔJ^{exp}	$\Delta^{\Delta J_{\mathrm{actPZ}}}_{\Delta J_{\mathrm{PZ}}}$
-	-	[mm]	[kJ/m²]				[%]	[kJ/m²]			[%]
0	1	0	2.132	0.000	2.132	0.000	0.00	-	-	2.082	-
0	2	0.2	2.184	8.0e–5	2.341	–0.621	6.71	2.157	2.341	2.121	7.86
0	6	1	2.415	2.0e–4	2.280	–0.062	–5.92	2.372	2.280	2.358	–4.04
0	11	2	2.759	2.8e–4	2.653	–0.087	–4.00	2.703	2.653	2.705	–1.88
0	16	3	3.177	3.8e–4	3.059	–0.119	–3.86	3.108	3.059	3.119	–1.60
0	21	4	3.691	5.6e–4	3.558	–0.134	–3.74	3.600	3.558	3.621	–1.18
0	24	4.6	4.056	7.1e–4	3.882	–0.156	–4.48	3.949	3.882	3.973	–1.73
0.5	1	0	2.132	0.000	2.132	0.540	0.00	-	-	2.082	-
0.5	2	0.2	2.183	0.540	2.264	0.444	3.58	0.552	0.703	0.549	21.5
0.5	6	1	2.414	0.612	2.279	0.576	–5.92	0.595	0.564	0.595	–5.50
0.5	11	2	2.755	0.700	2.633	0.604	–4.63	0.678	0.715	0.683	5.17
0.5	16	3	3.170	0.809	2.948	0.609	–7.53	0.776	0.877	0.790	11.5
0.5	21	4	3.682	0.943	3.417	0.698	–7.76	0.898	1.026	0.918	12.5
0.5	24	4.6	4.046	1.039	3.748	0.762	–7.95	0.984	1.130	1.009	12.9
–1	1	0	2.132	0.000	2.132	5.7e–6	0.00	-	-	2.082	-
–1	2	0.2	2.184	5.7e–6	2.352	–0.625	7.23	2.177	2.352	2.129	7.44
–1	6	1	2.415	1.6e–4	2.300	–0.066	–5.00	2.376	2.300	2.359	–3.30
–1	11	2	2.760	2.0e–4	2.654	–0.090	–3.99	2.713	2.654	2.705	–2.22
–1	16	3	3.178	2.8e–4	3.061	–0.120	–3.82	3.119	3.061	3.119	–1.89
–1	21	4	3.692	4.4e–4	3.560	–0.122	–3.71	3.612	3.560	3.621	–1.46
–1	24	4.6	4.058	5.6e–4	3.883	–0.156	–4.51	3.962	3.883	3.974	–2.03

The parameter R denotes the load ratio, N the load cycle number, and Δa the crack extension. The indices "max" and "min" denote maximum and minimum values during a load cycle. The values of the experimental cyclic *J*-integral ΔJ^{exp} are shown for comparison. Columns with Δ^{i}_{j} denote the relative difference between two values i, j.

In all cases the *J*-integrals for deformation plasticity J^{conv} equals the computational *J*-integral of ABAQUS, J^{VCE}. It is clear from Eq. (7.7) that $J^{\mathrm{conv}}_{\mathrm{PZ}} = J^{\mathrm{ep}}_{\mathrm{PZ}}$, unless gy-conditions appear. At the maximum load of every load cycle the deformation plasticity far-field *J*-integral comes close to the value around the plastic zone, $J^{\mathrm{conv}}_{\mathrm{far,max}} \approx J^{\mathrm{conv}}_{\mathrm{PZ,max}} = J^{\mathrm{ep}}_{\mathrm{PZ,max}}$, whereas at the minimum load of each load cycle, $J^{\mathrm{conv}}_{\mathrm{far,min}}$ strongly differs from the values of $J^{\mathrm{conv}}_{\mathrm{PZ,min}} = J^{\mathrm{ep}}_{\mathrm{PZ,min}}$. The reason has been already explained in detail in Ochensberger and Kolednik (2014), Section 4.2 therein: Artificial bulk configurational forces are induced in the back-face plasticity region since the conditions of proportional loading are violated during unloading. The deformation plasticity *J*-integral around the active plastic zone $J^{\mathrm{conv}}_{\mathrm{actPZ}}$ shows an oscillating curve that continuously decreases with every load cycle, so that after a certain number of load cycles the values are negative even at maximum load.

Tables 7.1 and 7.2 collect also additional results of $J^{\mathrm{ep}}_{\mathrm{actPZ}}$ and $J^{\mathrm{ep}}_{\mathrm{PZ}}$ for load ratios $R = 0.5$ and –1 under ssy- and lsy-conditions. Especially for $R = 0.5$ and lsy-conditions, the difference between the values at maximum load, $J^{\mathrm{ep}}_{\mathrm{actPZ,max}}$ and $J^{\mathrm{ep}}_{\mathrm{PZ,max}}$, can be significant.

Table 7.2 Values of the incremental plasticity *J*-integrals around the crack tip plastic zone, J^{ep}_{PZ}, and around the active plastic zone, J^{ep}_{actPZ}, for large-scale yielding conditions.

R	N	Δa	$J^{ep}_{PZ,max}$	$J^{ep}_{PZ,min}$	$J^{ep}_{actPZ,max}$	$J^{ep}_{actPZ,min}$	$\Delta^{J_{actPZ,max}}_{J_{PZ,max}}$	ΔJ^{ep}_{PZ}	ΔJ^{ep}_{actPZ}	ΔJ^{exp}	$\Delta^{\Delta J_{actPZ}}_{\Delta J_{PZ}}$
-	-	[mm]	[kJ/m²]				[%]	[kJ/m²]			[%]
0	1	0	10.56	0.000	10.56	0.008	0.00	-	-	10.42	-
0	2	0.2	10.83	0.008	15.27	–3.133	29.1	10.23	15.27	10.17	33.0
0	6	1	12.06	0.011	11.33	–0.575	–6.44	11.34	11.33	11.32	–0.09
0	11	2	14.02	0.019	13.30	–0.524	–5.41	13.01	13.30	13.06	2.18
0	16	3	16.81	0.045	16.19	–0.529	–3.83	15.12	16.19	15.24	6.61
0	21	4	21.40	0.143	21.25	–0.690	–0.71	18.04	21.25	18.12	15.1
0	24	4.6	27.95	0.367	27.86	–1.015	–0.32	21.91	27.86	22.51	21.4
0.5	1	0	10.56	0.000	10.56	2.832	0.00	-	-	10.42	-
0.5	2	0.2	10.81	2.832	14.85	3.520	27.2	2.578	3.910	2.568	34.1
0.5	6	1	12.00	3.135	10.72	1.743	–11.9	2.868	3.818	2.867	24.9
0.5	11	2	13.93	3.670	12.20	2.364	–14.2	3.300	3.823	3.321	13.7
0.5	16	3	16.69	4.511	15.05	3.111	–10.9	3.847	4.476	3.889	14.0
0.5	21	4	21.24	6.039	19.70	4.511	–7.82	4.628	5.357	4.695	13.6
0.5	24	4.6	27.87	7.923	26.83	6.075	–3.88	6.073	7.371	6.419	17.6
–1	1	0	10.56	0.000	10.56	5.2e–4	0.00	-	-	10.42	-
–1	2	0.2	10.84	5.2e–4	15.30	–3.608	29.1	10.69	15.30	10.57	30.1
–1	6	1	12.08	0.002	11.60	–0.484	–4.14	11.92	11.60	12.04	–2.76
–1	11	2	14.06	0.003	13.79	–0.454	–1.96	13.73	13.79	13.80	0.44
–1	16	3	16.90	0.004	17.04	–0.702	–0.82	16.45	17.04	16.63	3.46
–1	21	4	21.57	0.006	22.19	–1.166	–2.79	20.99	22.19	21.04	5.41
–1	24	4.6	27.96	0.020	29.22	–1.680	–4.31	26.48	29.22	26.13	9.38

The parameter R denotes the load ratio, N the load cycle number, and Δa the crack extension. The indices "max" and "min" denote maximum and minimum values during a load cycle. The values of the experimental cyclic *J*-integral ΔJ^{exp} are shown for comparison. General yielding conditions prevail for the rows marked in *grey*.

7.4.2 Bulk configurational forces in the crack tip plastic zone

In order to explore the differences that appear in Fig. 7.5 between J^{ep}_{actPZ} and J^{ep}_{PZ}, we analyze in this section the distribution of the bulk configurational force $\mathbf{f}^{ep}$ in the crack tip plastic zone. For easier understanding, it is useful to transform Eq. (7.6) into small strain plasticity (Simha et al. 2008),

$$\mathbf{f}^{ep} = \boldsymbol{\sigma} : \frac{\partial \boldsymbol{\varepsilon}^{p}}{\partial \mathbf{x}}, \tag{7.13}$$

where $\boldsymbol{\sigma}$ denotes the Cauchy stress tensor and $\boldsymbol{\varepsilon}^{p}$ the plastic part of the linear strain tensor $\boldsymbol{\varepsilon}$. Note that for crack and crack growth in *x*-direction, only the *x*-component of the configurational force $\mathbf{f}^{ep}$-vector,

$$f_x^{ep} = \sigma_{xx}\frac{\partial \varepsilon^{p}_{xx}}{\partial x} + 2\sigma_{xy}\frac{\partial \varepsilon^{p}_{xy}}{\partial x} + \sigma_{yy}\frac{\partial \varepsilon^{p}_{yy}}{\partial x}, \tag{7.14}$$

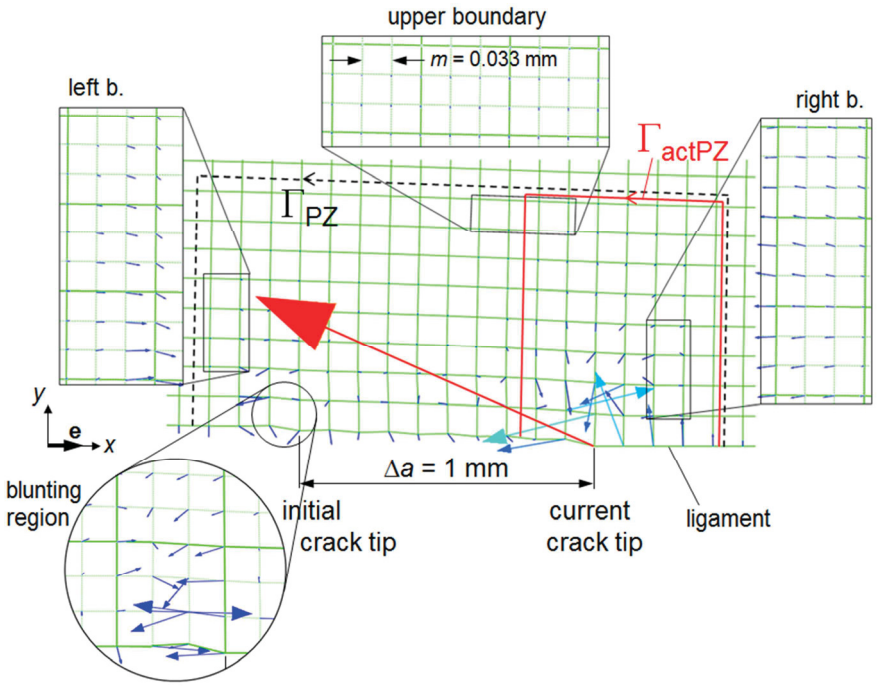

Fig. 7.6 Distribution of incremental plasticity bulk configurational force $\mathbf{f}^{\mathrm{ep}}$ in the entire crack tip plastic zone at a maximum load, $F_{\max} = 12.5\,\mathrm{kN}$, after a crack extension of $\Delta a = 1\,\mathrm{mm}$, compare Fig. 7.4a. Regions on the boundaries of the plastic zone and the bunting region of the initial crack tip are enlarged in detailed views; a finer mesh size of m = 0.033 mm is used for a better visualization of the $\mathbf{f}^{\mathrm{ep}}$-vectors.

contributes to the scalar J^{ep}-integral, see Eq. (7.5).

Figure 7.6 presents, for a load ratio R = 0, the distribution of the bulk configurational force $\mathbf{f}^{\mathrm{ep}}$ in the total crack tip plastic zone at maximum load $F_{\max} = 12.5\,\mathrm{kN}$ during the 6$^{\mathrm{th}}$ load cycle, after 1 mm of crack growth. Important regions are enlarged in the detailed views where a finer mesh of m = 0.033 mm is used to obtain a better visualization of the $\mathbf{f}^{\mathrm{ep}}$-vectors.[12]

On the left boundary of the crack tip plastic zone, $\mathbf{f}^{\mathrm{ep}}$-vectors appear with a positive f_x^{ep}-component, while f_x^{ep} is negative for $\mathbf{f}^{\mathrm{ep}}$-vectors on the right boundary. Along the upper boundary, $\mathbf{f}^{\mathrm{ep}}$-vectors emerge with x-components of almost zero; they only have a negative y-component f_y^{ep}. It is seen that in all cases the direction of $\mathbf{f}^{\mathrm{ep}}$-vectors clearly follows the gradient of the plastic strain, corresponding to Eq. (7.13); Fig. 7.4a includes schematically the directions of these $\mathbf{f}^{\mathrm{ep}}$-vectors. In the blunting region of the initial crack tip, the $\mathbf{f}^{\mathrm{ep}}$-vectors point to either direction, but the resulting configurational force, i.e. the sum of the x-components of all $\mathbf{f}^{\mathrm{ep}}$-vectors lying within this region, points into the negative x-direction.

The largest $\mathbf{f}^{\mathrm{ep}}$-vectors appear around the current crack tip, since there both stress and gradient of plastic strain are largest, Eq. (7.13). Due to symmetry, each $\mathbf{f}^{\mathrm{ep}}$-vector that emerges from a node directly along the ligament in front of the current crack tip does have a "companion" $\mathbf{f}^{\mathrm{ep}}$-vector from the lower specimen half. The resulting $\mathbf{f}^{\mathrm{ep}}$-vector of both

[12] For generating Fig. 7.6, the simulation was repeated with a FE-mesh size of m = 0.033 mm.

specimen halves has only a component in *x*-direction. This applies also for $\mathbf{f}_{\mathrm{tip}}^{\mathrm{ep}}$ which emerges from the current crack tip. For numerical reasons, $J_{\mathrm{tip}}^{\mathrm{ep}} = \mathbf{e} \cdot \left(-\mathbf{f}_{\mathrm{tip}}^{\mathrm{ep}}\right)$ has a finite value which depends on the FE-mesh size, see Kolednik et al. (2014). A decrease of the mesh size leads to a reduction of the magnitude of $J_{\mathrm{tip}}^{\mathrm{ep}}$ and yields finally $J_{\mathrm{tip}}^{\mathrm{ep}} = 0$. However, the values of $J_{\mathrm{actPZ}}^{\mathrm{ep}}$ (and $J_{\mathrm{PZ}}^{\mathrm{ep}}$) are not affected by a mesh refinement; Section 7.5.1 provides an example.

The variation of the difference between $J_{\mathrm{actPZ,max}}^{\mathrm{ep}}$ and $J_{\mathrm{PZ,max}}^{\mathrm{ep}}$ shown in Fig. 7.5a can be understood from Fig. 7.6 and Eq. (7.12): More and more bulk configurational forces $\mathbf{f}^{\mathrm{ep}}$ of the initial plastic zone become excluded from the integration contour Γ_{actPZ}, when it is shifted to the right during crack extension. First, the $\mathbf{f}^{\mathrm{ep}}$-vectors with positive f_x^{ep}-components from the left boundary are excluded, leading to the peak value of $J_{\mathrm{actPZ,max}}^{\mathrm{ep}}$ observed at $N = 2$. Next, the integration contour Γ_{actPZ} excludes the blunting region of the initial crack tip. Since the resulting $\mathbf{f}^{\mathrm{ep}}$ in this blunting region has a negative *x*-component, the value of $J_{\mathrm{actPZ,max}}^{\mathrm{ep}}$ drops below the value of $J_{\mathrm{PZ,max}}^{\mathrm{ep}}$. With further crack extension the difference between $J_{\mathrm{actPZ,max}}^{\mathrm{ep}}$ and $J_{\mathrm{PZ,max}}^{\mathrm{ep}}$ remains equal, since the excluded $\mathbf{f}^{\mathrm{ep}}$-vectors of the plastic wake have no *x*-component. It should be mentioned that a similar variation of $J_{\mathrm{actPZ}}^{\mathrm{ep}}$ is reported in Section 5.3 of Kolednik et al (2014) for a growing crack under constant load.

For lsy-conditions, the difference between the values of $J_{\mathrm{actPZ,max}}^{\mathrm{ep}}$ and $J_{\mathrm{PZ,max}}^{\mathrm{ep}}$ decreases with increasing crack extension, because the right boundary of the active plastic zone, with $\mathbf{f}^{\mathrm{ep}}$-vectors in negative *x*-direction, increases. Finally, the difference nearly vanishes under gy-conditions.

The differences between $J_{\mathrm{actPZ,min}}^{\mathrm{ep}}$ and $J_{\mathrm{PZ,min}}^{\mathrm{ep}}$ at minimum load F_{min} can be explained analogously. Note that, due to the appearance of compressive stresses during unloading, the $\mathbf{f}^{\mathrm{ep}}$-vectors at F_{min} point into the opposite *x*-direction compared to the F_{max}-stage. This has been explained already in Ochensberger and Kolednik (2014), see also Section 7.2.3. It can be shown that negative $J_{\mathrm{actPZ,min}}^{\mathrm{ep}}$-values originate for $R \leq 0$ from these negative stresses; the relevance of these negative $J_{\mathrm{actPZ,min}}^{\mathrm{ep}}$-values will be discussed in the next section.

7.5 Driving force for fatigue crack growth

For a cyclically loaded, *stationary* crack, Ochensberger and Kolednik (2014) proposed the cyclic, incremental plasticity *J*-integral around the crack tip plastic zone, $\Delta J_{\mathrm{PZ}}^{\mathrm{ep}}$, as physically appropriate driving force parameter. Consequently, for a *growing* fatigue crack it is reasonable to adopt the cyclic, incremental plasticity *J*-integral around the *active* crack tip plastic zone, $\Delta J_{\mathrm{actPZ}}^{\mathrm{ep}}$, as the appropriate driving force parameter for fatigue crack growth. One argument is that only the active plastic zone travels with the crack tip during crack extension; the initial plastic zone and the plastic wake do not move. Another reason is that plasticity far from the current crack tip cannot be responsible for fatigue crack propagation that occurs due to cyclic plastic deformation at the current tip.

It seems obvious that $\Delta J_{\mathrm{actPZ}}^{\mathrm{ep}}$ should be evaluated, analogously to Eq. (7.9), by the relation,

$$\Delta J_{\mathrm{actPZ}}^{\mathrm{ep}} = J_{\mathrm{actPZ,max}}^{\mathrm{ep}} + J_{\mathrm{actPZ,min}}^{\mathrm{ep}} - 2\sqrt{J_{\mathrm{actPZ,max}}^{\mathrm{ep}} J_{\mathrm{actPZ,min}}^{\mathrm{ep}}} \,. \tag{7.15}$$

At this point we arrive at a dilemma when the incremental plasticity *J*-integral at minimum load, $J^{\mathrm{ep}}_{\mathrm{actPZ,min}}$, is negative, as shown in Tables 7.1 and 7.2 for load ratios $R = 0$ and $R = -1$, since this leads to a complex square root term. Therefore, it should be clarified in which form the negative values of $J^{\mathrm{ep}}_{\mathrm{actPZ}}$ in a load cycle deliver a contribution to the driving force for fatigue crack growth. We do this by studying the relation between the incremental plasticity *J*-integral J^{ep} and the crack tip opening displacement δ_{t}.

7.5.1 Incremental plasticity J-integral J^{ep} and crack tip opening displacement

Fatigue crack growth in ductile metals and alloys is driven by cyclic plasticity at the current crack tip (Laird 1967, 1979). The crucial role of crack tip plasticity was confirmed by experiments, e.g. Tanaka (1989), Krupp et al. (2001), and Pippan et al. (2010), where it was shown that the crack growth rate of a fatigue crack $\mathrm{d}a/\mathrm{d}N$ is a function of the cyclic crack tip opening displacement at the current crack tip, $\mathrm{d}a/\mathrm{d}N \propto \Delta\delta_{\mathrm{t}}$ with $\Delta\delta_{\mathrm{t}} = \delta_{\mathrm{t,max}} - \delta_{\mathrm{t,min}}$.

A correct numerical evaluation of the crack tip opening displacement δ_{t} during fatigue crack propagation is difficult, since it requires a very fine FE-mesh. Experimental investigations using stereophotogrammetric measurements show that the crack tip opening displacement should be determined a distance behind the blunted crack tip, which corresponds to the width of the stretched zone (Kolednik and Stüwe 1985; Kolednik and Kutlesa 1989, Siegmund et al. 1990); a good approximation of this distance is for many materials given by $0.4\,\delta_{\mathrm{t}}$, see Kolednik and Stüwe (1987), Heerens et al. (1988). Therefore, δ_{t} should not be determined at a fixed distance behind the crack tip, since measurements at too large distances lead to an overestimate of δ_{t}, and vice versa. However, it is difficult to fulfill these requirements in practice. Dougherty et al. (1997) give a minimum element size *m* in order to determine accurate δ_{t}-values, $m/r_{\mathrm{pl}} \le 0.1$, where r_{pl} denotes the radius of the crack tip plastic zone. According to Solanki et al. (2003, 2004) the mesh size shall be further reduced by a factor $3 \div 4$. The relation $r_{\mathrm{pl}} = \beta JE/\sigma_{\mathrm{y}}^2$, with $\beta \approx 0.1$, yields for the maximum load of the 1st load cycle $r_{\mathrm{pl}} \approx 0.59$ mm and $r_{\mathrm{pl}} \approx 2.90$ mm for ssy- and lsy-conditions, respectively; this is roughly in agreement with Fig. 7.4a and Fig. 7.4b. The relation $J = k\,\sigma_{\mathrm{y}}\delta_{\mathrm{t}}$, with $J = J^{\mathrm{ep}}_{\mathrm{PZ}}$ and $k \approx 2$, yields values of the crack tip opening displacement, $\delta_{\mathrm{t}} \approx 3.95\,\mu\mathrm{m}$ and $\delta_{\mathrm{t}} \approx 19.6\,\mu\mathrm{m}$, for ssy- and lsy-conditions, respectively. According to the criterion by Solanki et al. (1997), a mesh size of approximately $m \approx 4\,\delta_{\mathrm{t}}$ would be sufficient for gaining accurate δ_{t}-values, which appears somewhat doubtful to us.

However, the computation of accurate δ_{t}-values is not very important for our purposes; our interest lies only in the correct reflection of crack tip opening and -closure behavior during the loading and unloading stages. Therefore, a mesh size of m = 0.1 mm should be sufficient for lsy-conditions; additional computations with smaller mesh size, $m = 10\,\mu\mathrm{m}$, are conducted for ssy-conditions. The crack tip opening displacement is taken one element behind the current crack tip, as e.g. in Solanki et al. (2004).

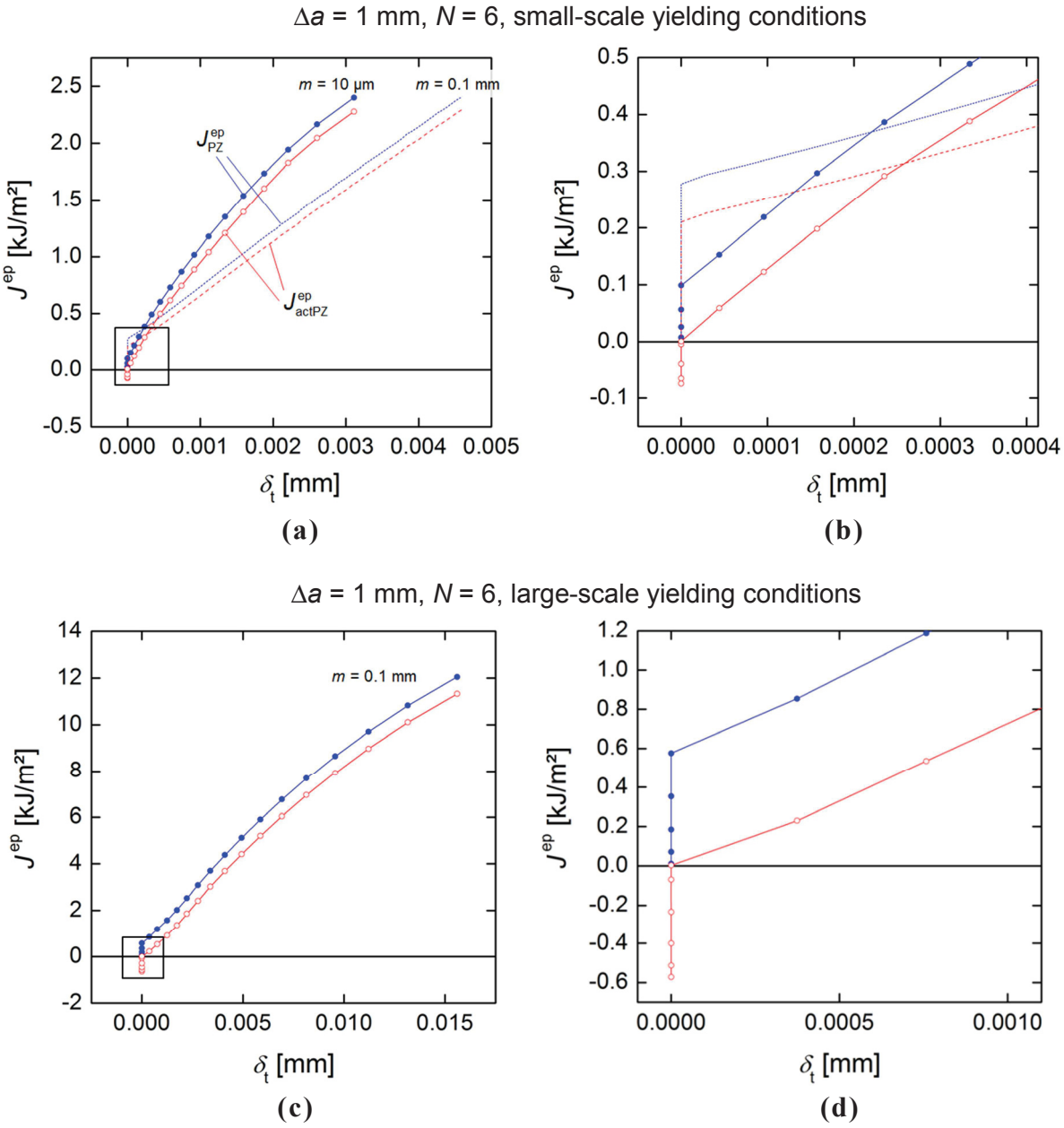

Fig. 7.7 Incremental plasticity *J*-integrals, J^{ep}_{actPZ} and J^{ep}_{PZ}, plotted against the crack tip opening displacement δ_t during re-loading after $\Delta a = 1\text{mm}$ crack extension. Values are depicted for **(a)** small-scale yielding, mesh sizes m = 0.1 mm and 10 μm; **(c)** large-scale yielding, m = 0.1 mm. **(b)** and **(d)** show enlarged views of the beginnings of the loading sequences. The results suggest that loading stages where J^{ep}_{actPZ} is negative do not contribute to fatigue crack propagation, since δ_t is zero.

Figure 7.7 shows the curves J^{ep}_{actPZ} versus δ_t during loading from F_{min} to F_{max} during the 6th load cycle, i.e. after a crack extension of $\Delta a = 1\text{mm}$. The values for J^{ep}_{PZ} are included for comparison. The curves for ssy-conditions are plotted in Fig. 7.7a; Fig. 7.7b gives a detailed view of the region near the minimum load. Figure 7.7c, d present the curves for lsy-

conditions. It is seen that $\delta_t = 0$ during the very initial loading stages. The curves suggest that the crack tip opening displacement δ_t does not start to increase before J^{ep}_{actPZ} becomes positive.

Thus, we state that negative values of J^{ep}_{actPZ} do not deliver a contribution to the fatigue crack growth rate, since the crack tip is closed during this stage. Moreover, from a thermodynamic view, a negative *x*-component of the $\mathbf{J}^{ep}_{actPZ}$-vector means that the crack feels a driving force for shortening its length. Therefore, the stage where the crack driving force is negative cannot deliver a contribution to the driving force for fatigue crack growth. For these reasons, we conclude that the negative values of J^{ep}_{actPZ} are not relevant for calculating the driving force for fatigue crack growth, and $\Delta J^{ep}_{actPZ} = J^{ep}_{actPZ,max}$ for $R = 0$.

It should be mentioned that the values of $J^{ep}_{actPZ,max}$ (and $J^{ep}_{PZ,max}$) are not affected by the decrease in mesh size *m* by a factor ten for ssy-conditions. For example, at maximum load we get $J^{ep}_{actPZ,max} = 2.279\ \text{kJ/m}^2$ for $m = 10\ \mu\text{m}$ and $J^{ep}_{actPZ,max} = 2.280\ \text{kJ/m}^2$ for $m = 0.1\ \text{mm}$. On the contrary, the values of the crack tip opening displacement show a big variation: at maximum load we get $\delta_t = 3.11\ \mu\text{m}$ for $m = 10\ \mu\text{m}$ and $\delta_t = 4.65\ \mu\text{m}$ for $m = 0.1\ \text{mm}$. This clearly demonstrates the advantage of the *J*-integral concept.

For negative load ratios $R < 0$ it can be also shown that negative $J^{ep}_{actPZ,min}$-values do not give a contribution to the cyclic *J*-integral ΔJ^{ep}_{actPZ}. Therefore, the driving force for fatigue crack growth is equal to the incremental plasticity *J*-integral around the active plastic zone at maximum load for zero-tension and tension-compression loading,

$$\Delta J^{ep}_{actPZ} = J^{ep}_{actPZ,max} \qquad \text{for} \qquad R \le 0\,. \tag{7.16}$$

Note that the exact upper boundary for the validity of Eq. (7.16) has not been determined. For positive load ratios $R > 0$, the curves J^{ep}_{actPZ} and J^{ep}_{PZ} versus δ_t are almost linear and do not have a vertical part near F_{min}. Since both the $J^{ep}_{actPZ,min}$- and $\delta_{t,min}$-values are positive at minimum load, Eq. (7.15) must be used to evaluate ΔJ^{ep}_{actPZ}.

Table 7.1 lists ΔJ^{ep}_{actPZ}-values with increasing load cycle number *N* and crack extension Δa for load ratios, $R = 0$, 0.5 and –1, under ssy-conditions. The results for ΔJ^{ep}_{PZ}, Eq. (7.9), are collected for comparison. The difference between ΔJ^{ep}_{actPZ} and ΔJ^{ep}_{PZ} is of the order of 2% for $R \le 0$; on the contrary, ΔJ^{ep}_{actPZ} can even exceed ΔJ^{ep}_{PZ} by 13% for $R = 0.5$. Table 7.2 lists corresponding values for lsy-conditions. Here, the difference between ΔJ^{ep}_{actPZ} and ΔJ^{ep}_{PZ} can become large for all load ratios. For $R = 0.5$, the values of $J^{ep}_{actPZ,min}$ are distinctively smaller than the $J^{ep}_{PZ,min}$-values which cause lower square root terms in Eq. (7.15) and, thus, significantly higher values of ΔJ^{ep}_{actPZ} compared to ΔJ^{ep}_{PZ}. Figure 7.8 presents, for a load ratio $R = 0$, the variations of ΔJ^{ep}_{actPZ} and ΔJ^{ep}_{PZ} with increasing crack extension. The variations of the cyclic crack tip opening displacement, $\Delta\delta_t = \delta_{t,max} - \delta_{t,min}$, with crack extension are shown for comparison.

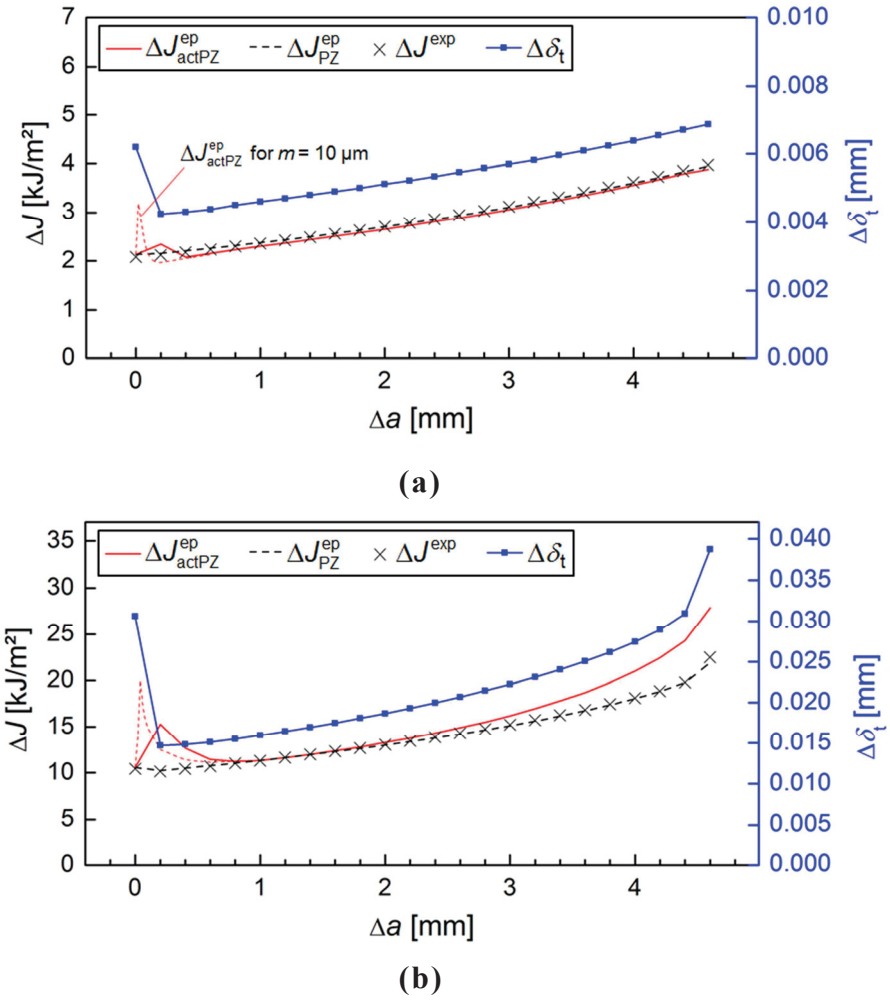

Fig. 7.8 Development of the cyclic, incremental plasticity cyclic *J*-integrals around the crack tip plastic zone, ΔJ^{ep}_{PZ}, and around the active plastic zone, ΔJ^{ep}_{actPZ}, with crack extension Δa. Values of the cyclic crack tip opening displacement $\Delta\delta_t$ and the experimental cyclic *J*-integral ΔJ^{exp} are drawn for comparison. **(a)** Small-scale yielding, **(b)** large-scale yielding conditions. The computations are made for a FE-mesh size of m = 0.1 mm; the first crack growth periods are re-calculated for a finer mesh size, m = 10 µm, see dotted curves.

The conclusion of this section is that the loading stages where $J^{ep}_{actPZ,min}$ becomes negative do not play a role for the calculation of the driving force for fatigue crack propagation. In the following section, the validity of the experimental cyclic *J*-integral ΔJ^{exp} proposed by Dowling and Begley (1976) shall be checked.

7.5.2 Comparison to the experimental cyclic J-integral ΔJ^{exp}

The experimental cyclic *J*-integral ΔJ^{exp} (Dowling and Begley, 1976) is computed from the area ΔA below a single loading branch of the load–displacement (*F*–*v*) curve, Eq. (7.8). The ΔJ^{exp}-values for $R = 0$ are drawn into Fig. 7.8 and listed in Tables 7.1 and 7.2. It is seen that ΔJ^{exp} fits very well to the values of the cyclic, incremental plasticity *J*-integral $\Delta J^{\mathrm{ep}}_{\mathrm{PZ}}$. This corresponds to the findings reported in Sections 7.2.2 and 7.2.3, and to Eq. (7.10). The experimental cyclic *J*-integral ΔJ^{exp} does not fit so well to $\Delta J^{\mathrm{ep}}_{\mathrm{actPZ}}$, although the error remains small for ssy-conditions. However, the error can reach 20% for lsy-conditions. The values listed for $\Delta^{\Delta J_{\mathrm{actPZ}}}_{\Delta J_{\mathrm{PZ}}}$ in Tables 7.1 and 7.2 are approximately equal to the relative difference between $\Delta J^{\mathrm{ep}}_{\mathrm{actPZ}}$ and ΔJ^{exp}. Note that a small error of about 2% has to be taken into account in the evaluation of ΔJ^{exp}, which seems to result from an inaccuracy of the geometry factor η taken from ASTM E1820 (2005), compare the values listed for $N = 1$ in Tables 7.1 and 7.2.

Tables 7.1 and 7.2 collect also the ΔJ^{exp}-values for load ratios $R = 0.5$ and -1. For load ratios $R < 0$, in presence of crack closure, the values of ΔJ^{exp} depend on the correct determination of ΔA. According to Dowling and Begley (1976), the opening load F_{op} shall be determined from the compliance change that is visible as kink in the *F*–*v*-curve, Fig. 7.2b. Ochensberger and Kolednik (2014) showed for stationary cracks that this procedure tends to overestimate the driving force. Instead, ΔA should be determined as the area above the load $F_{J^{\mathrm{ep}}_{\mathrm{PZ}}=0}$, where the incremental plasticity *J*-integral around the crack tip plastic zone reaches its minimum value, $J^{\mathrm{ep}}_{\mathrm{PZ,min}} = 0$. The same procedure is used for the evaluation of the ΔJ^{exp}-values listed in Tables 7.1 and 7.2 for $R = -1$. The results show that ΔJ^{exp} fits very well to $\Delta J^{\mathrm{ep}}_{\mathrm{PZ}}$, and Eq. (7.10) remains valid, unless gy-conditions prevail.

Crack closure does not occur for $R > 0$. It is seen that the misfit between ΔJ^{exp} and $\Delta J^{\mathrm{ep}}_{\mathrm{PZ}}$ is small for various load ratios under ssy- and lsy-conditions, see Tables 7.1 and 7.2. In both cases the misfit slightly increases with increasing crack extension.

The validity of Eq. (7.10) becomes clear from the following: the condition $J^{\mathrm{ep}}_{\mathrm{PZ}} = J^{\mathrm{conv}}_{\mathrm{PZ}}$, Eq. (7.7), is fulfilled for cyclic loading conditions as long as the crack tip plastic zone is surrounded by elastically deformed material, see Sections 7.2.2 and 7.2.3. The requirement for the validity of the condition $J^{\mathrm{conv}}_{\mathrm{PZ}} = J^{\mathrm{exp}}$ is that a single loading cycle of a growing fatigue crack can be treated like a stationary crack under monotonic loading; only then, the conventional *J*-integral and the experimental *J*-integral J^{exp} lead to the same results, see Rice et al. (1973), Kolednik (1991). This requirement is fulfilled during loading in each load cycle.

Table 7.1 shows that the experimental cyclic *J*-integral ΔJ^{exp} overestimates the driving force for fatigue crack growth $\Delta J^{\mathrm{ep}}_{\mathrm{actPZ}}$ by approximately 2% for ssy-conditions and $R = 0$ and $R = -1$. On the contrary, ΔJ^{exp} considerably underestimates $\Delta J^{\mathrm{ep}}_{\mathrm{actPZ}}$ for $R = 0.5$, whereby the misfit decreases up to 12% with increasing crack extension. For lsy-conditions, Table 7.2, ΔJ^{exp} underestimates $\Delta J^{\mathrm{ep}}_{\mathrm{actPZ}}$ for all load ratios. The misfit increases with crack extension to approximately 20% for $R = 0$ and to 5% for $R = -1$. For $R = 0.5$, the misfit of about 15% is rather independent of crack extension. The reason for the high misfit under $R = 0.5$, even for ssy-conditions, is currently not fully understood by the authors, but it might be caused by the

fact that proportional loading is fulfilled for each maximum load of a load cycle, which is required for the validity of $J_{\mathrm{PZ}}^{\mathrm{ep}} = J^{\mathrm{exp}}$, whereas this is not the case for the minimum load.

We can conclude this section by stating that the experimental cyclic *J*-integral does not exactly reflect the driving force for growing fatigue cracks in elastic–plastic materials, since it corresponds to the cyclic, incremental plasticity *J*-integral around the crack tip plastic zone, and not around the *active* plastic zone, $\Delta J^{\mathrm{exp}} \approx \Delta J_{\mathrm{PZ}}^{\mathrm{ep}} \neq \Delta J_{\mathrm{actPZ}}^{\mathrm{ep}}$. The difference between ΔJ^{exp} and $\Delta J_{\mathrm{actPZ}}^{\mathrm{ep}}$ can reach approximately 20% for lsy-conditions.

7.6 The effect of a single tensile overload

In this section, a further test shall be conducted in order to check whether the cyclic, incremental plasticity *J*-integral for a contour around the *active* plastic zone, $\Delta J_{\mathrm{actPZ}}^{\mathrm{ep}}$, is the appropriate parameter for the characterization of the driving force for fatigue crack propagation, and not the cyclic *J*-integral for a contour around the plastic zone, $\Delta J_{\mathrm{PZ}}^{\mathrm{ep}}$. It is investigated whether $\Delta J_{\mathrm{actPZ}}^{\mathrm{ep}}$ is able to reflect the well-known overload effect: Crack growth retardation occurs, after a single tensile overload has been superimposed to cyclic loading with constant load amplitude. With further crack extension the crack growth rate gradually increases, reaching again the crack growth rate pertaining to the constant fatigue load somewhat after the active plastic zone has escaped from the plastic zone produced by the overload (Schijve 1960, Christensen 1959, von Euw et al. 1972, Suresh 1983, Fleck 1988, Skorupa 1998).

The fatigue crack growth rate $\mathrm{d}a/\mathrm{d}N$ in ductile metals and alloys is proportional to the cyclic crack tip opening displacement $\Delta\delta_{\mathrm{t}}$; this is so also after applying an overload. This fact was confirmed by experiments, e.g. Pippan et al. (2005) and Bichler and Pippan (1999, 2007), and by numerical studies, e.g. Tvergaard (2005). For example, Bichler and Pippan (2007) conducted ΔK-controlled fatigue tests under ssy-conditions with load ratio R = 0.05, using C(T)-specimens fabricated of ductile austenitic CrNi steel. The constant ΔK-fatigue history, with ΔK = 70 MPa$\sqrt{\mathrm{m}}$, was interrupted by a single tensile overload with various overload ratios, $R_{\mathrm{OL}} = F_{\mathrm{OL}}/F_{\mathrm{max}} = 1.1 \div 2$. By analyzing fatigue striations (Zappfe and Worden 1951), which usually correlate with $\mathrm{d}a/\mathrm{d}N$ (Forsyth and Ryder 1960), and by conducting stereophotogrammetric measurements (Kolednik 1981) of the crack tip opening displacement δ_{t}, Pippan and Bichler (2007) demonstrated that the relation, $\mathrm{d}a/\mathrm{d}N \propto \Delta\delta_{\mathrm{t}}$, is valid also in the post-overload regime.

Our numerical test is conducted for zero-tension cyclic loading under ssy-conditions with applied maximum load, $F_{\mathrm{max}} = 12.5$ kN. A tensile overload, F_{OL} = 25 kN, is applied in the fourth load cycle after Δa = 0.6 mm crack extension (Fig. 7.3b); the overload ratio is $R_{\mathrm{OL}} = F_{\mathrm{OL}}/F_{\mathrm{max}} = 2$. Note that ssy-conditions still prevail during application of the overload, i.e. no back-face plasticity occurs. For our purpose, a FE-mesh size of m = 0.1 mm was seen to be sufficient.

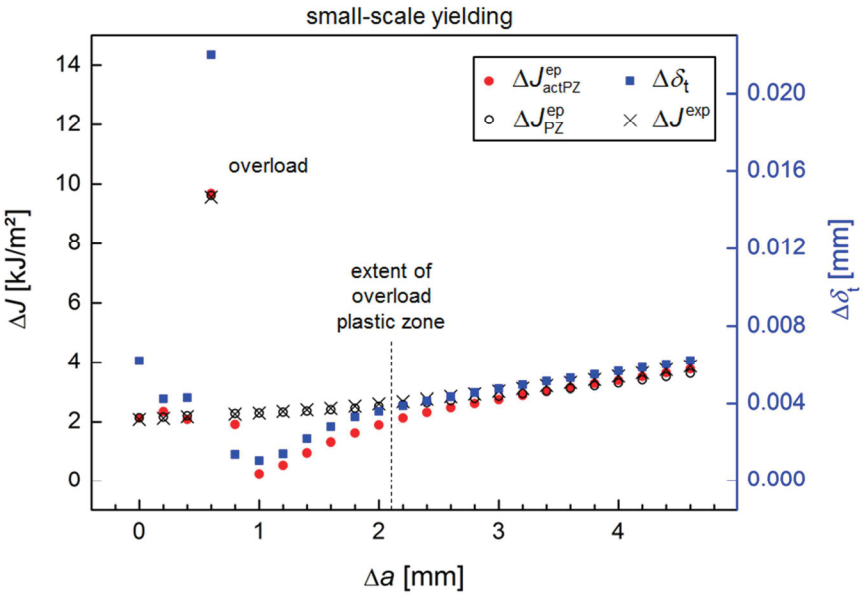

Fig. 7.9 Effect of a single tensile overload, applied during the 4th load cycle at $\Delta a = 0.6$ mm. The cyclic, incremental plasticity *J*-integrals around the crack tip plastic zone, ΔJ^{ep}_{PZ}, and around the active plastic zone, ΔJ^{ep}_{actPZ}, are plotted against crack extension Δa. Values of the cyclic crack tip opening displacement $\Delta\delta_t$ and the experimental cyclic *J*-integral ΔJ^{exp} are drawn for comparison. The parameter ΔJ^{ep}_{actPZ} correlates perfectly with $\Delta\delta_t$, exhibiting a crack growth retardation effect, whereas this is not the case for ΔJ^{ep}_{PZ} and ΔJ^{exp}.

Figure 7.9 presents the variations of ΔJ^{ep}_{actPZ}, ΔJ^{ep}_{PZ}, the cyclic experimental *J*-integral ΔJ^{exp}, and $\Delta\delta_t$ as functions of the crack extension Δa. It is seen that ΔJ^{ep}_{actPZ} varies analogously to $\Delta\delta_t$ and clearly shows the retardation effect, whereas this is not the case for ΔJ^{ep}_{PZ} and ΔJ^{exp}.

The minimum value of $\Delta J^{ep}_{actPZ} = 0.269$ kJ/m² is reached after 0.4 mm of crack growth following the overload cycle, i.e. $\Delta a = 1$ mm total crack extension. This gives a reduction of about 88% compared to the ΔJ^{ep}_{actPZ}-value at $\Delta a = 1$ mm for a constant fatigue load, see Fig. 7.8a and Table 7.1. This value is in excellent agreement with the experimental results obtained by Bichler and Pippan (2007) from 25 mm thick C(T)-specimens (plane strain dominance), subjected to $R_{OL} = 2$, where a maximal reduction in da/dN of about 84% was observed after approximately 0.5 mm crack growth following the overload.

The overload case study has confirmed that the cyclic, incremental plasticity *J*-integral for a contour around the active plastic zone, ΔJ^{ep}_{actPZ}, is a physically appropriate driving force parameter for assessing the fatigue crack growth rate.

7.7 Computational aspects in the evaluation of $\Delta J_{\mathrm{actPZ}}^{\mathrm{ep}}$

In the following, a few issues regarding the computation of $\Delta J_{\mathrm{actPZ}}^{\mathrm{ep}}$ shall be pointed out, which might be important for the practical application of the concept presented in the current paper.

The values of $J_{\mathrm{actPZ}}^{\mathrm{ep}}$ are not affected of the used FE-mesh size, especially, in comparison to the expensive numerical effort that is necessary to obtain accurate results for the crack tip opening displacement δ_{t}, see Fig. 7.7a.

Provided that the active plastic zone has left the plastic zone of the initial crack tip, the magnitude of $J_{\mathrm{actPZ}}^{\mathrm{ep}}$ is not significantly influenced by the magnitude of the integration contour Γ_{actPZ}. The reason is that the configurational forces in the plastic wake do not deliver a contribution to the value of $J_{\mathrm{actPZ}}^{\mathrm{ep}}$, see Section 7.4.2. Therefore, it is not important to find the exact shape of the active plastic zone (Fig. 7.4a).

However, one has to be careful during the initial stages of crack extension, especially, before the active plastic zone excludes the blunting region of the initial crack tip. In Section 7.4 we have shown that $J_{\mathrm{actPZ}}^{\mathrm{ep}}$ at maximum load exhibits a peak value after the onset of crack extension; compare the $J_{\mathrm{actPZ,max}}^{\mathrm{ep}}$-values listed for $N = 2$ in Tables 7.1 and 7.2. Note that both position and magnitude of this peak value depends on the FE-mesh size m: A smaller mesh size gives a higher peak at smaller crack growth distance. The effect is shown in Fig. 7.8, for a reduction of m by a factor ten and a crack extension increment per load cycle of $\Delta(\Delta a) = 2m$. In this way, the finer FE-mesh is connected to a smaller crack extension increment per load cycle. Nevertheless, graphs similar to Fig. 7.7 can be also drawn for the first load cycles, showing that the crack tip is closed during the stages where $J_{\mathrm{actPZ}}^{\mathrm{ep}}$ is negative and, thus, $\Delta J_{\mathrm{actPZ}}^{\mathrm{ep}} = J_{\mathrm{actPZ,max}}^{\mathrm{ep}}$, Eq. (7.16), is still valid and that $\Delta J_{\mathrm{actPZ}}^{\mathrm{ep}}$ correlates to $\Delta\delta_{\mathrm{t}}$.

The dependence of this peak value on the mesh size m is caused by the inhomogeneity of the plastic strain field around the crack tip, especially, near the blunted tip. A coarse mesh leads to a smoothing of stress and strain peaks and causes a reduction of the magnitude of the configurational force $\mathbf{f}^{\mathrm{ep}}$, see Eq. (7.13).

Furthermore, it should be noted that additional FE-analyses are conducted where the crack extension in each load cycle occurs at maximum load. Basically, the results do not change compared to the procedure with crack extension at minimum load, and the same conclusions can be drawn as presented above.

7.8 Summary

The current paper discusses the physically correct evaluation of the driving force for fatigue crack propagation in elastic–plastic materials using the *J*-integral concept. Numerical investigations are conducted for a two-dimensional compact tension specimen with a long crack under cyclic Mode I loading. The crack extends by an increment after each load cycle at the minimum load. The maximum load is varied so that small- and large-scale yielding conditions prevail. Three different load ratios are considered, from pure tension to tension-

compression loading. In general, maximum and minimum load are held constant during crack extension; in addition, the effect of a single tensile overload is also studied.

The results of the analyses show that the cyclic, incremental plasticity *J*-integral $\Delta J^{\mathrm{ep}}_{\mathrm{actPZ}}$, which is computed for a contour around the *active* plastic zone of the growing crack, is physically appropriate to characterize the growth rate of fatigue cracks in elastic–plastic materials.

The experimental cyclic *J*-integral ΔJ^{exp}, proposed by Dowling and Begley (1976), measures the cyclic, incremental plasticity *J*-integral for a contour around the *total* plastic zone, $\Delta J^{\mathrm{ep}}_{\mathrm{PZ}}$; the contour includes also the plastic zone around the initial crack tip and the plastic wake. The experimental cyclic *J*-integral ΔJ^{exp} reflects the driving force of a stationary crack, i.e. it is valid for the first load cycle. After crack extension, the incremental plasticity *J*-integral around the total plastic zone $J^{\mathrm{ep}}_{\mathrm{PZ}}$ differs from that around the active plastic zone $J^{\mathrm{ep}}_{\mathrm{actPZ}}$. Therefore, $\Delta J^{\mathrm{ep}}_{\mathrm{PZ}} \neq \Delta J^{\mathrm{ep}}_{\mathrm{actPZ}}$, and the experimental cyclic *J*-integral ΔJ^{exp} is not fully appropriate to reflect the driving force for a *growing* fatigue crack.

The difference between $\Delta J^{\mathrm{ep}}_{\mathrm{actPZ}}$ and $\Delta J^{\mathrm{ep}}_{\mathrm{PZ}}$ is most clearly seen in the overload case, where $\Delta J^{\mathrm{ep}}_{\mathrm{actPZ}}$ is able to correctly reflect the well-known crack growth retardation effect, whereas $\Delta J^{\mathrm{ep}}_{\mathrm{PZ}}$ and ΔJ^{exp} would predict a constant crack growth rate.

Acknowledgements

Financial support by the Austrian Federal Government and the Styrian Provincial Government within the research activities of the K2 Competence Center on “Integrated Research in Materials, Processing and Product Engineering”, under the frame of the Austrian COMET Competence Center Programme, is gratefully acknowledged (strategic project A4.20-WP3).

8 Fatigue crack growth after an overload

In Paper II it has been shown that the parameter ΔJ^{ep}_{actPZ} is able to accurately reflect crack growth retardation after a single overload. However, the main reason for this effect has not been investigated. The overload effect is the most famous load history effect in fatigue under variable load amplitude, but its major reason is still not fully clarified (e.g. Anderson 1995, Suresh 1998). Clear understanding of load history effects on the fatigue crack growth rate is of great importance for the development of reliable fatigue lifetime predictions models under variable amplitude loading since load fluctuations commonly occur in service.

What is the main reason for crack growth retardation after an overload? Is it *crack flank contact* behind or *residual stresses* around the propagating crack tip? This is the main question to be answered in Paper III.

Numerous researchers claim that crack flank contact is the most dominant mechanism for the overload effect (see e.g. Suresh 1998). The main justification for this opinion rests on the *delayed* crack growth retardation phenomenon, i.e. crack growth retardation does not occur immediately after the overload. Some crack growth into the overload plastic zone is needed so that residual stresses *behind* the crack tip result in plasticity-induced crack closure. On the contrary, crack growth retardation should occur immediately if residual stresses around the moving crack tip are more dominant (e.g. Anderson 1995, Suresh 1998). Therefore, we investigate also the delayed crack growth retardation phenomenon in Paper III.

In the following paper, numerical case studies are performed, similar as in Paper II, for various overload ratios, $R_{OL} = F_{OL}/F_{max}$ and various load ratios, $R = F_{min}/F_{max}$, under small-scale yielding and *plane strain* conditions. Important to mention is that the simulations are first performed with crack flank contact, and then compared to a *fictive* case where crack flank overlap is possible, i.e. without contact. This enables a separation of the effect of crack flank contact on the overload effect.

The studies on the variations of J^{ep}_{actPZ}, Eq. (8.3), during cyclic loading after an overload, in combination with an analysis of the configurational force distribution, leads to the following conclusions of Paper III:

- The main features of the overload effect, i.e. the strong reduction of the fatigue crack driving force ΔJ^{ep}_{actPZ} and the delayed retardation phenomenon, occur, no matter whether crack flank contact does exist or not.
- The major mechanism for the reduction of ΔJ^{ep}_{actPZ} is the reduction of the stresses around the propagating crack tip. The appearance of delayed crack growth retardation is related to a stronger crack tip blunting by the overload.
- Crack flank contact causes, for load ratios $R \geq 0$, only a little further decrease of the stresses around the current crack tip; for example, the maximum reduction in ΔJ^{ep}_{actPZ} is

for $R = 0$ and $R_{OL} = 2$ only 6% smaller compared to the overlap case. Therefore, crack flank contact may decide whether a crack arrests or not. The role of crack flank contact becomes more important for tension-compression loading, $R < 0$.

- The ability of the effective stress intensity range ΔK_{eff} to reflect the overload effect is also checked. It is shown that ΔK_{eff} can be used to accurately determine the maximum crack growth retardation after an overload. However, ΔK_{eff} does not deliver the delayed retardation phenomenon and significantly underestimates the magnitude of the fatigue crack driving force for larger crack extensions after the overload.

It is important to highlight that these findings are obtained for a perfectly *flat* crack under *plane strain* conditions. For a real three-dimensional specimen, with rough crack flanks, the influence of the lateral contraction at the side surfaces of the specimen might lead to a considerably higher contribution of crack flank contact to the overload effect.

Paper III:

Overload effect revisited – Investigation by use of configurational forces

W. Ochensberger and O. Kolednik

revised version submitted to

International Journal of Fatigue (2015)

Abstract

The configurational force concept enables the derivation of the incremental plasticity *J*-integral J^{ep}, which is, in contrast to the conventional *J*-integral, physically appropriate to characterize the crack driving force in cyclically loaded elastic–plastic materials with growing cracks. In this paper we apply J^{ep}, combined with an analysis of the configurational force distribution, for the investigation of fatigue crack growth retardation after a single tensile overload. The motivation for this investigation is that the main reason for the overload effect, i.e. crack flank contact behind or residual stresses around the growing crack tip, is today still an open question in fatigue. Numerical case studies are performed for two-dimensional Compact Tension specimens with long cracks that grow under cyclic Mode I loading and plane strain conditions. Variables of the numerical case studies are the overload ratio and the load ratio during constant cyclic loading. The influence of crack flank contact is examined by a comparison of two different simulations: The first simulation assumes frictionless contact between the upper and lower crack flank; in the second, fictive case, it is assumed that crack flank overlap is possible. The results show that all features of the overload effect even occur, if crack flank contact is not possible. Finally, the ability of the effective stress intensity range ΔK_{eff} to characterize the overload effect is also discussed.

Keywords: Fatigue crack growth; Crack driving force; Cyclic *J*-integral; Crack closure; Residual stresses

8.1 Introduction

The overload effect, i.e. crack growth retardation following a single tensile overload, is an abundantly studied phenomenon, see e.g. Schijve (1961); Christensen (1959); von Euw et al. (1972); Suresh (1983); Fleck (1988); Skorupa (1998). Various mechanisms can contribute to this effect (e.g. Anderson 1995, Suresh 1998); the two most important mechanisms are crack flank contact behind (e.g. Elber 1970, 1971; von Euw et al. 1972; Fleck 1988; Ward-Close and Ritchie 1988; Ward-Close et al. 1989; Blom 1989) and residual stresses around the moving crack tip (e.g. Drew et al. 1982; Suresh 1983; Ling and Schijve 1992; Sadananda et al. 1999). The question, which of the two mechanisms is more dominant, is still a contentious issue.

The preferred opinion among fatigue experts is that crack flank contact is predominant (e.g. Anderson 1995, Suresh 1998). The main justification for this opinion is the delayed retardation phenomenon, i.e. crack growth retardation does not occur immediately after the overload (e.g. Schijve 1961; Elber 1970, 1971; von Euw et al. 1972; Fleck 1988; Ward-Close and Ritchie 1988; Ward-Close et al. 1989; Blom 1989; Bichler and Pippan 1999, 2007). Although many experiments confirm the role of crack flank contact in influencing the overload effect, some experimental observations are not fully consistent with this mechanism, see e.g. Suresh (1983), Drew et al. (1982), Ling and Schijve (1992). Especially, Sadananda et al. (1999) raise doubts on the significance of crack flank contact, and they claim that residual stresses around the crack tip are more important for the overload effect.

This paper focuses on the question, what is the primary reason for crack growth retardation after a single tensile overload? We aim to shed new light on this topic by using the concept of configurational forces.

The concept of configurational forces has enabled the derivation of the *J*-integral J^{ep} for elastic–plastic materials with incremental theory of plasticity (Simha et al. 2008). Even for strongly non-proportional loading conditions, such as crack extension under monotonic or cyclic loading, J^{ep} has the physical meaning of a driving force term for a crack in an elastic–plastic material; however, it is path dependent (Simha et al. 2008). It is well known that the classical *J*-integral (Rice 1968a,b) does not provide such a true driving force term when applied to elastic–plastic materials, see e.g. Anderson (1995). The reason is that the classical *J*-integral is based on deformation theory of plasticity, which is not applicable for non-proportional loading conditions.

In two recent papers, Ochensberger and Kolednik (2014, 2015) have successfully applied the incremental plasticity *J*-integral J^{ep} for the characterization of the growth rate of fatigue cracks in elastic–plastic materials. This is important for low-cycle fatigue and the growth of short fatigue cracks, where linear elastic fracture mechanics becomes invalid. It can be expected that the application of J^{ep}, in combination with the analysis of the configurational force distribution, will provide us with new insight into the question of the most important mechanism for the overload effect.

In the next section, we briefly introduce the J^{ep}-integral and describe, how J^{ep} is used for the assessment of the fatigue crack propagation rate.

8.2 Incremental plasticity J-integral J^{ep} and driving force for fatigue crack growth

8.2.1 Configurational forces and J-integral for elastic–plastic materials

Configurational forces are thermodynamic driving forces that act on various types of defects in materials, e.g. vacancies, dislocations, voids, cracks (Eshelby 1951, 1970). The benefit of the concept of configurational forces is that it enables the derivation of the *J*-integral independent of the constitutive relations of the material, see e.g. Simha et al. (2003). Kolednik et al. (2014) provide an extensive literature review for the application of the configurational force concept for studying the behavior of cracks, which shall not be repeated at this point. Only the definition of the *J*-integral for elastic–plastic materials with incremental theory of plasticity J^{ep} is presented below.

Assume a loaded elastic–plastic body $\mathcal{B}$, described by incremental theory of plasticity, with a crack and a crack tip plastic zone, as illustrated in Fig. 8.1a. The scalar *J*-integral J^{ep} is evaluated by multiplying the *J*-integral vector $\mathbf{J}^{ep}$ with the unit vector in the nominal crack growth direction **e**,

$$J^{ep} = \mathbf{e} \cdot \mathbf{J}^{ep} = -\mathbf{e} \cdot \left(\mathbf{f}_{tip}^{ep} + \int_{\mathcal{D}} \mathbf{f}^{ep} \, \mathrm{d}A \right). \tag{8.1}$$

The *J*-integral vector $\mathbf{J}^{ep}$, calculated for an arbitrary contour Γ, is given as the sum of the configurational force vector $\mathbf{f}_{tip}^{ep}$ emanating from the crack tip and the bulk configurational force vectors $\mathbf{f}^{ep}$ that originate inside the contour Γ (Simha et al. 2008). Note that the contour Γ is drawn around the crack tip from the lower to the upper crack flank and that $\mathcal{D}$ is the area enclosed by Γ, but excluding the crack tip. The bulk configurational force vector $\mathbf{f}^{ep}$ is calculated as the divergence of the second-rank configurational stress tensor **C** (Eshelby 1951, 1970),

$$\mathbf{f}^{ep} = -\nabla \cdot \mathbf{C} = -\nabla \cdot \left(\phi_e \mathbf{I} - \mathbf{F}^T \mathbf{S} \right). \tag{8.2}$$

In Eq. (8.2), the parameter ϕ_e denotes the elastic part of the strain energy density, **I** the identity tensor, $\mathbf{F}^T$ the transposed of the deformation gradient tensor **F**, and **S** the 1st Piola-Kirchhoff stress. The bulk configurational force $\mathbf{f}^{ep}$ is non-zero in the plastically deformed regions of the body. The magnitude of $\mathbf{f}^{ep}$ is proportional to the stress and the gradient of the plastic strain, see Section 8.4.4 and Simha et al. (2008). Equation (8.2) is also used for calculating the configurational force at the crack tip $\mathbf{f}_{tip}^{ep}$ by forming a limit value, see Simha et al. (2008).

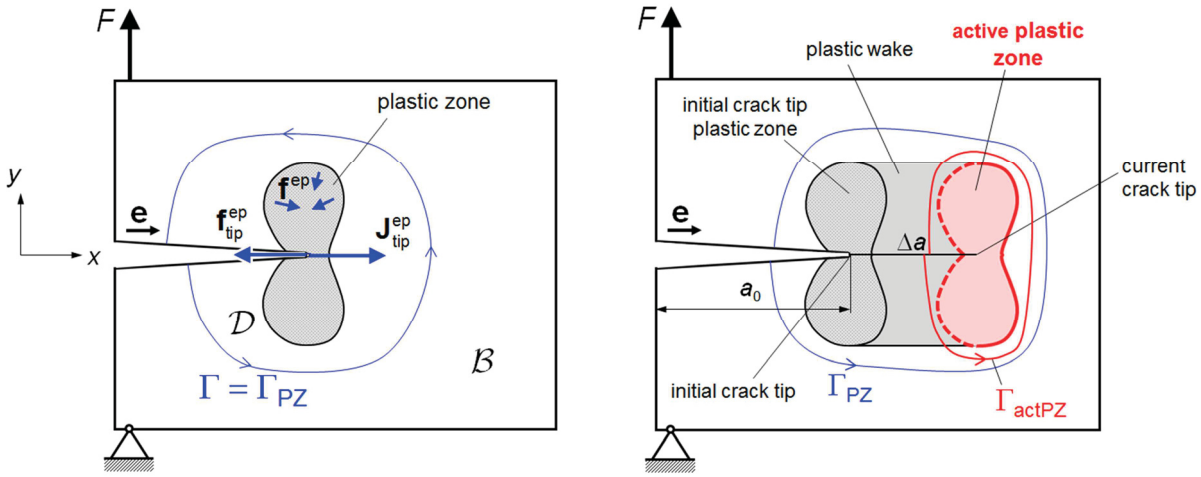

(a) **(b)**

Fig. 8.1 **(a)** Homogeneous, elastic–plastic body $\mathcal{B}$ with a crack and the crack tip plastic zone. **(b)** Body after crack extension Δa.

The configurational forces and the *J*-integral J^{ep} can be evaluated, if the stresses and the strains in the body $\mathcal{B}$ are known. The advantages of the incremental plasticity *J*-integral J^{ep} in comparison to the classical *J*-integral (Rice 1968a,b) are:

- J^{ep} has the physical meaning of a driving force term in elastic–plastic materials with incremental theory of plasticity,
- J^{ep} is applicable under non-proportional loading conditions, such as for cyclic loading and/or for growing cracks.

However, since bulk configurational forces $\mathbf{f}^{ep}$ are induced in plastically deformed regions, such as the crack tip plastic zone, J^{ep} becomes path dependent, see Eq. (8.1) and Fig. 8.1a.

How the incremental plasticity *J*-integral J^{ep} can be used for the characterization of the fatigue crack growth rate, is briefly reviewed in the next section.

8.2.2 Driving force for fatigue crack growth in the regime of non-linear fracture mechanics

A "driving force" for fatigue crack growth should allow the characterization of the growth rate d*a*/d*N* of fatigue cracks (e.g. Suresh 1998). The stress intensity range ΔK (Paris et al. 1961; Paris and Erdogan 1963) or the effective stress intensity range ΔK_{eff} (Elber 1970, 1971) are such terms; they can be used if linear elastic fracture mechanics is valid. If this is not the case, the cyclic incremental plasticity *J*-integral, ΔJ^{ep}_{actPZ}, should be applied, calculated for a contour Γ_{actPZ} around the *active* plastic zone of the moving crack tip, see Fig. 1b. The parameter ΔJ^{ep}_{actPZ} is evaluated from the relation,

$$\Delta J^{ep}_{actPZ} = J^{ep}_{actPZ,max} + J^{ep}_{actPZ,min} - 2\sqrt{J^{ep}_{actPZ,max} J^{ep}_{actPZ,min}}\,, \tag{8.3}$$

with $J^{\mathrm{ep}}_{\mathrm{actPZ,max}}$ and $J^{\mathrm{ep}}_{\mathrm{actPZ,min}}$ as the maximum and minimum values of the incremental plasticity *J*-integrals during the considered load cycle. Note that $J^{\mathrm{ep}}_{\mathrm{actPZ,min}} \geq 0$, see Sect. 8.4.2. The expression of the cyclic *J*-integral, Eq. (8.3), was derived in Ochensberger and Kolednik (2015); see Section 6.5.2 and "Appendix" therein.

The validity of the term $\Delta J^{\mathrm{ep}}_{\mathrm{actPZ}}$ as driving force parameter for fatigue crack growth and the application of Eq. (8.3) have been demonstrated by comparisons with the cyclic crack tip opening displacement $\Delta\delta_{\mathrm{t}} = \delta_{\mathrm{t,max}} - \delta_{\mathrm{t,min}}$, see Ochensberger and Kolednik (2015). This has been done because the crack growth rate in fatigue is driven by cyclic plasticity around the current crack tip, i.e. $\mathrm{d}a/\mathrm{d}N \propto \Delta\delta_{\mathrm{t}}$ (e.g. Tanaka 1989, Krupp et al. 2001, Pippan et al. 2010). Ochensberger and Kolednik (2015) have shown that negative values of $J^{\mathrm{ep}}_{\mathrm{actPZ}}$, which originate from compressive stresses during unloading, do not deliver a contribution to the driving force for fatigue crack growth, since $\delta_{\mathrm{t}} = 0$ during these stages. As a consequence, Eq. (8.3) is simplified to the relation $\Delta J^{\mathrm{ep}}_{\mathrm{actPZ}} = J^{\mathrm{ep}}_{\mathrm{actPZ,max}}$ for load ratios $R \leq 0$.

For *stationary* fatigue cracks, the active and the initial crack tip plastic zone coincide, $\Gamma_{\mathrm{actPZ}} = \Gamma_{\mathrm{PZ}}$ (Fig. 8.1), and $\Delta J^{\mathrm{ep}}_{\mathrm{actPZ}}$ becomes equal to the cyclic incremental plasticity *J*-integral around the *total* crack tip plastic zone $\Delta J^{\mathrm{ep}}_{\mathrm{PZ}}$. For this case, $\Delta J^{\mathrm{ep}}_{\mathrm{PZ}}$ corresponds exactly to the experimental cyclic *J*-integral ΔJ^{exp} introduced by Dowling and Begley (1976), which is determined from the area below a single loading branch of the load–displacement (*F*–*v*) record (Ochensberger and Kolednik 2014). Hence, ΔJ^{exp} is a fully appropriate driving force parameter for stationary fatigue cracks. For *growing* fatigue cracks, the experimental cyclic *J*-integral ΔJ^{exp} reflects the magnitude of the cyclic incremental plasticity *J*-integral around the *total* crack tip plastic zone $\Delta J^{\mathrm{ep}}_{\mathrm{PZ}}$, calculated for a contour Γ_{PZ} around the *total* crack tip plastic zone; the contour includes the plastic zone of the initial crack tip, the plastic wake and the active plastic zone. But $\Delta J^{\mathrm{ep}}_{\mathrm{PZ}}$ is not equal to the cyclic incremental plasticity *J*-integral around the *active* crack tip plastic zone $\Delta J^{\mathrm{ep}}_{\mathrm{actPZ}}$, which is the real driving force. Therefore, the experimental cyclic *J*-integral ΔJ^{exp} is not fully appropriate to measure the driving force for a *growing* fatigue crack. The difference between $\Delta J^{\mathrm{ep}}_{\mathrm{actPZ}}$ and ΔJ^{exp} (or $\Delta J^{\mathrm{ep}}_{\mathrm{PZ}}$) can become large for lsy-conditions. Important is that in this case $\Delta J^{\mathrm{ep}}_{\mathrm{actPZ}} > \Delta J^{\mathrm{ep}}_{\mathrm{PZ}} \approx \Delta J^{\mathrm{exp}}$, so that the experimental cyclic *J*-integral underestimates $\mathrm{d}a/\mathrm{d}N$, which can lead to a non-conservative assessment of the lifetime.

The difference between $\Delta J^{\mathrm{ep}}_{\mathrm{actPZ}}$ and ΔJ^{exp} (or $\Delta J^{\mathrm{ep}}_{\mathrm{PZ}}$) is most clearly seen, if the constant fatigue load is superimposed by a single tensile overload. The parameter $\Delta J^{\mathrm{ep}}_{\mathrm{actPZ}}$ predicts correctly the crack growth retardation, whereas ΔJ^{exp} and $\Delta J^{\mathrm{ep}}_{\mathrm{PZ}}$ would predict a constant crack growth rate (Ochensberger and Kolednik 2015). It should be stressed that the two main mechanisms of the overload effect, crack flank contact behind and residual stresses around the moving crack tip, have not been investigated in Ochensberger and Kolednik (2015); this is the topic of the current paper.

8.3 Numerical procedure

8.3.1 Finite element modeling of overload experiments

We apply the same finite element (FE) model as in Ochensberger and Kolednik (2015). Therefore, only some important details shall be given in the following.

A two-dimensional compact tension (C(T)-) specimen (ASTM E1820, 2005) under plane strain conditions is modelled with a straight crack in horizontal *x*-direction. The dimensions of the specimen are width $W = 50\text{mm}$, height H = 60 mm, nominal thickness B = 25 mm, and initial crack length $a_0 = 25\text{mm}$ (Fig. 8.2). The specimen is cyclically loaded in Mode I by prescribing the load F at the load application point.

The specimens consist of homogeneous, isotropic, elastic–ideally plastic material following incremental theory of plasticity. The material data are Young's modulus E = 200 GPa, Poisson's ratio ν = 0.3, and yield strength σ_y = 270 MPa. A small elastic strip, with same E and ν, is modelled along the left boundary to prevent large plastic deformation at the load application point (Fig. 8.2). This can be done, since the plastic zone does not touch this elastic strip.

The simulations are conducted using the FE-program ABAQUS. Due to symmetry, only half of the C(T)-specimen is modelled. Bilinear 4-node continuum elements are used for the mesh. Region A, with a dimension 13.5×3.0 mm², consists mainly of elements with mesh size m = 0.10 mm. The inner region B⊂A, with a dimension of 0.6×0.3 mm², is discretized with a finer mesh of m = 0.01 mm; its location is seen in Fig. 8.2. The fine mesh enables a detailed analysis of the post-overload period, Section 8.4. The dimensions of B are chosen so that the active plastic zone travels inside B during maximum reduction of the fatigue crack driving force after overload. Geometric nonlinearity is selected to account for large deformations around the crack tip.

Since crack flank contact plays a crucial role in our investigation, frictionless contact between the upper crack surface and the lower rigid surface is modeled (Fig. 8.2). Nodes on the plane $y = 0$, except those on the crack flank, are constrained in y-direction, but unconstrained in x-direction; the specimen is fixed in x-direction at the load application point. The rigid surface avoids an overlapping of the upper crack flank during unloading, so that the vertical displacements of the nodes lying on the upper crack flank cannot become negative, $u_y \geq 0$. In the following, this case is indicated by a superscript "contact".

In order to estimate the influence of crack flank contact on the overload effect, we consider a second, *fictive* case where crack flank overlap is possible. The rigid surface in the FE-model is removed so that the vertical displacements at nodes on the upper crack flank can become negative, i.e. crack flank contact does not appear. This is in reality not possible, because the crack flanks cannot penetrate. A superscript "overlap" designates this fictive case. Metzger et al. (2014) have applied a similar procedure; however, they studied the behavior of the conventional, cyclic J-integral under constant tension-compression loading.

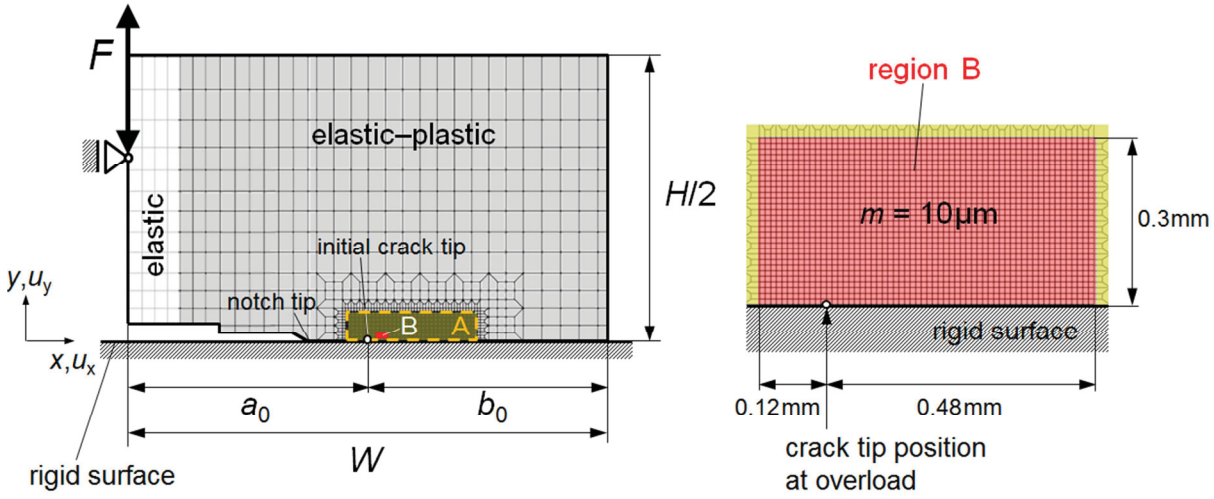

Fig. 8.2 FE-model of the C(T)-specimen with boundary conditions. Without the rigid surface, crack flank overlap is possible, i.e. the vertical displacements on the upper crack flank can become negative. The figure on the right shows a detail of the fine-mesh region B.

Fatigue crack propagation is modeled for constant amplitude loading (CL case), $\Delta F = F_{\max} - F_{\min} = \text{constant}$, as well as for the case with a single tensile overload F_{OL} (OL case). In our simulations, one load cycle consists of loading and unloading between maximum and minimum load, $F_{\max}$ and $F_{\min}$, and subsequent crack extension at $F_{\min} = \text{constant}$.[13] Crack extension is modeled using the node release technique (Ohji et al. 1975; Newman 1976). The crack extension increment per load cycle is two element lengths $2m$, i.e. 0.20 mm in Region A, and 0.02 mm in Region B. The simulation is terminated after $N = 51$ load cycles when the total crack length reaches $a = 31.4$ mm.

The maximum load during constant cyclic loading is $F_{\max} = 12.5\,\mathrm{kN}$. In the OL case, a single tensile overload F_{OL} is applied in the fourth load cycle, i.e. after 0.6 mm of crack growth. If not specified otherwise, the load ratio is $R = F_{\min}/F_{\max} = 0$ (zero-tension loading) and the overload ratio is $R_{\mathrm{OL}} = F_{\mathrm{OL}}/F_{\max} = 2$. The loads $F_{\max}$ and F_{OL} have been chosen so that small-scale yielding conditions prevail, i.e. no plastic deformation appears at the back-face of the specimen. This has been done to enable a comparison to the characterization with the effective stress intensity range ΔK_{eff}, see Section 8.6.

8.3.2 Configurational force and J-integral post-processing

After the FE stress and strain analysis with incremental theory of plasticity, the configurational force vectors $\mathbf{f}^{\mathrm{ep}}$ are computed from Eq. (8.2) at each node n of the FE mesh by a self-written post-processing routine, which is based on the papers of Müller et al. (2002, 2004) and Denzer et al. (2003). The incremental plasticity J-integral for a contour around the

[13] Regarding the preferred load level for simulating incremental crack extension via node release technique, the reader is referred to Solanki et al. (2004).

active plastic zone, $J^{\mathrm{ep}}_{\mathrm{actPZ}}$, is then calculated by a summation of all $\mathbf{f}^{\mathrm{ep}}$-vectors emanating from all nodes *n* located within Γ_{actPZ},

$$J^{\mathrm{ep}}_{\mathrm{actPZ}} = \sum_{n \text{ within } \Gamma_{\mathrm{actPZ}}} -\left(\mathbf{e}\cdot\mathbf{f}^{\mathrm{ep}}\right)\Delta A_n \,. \tag{8.4}$$

Note that the crack tip node must be included in the summation, compare Eq. (8.1). In Eq. (8.4) the parameter ΔA_n denotes the element area corresponding to a specific node *n*. The *J*-integral values for other contours Γ are calculated analogously.

The shape of the active plastic zone is determined by letting ABAQUS mark those integration points where the plastic strain $\boldsymbol{\varepsilon}^{\mathrm{p}}$ changes during the re-loading phase, i.e. the loading interval from $F_{\min}$ to $F_{\max}$, of a considered load cycle.[14] The integration path Γ_{actPZ} includes all these integration points. The size of Γ_{actPZ} is held constant when calculating the variation of $J^{\mathrm{ep}}_{\mathrm{actPZ}}$ during a single load cycle. The driving force for fatigue crack growth, i.e. the value of the cyclic incremental plasticity *J*-integral for a contour around the active plastic zone $\Delta J^{\mathrm{ep}}_{\mathrm{actPZ}}$, is calculated from Eq. (8.3).

The accuracy of the *J*-integral evaluation has been discussed in Ochensberger and Kolednik (2015). It has been shown that the values of $J^{\mathrm{ep}}_{\mathrm{actPZ}}$ and $\Delta J^{\mathrm{ep}}_{\mathrm{actPZ}}$ are not very sensitive to the exact shape of the integration contour Γ_{actPZ} or to the FE-mesh size *m*. This means that an accurate determination of $J^{\mathrm{ep}}_{\mathrm{actPZ}}$-values is numerically not very expensive, in contrast to that of the crack tip opening displacement δ_{t}.

8.4 Analysis of crack growth retardation after a single tensile overload

8.4.1 Variation of the fatigue crack driving force $\Delta J^{\mathrm{ep}}_{\mathrm{actPZ}}$ following an overload

Figure 8.3a presents the variations of the cyclic incremental plasticity *J*-integral around the active plastic zone, $\Delta J^{\mathrm{ep}}_{\mathrm{actPZ}}$, with increasing crack extension Δa after the overload. Shown are the values with and without crack flank contact, $\left(\Delta J^{\mathrm{ep}}_{\mathrm{actPZ}}\right)^{\mathrm{contact}}_{\mathrm{OL}}$ (full dots) and $\left(\Delta J^{\mathrm{ep}}_{\mathrm{actPZ}}\right)^{\mathrm{overlap}}_{\mathrm{OL}}$ (open dots). The values of the driving force for the constant load case, $\left(\Delta J^{\mathrm{ep}}_{\mathrm{actPZ}}\right)^{\mathrm{contact}}_{\mathrm{CL}}$, are plotted as solid line for comparison. Figure 8.3b,c show details for the ranges $\Delta a = 0 \div 0.8$ mm and $\Delta a = 4.0 \div 5.8$ mm after overload. The fine mesh region B extends to $\Delta a = 0.4$ mm. The load cycle numbers *N* are written on the upper axes of the graphs.

The driving force for the constant load (CL) case, $\left(\Delta J^{\mathrm{ep}}_{\mathrm{actPZ}}\right)^{\mathrm{contact}}_{\mathrm{CL}}$, continuously increases due to crack extension. The small peak in the 2nd load cycle occurs, since the active plastic zone still includes the blunting region of the initial crack tip, whereas this is not the case for

[14] Note that *new* plastic deformation does not occur along the crack flanks during re-loading of the specimen to the maximum load. In the following unloading cycle, plasticity at the crack flanks can occur (inside and outside of the integration path Γ_{actPZ}). However, this does not deliver a contribution to the driving force, since the configurational forces at the crack flanks have no component in *x*-direction due to the vertical gradient of the plastic strain.

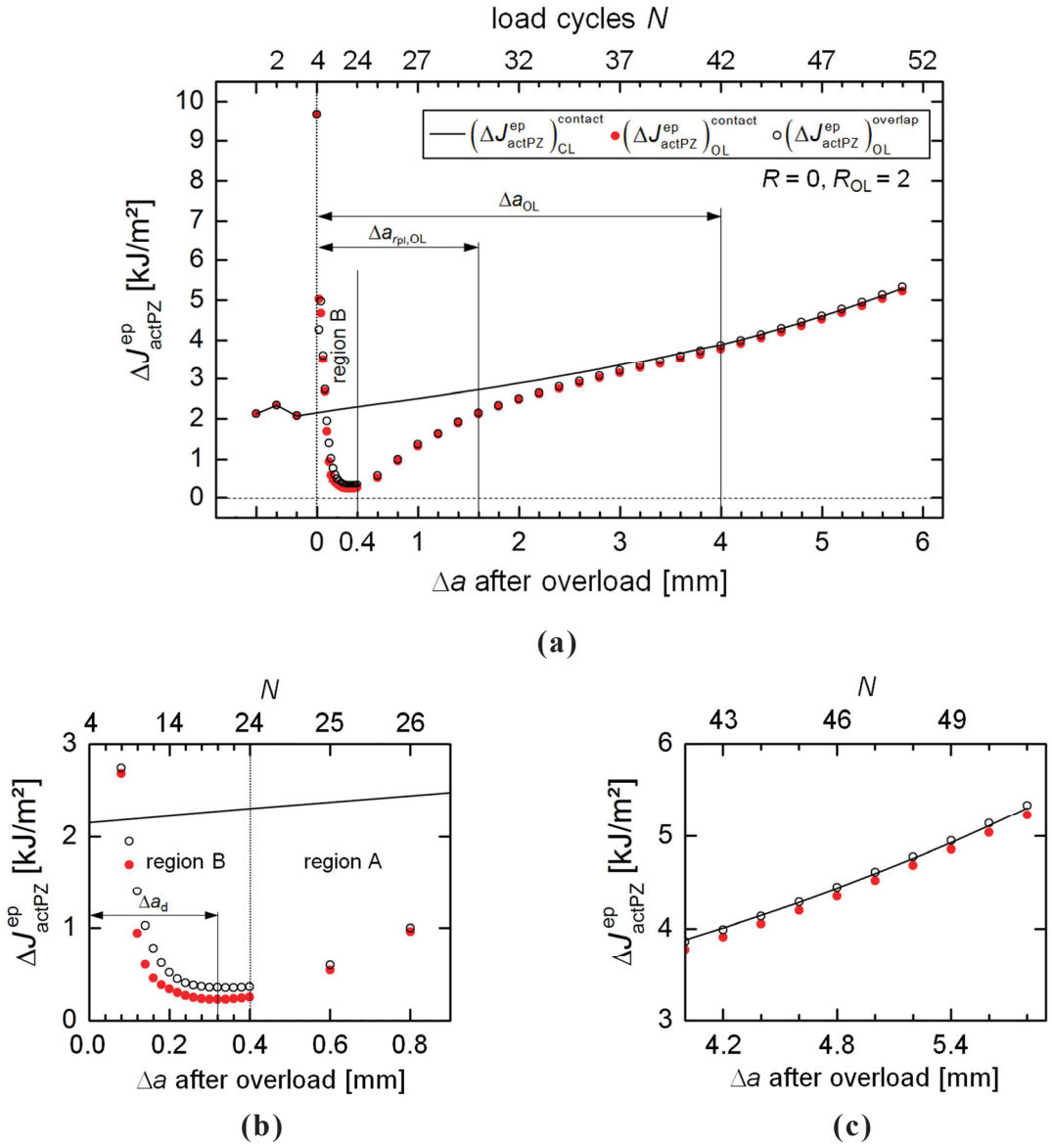

Fig. 8.3 Effect of a single tensile overload on the driving force for fatigue crack growth, ΔJ^{ep}_{actPZ}, with and without crack flank contact for load ratio $R = 0$ and overload ratio $R_{OL} = 2$. The ΔJ^{ep}_{actPZ}-values are plotted against crack extension Δa from the overload. **(a)** Overview. **(b) (c)** Details for $\Delta a = 0 \div 0.8$ mm and $\Delta a = 4.0 \div 5.8$ mm.

larger crack extensions, $N \geq 3$, see Ochensberger and Kolednik (2015). It should be noted that the difference between $\left(\Delta J^{ep}_{actPZ}\right)^{contact}_{CL}$ and $\left(\Delta J^{ep}_{actPZ}\right)^{overlap}_{CL}$ is negligible for the CL case and $R \geq 0$.

In the overload case, the ΔJ^{ep}_{actPZ}-variations with and without crack flank contact appear quite similar in Fig. 8.3a. The ΔJ^{ep}_{actPZ}-values rapidly decrease after the overload and fall within a short crack growth distance below the CL-values. Delayed retardation is visible: in the 8th load cycle, i.e. the 4th load cycle after the overload, ΔJ^{ep}_{actPZ} is still somewhat larger than $\left(\Delta J^{ep}_{actPZ}\right)^{contact}_{CL}$. After reaching a minimum value at the crack extension Δa_d, ΔJ^{ep}_{actPZ} gradually

Table 8.1 Characteristic overload-affected crack growth distances, Δa_{d}, $\Delta a_{r\mathrm{pl,OL}}$, and Δa_{OL}, for various load ratios R and overload ratios R_{OL}, compare Fig. 8.3a,b.

		with crack flank contact			without contact (overlap)		
R	R_{OL}	Δa_{d}	$\Delta a_{r\mathrm{pl,OL}}$	Δa_{OL}	Δa_{d}	$\Delta a_{r\mathrm{pl,OL}}$	Δa_{OL}
[-]	[-]	[mm]			[mm]		
0	2.0	0.32	1.60	> 6	0.34	1.60	4.00
0	1.6	0.22	1.20	3.60	0.22	1.20	2.80
0	1.2	0.14	0.80	1.20	0.14	0.80	1.20
0.5	2.0	0.16	1.60	3.20	0.16	1.60	3.00
–1	2.0	0.38	1.60	> 6	0.34	1.60	4.00

increases with further crack extension until the values for constant cyclic loading are reached; the position of maximum reduction in the driving force for fatigue crack growth Δa_{d} is denoted as *delay distance*, see e.g. Suresh (1998), Skorupa (1998). The parameter Δa_{OL} denotes the total crack growth distance affected by the overload (e.g. Skorupa 1998); it is taken in the current study as the value where the difference between $\left(\Delta J^{\mathrm{ep}}_{\mathrm{actPZ}}\right)_{\mathrm{OL}}$ and $\left(\Delta J^{\mathrm{ep}}_{\mathrm{actPZ}}\right)_{\mathrm{CL}}$ falls below 1%. This value, Δa_{OL}, is significantly larger than the distance $\Delta a_{r\mathrm{pl,OL}}$ where the active plastic zone has escaped from the plastic zone produced by the overload, Fig. 8.3a. The characteristic overload-affected crack growth distances, Δa_{d}, $\Delta a_{r\mathrm{pl,OL}}$, and Δa_{OL}, are collected in Table 8.1 for the contact- and overlap cases. Table 8.2 lists the cyclic J-integral values for these characteristic crack growth distances and for some additional Δa-values.

On closer examination, it can be observed from Fig. 8.3b and Fig. 8.3c that the values of $\left(\Delta J^{\mathrm{ep}}_{\mathrm{actPZ}}\right)^{\mathrm{contact}}_{\mathrm{OL}}$ lie, in general, below the $\left(\Delta J^{\mathrm{ep}}_{\mathrm{actPZ}}\right)^{\mathrm{overlap}}_{\mathrm{OL}}$-values. Immediately after the overload, the difference between these parameters first increases and then decreases with crack extension, Fig. 8.3b. The parameter $\left(\Delta J^{\mathrm{ep}}_{\mathrm{actPZ}}\right)^{\mathrm{contact}}_{\mathrm{OL}}$ reaches a minimum value of 0.229 kJ/m² after $\Delta a_{\mathrm{d}} = 0.32$ mm crack extension from the overload, $N = 20$. In the overlap case, the minimum value is slightly higher, $\left(\Delta J^{\mathrm{ep}}_{\mathrm{actPZ}}\right)^{\mathrm{overlap}}_{\mathrm{OL}} = 0.356$ kJ/m² at $\Delta a_{\mathrm{d}} = 0.34$ mm, $N = 21$. The relative reduction of the driving force compared to cyclic loading with constant load amplitude is quantified by the parameter

$$\Delta^{\mathrm{CL}}_{\mathrm{i}} = \frac{\left(\Delta J^{\mathrm{ep}}_{\mathrm{actPZ}}\right)^{\mathrm{contact}}_{\mathrm{CL}} - \left(\Delta J^{\mathrm{ep}}_{\mathrm{actPZ}}\right)^{\mathrm{i}}_{\mathrm{OL}}}{\left(\Delta J^{\mathrm{ep}}_{\mathrm{actPZ}}\right)^{\mathrm{contact}}_{\mathrm{CL}}}, \tag{8.5}$$

where the index i stands for “contact” or “overlap”, respectively. The maximum possible reduction is 90% and 84%, respectively. Data for other Δa-values are listed in the columns $\Delta^{\mathrm{CL}}_{\mathrm{contact}}$ and $\Delta^{\mathrm{CL}}_{\mathrm{overlap}}$ in Table 8.2. Note that the $\left(\Delta J^{\mathrm{ep}}_{\mathrm{actPZ}}\right)^{\mathrm{contact}}_{\mathrm{OL}}$-values do not fully reach the CL-values within the modeled crack extension, whereas the $\left(\Delta J^{\mathrm{ep}}_{\mathrm{actPZ}}\right)^{\mathrm{overlap}}_{\mathrm{OL}}$-values do so after $\Delta a_{\mathrm{OL}} = 4$ mm (Fig. 8.3c, Table 8.1).

Table 8.2 Values of the cyclic incremental plasticity *J*-integral around the active plastic zone, ΔJ^{ep}_{actPZ}, Eq. (8.3), for load ratio $R = 0$ and various overload ratios R_{OL}.

R_{OL}	N	Δa	$\left(\Delta J^{ep}_{actPZ}\right)^{contact}_{CL}$	$\left(\Delta J^{ep}_{actPZ}\right)^{contact}_{OL}$	$\left(\Delta J^{ep}_{actPZ}\right)^{overlap}_{OL}$	$\Delta J^{\Delta K_{eff}}_{OL}$	$\Delta^{CL}_{contact}$	$\Delta^{CL}_{overlap}$	$\Delta^{CL}_{\Delta Keff}$
[-]	[-]	[mm]	[kJ/m²]				[%]		
2.0	20	*0.32*	2.250	*0.229*	0.358	*0.214*	*89.8*	84.1	*90.5*
2.0	21	*0.34*	2.259	0.231	*0.356*	0.221	89.7	*84.2*	90.2
2.0	30	1.6	2.728	2.125	2.152	0.792	22.1	21.1	71.0
2.0	42	4.0	3.882	3.776	3.865	2.425	2.73	0.44	37.5
2.0	51	5.8	5.304	5.229	5.332	4.190	1.41	–0.53	21.0
1.6	15	*0.22*	2.235	*0.631*	*0.735*	*0.626*	*71.8*	*67.1*	*72.0*
1.6	28	1.2	2.578	2.252	2.272	1.249	12.6	11.9	51.5
1.6	36	2.8	3.246	3.198	3.221	2.350	1.48	0.77	27.6
1.6	40	3.6	3.671	3.637	3.668	2.998	0.93	0.08	18.3
1.6	51	5.8	5.304	5.308	5.342	4.810	–0.08	–0.72	9.31
1.2	11	*0.14*	2.204	*1.721*	*1.726*	*1.566*	*21.9*	*21.7*	*28.9*
1.2	26	0.8	2.438	2.381	2.371	1.919	2.34	2.75	21.3
1.2	28	1.2	2.578	2.577	2.584	2.213	0.04	–0.23	14.2
1.2	42	4.0	3.882	3.911	3.908	3.828	–0.75	–0.67	1.39
1.2	51	5.8	5.304	5.344	5.342	5.287	–0.75	–0.72	0.32

The subscripts "CL" and "OL" denote constant loading and the overload case. The superscripts "contact" and "overlap" denote the cases with and without crack flank contact. The cyclic *J*-integral value $\Delta J^{\Delta K_{eff}}_{OL}$ is calculated from the effective stress intensity range ΔK_{eff}, Eq. (8.8), for the contact case. The parameters Δ^{CL}_{i} give the relative reduction in driving force with respect to the CL case, see Eq. (8.5).

It should be mentioned that Bichler and Pippan (2007) carried out overload experiments on C(T)-specimens made of ductile austenitic CrNi-steel under constant cyclic loading with a load ratio $R = 0.05$ and ssy-conditions. Variables of these tests were the overload ratio, $R_{OL} = 1.1 \div 2$, and the specimen thickness. For 25 mm thick specimens (plane strain dominance) and $R_{OL} = 2$, they found by an analysis of the fatigue striations after the overload a maximal reduction of the fatigue crack growth rate, da/dN, of about 84% after $\Delta a_d \approx 0.5$ mm crack extension from the overload. This is in good agreement with our modeling result, see Table 8.2.

The results of this section show that the retardation effect after an overload is only slightly more pronounced, if crack flank contact is taken into account, compared to the case when the crack flanks are allowed to overlap during the unloading. The main features of the overload effect, including the strong reduction of the driving force and the delayed retardation phenomenon, occur independent of crack flank contact. Compared to the constant load case, the minimum ΔJ^{ep}_{actPZ} with crack flank contact is only 6% lower than for the overlap case.

However, the relative difference between the minimum values of $\left(\Delta J^{\mathrm{ep}}_{\mathrm{actPZ}}\right)^{\mathrm{contact}}_{\mathrm{OL}}$ and $\left(\Delta J^{\mathrm{ep}}_{\mathrm{actPZ}}\right)^{\mathrm{overlap}}_{\mathrm{OL}}$, calculated analogously to Eq. (8.5), can be significant (about 50%). Therefore, crack flank contact may decide whether a crack arrests or not, i.e. whether the fatigue crack driving force becomes smaller than the effective threshold for fatigue crack propagation; this criterion has been used for modeling the fatigue crack growth rate and possible crack arrest in inhomogeneous materials (Kolednik et al. 2009, 2015).

It should be stressed that these results are valid for a perfectly flat crack, a load ratio $R = 0$, and plane strain conditions. For a real three-dimensional specimen, as e.g. in the numerical studies by Roychowdhury and Dodds (2005), the contribution of crack flank contact to the overload effect might be considerably higher due to the different stress state and the lateral contraction at the side surface of the specimen.

8.4.2 Variation of the J-integral $J^{\mathrm{ep}}_{\mathrm{actPZ}}$ in the post-overload regime

In order to understand the variation of the driving force $\Delta J^{\mathrm{ep}}_{\mathrm{actPZ}}$ following an overload, it is useful to study the behavior of the $J^{\mathrm{ep}}_{\mathrm{actPZ}}$-values during cyclic loading, compare Eq. (8.3). In addition, the variation of the crack tip opening displacement δ_{t} is also analyzed. The values of δ_{t} are determined one element length *m* behind the crack tip. Figure 8.4a shows variations of $\left(J^{\mathrm{ep}}_{\mathrm{actPZ}}\right)^{\mathrm{contact}}_{\mathrm{OL}}$ and $\left(J^{\mathrm{ep}}_{\mathrm{actPZ}}\right)^{\mathrm{overlap}}_{\mathrm{OL}}$ against time *t* for the last load cycle before the overload, load cycle number $N = 3$, and the first 20 load cycles after the overload, $N = 4 \div 24$, time $t = 9 \div 72$, crack extension after overload $\Delta a = 0 \div 0.4$ mm. Time $t = 3N - 2$, with $N \in \mathbb{N}$, corresponds to the state at maximum load F_{max}; time $t = 3N - 1$ corresponds to the state after unloading to the minimum load F_{min}; time $t = 3N$ corresponds to the state when the crack extension step is finished. Note that at $t = 3N$, the contour Γ_{actPZ} is updated for the upcoming load cycle; thus, two values of $J^{\mathrm{ep}}_{\mathrm{actPZ}}$ exist after the crack extension step. The *J*-integral values at F_{max} are marked with full and open dots for $\left(J^{\mathrm{ep}}_{\mathrm{actPZ,max}}\right)^{\mathrm{contact}}_{\mathrm{OL}}$ and $\left(J^{\mathrm{ep}}_{\mathrm{actPZ,max}}\right)^{\mathrm{overlap}}_{\mathrm{OL}}$, respectively. The dash-dotted line marks the maximum *J*-values for the CL case. Figure 8.4b shows in more detail the interval $t = 47 \div 66$.

It can be observed from Fig. 8.4a that the *J*-integral value at maximum load for the contact case, $\left(J^{\mathrm{ep}}_{\mathrm{actPZ,max}}\right)^{\mathrm{contact}}_{\mathrm{OL}}$, strongly decreases with crack extension and reaches its minimum value at $t = 58$, $\Delta a_{\mathrm{d}} = 0.32$ mm. Subsequently, the values increase again. Very interesting is the behavior of the *J*-integral values at minimum load: At $t = 11$, after unloading from F_{OL} to $F_{\mathrm{min}} = 0$, $\left(J^{\mathrm{ep}}_{\mathrm{actPZ}}\right)^{\mathrm{contact}}_{\mathrm{OL}} \approx 0$, but the *J*-integral becomes distinctly negative after the crack extension step, $t = 12$; reasoning is given in Sections 8.4.3. and 8.4.4. Nearly the same negative *J*-value is reached at F_{min} in the following load cycle, but here the values before and after the crack extension step at $t = 14$ and 15 are almost equal. With increasing crack extension, the $\left(J^{\mathrm{ep}}_{\mathrm{actPZ,min}}\right)^{\mathrm{contact}}_{\mathrm{OL}}$-values continuously increase and for times $t \geq 33$ their magnitude remains roughly zero, i.e. are of the order of 10^{-3} kJ/m^2.

The negative $J^{\mathrm{ep}}_{\mathrm{actPZ}}$-values between $t = 12$ and $t \approx 39$ do not contribute to the driving force, since the crack tip is closed during these stages, i.e. the crack tip opening displacement $\delta_{\mathrm{t}} = 0$, see Section 8.2.2. This fact has been extensively studied in Ochensberger and

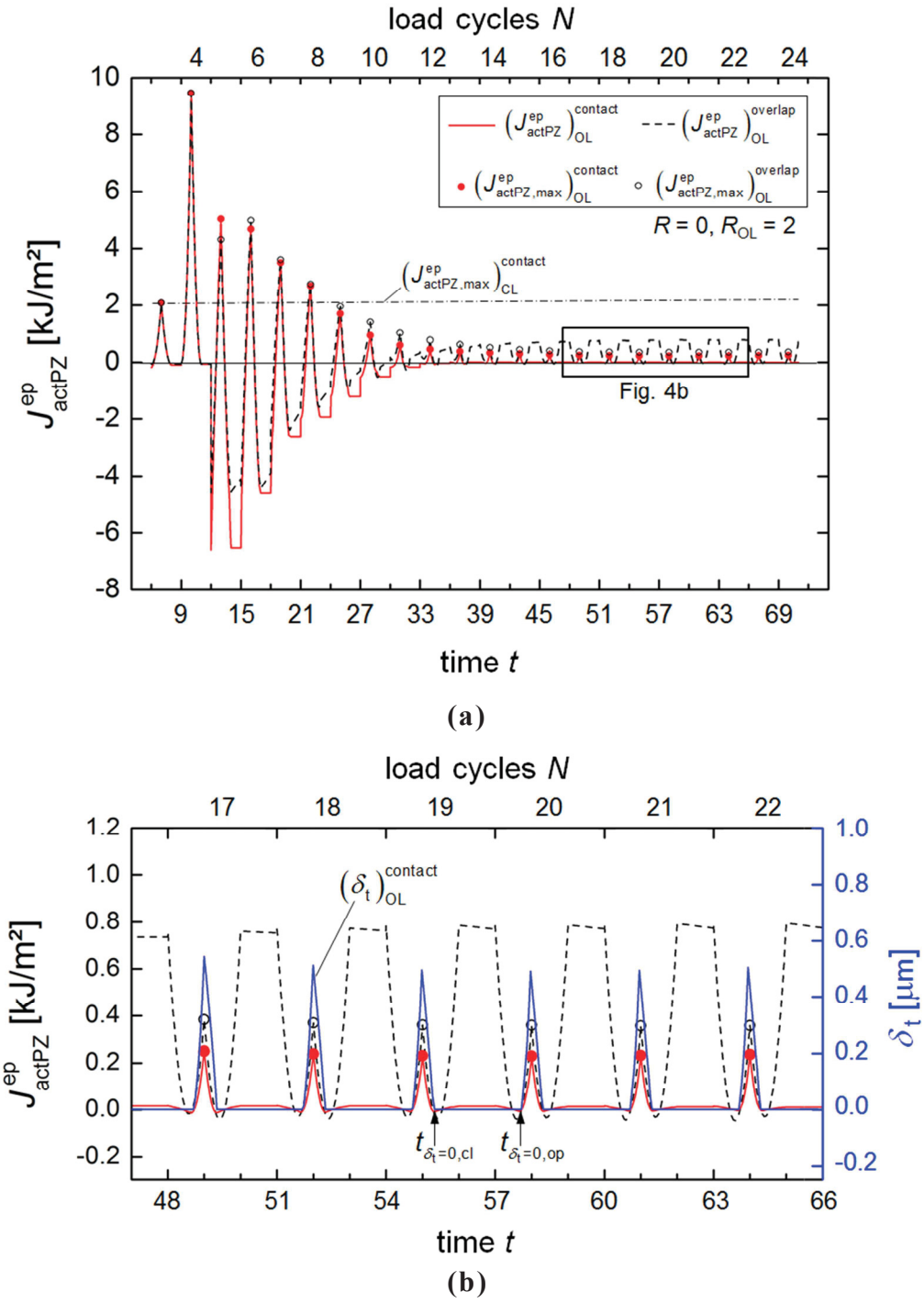

Fig. 8.4 **(a)** Variations of the incremental plasticity J-integrals around the active plastic zone J^{ep}_{actPZ} for the contact and overlap cases, load ratio $R = 0$ and overload ratio $R_{OL} = 2$. The OL-cycle starts at time $t = 9$. **(b)** Detail of the time interval $t = 47 \div 66$. The variation of the crack tip opening displacement $(\delta_t)^{contact}_{OL}$ is included for comparison.

Kolednik (2015). As a consequence, $J^{ep}_{actPZ,min}$ can be set to zero in Eq. (8.3) if it is negative. The variation of the crack tip opening displacement δ_t is drawn as blue curve in Fig. 8.4b. It is seen that, in the interval with maximum reduction of the driving force, the crack tip is

closed during the larger times of the unloading and loading periods, e.g. from $t_{\delta_t=0,\mathrm{cl}}$ where the crack tip closes to $t = 56$, or from $t = 57$ to $t_{\delta_t=0,\mathrm{op}}$ where the crack tip opens. It is also seen from Fig. 8.4b that $J^{\mathrm{ep}}_{\mathrm{actPZ}} = 0$ at $t_{\delta_t=0,\mathrm{cl}}$ and $t_{\delta_t=0,\mathrm{op}}$. It is interesting that $J^{\mathrm{ep}}_{\mathrm{actPZ}}$ reaches a very small positive value, while the crack tip is closed, see below and Section 8.4.4.

Since $J^{\mathrm{ep}}_{\mathrm{actPZ,min}} = 0$, Eq. (8.3) simplifies to $\Delta J^{\mathrm{ep}}_{\mathrm{actPZ}} = J^{\mathrm{ep}}_{\mathrm{actPZ,max}}$, and the $\Delta J^{\mathrm{ep}}_{\mathrm{actPZ}}$-values presented in Fig. 8.3 and Table 8.2 are equal to the maximum $J^{\mathrm{ep}}_{\mathrm{actPZ}}$-values of Fig. 8.4.

The relation $\Delta J^{\mathrm{ep}}_{\mathrm{actPZ}} = J^{\mathrm{ep}}_{\mathrm{actPZ,max}}$ also applies in the case where crack flank overlap is possible; negative $J^{\mathrm{ep}}_{\mathrm{actPZ}}$-values during the unloading stages for $t = 12 \div 29$, Fig. 8.4a, do not contribute to the driving force $\Delta J^{\mathrm{ep}}_{\mathrm{actPZ}}$, since the crack tip is closed, $\delta_t \le 0$. Compared to the contact case, the curve for $\left(J^{\mathrm{ep}}_{\mathrm{actPZ}}\right)^{\mathrm{overlap}}_{\mathrm{OL}}$ shows two important differences: (i) The J-values at maximum load $\left(J^{\mathrm{ep}}_{\mathrm{actPZ,max}}\right)^{\mathrm{overlap}}_{\mathrm{OL}}$ are, in general, higher than $\left(J^{\mathrm{ep}}_{\mathrm{actPZ,max}}\right)^{\mathrm{contact}}_{\mathrm{OL}}$, Fig. 8.4a and Fig. 8.3b. (ii) In the interval with maximum reduction of the driving force, the J-integral $\left(J^{\mathrm{ep}}_{\mathrm{actPZ}}\right)^{\mathrm{overlap}}_{\mathrm{OL}}$ increases during the unloading stage from zero at time $t_{\delta_t=0,\mathrm{cl}}$ to a high positive value. Although it can become even higher than the J-value at maximum load $\left(J^{\mathrm{ep}}_{\mathrm{actPZ,max}}\right)^{\mathrm{overlap}}_{\mathrm{OL}}$, Fig. 8.4b, this value does not contribute to the driving force $\Delta J^{\mathrm{ep}}_{\mathrm{actPZ}}$, since the crack tip is closed. The reasoning, why such high $\left(J^{\mathrm{ep}}_{\mathrm{actPZ}}\right)^{\mathrm{overlap}}_{\mathrm{OL}}$ can appear during unloading, will be given in Section 8.4.4.

8.4.3 To the appearance of delayed crack growth retardation

Especially high (at maximum load) and low (at minimum load) values of $J^{\mathrm{ep}}_{\mathrm{actPZ}}$ appear in the period $t = 12 \div 24$, see Fig. 8.4a. This effect can be explained analogously to the occurrence of the peak value of $\Delta J^{\mathrm{ep}}_{\mathrm{actPZ}}$ observed at $N = 2$ in Fig. 8.3a: Up to a distance of $\Delta a = 0.08$ mm from the overload, $N = 8$, the crack tip blunting region induced by the overload still lies within the active plastic zone, which travels to the right with crack extension. For the first four load cycles after the overload, the extension of the active plastic zone in $-x$-direction is 0.07 mm, counted from the current crack tip. Since the x-components of the configurational forces in this overload blunting region at $F_{\max}$ are negative, they deliver a positive contribution to J^{ep}, see Eq. (8.4). Therefore, the magnitude of $J^{\mathrm{ep}}_{\mathrm{actPZ,max}}$ is increased. For the $J^{\mathrm{ep}}_{\mathrm{actPZ,min}}$-values, we have to consider that J^{ep} changes its sign during unloading due to the appearance of compressive stresses around the crack tip; this is explained shortly in Section 8.4.4. and in more detail in Ochensberger and Kolednik (2014).

It should be noted that such delayed crack growth retardation has been analyzed by quantitative fracture surface inspection in von Euw et al. (1972) and Bichler and Pippan (1999, 2007).

8.4.4 Effects of crack flank contact and residual stresses on crack growth retardation

The driving force for fatigue crack growth $\Delta J^{\mathrm{ep}}_{\mathrm{actPZ}}$ reaches its minimum value in the 20$^{\mathrm{th}}$ load cycle, $t = 58$, $\Delta a_{\mathrm{d}} = 0.32$ mm after the overload (Figs. 3a,b). Since $J^{\mathrm{ep}}_{\mathrm{actPZ,min}} = 0$, Section 8.4.2, the reason for the strongly decreased $\Delta J^{\mathrm{ep}}_{\mathrm{actPZ}}$-value is the strongly reduced $J^{\mathrm{ep}}_{\mathrm{actPZ,max}}$-value, compared to the value for the CL case, Fig. 8.4a. This reduction can be deduced from the configurational force distribution in the active plastic zone. For the explanation, the

following formulation for the bulk configurational force $\mathbf{f}^{\mathrm{ep}}$ for small-strain plasticity[15] is helpful (Simha et al. 2008),

$$\mathbf{f}^{\mathrm{ep}} = \boldsymbol{\sigma} : \frac{\partial \boldsymbol{\varepsilon}^{\mathrm{p}}}{\partial \mathbf{x}} . \tag{8.6}$$

Here, $\boldsymbol{\sigma}$ is the Cauchy stress tensor and $\boldsymbol{\varepsilon}^{\mathrm{p}}$ the plastic part of the linear strain tensor $\boldsymbol{\varepsilon}$. According to Eq. (8.1), only the *x*-component of the configurational force,

$$f_x^{\mathrm{ep}} = \sigma_{xx} \frac{\partial \varepsilon_{xx}^{\mathrm{p}}}{\partial x} + 2\sigma_{xy} \frac{\partial \varepsilon_{xy}^{\mathrm{p}}}{\partial x} + \sigma_{yy} \frac{\partial \varepsilon_{yy}^{\mathrm{p}}}{\partial x} , \tag{8.7}$$

contributes to the scalar J^{ep}-integral, if the crack grows in *x*-direction, see Fig. 8.1.

In the overload cases, the $\mathbf{f}^{\mathrm{ep}}$-vectors in the active plastic zone at t = 58 are significantly smaller than in the constant load case, which leads to a reduction of $J^{\mathrm{ep}}_{\mathrm{actPZ,max}}$, compare Eq. (8.4). The smaller $\mathbf{f}^{\mathrm{ep}}$-vectors can be attributed to significantly reduced stresses and plastic strain gradients in the post-overload period, Eq. (8.6). Figure 8.5 shows, for example, that the normal stress component σ_{yy} around the crack tip is in the OL case (Fig. 8.5e,h) distinctively lower than in the CL case (Fig. 8.5b). As a consequence of these smaller stresses, the magnitude of the active plastic zone becomes also smaller, which additionally diminishes $J^{\mathrm{ep}}_{\mathrm{actPZ,max}}$, Eq. (8.4). In the contact case, the extension of the active plastic zone in *y*-direction decreases from the 5$^{\mathrm{th}}$ to the 20$^{\mathrm{th}}$ load cycle from $r_{\mathrm{actPZ},y}$ = 0.24 mm at Δa = 0.02 mm to 0.08 mm at Δa_{d} = 0.32 mm, whereas $r_{\mathrm{actPZ},y}$ remains 0.90 mm in the CL case. With further crack growth, $r_{\mathrm{actPZ},y}$ gradually increases and reaches at Δa_{OL} the magnitude of the value for constant cyclic loading.

Such a strong reduction of the active plastic zone size does not appear in the overlap case; $r_{\mathrm{actPZ},y} \approx 0.24$ mm for $N = 5 \div 20$. This can be understood from Fig. 8.5d,g: At minimum load, high compressive stresses appear in front of the crack tip if crack flanks can overlap, whereas much lower compressive stresses appear in front of the crack tip in the presence of crack flank contact. Consequently, the near-tip region experiences in the overlap case a higher stress amplitude during re-loading to the maximum load, which results in a larger active plastic zone. This becomes evident from Fig. 8.5f,i where the equivalent stress σ_{eq} is plotted at t = 58. The active plastic zone corresponds to the red area, i.e. where the yield strength is reached, $\sigma_{\mathrm{eq}} = \sigma_{\mathrm{y}}$. A comparison of the OL- and CL cases with crack flank contact shows that distinctively higher stresses appear at maximum load in the CL case, Fig. 8.5b, leading to higher equivalent stresses and a significant larger active plastic zone, Fig. 8.5c. This is connected to distinctively lower compressive stresses at minimum load (Fig. 8.5a).

[15] Simha et al. (2008) derived also the expression for large-strain plasticity.

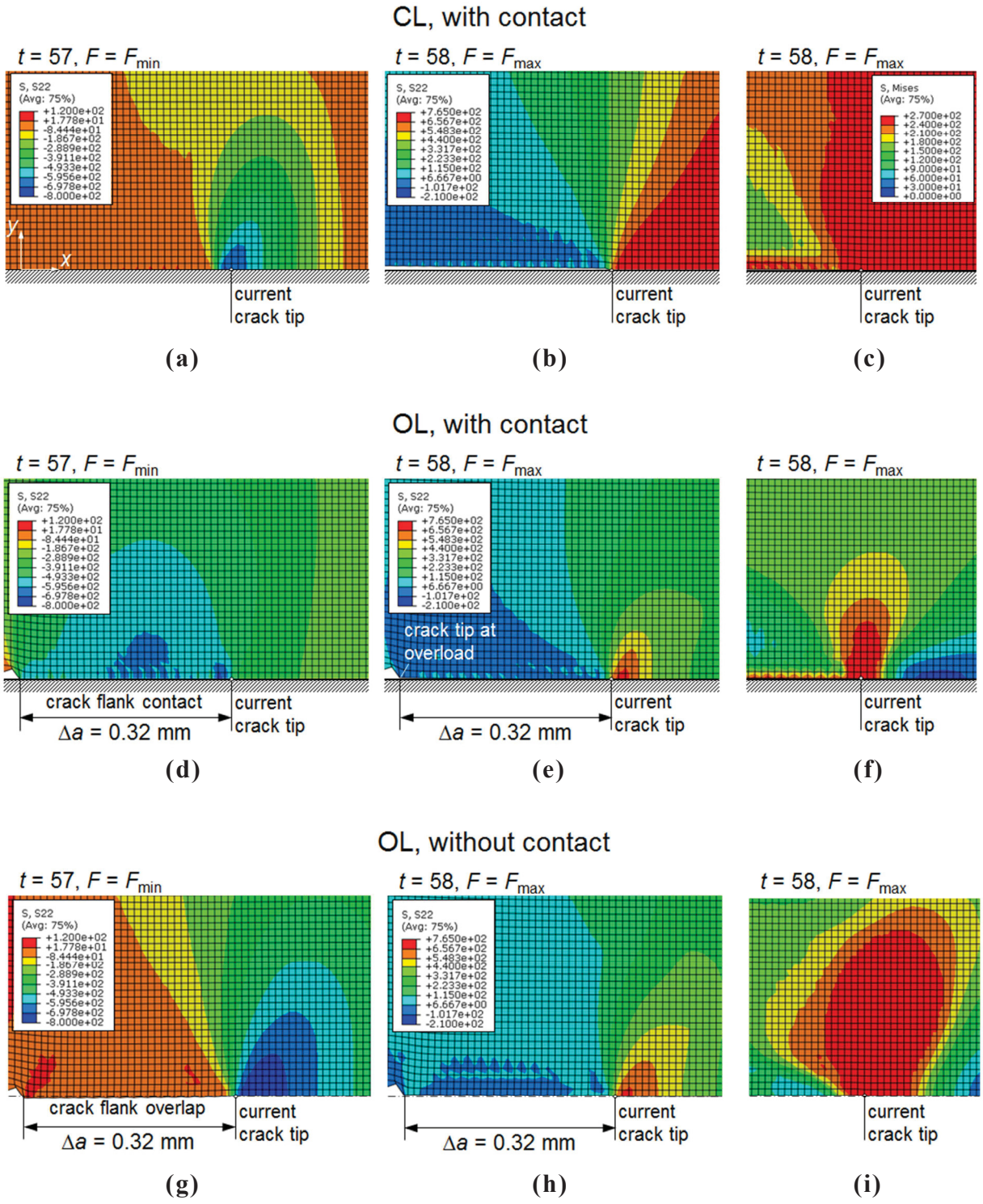

Fig. 8.5 Contour plots of the normal stress σ_{yy} at minimum load (time $t = 57$, $\Delta a = 0.32$ mm after overload), at maximum load ($t = 58$) of the 20th load cycle, and map of equivalent stress σ_{eq} at $t = 58$. **(a) (b) (c)** Constant cyclic loading (CL) with load ratio $R = 0$, **(d) (e) (f)** overload (OL) case for overload ratio $R_{OL} = 2$ with crack flank contact, **(g) (h) (i)** OL case without crack flank contact. The legend for **(f) (i)** is the same as in **(c)**.

In the OL case with crack flank overlap, the larger magnitude of the active plastic zone also contributes to higher values of $\left(J^{\mathrm{ep}}_{\mathrm{actPZ,max}}\right)^{\mathrm{overlap}}_{\mathrm{OL}}$ compared to the contact case. However, the main contribution arises from larger configurational forces $\mathbf{f}^{\mathrm{ep}}$ in the near-tip region at $F_{\max}$, since both stress and gradients of plastic strain are larger when crack flank overlap is possible, Eq. (8.7).

Equation (8.7) makes also clear that the *x*-component of the configurational force will change its sign, if the normal stress components near the crack tip changes during the unloading from tensile at maximum load to compressive, whereas the signs of the plastic strain gradients do not change. This explains the occurrence of negative $J^{\mathrm{ep}}_{\mathrm{actPZ}}$-values in Fig. 8.4a; for more details see Ochensberger and Kolednik (2014). If the compressive load is so high that also the plastic strain components (and the gradients) change their sign, the $J^{\mathrm{ep}}_{\mathrm{actPZ}}$-values can become positive again and large, as seen in Fig. 8.4b in the overlap case. On the contrary, the components of the plastic strain gradient are very low near minimum load in the presence of crack flank contact. This is the reason why configurational forces almost disappear in the active plastic zone and $\left(J^{\mathrm{ep}}_{\mathrm{actPZ,min}}\right)^{\mathrm{contact}}_{\mathrm{OL}}$ becomes roughly zero, Fig. 8.4b.

The conclusion of this section is that the strong reduction in the fatigue crack driving force $\Delta J^{\mathrm{ep}}_{\mathrm{actPZ}}$ following an overload is attributed to a significant reduction of the near-tip stresses, which occurs, for R = 0 and R_{OL} = 2 and the assumed plane strain conditions, independent of crack flank contact. Crack flank contact further reduces the near-tip stresses, which significantly affect the size of the active plastic zone, but this leads only to a little further decrease of $\Delta J^{\mathrm{ep}}_{\mathrm{actPZ}}$.

8.5 Influences of overload ratio and load ratio on the overload effect

It is well-known that the overload effect depends on the overload ratio R_{OL} and the load ratio R (e.g. Suresh 1998; Skorupa 1998; Sadananda et al. 1999; Roychowdhury and Dodds 2005). The parameters R_{OL} and R are varied separately in order to study how they influence the findings of Section 8.4.

8.5.1 Variation of overload ratio R_{OL}

Figure 8.6a presents, similar to Fig. 8.3a, the variations of the fatigue crack driving force $\Delta J^{\mathrm{ep}}_{\mathrm{actPZ}}$ with and without contact for R = 0 and three different overload ratios R_{OL} = 2, 1.6 and 1.2; the constant load case is marked as solid line. Figures 8.6b,c show details for the ranges Δa = 0 ÷ 0.8 mm and Δa = 4.0 ÷ 5.8 mm after overload. The characteristic overload-affected crack growth distances and the cyclic *J*-integral values $\Delta J^{\mathrm{ep}}_{\mathrm{actPZ}}$ for the contact and overlap cases are collected in Tables 8.1 and 8.2.

It is seen that the variations of $\Delta J^{\mathrm{ep}}_{\mathrm{actPZ}}$ with and without crack flank contact exhibit a very uniform behavior if R_{OL} is decreased: Only the degree of crack growth retardation and the overload-affected crack growth distances, Δa_{d}, $\Delta a_{r\mathrm{pl,OL}}$, and Δa_{OL}, become smaller (Fig. 8.6a, Tables 8.1 and 8.2). The reason is that lower compressive stresses are induced after unloading from F_{OL} in a smaller overload plastic zone. Consequently, higher stresses appear around the

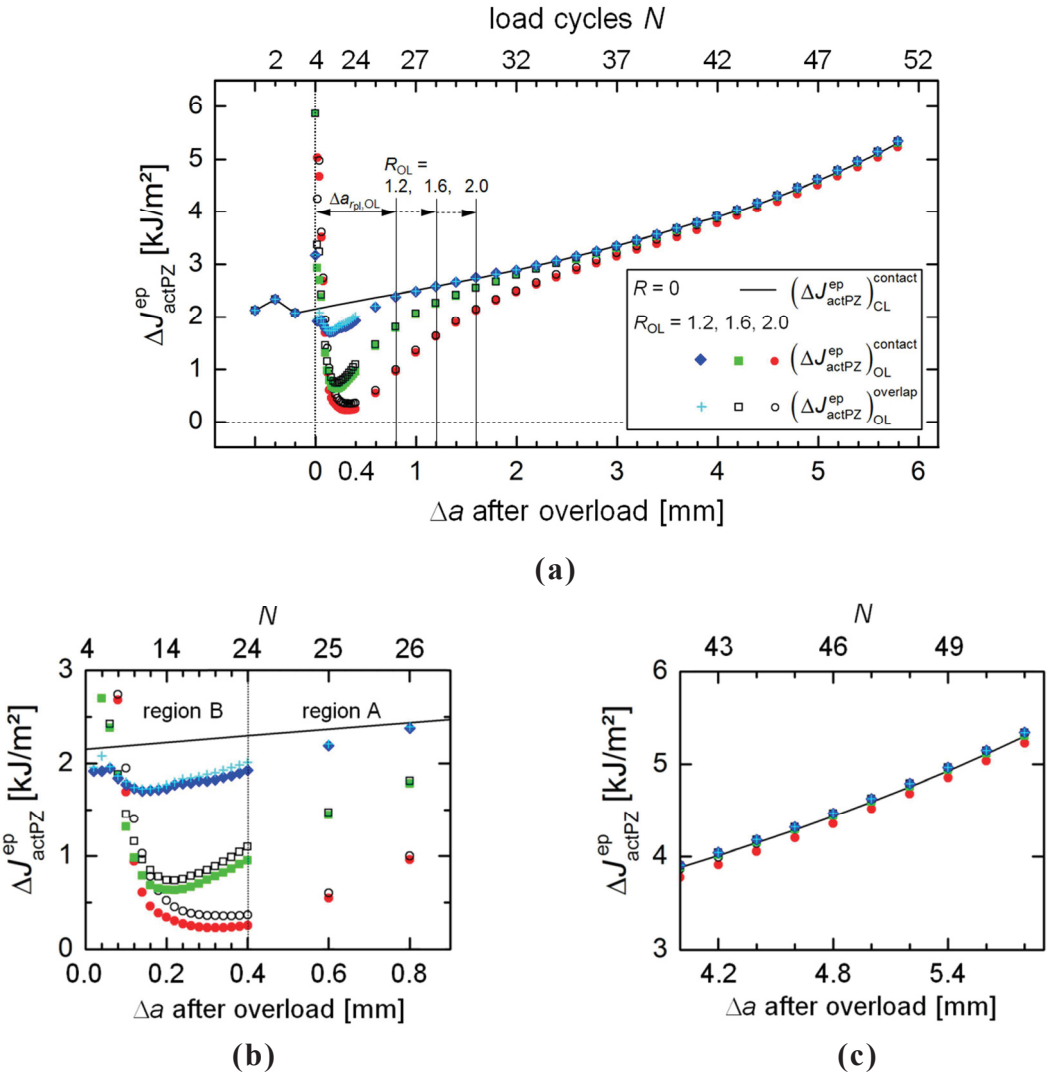

Fig. 8.6 Overload effect for load ratio $R = 0$ and various overload ratios $R_{OL} = 1.2$, 1.6 and 2. Driving force for fatigue crack growth ΔJ^{ep}_{actPZ} with and without crack flank contact plotted against crack extension Δa from the overload. **(a)** Overview; vertical lines indicate the distances $\Delta a_{rpl,OL}$, compare Table 8.1. **(b) (c)** Details for $\Delta a = 0 \div 0.8$ mm and $\Delta a = 4.0 \div 5.8$ mm.

crack tip after re-loading to F_{max} which implies larger $\mathbf{f}^{ep}$-vectors, Eq. (8.6), and larger magnitudes of the active plastic zone. Therefore, ΔJ^{ep}_{actPZ} exhibits higher values compared to the case with $R_{OL} = 2$. The shorter delay-distance Δa_d is connected to weaker crack-tip blunting induced by the smaller overload. For $R_{OL} = 1.2$, crack growth retardation occurs already in the first load cycle after the overload, $N = 5$ (Fig. 8.6b).

Tables 8.1 and 8.2 suggest a roughly linear decrease of the OL-affected crack growth distances, Δa_d and Δa_{OL}, and of the maximum relative reduction of the fatigue crack driving force, $\Delta^{CL}_{contact}$ and $\Delta^{CL}_{overlap}$, Eq. (8.5), with decreasing R_{OL}; the parameter $\Delta a_{rpl,OL}$ exhibits exactly a linear behavior. The relative difference between the minimum values of the driving forces for the contact and overlap cases, $\left(\Delta J^{ep}_{actPZ}\right)^{contact}_{OL}$ and $\left(\Delta J^{ep}_{actPZ}\right)^{overlap}_{OL}$, at Δa_d becomes

55%, 16% and 0.3% for R_{OL} = 2, 1.6 and 1.2, respectively. This decreasing difference indicates that the role of crack flank contact decreases with decreasing R_{OL} as has been reported e.g. in Roychowdhury and Dodds (2005).

8.5.2 Variation of load ratio R

Figure 8.7a presents, similar to Fig. 8.3a, the variations of the driving force ΔJ^{ep}_{actPZ} with and without contact for R_{OL} = 2 and three different load ratios, R = 0, 0.5 and –1. The solid lines denote the constant load cases with crack flank contact. The dashed green line denotes the constant load case for crack flank overlap under R = –1. Figures 8.7b,c show details for Δa = 0 ÷ 0.8 mm and Δa = 4.0 ÷ 5.8 mm after overload. The characteristic overload-affected crack growth distances are listed in Table 8.1, and the ΔJ^{ep}_{actPZ}- and Δ^{CL}_{i} -values for R = 0.5 and –1 are given in Table 8.3.

First, we consider the effect of the load ratio on the constant load (CL) cases. For positive load ratios, the J-integral values at minimum load are positive, $\left(J^{ep}_{actPZ,min}\right)_{CL} > 0$, which leads to non-zero square root terms in Eq. (8.3) and lower values of the fatigue driving force $\left(\Delta J^{ep}_{actPZ}\right)_{CL}$, compared to the case with $R = 0$. Figure 8.7a shows that the fatigue crack driving force $\left(\Delta J^{ep}_{actPZ}\right)_{CL}$ for $R = 0.5$ is roughly one third of that for $R = 0$. It is also seen that the $\left(\Delta J^{ep}_{actPZ}\right)^{contact}_{CL}$-curves for $R = 0$ and $R = -1$ coincide. This can be explained by the observation that the crack tip is closed when J^{ep}_{actPZ} becomes negative (Section 8.4.2.), so that the driving force is not influenced by further unloading. The difference between $\left(\Delta J^{ep}_{actPZ}\right)^{contact}_{CL}$ and $\left(\Delta J^{ep}_{actPZ}\right)^{overlap}_{CL}$ is zero or negligible for $R \geq 0$. This is, however, not so for negative load ratios. Figure 8.7 shows that, for $R = -1$, the driving force for the overlap case is roughly 10% larger than that of the contact case. The reason lies in the higher $\left(J^{ep}_{actPZ,max}\right)^{overlap}_{CL}$-values, see Section 8.4.4 and below.

Next, we consider the effects of an overload with R_{OL} = 2 for the three load ratios. Figures 8.7a,b show that, for $R = 0.5$, the fatigue crack driving force ΔJ^{ep}_{actPZ} becomes roughly zero, i.e. of the order of 10^{-3} kJ/m^2, already after a crack extension of $\Delta a = 0.12$ mm following the overload and remains small up to $\Delta a \approx 0.30$ mm (Fig. 8.7b). The minimum of ΔJ^{ep}_{actPZ} appears at Δa_d = 0.16 mm (Table 8.3). These findings are valid with and without crack flank contact.

The results indicate that the crack growth retardation effect of an overload is higher for a positive load ratio than for $R = 0$. A reason might be that, for a constant overload ratio $R_{OL} = F_{OL}/F_{max}$, the ratio $F_{OL}/\Delta F$ increases with increasing positive R (e.g. Skorupa 1998). An additional overload experiment has been conducted with R_{OL} = 2 and R = 0.8 where a nearly zero crack driving force was also predicted. Note that $\Delta J^{ep}_{actPZ} \approx 0$ implies that the crack tip remains closed during the load cycle, $\Delta\delta_t \approx 0$, hence, the fatigue crack growth rate da/dN is zero.

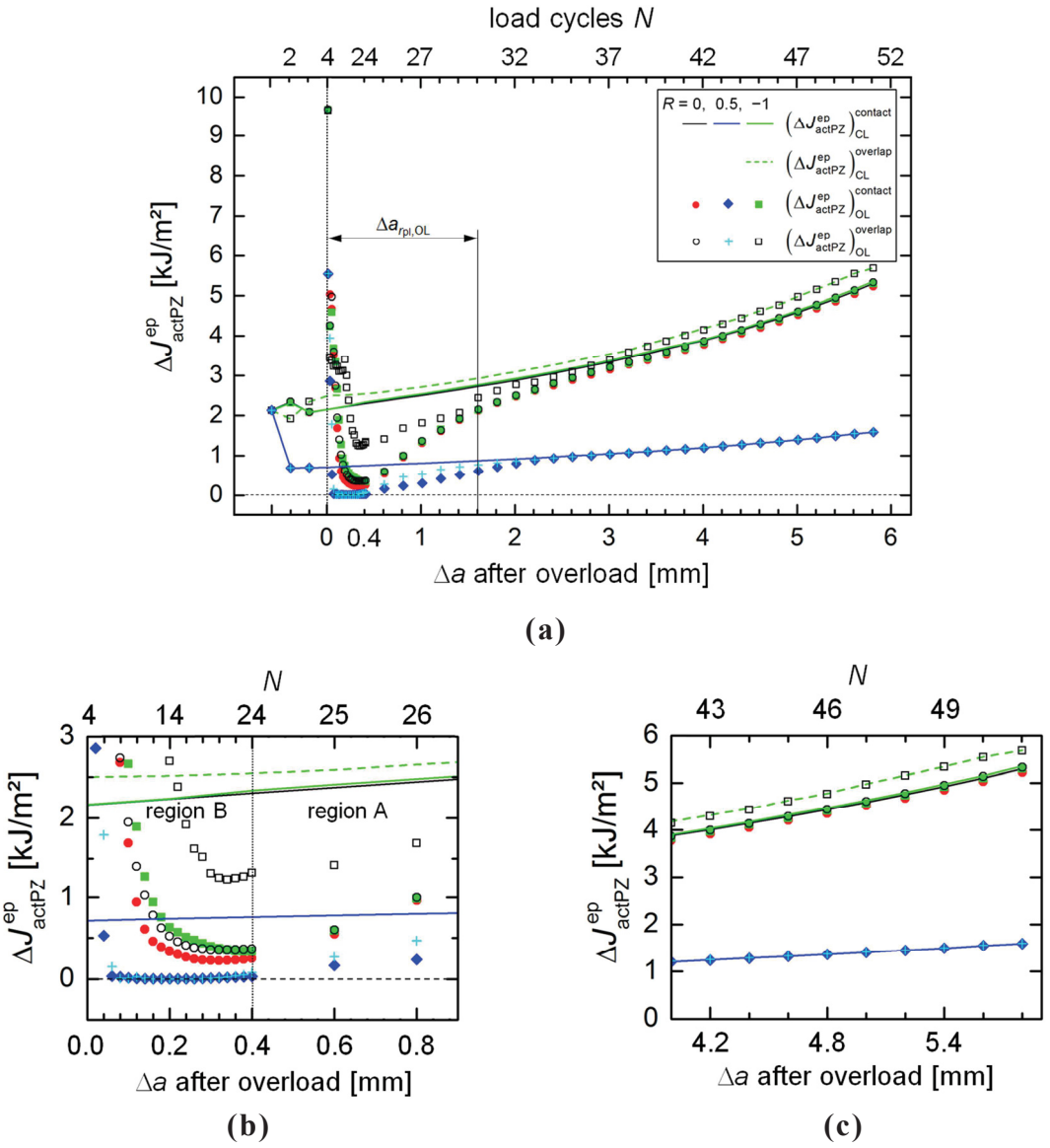

Fig. 8.7 Overload effect for overload ratio $R_{OL} = 2$ and various load ratios $R = 0,\ 0.5,\ -1$. Driving force for fatigue crack growth ΔJ^{ep}_{actPZ} with and without crack flank contact plotted against crack extension Δa from the overload. **(a)** Overview. **(b) (c)** Details for $\Delta a = 0 \div 0.8$ mm and $\Delta a = 4.0 \div 5.8$ mm.

The configurational force analysis reveals that, in the range $\Delta a = 0.12 \div 0.3$ mm, the $\mathbf{f}^{ep}$-vectors remain very small in the near-tip region at F_{max}, so that $J^{ep}_{actPZ,max} \approx 0$. The active plastic zone is in the contact case smaller than one element length, $r^{contact}_{actPZ,y} < 0.01$ mm. Therefore, the simulation was repeated with a FE-mesh size of $m = 0.001$ mm to determine the size of the active plastic zone for the integration path Γ_{actPZ}. The difference between $\left(\Delta J^{ep}_{actPZ}\right)^{contact}_{OL}$ and $\left(\Delta J^{ep}_{actPZ}\right)^{overlap}_{OL}$ during $\Delta a = 0.4 \div 2.2$ mm, Fig. 8.7a, originates from lower, positive J-integral values at minimum load for the overlap case, see Eq. (8.3). In the range $\Delta a > 2.2$ mm, crack flank contact does disappear, and the driving force ΔJ^{ep}_{actPZ} reaches the CL-values for both OL cases (Fig. 8.7a,c and Table 8.3).

Table 8.3 Values of the cyclic incremental plasticity *J*-integral around the active plastic zone, $\Delta J^{\mathrm{ep}}_{\mathrm{actPZ}}$, Eq. (3), and $\Delta J^{\Delta K_{\mathrm{eff}}}_{\mathrm{OL}}$, Eq. (8.8), for load ratios R = 0.5 and −1, and overload ratio R_{OL} = 2. The parameters $\Delta^{\mathrm{CL}}_{\mathrm{i}}$ give the relative reduction in driving force with respect to the constant load case, Eq. (8.5).

R	N	Δa	$\left(\Delta J^{\mathrm{ep}}_{\mathrm{actPZ}}\right)^{\mathrm{contact}}_{\mathrm{CL}}$	$\left(\Delta J^{\mathrm{ep}}_{\mathrm{actPZ}}\right)^{\mathrm{contact}}_{\mathrm{OL}}$	$\left(\Delta J^{\mathrm{ep}}_{\mathrm{actPZ}}\right)^{\mathrm{overlap}}_{\mathrm{OL}}$	$\Delta J^{\Delta K_{\mathrm{eff}}}_{\mathrm{OL}}$	$\Delta^{\mathrm{CL}}_{\mathrm{contact}}$	$\Delta^{\mathrm{CL}}_{\mathrm{overlap}}$	$\Delta^{\mathrm{CL}}_{\Delta K\mathrm{eff}}$
[-]	[-]	[mm]	[kJ/m²]				[%]		
0.5	12	*0.16*	0.734	*6.5e–4*	*–4.2e–4*	*0.002*	*100*	*100*	*99.7*
0.5	30	1.6	0.877	0.620	0.773	0.429	29.3	11.9	51.1
0.5	37	3.0	1.053	1.039	1.048	0.895	1.33	0.47	15.0
0.5	38	3.2	1.080	1.073	1.082	0.921	0.65	–0.19	14.7
0.5	51	5.8	1.600	1.595	1.602	1.386	0.31	–0.13	13.4
–1	21	*0.34*	2.304	0.356	*1.240*	0.351	84.6	*46.2*	84.8
–1	23	*0.38*	2.325	*0.340*	1.277	*0.347*	*85.4*	45.1	*85.1*
–1	30	1.6	2.769	2.136	2.441	0.964	22.9	11.9	65.2
–1	42	4.0	3.906	3.825	4.146	2.639	2.07	–6.14	32.4
–1	51	5.8	5.357	5.299	5.685	4.200	1.08	–6.12	21.6

For negative load ratio, $R=-1$, the driving force with crack flank contact $\left(\Delta J^{\mathrm{ep}}_{\mathrm{actPZ}}\right)^{\mathrm{contact}}_{\mathrm{OL}}$ is, compared to the case $R=0$, slightly larger. The largest difference occurs during the rapid decrease of $\Delta J^{\mathrm{ep}}_{\mathrm{actPZ}}$ after the overload (Fig. 8.7b). The reason for the difference can be easily understood by comparing two specimens during unloading and first re-loading after the OL. The crack in the specimen with $R=-1$ opens at a lower load than the crack in the specimen with $R=0$. Therefore, the near-tip region becomes higher stressed during loading to $F_{\max}$, and $\left(\Delta J^{\mathrm{ep}}_{\mathrm{actPZ}}\right)^{\mathrm{contact}}_{\mathrm{OL}}$ becomes larger. Also in the subsequent load cycles, the closure and opening loads where crack flank contact appears or disappears will be lower for $R=-1$, but the difference diminishes. The overload leads to a maximum reduction of the driving force of 85.4% of the CL-value at $\Delta a_{\mathrm{d}}=0.38$ mm for $R=-1$, compared to 89.8% at $\Delta a_{\mathrm{d}}=0.32$ mm for $R=0$.

The significant higher $\left(J^{\mathrm{ep}}_{\mathrm{actPZ,max}}\right)^{\mathrm{overlap}}_{\mathrm{CL}}$-values for $R=-1$ compared to $R=0$ originate from the fact that the crack tip region experiences the full compressive loading to $F_{\min}$, since crack flank overlap is possible.

The following conclusions can be drawn from the results of this section: The overload effect becomes less pronounced with decreasing overload ratio R_{OL}. The conclusion of Section 8.4, that (for $R=0$) the retardation effect after an overload is mainly caused by the reduction of the near-tip stresses and only slightly influenced by crack flank contact, holds also for positive load ratios. For R = 0.5, the fatigue crack driving force can reach a value of zero, although no crack flank contact appears. It is clear that the role of crack flank contact becomes, however, more important under tension-compression loading, $R<0$.

The computations in this paper have been conducted for an elastic–ideally plastic material behavior. We performed additional numerical overload experiments for a material

with isotropic hardening. The selected material is an annealed steel with German designation St37, also used in Simha et al. (2008), Kolednik et al. (2014), Ochensberger and Kolednik (2014), which can be described by the Ramberg–Osgood law. Young's modulus, Poisson's ratio, and yield stress are the same as given in Section 3.1; the ultimate tensile stress is σ_u = 426 MPa, the average strain hardening exponent is n = 0.2. Basically, the results do not change compared to the cases with ideally plastic material. We only observed that the overload effect is slightly smaller.

8.6 Characterization of overload effects with the effective stress intensity range ΔK_{eff}

For the assessment of the fatigue crack growth rate in presence of crack flank contact, Elber (1970, 1971) proposed to apply the effective stress intensity range, $\Delta K_{\mathrm{eff}} = K_{\max} - K_{\mathrm{op}}$, with K_{op} as the stress intensity at the crack opening load F_{op}, i.e. where crack flank contact fully disappears during re-loading of the specimen. According to Elber (1970, 1971), F_{op} can be determined from the compliance changes, visible as kinks in the load–displacement (F–v) curve (e.g. Elber 1970, 1971; Fleck 1988; Suresh 1998). The parameter ΔK_{eff} can be applied to quantify the overload effect, provided that small-scale yielding conditions prevail after the overload (Schijve 2009). Hereby crack growth retardation is related to an enhancement of the crack opening level, K_{op}, which leads to a reduction of ΔK_{eff} (e.g. Elber 1970, 1971; von Euw et al. 1972; Fleck 1988; Suresh 1998).

In the following, the application of the effective stress intensity range ΔK_{eff} for the description of the overload effect shall be checked. To do so, we compare the variations of ΔK_{eff} to the variations of the driving force for the contact cases, $\left(\Delta J^{\mathrm{ep}}_{\mathrm{actPZ}}\right)^{\mathrm{contact}}_{\mathrm{OL}}$, presented in Sections 8.4 and 8.5. The values of the stress intensity factor K are evaluated from the load F, following ASTM E1820 (2005). For the evaluation of K_{op}, the crack opening load F_{op} is determined from the compliance change of a loading branch of the F–v-curve. In Fig. 8.8a, examples are presented for the 24$^{\mathrm{th}}$ and 37$^{\mathrm{th}}$ load cycle, Δa = 1 mm and 3 mm, after an overload with R = 0 and R_{OL} = 2; the solid line (F–v^{contact}) denotes the contact case, the dashed line (F–v^{overlap}) the overlap case. Crack flank contact disappears (point "op") when the F–v-curves for the contact and overlap cases exhibit the same compliance. Note that the overlap case cannot exhibit a compliance change, since crack flank contact is not possible. In order to identify accurately the point of crack opening ("op") the *offset procedure* is applied (Fig. 8.8b); see e.g. Kikukawa et al. (1976), Fleck (1988), or Suresh (1998) for details. In our cases, the offset displacement v^* is computed by subtracting the load-line displacement corresponding to the overlap case, v^{overlap}, from the displacement of the real (contact) case, $v^* = v^{\mathrm{contact}} - v^{\mathrm{overlap}}$. Hereby, the compliance change becomes easier visible, compare Figs. 8.8a,b.

For comparison purposes, it is necessary to transform ΔK_{eff} into a cyclic J-integral value,

$$\Delta J^{\Delta K_{\mathrm{eff}}} = \Delta K_{\mathrm{eff}}^2 / E' , \tag{8.8}$$

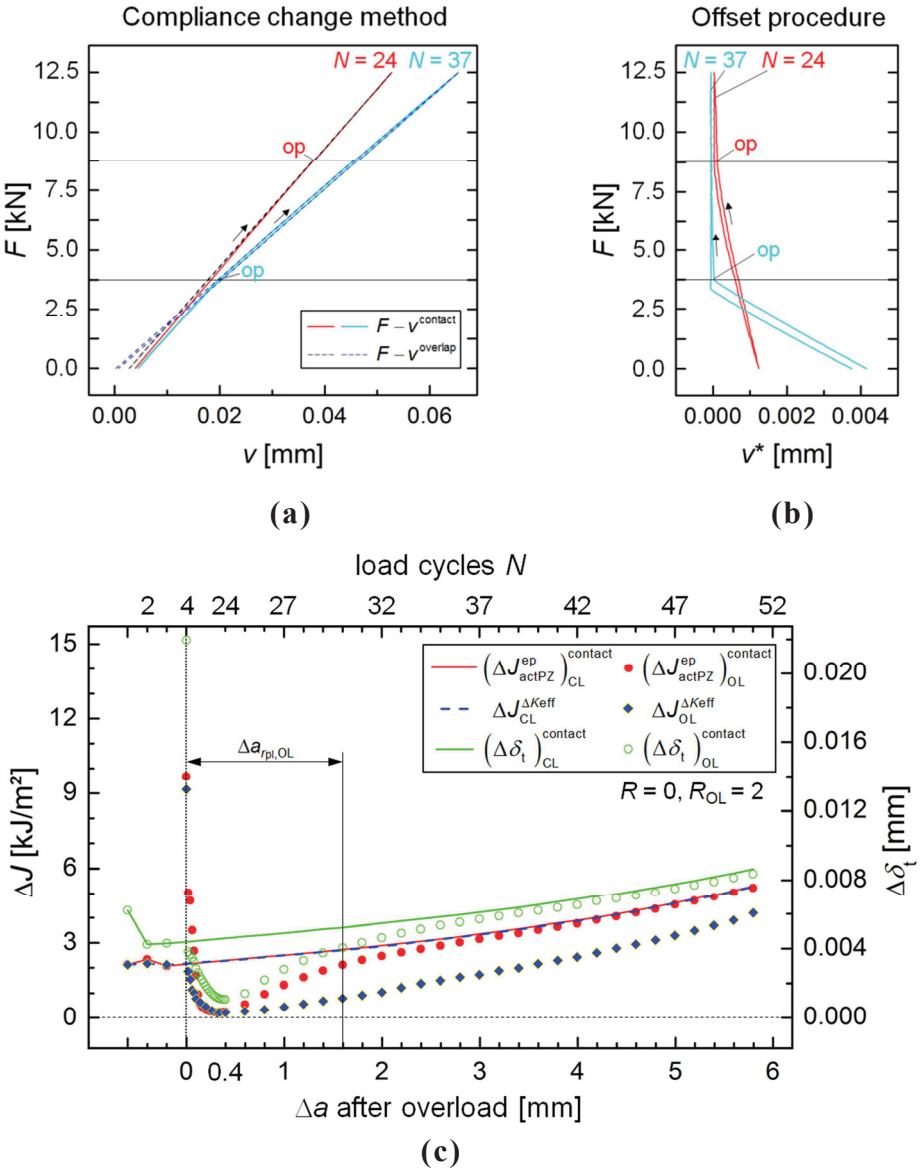

Fig. 8.8 **(a)** Effect of crack flank contact on the specimen compliance: F–v-curve for the 24th and 37th load cycle. **(b)** Determination of crack opening with the offset procedure. **(c)** Cyclic J-integral calculated from the effective stress intensity range $\Delta J_{\mathrm{OL}}^{\Delta K_{\mathrm{eff}}}$, Eq. (8.8), cyclic crack tip opening displacement $\left(\Delta\delta_{\mathrm{t}}\right)_{\mathrm{OL}}^{\mathrm{contact}}$ and $\left(\Delta J_{\mathrm{actPZ}}^{\mathrm{ep}}\right)_{\mathrm{OL}}^{\mathrm{contact}}$ versus crack extension Δa after overload for $R_{\mathrm{OL}} = 2$ and $R = 0$. The respective values for constant loading are also included.

analogously to the relation, $\Delta J = \Delta K^2 / E'$ (Dowling and Begley 1976; Wüthrich 1982; Anderson 1995). $E' = E/\left(1-\nu^2\right)$ for plane strain conditions, and the superscript "ΔK_{eff}" indicates that ΔJ has been calculated via the effective stress intensity range.

Figure 8.8c presents the variations of $\Delta J_{\mathrm{OL}}^{\Delta K_{\mathrm{eff}}}$ and $\left(\Delta J_{\mathrm{actPZ}}^{\mathrm{ep}}\right)_{\mathrm{OL}}^{\mathrm{contact}}$ after an overload for $R = 0$ and $R_{\mathrm{OL}} = 2$. The variation of the cyclic crack tip opening displacement $\left(\Delta\delta_{\mathrm{t}}\right)_{\mathrm{OL}}^{\mathrm{contact}}$ is shown for comparison. Note that Bichler and Pippan (1999, 2007) demonstrated the proportionality between the fatigue crack growth rate da/dN and $\Delta\delta_{\mathrm{t}}$ by comparisons of the fatigue striations

with the crack tip opening displacement δ_t, determined by stereophotogrammetric measurements (Stampfl et al. 1996a,b). The cyclic crack tip opening displacement is computed 0.1 mm behind the actual crack tip, which corresponds to the largest mesh size applied in region A. It should be remarked here that the δ_t-values are strongly mesh dependent, and a very fine FE mesh would be required for the calculation of accurate δ_t-values. However, a distance of 0.1mm is sufficient for our purposes, to estimate the relative change in δ_t with crack extension after an overload. In contrast to δ_t, the values of J^{ep}_{actPZ} are only weakly mesh dependent, see Ochensberger and Kolednik (2015).

Figure 8.8c shows that the cyclic incremental plasticity *J*-integral around the active plastic zone, $\left(\Delta J^{ep}_{actPZ}\right)^{contact}_{OL}$, reflects very well the variation of the cyclic crack tip opening displacement. The parameter $\Delta J^{\Delta K_{eff}}_{OL}$ is not able to reflect the delayed retardation phenomenon, but gives good approximations of $\left(\Delta J^{ep}_{actPZ}\right)^{contact}_{OL}$ during the period of maximum retardation. The minimum driving force at Δa_d is accurately predicted. With further increasing Δa, however, $\Delta J^{\Delta K_{eff}}_{OL}$ significantly underestimates the true fatigue crack driving force $\left(\Delta J^{ep}_{actPZ}\right)^{contact}_{OL}$, and the values for constant fatigue load are clearly missed even for large crack extensions. The values of $\Delta J^{\Delta K_{eff}}_{OL}$ and of the relative reduction of the fatigue crack driving force $\Delta^{CL}_{\Delta K_{eff}}$ for different Δa-values are included in Table 8.2. The misfit between $\Delta J^{\Delta K_{eff}}_{OL}$ and $\left(\Delta J^{ep}_{actPZ}\right)^{contact}_{OL}$ first increases to 67% at $\Delta a = 2$ mm, and decreases with further crack extension to 21% at $\Delta a = 5.8$ mm. Tables 8.2 and 8.3 show that $\Delta J^{\Delta K_{eff}}_{OL}$ accurately predicts the minimum in $\left(\Delta J^{ep}_{actPZ}\right)^{contact}_{OL}$ also for other R_{OL}- or R-values; however, the large error after the maximum retardation period remains, except for $\Delta a > 4$ mm under $R = 0$ and $R_{OL} = 1.2$.

It should be mentioned that such underestimations of the fatigue crack driving force by ΔK_{eff}, which we found under the assumption of plane strain conditions, Fig. 8.8c, have been already reported by Fleck (1988), who performed overload experiments on 24 mm thick and 3 mm thin C(T)-specimens. The effect is referred to as *discontinuous crack closure/opening phenomenon*: After an overload, a "residual hump" is created on the crack surface, which leads to higher crack opening loads and too low ΔK_{eff}-values, compared to constant cyclic loading. Thus, ΔK_{eff} does not reflect the true stress intensity range experienced by the crack tip after the period of maximum retardation following an overload (Fleck 1988). This finding has been also confirmed by three-dimensional finite element studies, e.g., in Roychowdhury and Dodds (2005).

It can be concluded from this section that the effective stress intensity range ΔK_{eff} is able to quantify accurately the maximum retardation after an overload. However, ΔK_{eff} does not deliver the delayed retardation phenomenon and significantly underestimates the driving force for fatigue crack growth for longer crack extensions after the overload. The reason is that ΔK_{eff} is not able to reflect fully the behavior of the actual crack tip, which determines the fatigue crack propagation rate.

8.7 Summary

It has been demonstrated in this paper that the cyclic incremental plasticity *J*-integral $\Delta J^{\mathrm{ep}}_{\mathrm{actPZ}}$, which is computed by Eq. (8.3) for a contour around the *active* plastic zone of the growing crack, is an appropriate tool for the description of the overload effect in fatigue. The parameter $\Delta J^{\mathrm{ep}}_{\mathrm{actPZ}}$ is able to reflect the variation of the cyclic crack tip opening displacement at the current crack tip, $\Delta\delta_{\mathrm{t}}$, but with much less computational effort.

The computation of the *J*-integral $J^{\mathrm{ep}}_{\mathrm{actPZ}}$ during cyclic loading after an overload, in combination with a configurational force analysis, demonstrate that the main features of the overload effect, i.e. the strong reduction in the fatigue crack driving force $\Delta J^{\mathrm{ep}}_{\mathrm{actPZ}}$ and the delayed retardation phenomenon, occur, no matter whether crack flank contact does exist or not. The reduction in $\Delta J^{\mathrm{ep}}_{\mathrm{actPZ}}$ after an overload is mainly caused by a significant reduction of the near-tip stresses. Crack flank contact further reduces the near-tip stresses, but this leads, for a load ratio $R \geq 0$, only to little or no further decrease of $\Delta J^{\mathrm{ep}}_{\mathrm{actPZ}}$. For example, the analyses for $R = 0.5$ showed that the driving force can even reach a value of zero, although no crack flank contact appears.

It should be stressed that this does not mean that crack flank contact is unimportant. Even if the additional reduction of the driving force due to crack flank contact is small, e.g. our analyses for $R = 0$ gave a further reduction of 6% compared to the constant load case, this difference may decide whether a crack arrests or not. It is clear that the role of crack flank contact becomes more important under tension-compression loading, $R < 0$.

Note that all simulations in the current paper were conducted for two-dimensional specimens with a perfectly flat crack under plane strain assumptions, and for a non-hardening material. For a real three-dimensional specimen with rough crack flanks, the contribution of crack flank contact to the overload effect might be appreciably higher.

The results in this paper also show that the effective stress intensity range ΔK_{eff} can be used to determine the maximum crack growth retardation after an overload. However, ΔK_{eff} does not deliver the delayed retardation phenomenon and significantly underestimates the driving force for fatigue crack growth for longer crack extensions after the overload.

It should be mentioned that the development of a procedure, which enables the experimental determination of the correct fatigue crack driving force $\Delta J^{\mathrm{ep}}_{\mathrm{actPZ}}$ is currently under investigation.

Acknowledgements

Financial support by the Austrian Federal Government and the Styrian Provincial Government within the research activities of the K2 Competence Center on “Integrated Research in Materials, Processing and Product Engineering”, under the frame of the Austrian COMET Competence Center Programme, is gratefully acknowledged (strategic projects A4.20-WP3 and WP4).

9 Discussion

9.1 *Evaluation of the fatigue crack driving force for a stationary crack under general yielding conditions*

Paper I shows that the incremental plasticity cyclic J-integral ΔJ_{PZ}^{ep}, evaluated for a contour Γ_{PZ} around the crack tip plastic zone, characterizes the driving force of a *stationary* crack in an elastic–plastic material under cyclic loading. The parameter ΔJ_{PZ}^{ep} can be readily calculated if small- or large-scale yielding conditions prevail in the specimen, since a contour Γ_{PZ} can be easily drawn around the crack tip plastic zone (e.g. Fig. 6.1a and Fig. 6.4a). A problem appears if general yielding conditions prevail where a complete path through plastically deformed material exists between crack tip and back face region, so that a clean solution does not exist for separating the crack tip plastic zone by a contour Γ_{PZ}. Figure 9.1 illustrates this problem.

In the following it is investigated whether it is possible to find ΔJ_{PZ}^{ep} for gy-conditions in an *approximative* way and how this value fits to the value of the conventional cyclic J-integral ΔJ_{PZ}^{conv} and the experimental cyclic J-integral ΔJ^{exp}.

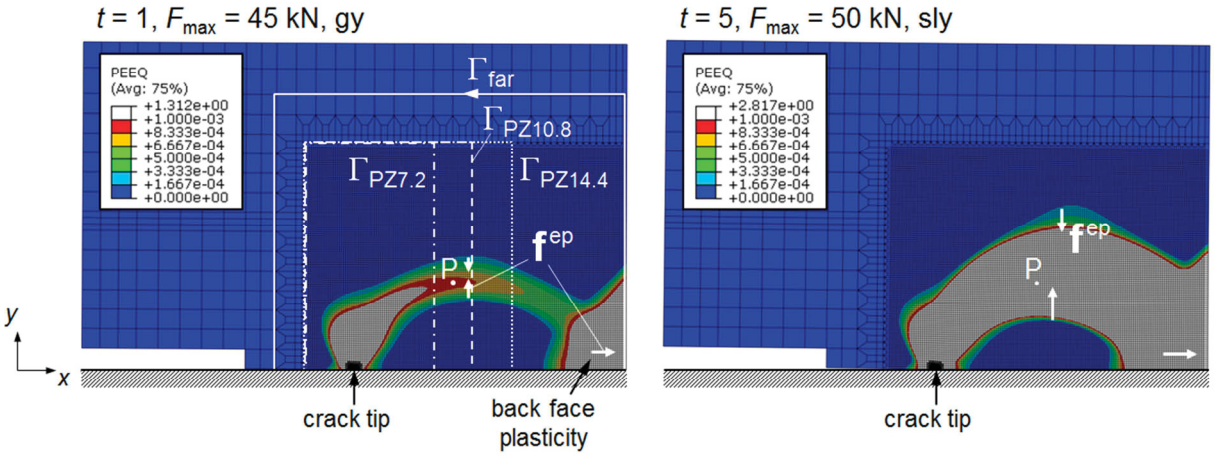

Fig. 9.1 Maps of the equivalent plastic strain ε_{eq}^{p} (or PEEQ) at **(a)** $F_{max,gy} = 45$ kN (time $t = 1$), *onset* of *general yielding*, and **(b)** $F_{max,sly} = 50$ kN (time $t = 5$), *severe ligament yielding* conditions. Global directions of the bulk configurational force $\mathbf{f}^{ep}$ are schematically inticated. In **(a)**, relevant J-integral contours are indicated.

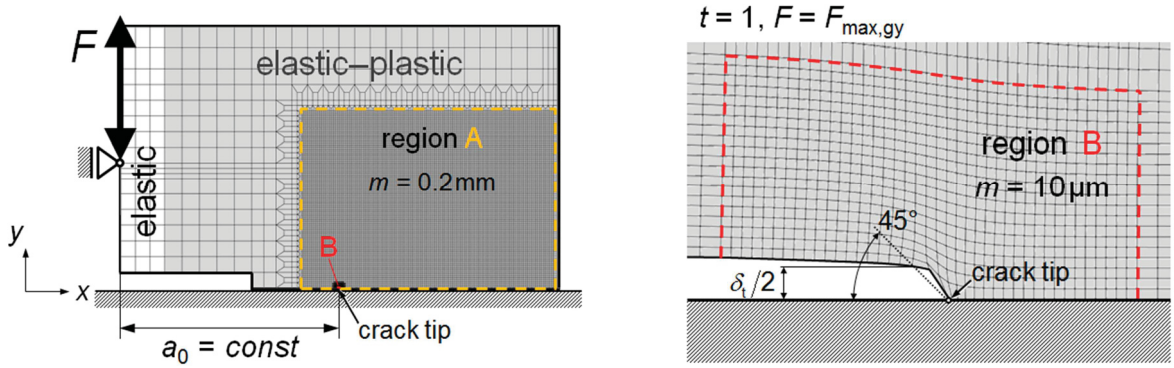

(a) **(b)**

Fig. 9.2 **(a)** FE-model with boundary conditions and different mesh regions A and B; region A has mainly a mesh size of m = 0.2 mm. **(b)** shows a detail of the fine mesh region B around the crack tip, with a mesh size m = 10 µm. The procedure for the determination of the crack tip opening displacement δ_t is also shown.

Numerical experiments are performed for the same finite element model as presented in Section 6.3, see Fig. 9.2a. Only some details are different:

The material tested is the annealed mild steel St37, which has been introduced in Section 6.5.4. An ideally plastic behavior would lead to convergence problems for load-prescribed tests in combination with general yielding. One numerical experiment consists of four load cycles. In the first two load cycles, N = 1, 2, the maximum load is set to $F_{\max,gy} = 45\,\mathrm{kN}$ resulting in general yielding (Fig. 9.1a); this load is known as *plastic limit load* (e.g. Anderson 1995). In the load cycles N = 3, 4, a higher load is chosen $F_{\max,sly} = 50\,\mathrm{kN}$ so that plastic deformation along the ligament significantly increases (Fig. 9.1b); this will be denoted as *severe ligament yielding* (sly) in the following. The equivalent plastic strain is, for example, $\varepsilon^{p}_{eq} = 0.06\,\%$ in point P for gy-conditions, see Fig. 9.1a; $\varepsilon^{p}_{eq} = 0.56\,\%$ for sly-conditions.

In order to get accurate crack tip opening displacement δ_t-values, a smaller element size is used in the near-tip region. Region A consists mainly of elements with mesh size $m = 0.2\,\mathrm{mm}$. Region $\mathrm{B} \subset \mathrm{A}$, with a dimension of $0.4 \times 0.2\,\mathrm{mm}^2$, is discretized with a finer mesh size of $m = 10\,\mu\mathrm{m}$, see Fig. 9.2b. The value of δ_t is taken at the intersection of a 45° line, drawn from the crack tip, with the upper crack flank (e.g. Anderson 1995, Suresh 1998, Kuna 2008).

J-integrals are evaluated for deformation plasticity and incremental plasticity, J^{conv}_{PZ} and J^{ep}_{PZ}, see Eq. (6.13) and Eq. (6.14). Three different contours are chosen, $\Gamma_{PZ7.2}$ (*dashed-dotted line*), $\Gamma_{PZ10.8}$ (*dashed line*), $\Gamma_{PZ14.4}$ (*dots*), see Fig. 9.1a; the number denotes the distance (in mm) of the right boundary of the contour in x-direction from the crack tip. The values of the cyclic J-integrals are calculated from Eq. (6.19) and Eq. (6.22), respectively.

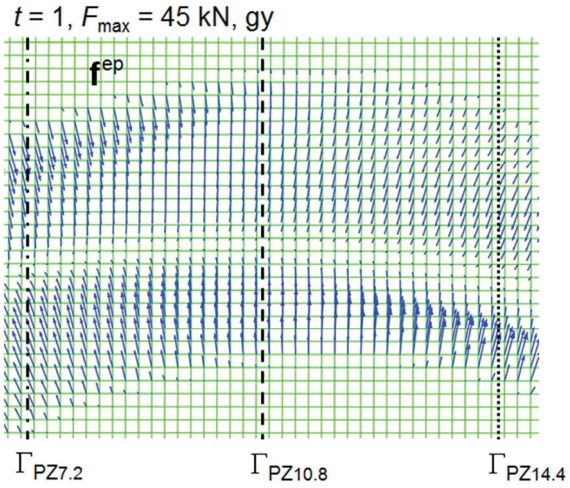

Fig. 9.3 Distribution of incremental plasticity bulk configurational forces for general yielding conditions in the plastically deformed region between the right boundaries of the three integration contours. Mesh size $m = 0.2$ mm.

Table 9.1 lists, for load ratio $R = 0$, the values $J^{ep}_{PZ7.2}$, $J^{ep}_{PZ10.8}$ and $J^{ep}_{PZ14.4}$ at maximum and minimum load of the 2nd and 4th load cycle, i.e. for gy- and sly-conditions, respectively. It is seen that $J^{ep}_{PZ,max}$ at maximum load remains almost constant for changes of Γ_{PZ}; the maximal relative difference is about 1% for gy, and it even decreases if the load is increased. The reason is that the x-components of $\mathbf{f}^{ep}$-vectors in the plastically deformed region between $\Gamma_{PZ7.2}$ and $\Gamma_{PZ14.4}$ almost cancel each other out when they are summed up along a vertical line, see Fig. 9.3. On the contrary, $J^{ep}_{PZ,min}$ at minimum load $F_{min} = 0$ exhibits stronger relative variations of about 17% and 35% for gy and sly; however, the *absolute* differences remain smaller than 0.9 kJ/m².

For load ratios $R = 0.5$ and $R = -1$, the influence for variations of Γ_{PZ} on the J^{ep}_{PZ}-values is basically the same. For $R = 0.5$, the relative variation of $J^{ep}_{PZ,min}$ is weaker due to the higher minimum load, $F_{min} > 0$. For $R = -1$, $J^{ep}_{PZ,min}$ becomes even negative.

Table 9.1 collects also results for the conventional J-integrals $J^{conv}_{PZ10.8}$ and J^{conv}_{far}. For $R = 0$ and $R = 0.5$, the value of $J^{conv}_{PZ,max}$ remains constant for gy- and sly-conditions, $J^{conv}_{PZ,max} = J^{conv}_{far,max}$. This does not apply at minimum load, since the conditions of proportional loading are violated during unloading; see also Section 6.4.2 for details. For $N = 2$, $J^{conv}_{PZ,min}$ varies by about 20% for gy; the deviation decreases to 5% for sly. Note that J^{conv}_{PZ} varies for $R = -1$ even at maximum load; the reason is currently not fully understood.

Table 9.1 shows that J^{conv}_{PZ} exhibits in general higher values than J^{ep}_{PZ}. For gy-conditions, $N = 2$, the relative difference between $J^{ep}_{PZ,max}$ and $J^{conv}_{PZ,max} = J^{conv}_{far,max}$ is only about 2% at maximum load, but it increases for sly-conditions, $N = 4$, up to approximately 20%. The values of $J^{conv}_{PZ,min}$ and, especially, $J^{conv}_{far,min}$ lie distinctively higher than $J^{ep}_{PZ,min}$ at minimum load. This has important consequences for the corresponding conventional cyclic J-integrals, see below.

Table 9.1 Values of the incremental plasticity and deformation plasticity *J*-integrals around the crack tip plastic zone, J_{PZ}^{ep} and J_{PZ}^{conv}, for general yielding (gy) and severe ligament yielding (sly) conditions. The conventional far-field *J*-integral J_{far}^{conv} is also included for comparison.

	R	$J_{PZ7.2,max}^{ep}$	$J_{PZ7.2,min}^{ep}$	$J_{PZ10.8,max}^{ep}$	$J_{PZ10.8,min}^{ep}$	$J_{PZ14.4,max}^{ep}$	$J_{PZ14.4,min}^{ep}$	$J_{PZ10.8,max}^{conv}$	$J_{PZ10.8,min}^{conv}$	$J_{far,max}^{conv}$	$J_{far,min}^{conv}$
	-	[kJ/m²]						[kJ/m²]			
gy	0	38.03	0.515	38.22	0.578	38.43	0.608	39.09	1.570	39.10	10.59
sly	0	82.88	2.502	82.81	3.356	82.65	2.954	99.47	18.96	99.44	47.26
gy	0.5	38.03	12.51	38.22	12.64	38.43	12.77	39.10	13.56	39.12	17.98
sly	0.5	83.95	34.92	83.91	35.45	83.73	35.19	101.1	51.97	101.0	66.21
gy	–1	37.83	–0.187	38.01	–0.171	38.22	–0.183	40.64	0.954	44.65	13.43
sly	–1	75.34	–5.226	75.21	–5.150	75.24	–5.688	96.38	11.62	145.1	74.41

Table 9.2 Values of the incremental plasticity, deformation plasticity and experimental cyclic *J*-integrals, ΔJ_{PZ}^{ep}, ΔJ_{PZ}^{conv} and ΔJ^{exp} for gy- and sly-conditions.

	R	ΔJ_{PZ}^{ep}	ΔJ_{PZ}^{conv}	ΔJ^{exp}	Δ_{conv}^{ep}	Δ_{exp}^{ep}	Δ_{exp}^{conv}
	-	[kJ/m²]			[%]		
gy	0	29.69	24.99	27.89	15.83	6.081	–11.60
sly	0	56.58	31.58	34.68	44.20	38.71	–9.834
gy	0.5	6.926	6.608	6.769	4.460	2.116	–2.451
sly	0.5	10.58	8.099	8.401	23.47	20.62	–3.720
gy	–1	37.83	29.14	37.71	22.97	0.317	–29.41
sly	–1	75.34	41.07	84.75	45.49	–12.49	–106.4

Now, we want to compare the cyclic *J*-integrals, ΔJ_{PZ}^{ep} and ΔJ_{PZ}^{conv}, with the experimental cyclic *J*-integral ΔJ^{exp} and check if they increase during re-loading proportional to the cyclic crack tip opening displacement $\Delta\delta_t$ for different load ratios *R*.

Table 9.2 lists the cyclic *J*-integral values for load ratios $R = 0$, 0.5 and –1, and load cycles $N = 2$ (gy) and $N = 4$ (sly). Hereby, ΔJ_{PZ}^{ep} and ΔJ_{PZ}^{conv} are evaluated after Eq. (6.19) and Eq. (6.22), using the $J_{PZ7.2}$-values in Table 9.1. For $R = -1$, $J_{PZ,min}^{ep}$ (Table 9.1) is set to zero according to the results of Section 6.4.4. The quantity ΔJ^{exp} is computed according to the corrected procedure in Sect. 6.5.3. The last three columns in Table 9.2 show the relative differences between all cyclic *J*-integrals.

It is seen that ΔJ^{exp} gives rather good approximations of ΔJ_{PZ}^{ep} for gy, taking a 2% underestimation due to the geometry factor η into account, see Section 6.5.3. The difference becomes large for sly-conditions. The conventional cyclic *J*-integral ΔJ_{PZ}^{conv} and ΔJ^{exp} differ especially for low load ratios. The reason is probably connected to the fact that $J_{PZ}^{conv} \neq J^{exp}$ at the minimum load. It can be shown that $J_{PZ}^{conv} = J_{far}^{conv} \cong J^{exp}$ at F_{max} is still valid for $R = 0$ and 0.5 under sly-conditions; the misfit between J_{far}^{conv} and J^{exp} is less than 3%. This is, however, not the case for $R = -1$, see Table 9.1. The difference between ΔJ_{PZ}^{ep} and ΔJ_{PZ}^{conv} is always significant, except for $R = 0.5$ and gy. The reason is mainly attributed to the higher $J_{PZ,min}^{conv}$-values, which give higher square-root terms in Eq. (6.22).

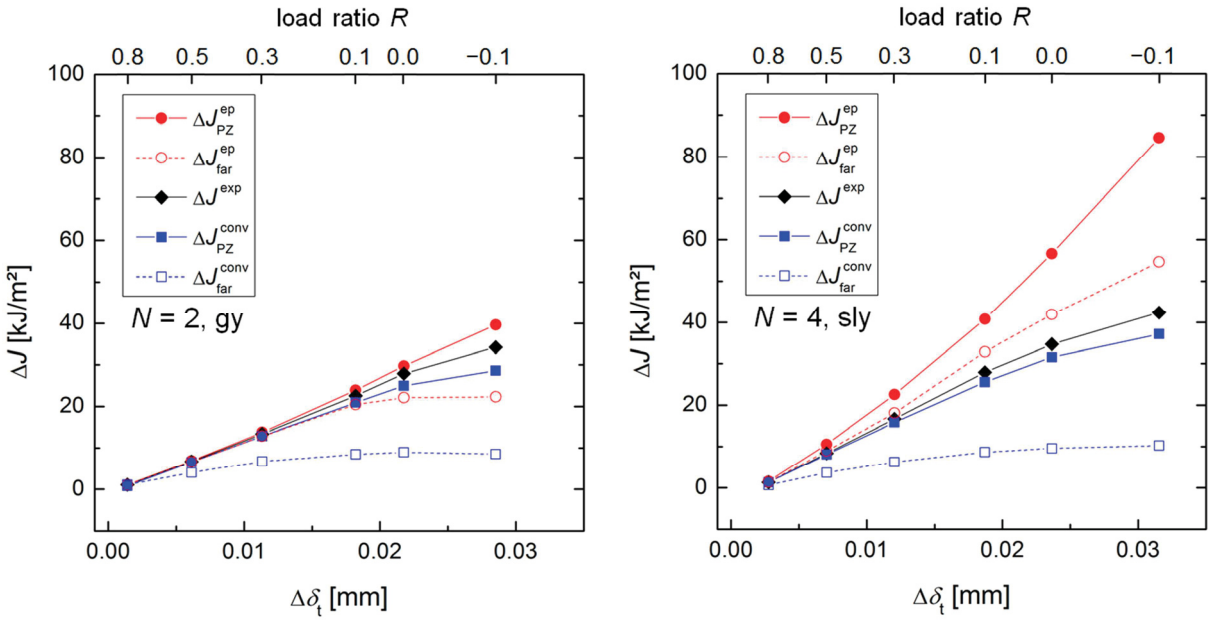

Fig. 9.4 Cyclic J-integrals ΔJ_{PZ}^{ep}, ΔJ_{PZ}^{conv} and ΔJ^{exp} plotted against the cyclic crack tip opening displacement $\Delta\delta_t$: **(a)** at $F_{max,gy} = 45$ kN ($N = 2$), onset of general yielding, and **(b)** at $F_{max,sly} = 50$ kN ($N = 4$), severe ligament yielding. The far-field cyclic J-integrals, ΔJ_{far}^{ep} and ΔJ_{far}^{conv}, are also included. Additional results for different load ratios R confirm the proportionality between ΔJ_{PZ}^{ep} and $\Delta\delta_t$.

Figure 9.4 presents, similar to Fig. 6.11b, the increase of the cyclic J-integral values (Table 9.2) with increasing cyclic crack tip opening displacement $\Delta\delta_t$. For generating Fig. 9.3, additional simulations are performed with load ratios between $R = -1$ and 0.8. Thereby, it was confirmed that J_{PZ}^{ep} exhibits a minimum of zero for $R = -0.1$, see Section 6.5.3.

It is seen from Fig. 9.4a,b that the magnitude of ΔJ_{PZ}^{ep} increases, for gy, exactly linear and, for sly, almost linear with increasing $\Delta\delta_t$. The experimental cyclic J-integral ΔJ^{exp} deviates from this line with decreasing load ratio R. The parameter ΔJ_{PZ}^{conv} deviates even stronger. The increasing misfit between ΔJ_{PZ}^{conv} and ΔJ_{PZ}^{ep} for decreasing R is mainly connected to the higher minimum $J_{PZ,min}^{conv}$-values due to the stronger non-proportional loading, see Table 9.1 and Eq. (6.22). This effect does not appear for large-scale yielding conditions, Fig. 6.11b, where an "elastic corridor" does exist between the crack tip- and back face plastic zone, hence, $J_{PZ,min}^{conv}$ equals $J_{PZ,min}^{ep}$.

It should be mentioned that the variation of the path Γ_{PZ} would give a maximal change by about 5% of ΔJ_{PZ}^{ep} and ΔJ_{PZ}^{conv}, but this does not change the trend depicted in Fig. 9.4.

It is seen that ΔJ_{far}^{ep} and ΔJ_{far}^{conv} strongly deviate from the corresponding ΔJ_{PZ}-values: ΔJ_{far}^{ep} exhibits lower values than ΔJ_{PZ}^{ep} due to the anti-shielding effect of the back face plastic zone (Sect. 6.4). For example, for $R = 0$ and $N = 2$, 4, $J_{far,max}^{ep}$ lies about 24% and 36% below the value of $J_{PZ,max}^{ep}$; compare also Sect. 5.1. The values of ΔJ_{far}^{conv} lie even lower than ΔJ_{far}^{ep},

which is caused by higher J-values at minimum load, see Table 9.1 and Eq. (6.28). This confirms that the far-field cyclic J-integrals are *not* appropriate for characterizing the crack driving force of cyclically loaded, stationary cracks.

It can be concluded that $\Delta J_{\mathrm{PZ}}^{\mathrm{ep}}$ seems to have, for *stationary* fatigue cracks, a useful physical meaning as a crack driving force term also beyond the onset of general yielding although it can be determined only in an approximative way. Changes of Γ_{PZ}, like in Fig. 9.1a, almost do not influence the magnitude of $\Delta J_{\mathrm{PZ}}^{\mathrm{ep}}$. Important is only that Γ_{PZ} does not intersect the back face plasticity region. The condition Eq. (6.23) still seems to hold approximately at onset of general yielding conditions and positive load ratios. However, the conventional and experimental cyclic J-integral, $\Delta J_{\mathrm{PZ}}^{\mathrm{conv}}$ and ΔJ^{exp}, give inaccurate estimations of the fatigue crack driving force in the presence of severe ligament yielding conditions.

For a *growing* crack under cyclic loading, Paper II shows that the incremental plasticity cyclic J-integral $\Delta J_{\mathrm{actPZ}}^{\mathrm{ep}}$, which is computed for a contour Γ_{actPZ} around the *active* plastic zone of the growing crack, Eq. (7.15), is the correct driving force parameter. The contour Γ_{actPZ} can be easily determined for ssy- or lsy-conditions as described in Sect. 7.3. The problem of extracting the correct value of $\Delta J_{\mathrm{actPZ}}^{\mathrm{ep}}$ under gy-conditions is even more difficult than for a stationary crack, since the active plastic zone approaches the back face plasticity region. This requires similar studies as presented in this section.

It can be expected that the determination of $\Delta J_{\mathrm{actPZ}}^{\mathrm{ep}}$ in an approximative way works at onset of gy-conditions. In this case, the part of the active plastic zone that travels with crack extension must be included in the contour Γ_{actPZ}; the back-face plasticity region shall be not included since it does not move. This has been done for the calculation of the $\Delta J_{\mathrm{actPZ}}^{\mathrm{ep}}$-values listed in Paper II in Table 7.2 under $N = 24$, $\Delta a = 4.6$ mm. Here the right boundary of Γ_{actPZ} is chosen to be located where $\mathbf{f}^{\mathrm{ep}}$-vectors emerge with x-components of almost zero (like $\Gamma_{\mathrm{PZ10.8}}$ in Fig. 9.3). The last data point in Fig. 7.8b suggests a steep increase of $\Delta J_{\mathrm{actPZ}}^{\mathrm{ep}}$, in accordance with an increase in the cyclic crack tip opening displacement $\Delta\delta_{\mathrm{t}}$.

Note that the growth of *long* fatigue cracks under gy-conditions are in practice not really meaningful since final failure can happen very soon. Instead, the gowth of *short* fatigue cracks under gy-conditions is of greater practical importance.

9.2 On the characterization of short fatigue cracks in elastic–plastic materials

Short fatigue cracks are of great practical importance since every fatigue crack is initially short. In most cases short cracks cannot be treated with ΔK, since the crack tip plastic zone becomes easily comparable to the crack length so that LEFM is not valid any more; see Section 3.1 and, e.g., Suresh (1998). Dowling (1977) proposed a special type of experimental cyclic J-integral for short fatigue cracks,

$$\Delta J_{\mathrm{sc}}^{\mathrm{exp}} = 3.2\,\Delta\phi_{\mathrm{e}}\,a + 5.0\,\Delta\phi_{\mathrm{p}}\,a\,. \tag{9.1}$$

The parameter ΔJ_{sc}^{exp} shall measure the fatigue driving force of small *semi-circular* cracks in initially smooth low-cycle fatigue specimens, i.e. a tensile test where a crack is initiated on the specimen surface during cyclic loading. In Eq. (9.1), a denotes the crack length, $\Delta\phi_e$ and $\Delta\phi_p$ are the elastic and plastic components of the cyclic strain energy density. The magnitude of $\Delta\phi_e$ and $\Delta\phi_p$ are determined from the stress–strain ($\sigma-\varepsilon$) curve of a LCF-test, analogously to the determination of ΔA from the F–v-record, Fig. 3.3b, for ΔJ^{exp}, Eq. (3.4); see e.g. Suresh (1998) for details. The pre-factors in Eq. (9.1) originate from the derivation of ΔJ_{sc}^{exp} for a semi-circular crack, see Dowling (1977). It should be noted that Eq. (9.1) is, nevertheless, commonly applied for short fatigue cracks (also with other crack geometries).

The parameter ΔJ_{sc}^{exp} and modifications for other crack geometries have been successfully applied for correlating the growth rate of short fatigue cracks (e.g. Dowling 1977, McClung et al. 1997, Döring et al. 2006, Pippan and Grosinger 2013). However, doubts about the validity of this parameter have been raised, since it is based, like the experimental cyclic J-integral ΔJ^{exp} for long cracks in Eq. (3.4), on the classical J-integral (Suresh 1998).

It can be expected that the incremental plasticity J-integral J^{ep}, in combination with a configurational force analysis, is able to provide us with new insights about the validity of the experimental cyclic J-integral ΔJ_{sc}^{exp}.

We have already started with numerical tests for short surface and interior cracks, using Single Edge Notched Tension (SENT) and Center Cracked Tension (CCT) specimens (see e.g. Anderson 1995). Note that Compact Tension (CT) specimens are not appropriate, and are commonly not used for experimental tests on short fatigue cracks. The methodological approach is the same as for long fatigue cracks (Sections 6.3, 7.3): First, *stationary* cracks, then *growing* cracks are treated under various prescribed maximum loads, so that ssy-, lsy-, and gy- conditions prevail, and different load ratios. It shall be also checked for which magnitude of the crack tip plastic zone ΔK is not applicable any more.

The intention of these future investigations is (i) to demonstrate that the parameter ΔJ_{actPZ}^{ep} works also for the characterization of the growth rate of short fatigue cracks, and (ii) to clarify whether the experimental cyclic J-integral ΔJ_{sc}^{exp} can be used to measure the driving force for short fatigue cracks.

9.3 Proposal for the experimental estimation of the driving force for fatigue crack growth

The maybe most important question that arises from Paper II in the context of long fatigue cracks would be: How can we measure the magnitude of the correct fatigue crack driving force ΔJ_{actPZ}^{ep} in experiments? The problem is that the experimental cyclic J-integral ΔJ^{exp}, proposed by Dowling and Begley (1976), measures the incremental plasticity cyclic J-integral ΔJ_{PZ}^{ep}, which is computed for a contour Γ_{PZ} encompassing the *entire* crack tip plastic zone, Fig. 7.1b, but *not* the *active* plastic zone, $\Delta J^{exp} = \Delta J_{PZ}^{ep} \neq \Delta J_{actPZ}^{ep}$. The difference between $\Delta J^{exp} = \Delta J_{PZ}^{ep}$ and ΔJ_{actPZ}^{ep} can be seen in Tables 7.1 and 7.2 and Fig. 7.8.

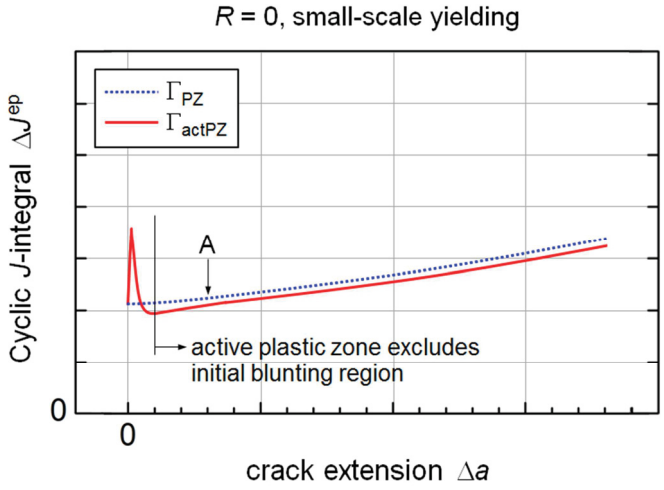

Fig. 9.5 Schematic variations of incremental plasticity cyclic *J*-integrals for a contour around the entire plastic zone, ΔJ^{ep}_{PZ}, and the active plastic zone, ΔJ^{ep}_{actPZ}, against crack extension Δa during cyclic loading; load ratio $R = 0$ and ssy-conditions are assumed. The peak in ΔJ^{ep}_{actPZ} is induced by crack tip blunting of the initial crack tip after monotonic loading in the first load cycle.

A possible solution for this problem could be the introduction of a correction factor in the ΔJ^{exp}-procedure, so that the new, improved experimental procedure enables the estimation of the correct fatigue crack driving force ΔJ^{ep}_{actPZ}. This requires further investigations in addition to Paper II. An idea how to determine the difference between ΔJ^{exp} and ΔJ^{ep}_{actPZ} shall be presented in the following.

Due to the validity of Eq. (7.10), it is reasonable that a correction factor for ΔJ^{exp} can be developed by investigating the relative difference between ΔJ^{ep}_{actPZ} and ΔJ^{ep}_{PZ} during fatigue crack propagation. Figure 9.5 shows schematically the characteristic evolution of ΔJ^{ep}_{actPZ} and ΔJ^{ep}_{PZ} with increasing crack extension during cyclic loading. Hereby, it is assumed that the crack grows under constant fatigue load with load ratio $R = 0$ and small-scale yielding conditions; compare Figs. 7.4a, 7.6 and 7.8. Figure 9.6 presents, similar to Fig. 5.6, schematically the directions and magnitudes of the configurational forces $\mathbf{f}^{ep}$ at maximum load after a crack extension Δa up to point A (Fig. 9.5). Note that Fig. 9.6 is similar to Fig. 5.6 for crack extension under monotonic loading; differences occur only due to the different boundary conditions.

Analogously to the case for crack extension under monotonic loading, Section 5.2.1, it becomes clear from Fig. 9.6 that the difference between ΔJ^{ep}_{actPZ} and ΔJ^{ep}_{PZ}, Fig. 9.5, is related to the net contribution of the configurational forces on the left boundary of the initial crack tip plastic zone and in the initial blunting region.

The difference between ΔJ^{ep}_{actPZ} and $\Delta J^{exp} = \Delta J^{ep}_{PZ}$ is *small* and *constant* for longer crack extensions under ssy-conditions; see also Fig. 7.8a. This is not the case for fatigue crack propagation under lsy- or gy-conditions (Fig. 7.8b). The reason is that the right boundary of

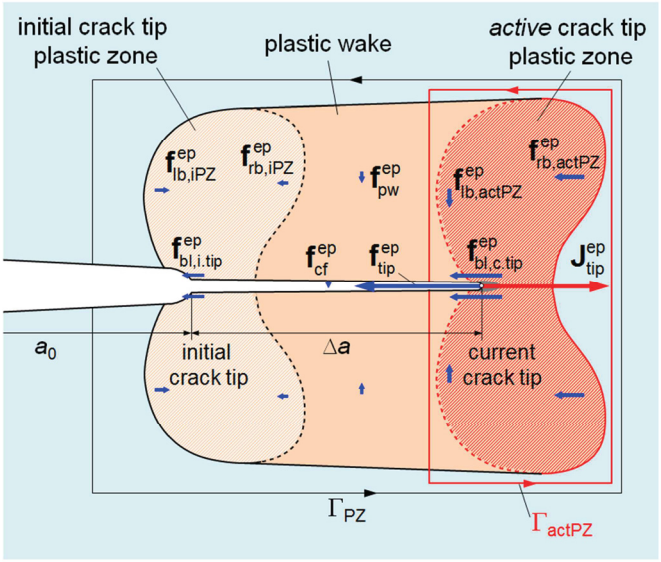

Fig. 9.6 Schematic distribution of incremental plasticity bulk configurational forces $\mathbf{f}^{ep}$ in the entire crack tip plastic zone after crack extension Δa (up to point A, Fig. 9.5) under constant fatigue load. The integration contour Γ_{PZ} surrounds the initial crack tip plastic zone, the plastic wake and the active plastic zone of the moving crack tip. Γ_{actPZ} surrounds the active crack tip plastic zone. On the contrary to monotonic loading, $\mathbf{f}^{ep}$-vectors located in the initial crack tip plastic zone decrease significantly after some load cycles with crack extension.

the active plastic zone, with configurational force vectors $\mathbf{f}^{ep}_{rb,actPZ}$ in negative x-direction, increases with increasing crack extension; see Sect. 7.4.2. Therefore, ΔJ^{ep}_{actPZ} increases stronger than ΔJ^{ep}_{PZ} and ΔJ^{exp} as seen in Fig. 7.8b. This implies that the experimental cyclic J-integral ΔJ^{exp} can lead to strong underestimations of the fatigue crack driving force ΔJ^{ep}_{actPZ} for lsy-conditions and, especially, for gy-conditions, which can be *dangerous* since the crack grows in reality faster as predicted via ΔJ^{exp}.

For future work, numerical case studies are planned on how the initial crack tip blunting region influences the difference between ΔJ^{ep}_{actPZ} and ΔJ^{exp} under ssy-conditions, and how this difference can be estimated even for more complicated cases, such as fatigue crack growth under lsy- or gy-conditions.

9.4 Does the effective stress intensity range ΔK_{eff} exactly characterize the fatigue crack driving force in the regime of LEFM?

Paper III shows that the incremental plasticity cyclic J-integral ΔJ^{ep}_{actPZ} is able to accurately reflect the overload effect, and that it is possible, in combination with an configurational force analysis, to understand the most dominant mechanisms for the delayed crack growth retardation phenomenon. It can be expected that the procedure outlined in Paper III provides us also with new insights into the most dominant mechanism for other types of load history effects on the fatigue crack growth rate; see Skorupa (1998) for some examples.

Somewhat surprisingly, we encountered a problem in the application of the effective stress intensity range ΔK_{eff}, which seems to have not been reported in the literature: In Paper III it is seen that ΔK_{eff} can significantly underestimate the driving force for fatigue crack growth for longer crack extensions following an overload (Fig. 8.8c). However, ΔK_{eff} can give erroneous results in the regime of LEFM even for *constant* fatigue loads. This problem shall be briefly addressed in the following.

Numerous simulations and experiments on plasticity-induced crack closure show that crack tip opening occurs at around 20% of $F_{\max}$ for plane strain and steady state crack growth under constant load amplitude (e.g. Fleck 1986, Sehitoglu and Sun 1991, McClung 1991, Bichler and Pippan 2007). This is also confirmed by the numerical case studies in Paper II and Paper III (for sufficiently large crack extensions after the overload). However, the (global) crack opening load F_{op}, i.e. determined via compliance change method, lies with approximately 2% of $F_{\max}$ significant below the (local) crack tip opening load $F_{\delta_t=0}$, i.e. where the crack tip opening displacement δ_t becomes non-zero during re-loading (Fig. 8.4b). Note that Riddell et al. (1999) have already shown via near-tip displacement measurements that the crack tip can be still closed at F_{op}; the phenomenon is referred to as *local crack opening*. Nevertheless, Fig. 8.8c shows, for constant cyclic loading with R = 0, that $\Delta J_{\text{CL}}^{\Delta K_{\text{eff}}}$, Eq. (8.8), reflects very well the values of $\Delta J_{\text{actPZ}}^{\text{ep}}$. However, a substitution of $F_{\delta_t=0}$ for F_{op} in the evaluation of ΔK_{eff} (and $\Delta J_{\text{CL}}^{\Delta K_{\text{eff}}}$), would lead to a very strong underestimation of the $\Delta J_{\text{actPZ}}^{\text{ep}}$-magnitude of about 55%; this can be shown also for negative load ratios.

This demonstrates that a *global* parameter like the effective stress intensity range ΔK_{eff} does not fully reflect the *local* behavior of the crack tip during fatigue crack growth. This is confirmed by the overload case studies presented in Paper III and also by the following: For positive load ratios $R > 0$ crack flank contact does not occur, so that $\Delta K_{\text{eff}} = \Delta K = K_{\max} - K_{\min}$ since $K_{\text{op}} = K_{\min}$. For such cases, it can be shown that the parameter $\Delta J_{\text{CL}}^{\Delta K}$, evaluated after Eq. (8.8) from ΔK, reflects the magnitude of $\Delta J_{\text{PZ}}^{\text{ep}}$. This is reasonable, since $\Delta J_{\text{PZ}}^{\text{ep}}$ equals the experimental cyclic J-integral ΔJ^{exp} (see Paper II) and ΔJ^{exp} reflects the magnitude of $\Delta J^{\Delta K}$ (see e.g. Dowling and Begley 1976, Banks-Sills and Volpert 1991),

$$\Delta J_{\text{PZ}}^{\text{ep}} = \Delta J^{\text{exp}} = \Delta J^{\Delta K} \qquad \text{for} \qquad R > 0 \,. \tag{9.2}$$

Thus, it can be stated that the stress intensity range ΔK does not correspond to $\Delta J_{\text{actPZ}}^{\text{ep}}$, but to $\Delta J_{\text{PZ}}^{\text{ep}} = \Delta J^{\text{exp}}$. However, note that the results of Paper II show that the difference between $\Delta J_{\text{actPZ}}^{\text{ep}}$ and $\Delta J_{\text{PZ}}^{\text{ep}}$ is, in general, negligible for small-scale yielding conditions. One has to be only careful in the presence of crack flank contact, since the parameter ΔK_{eff} is very sensitive to the "correct" determinations of the crack opening load F_{op}. This applies especially in the case where an overload has been applied, see Section 8.6.

For future work, additional investigations are planned on the *exact* role of ΔK or ΔK_{eff} as a crack driving force parameter for fatigue crack growth. Probably, this will provide us also with a better understanding of the difference between $\Delta J_{\text{actPZ}}^{\text{ep}}$ and ΔJ^{exp} under ssy-conditions.

10 Summary

The aim of the current thesis was to develop a numerical procedure for the physically correct characterization of the driving force for cyclically loaded cracks that grow in elastic–plastic materials, in order to describe the crack growth rate during fatigue.

The concept of configurational forces was applied for this challenge. The reason is that the concept enables the derivation of the *J*-integral without restrictions about constitutive assumptions for a material. The *J*-integral for incremental theory of plasticity, J^{ep}, provides, in contrast to the conventional *J*-integral, a true driving force term when applied to elastic–plastic materials even under strongly non-proportional loading conditions. Therefore, J^{ep} should be applied for the assessment of the crack driving force for crack growth in elastic–plastic materials for monotonic loading. When characterizing the growth rate of fatigue cracks in elastic–plastic materials, a cyclic incremental plasticity *J*-integral ΔJ^{ep} should be used as crack driving force parameter. However, at the start of this thesis it was neither clear (i) which integration path should be considered, since J^{ep} is in general path dependent, nor (ii) how the cyclic *J*-integral ΔJ^{ep} should be calculated with J^{ep}_{max} and J^{ep}_{min} so that it describes the driving force for fatigue crack growth.

The properties of J^{ep} and the distribution of the configurational body forces have been worked out for long fatigue cracks in two-dimensional Compact Tension specimens under plane strain and cyclic Mode I loading conditions. Stationary and growing cracks have been considered; incremental crack extension after each load cycle has been modeled using the node release technique. The maximum load has been varied in order to obtain small-scale, large-scale and general yielding conditions. Different load ratios have been applied. The case of a single tensile overload was also carefully investigated.

The main conclusions of the thesis are:

- The incremental plasticity cyclic *J*-integral ΔJ^{ep}_{actPZ}, computed for an integration contour Γ_{actPZ} around the *active* plastic zone of the growing crack tip, is the physically correct driving force for the description of fatigue crack growth in elastic–plastic materials. The cyclic *J*-integral should be evaluated by the relation $\Delta J = J_{max} + J_{min} - 2\sqrt{J_{max} J_{min}}$; the quantities J_{max} and J_{min} denote the maximum and minimum J^{ep}_{actPZ}-values achieved in a single load cycle. The parameter ΔJ^{ep}_{actPZ} is able to reflect the variation of the cyclic crack tip opening displacement at the current crack tip, $\Delta\delta_t$, but with much less computational effort.
- The experimental cyclic *J*-integral ΔJ^{exp}, proposed by Dowling and Begley (1976), reflects the magnitude of the incremental plasticity cyclic *J*-integral ΔJ^{ep}_{PZ}, computed for a contour Γ_{PZ} enclosing the *entire* crack tip plastic zone. After crack extension, the contour Γ_{PZ} includes the initial crack tip plastic zone, the plastic wake and the active

plastic zone. Therefore, ΔJ^{exp} is exactly correct only for *stationary* fatigue cracks, since the entire and the active crack tip plastic zones coincide and $\Delta J_{\mathrm{PZ}}^{\mathrm{ep}} = \Delta J_{\mathrm{actPZ}}^{\mathrm{ep}}$. After crack extension, however, $\Delta J_{\mathrm{PZ}}^{\mathrm{ep}} \neq \Delta J_{\mathrm{actPZ}}^{\mathrm{ep}}$. Thus, ΔJ^{exp} is *not* fully appropriate to measure the driving force for *growing* fatigue cracks.

- Basically, this result rests on the finding that the conventional cyclic *J*-integral $\Delta J_{\mathrm{PZ}}^{\mathrm{conv}}$ reflects the magnitude of $\Delta J_{\mathrm{PZ}}^{\mathrm{ep}}$ if the contour Γ_{PZ} goes only through *elastically* deformed regions, since then deformation- and incremental plasticity yield identical results. For a growing fatigue crack, the contour around the active plastic zone Γ_{actPZ} crosses the plastic wake, therefore, $\Delta J_{\mathrm{actPZ}}^{\mathrm{conv}} \neq \Delta J_{\mathrm{actPZ}}^{\mathrm{ep}}$.
- The difference between $\Delta J_{\mathrm{actPZ}}^{\mathrm{ep}}$ and $\Delta J_{\mathrm{PZ}}^{\mathrm{ep}}$ is caused by the net-contribution of the bulk configurational forces that are located within the blunting region of the initial crack tip. This finding might be a clue for working out a new, improved experimental procedure, which enables the estimation of the fatigue crack driving force $\Delta J_{\mathrm{actPZ}}^{\mathrm{ep}}$.
- The application of the experimental cyclic *J*-integral ΔJ^{exp} for the characterization of *stationary* fatigue cracks in elastic–plastic materials works even at onset of general yielding, i.e. a complete path through plastically deformed material exists between crack tip and back face region. Beyond that, i.e. under severe ligament yielding conditions, only the new parameter $\Delta J_{\mathrm{actPZ}}^{\mathrm{ep}} = \Delta J_{\mathrm{PZ}}^{\mathrm{ep}}$ is appropriate.
- The parameter $\Delta J_{\mathrm{actPZ}}^{\mathrm{ep}}$ is also able to reflect very accurately the well-known *delayed* crack growth retardation effect after an overload. Moreover, in combination with an analysis of the configurational body forces in the plastic zone, insights can be obtained into the exact mechanisms that are responslibe for the overload effect. For our cases under plane strain assumptions, it has been shown that *residual stresses* around the propagating crack tip mainly cause the overload effect, whereas crack flank contact does not play such a crucial role. Analyses for pure tension cyclic loading show that the fatigue crack can even stop although crack flank contact did not exist. It should be stressed that the contribution of crack flank contact to the overload effect might be appreciably higher for a three-dimensional specimen, due to the lateral contraction at the side surface of the specimen.
- The experimental cyclic *J*-integral ΔJ^{exp} is not appropriate to characterize the crack growth rate after an overload. The reason becomes clear from the parameter $\Delta J_{\mathrm{PZ}}^{\mathrm{ep}}$: The contour Γ_{PZ} surrounds the entire crack tip plastic zone and goes only through elastically deformed regions where residual stresses *cannot* appear. Therefore, $\Delta J_{\mathrm{PZ}}^{\mathrm{ep}}$ and ΔJ^{exp} predict a constantly increasing crack growth rate, such as for a constant fatigue load.
- The current thesis also shows that problems can appear when using the effective stress intensity range ΔK_{eff} as fatigue crack driving force term for the regime of linear elastic fracture mechanics. The reason is related to the fact that a *global* parameter like ΔK_{eff} is, in contrast to $\Delta J_{\mathrm{actPZ}}^{\mathrm{ep}}$, not able to reflect fully the *local* behavior of the propagating crack tip, which is crucial for the fatigue crack growth rate. As a consequence, ΔK_{eff} can lead to significant underestimations of the driving force for

fatigue crack growth; this is seen especially for fatigue crack growth for longer crack extensions after an overload.

11 References

Anderson TL (1995) Fracture mechanics, 3rd ed. CRC Press, Boca Raton, FL

ASTM E1820-05 (2005) Standard test method for measurement of fracture toughness. In: Annual Book of ASTM Standards, vol 03.01. ASTM International, West Conshohocken, PA, USA

Atkins AG, Mai YW (1986) Residual strain energy in elastoplastic adhesive and cohesive fracture. Int J Fract 30:203–221

Banks-Sills L, Volpert Y (1991) Application of the cyclic *J*-integral to fatigue crack propagation of Al 2024-T351. Eng Fract Mech 40:355–370

Bathe KJ (2007) Finite element procedures. Prentice Hall

Bichler C, Pippan R (1999) Direct observation of the residual plastic deformation caused by a single overload. In: Advances in fatigue crack closure measurement and analysis, vol. 2, McClung RC and Newman JC Jr. (editors). West Conshohocken, PA: ASTM STP 1342:191–206.

Bichler C, Pippan R (2007) Effect of single overloads in ductile metals: A reconsideration. Eng Fract Mech 74:1344–1359

Blom AF (1989) Overload retardation during fatigue crack propagation in steels of different strengths. Scand J Metall 18:197–202

Bonet J, Wood RD (2008) Nonlinear continuum mechanics for finite element analysis, 2nd ed. Cambridge Univ Press, Cambridge, UK

Brocks W, Cornec A, Scheider I (2003) Computational aspects of nonlinear fracture mechanics. In: de Borst R, Mang HA (eds) Comprehensive structural integrity, numerical and computational methods, vol 3. Elsevier, New York, pp 127–209

Broek D (1982) Elementary engineering fracture mechanics. Kluwer Academic Publishers Group

Chadwick P (1999) Continuum mechanics. Concise theory and problems. Dover Publications, Inc, Mineola, New York

Chakrabarty J (2006) Theory of plasticity, 3rd ed. Elsevier Butterworth-Heinemann, Jordan Hill, Oxford

Christensen RH (1959) Metal fatigue. New-York: McGraw-Hill

Denzer R, Barth FJ, Steinmann P (2003) Studies in elastic fracture mechanics based on the material force method. Int J Num Meth Eng 58: 1817–1835

Döring R, Hoffmeyer J, Seeger T, Vormwald M (2006) Short fatigue crack growth under nonproportional multiaxial elastic–plastic strains. Int J Fatigue 28:972–982

Dougherty JD, Padovan J, Srivatsan TS (1997) Fatigue crack propagation and closure behavior of modified 1071 steel: finite element study. Eng Fract Mech 56:189–212

Dowling NE, Begley JA (1976) Fatigue crack growth during gross plasticity and the *J*-integral. ASTM STP 590:82–103

Dowling NE (1976) Geometry effects and the *J*-integral approach to elastic–plastic fatigue crack growth. ASTM STP 601:19–32

Dowling NE (1977) Crack growth during low-cycle fatigue of smooth axial specimens. ASTM STP 637:97–121

Drew M, Thompson KRL, Keys LH (1982) The effect of overloads on fatigue crack propagation in offshore structural steels. In: Gifkins RC, editor. Strength of Metals and Alloys (ICSMAG), vol. 2, Pergamon Press, 867–73

Eftis J, Liebowitz H (1975) On fracture toughness evaluation for semi-brittle fracture. Eng Fract Mech 7:101–135

Elber W (1970) Fatigue crack closure under cyclic tension. Eng Fract Mech 2:37–45

Elber W (1971) The significance of fatigue crack closure. ASTM STP 486:230–42

Eshelby JD (1951) The force on an elastic singularity. Philos Trans R Soc A 244:87–112

Eshelby JD (1970) Energy relations and the energy-momentum tensor in continuum mechanics. In: Kanninen M, Adler W, Rosenfield A, Jaffee R (eds) Inelastic behavior of solids. McGraw-Hill, New York, pp 77–115

ESIS P2-92 (1992) ESIS procedure for determining the fracture behavior of materials. European Structural Integrity Society, Delft, The Netherlands

Fischer FD, Predan J, Kolednik O, Simha NK (2007) Application of material forces to fracture of inhomogeneous materials: illustrative examples. Arch Appl Mech 77:95–112

Fischer FD, Simha NK, Predan J, Schöngrundner R, Kolednik O (2012a) On configurational forces at boundaries in fracture mechanics. Int J Fract 174:61–74

Fischer FD, Predan J, Fratzl P, Kolednik O (2012b) Semi-analytical approaches to assess the crack driving force in periodically heterogeneous elastic materials. Int J Fract 173:57–70

Fischer FD, Predan J, Müller R, Kolednik O (2014) On problems with the determination of the fracture resistance for materials with spatial variations of the Young's modulus. Int J Fract 190:23–38

Fleck NA (1986) Finite element analysis of plasticity-induced crack closure under plane strain conditions. Eng Fract Mech 25:441–449

Fleck NA (1988) Influence of stress state on crack growth retardation. In: Fong JT, Fields RJ, editors. Basic Questions in Fatigue, ASTM STP 924, vol. 1. ASTM:157–183

Forsyth PJE, Ryder DA (1960) Fatigue fracture. Aircraft Eng 32:96–99

Griffith AA (1920) The phenomena of rupture and flow in solids. Philos Trans R Soc A 221:163–198

Gross D, Seelig T (2007) Bruchmechanik. Springer, Berlin Heidelberg New York

Gurtin ME (1982) An introduction to continuum mechanics. Academic Press, New York

Gurtin ME (1995) The nature of configurational forces. Arch Rational Mech Anal 131:67–100

Gurtin ME, Podio-Guidugli P (1996) Configurational forces and the basic laws for crack propagation. J Mech Phys Solids 44:905–927

Gurtin ME (2000) Configurational forces as basic concepts of continuum physics. Springer, New York

Heerens J, Cornec A, Schwalbe K-H (1988) Results of a round robin on stretch zone width determination. Fatigue Fract Eng Mater Struct 11:19–29

Honein T, Herrmann G (1997) Conservation laws in nonhomogeneous plane elastostatics. J Mech Phys Solids 45:789–805

Hutchinson JW (1968) Singular behavior at the end of a tensile crack tip in a hardening material. J Mech Phys Solids 16:13–31

Hutchinson JW, Paris PC (1979) Stability analysis of *J*-controlled crack growth. ASTM STP 668:37–64

Irwin GR (1957) Analysis of stresses and strains near the end of a crack traversing a plate. ASME J Appl Mech 24:361–364

Kachanov LM (1971) Foundations of the theory of plasticity. North-Holland Publishing Company, Amsterdam

Kfouri AP, Miller KJ (1976) Crack separation energy rate for crack advance in finite growth steps. Proc Inst Mech Eng 190:571–584

Kfouri AP, Rice JR (1977) Elastic/plastic separation energy rate for crack advance in finite growth steps. In: Taplin DMR (ed) Fracture 1977, vol 1. University of Waterloo Press,Waterloo, pp 43–59

Kienzler R, Herrmann G (2000) Mechanics in material space. Springer, Berlin

Kikukawa M, Jono M, Tanaka K (1976) Fatigue crack closure behavior at low stress intensity level. In. Proceedings of the 2nd International Conference on Mechanical Behavior of Materials, ICM2. Boston: pp 254–277

Kolednik O (1981) A contribution to stereophotogrammetry with the scanning electron microscope. Pract Metall 18:562–573

Kolednik O, Stüwe HP (1985) The stereophotogrammetric determination of the critical crack tip opening displacement. Eng Fract Mech 21:145–155

Kolednik O, Stüwe HP (1987) A proposal for estimating the slope of the blunting line. Int J Fract 33:R63–R66

Kolednik O, Kutlesa P (1989) On the influence of specimen geometry on the critical crack-tip-opening displacement. Eng Fract Mech 33:215–223

Kolednik O (1991) On the physical meaning of the J–Δa-curves. Eng Fract Mech 38:403–412

Kolednik O (1993) A simple model to explain the geometry dependence of the J–a-curves. Int J Fract 63:263–274

Kolednik O, Turner CE (1994) Application of energy dissipation rate arguments to ductile instability. Fatigue Fract Eng Mater Struct 17:1129–1145

Kolednik O, Predan J, Gubeljak N, Fischer FD (2009) Modeling fatigue crack growth in a bimaterial specimen with the configurational forces concept. Mat Sci Eng A 519:172–183

Kolednik O, Predan J, Fischer FD (2010) Reprint of "Cracks in inhomogeneous materials: Comprehensive assessment using the configurational forces concept". Eng Fract Mech 77:3611–3624

Kolednik O (2012) Fracture mechanics. In: Nicolais L, Borzacchiello A, eds. Encyclopedia of composites, 2nd ed. John Wiley and Sons, Hoboken

Kolednik O, Schöngrundner R, Fischer FD (2014) A new view on *J*-integrals in elastic–plastic materials. Int J Fract 187:77–107

Kolednik O, Zechner J, Predan J (2015) Improvement of fatigue life by compliant and soft interlayers. Sripta Mater, submitted

Krupp U, Floer W, Lei J, Hu Y, Christ H, Schick HJ, Fritzen CP (2002) Mechanisms of short crack initiation and propagation in a beta-titanium alloy. Phil Mag A82:3321–3332

Kuna M (2008) Numerische Beanspruchungsanalyse von Rissen. FEM in der Bruchmechanik. Vieweg-Teubner Verlag, Wiesbaden

Laird C (1967) The influence of metallurgical structure on the mechanisms of fatigue crack propagation. ASTM STP 415:131–68

Laird C (1979) Mechanisms and theories of fatigue. ASM, Metals Park, OH, pp 149–203

Lamba HS (1975) The *J*-integral applied to cyclic loading. Eng Fract Mech 7:693–703

Lambert Y, Saillard P, Bathias C (1988) Application of the *J* concept to fatigue crack growth in large-scale yielding. ASTM STP 969:318–329

Ling MR, Schijve J (1992) The effect of intermediate heat treatments on overload induced retardations during fatigue crack growth in an Al alloy. Fatigue Fract Mat Struct 15:421–30

Maierhofer J, Gänser H-P, Pippan R (2014) Modified NASGRO equation for physically short cracks. Int J Fatigue 59:200–207

Maierhofer J, Gänser H-P, Pippan R (2015) Modified Kitagawa–Takahashi diagram accounting for finite notch depths. Int J Fatigue 70:503–509

Malvern LE (1969) Introduction to the mechanics of a continuous medium. Prentice-Hall, New Jersey

Marsden JE, Hughes TJR (1983) Mathematical foundations of elasticity. Dover Publications, Inc, Mineola, New York

Maugin GA, Trimarco C (1992) Pseudo-momentum and material forces in nonlinear elasticity: variational formulation and application to brittle fracture. Acta Mech 94:1–28

Maugin GA (1995) Material forces: concepts and applications. ASME J Appl Mech Rev 48:213–245

Maugin GA (2011) Configurational forces: thermomechanics, physics, mathematics and numerics. CRC Press, Boca Raton

McClung RC (1991) The influence of applied stress, crack length, and stress intensity factor on crack closure. Met Trans 22A:1559–71

McClung RC, Chell GG, Russell DA, Orient GE (1997) A practical methodology for elastic–plastic fatigue crack growth. ASTM STP 1296:317–337

McMeeking RM (1977) Path dependence of the *J*-integral and the role of *J* as a parameter characterizing the near tip field. ASTM STP 631:28–41

McMeeking RM, Parks DM (1979) On criteria for *J*-dominance of crack-tip fields in large-scale yielding. ASTM STP 668:175–194

Metzger M, Seifert T, Schweizer C. Does the cyclic *J*-integral describe the crack-tip opening displacement in the presence of crack closure? Eng Fract Mech 2015;134:459–473.

Müller R, Kolling S, Gross D (2002) On configurational forces in the context of the finite element method. Int J Numer Methods Eng 53:1557–1574

Müller R, Gross D, Maugin GA (2004) Use of material forces in adaptive finite element methods. Comput Mech 33:421–434

Newman JC (1976) A finite element analysis of fatigue crack closure. ASTM STP 590:281–301

Nguyen TD, Govindjee S, Klein PA, Gao H (2005) A material force method for inelastic fracture mechanics. J Mech Phys Solids 53:91–121

Ochensberger W, Kolednik O (2014) A new basis for the application of the *J*-integral for cyclically loaded cracks in elastic–plastic materials. Int J Fract189:77–101

Ochensberger W, Kolednik O (2015) Physically appropriate characterization of fatigue crack propagation rate in elastic–plastic materials using the *J*-integral concept. Int J Fract 192:25–45

Ohji K, Ogura K, Yoshiji O (1975) Cyclic analysis of a propagating crack and its correlation with fatigue crack growth. Eng Fract Mech 7: 457–464

Özenç K, Kaliske M, Lin G, Bhashyam G (2014) Evaluation of energy contributions in elasto–plastic fracture: A review of the configurational force approach. Eng Fract Mech 115:137–153

Paris PC, Gomez MP, Anderson WP (1961) A rational analytic theory of fatigue. The trend in Eng 13:9–14

Paris PC, Erdogan F (1963) A critical analysis of crack propagation laws. ASME J Basic Eng 85:528–34

Parks DM (1977) The virtual crack extension method for nonlinear material behavior. Comput Meth Appl Mech Eng 12:353–364

Pippan R, Bichler C, Tabernig B, Weinhandl H (2005) Overloads in ductile and brittle materials. Fatigue Fract Eng Mater Struct 28:971–981

Pippan R, Zelger C, Gach E, Bichler C, Weinhandl H (2010) On the mechanism of fatigue crack propagation in ductile metallic materials. Fatigue Fract Eng Mater Struct 34:1–16

Pippan R, Grosinger W (2013) Fatigue crack closure: From LCF to small scale yielding. Int J Fatigue 46:41–48

Rice JR (1967) Mechanics of crack tip deformation and extension by fatigue. ASTM STP 415:247–309

Rice JR (1968a) A path independent integral and the approximate analysis of strain concentration by notches and cracks. ASME J Appl Mech 35:379–386

Rice JR (1968b) Mathematical analysis in the mechanics of fracture. In: Liebowitz H (ed) Fracture – an advanced treatise, vol 2. Academic Press, New York, pp 191–311

Rice JR, Rosengren GF (1968) Plane strain deformation near a crack tip in a power-law hardening material. J Mech Phys Solids 16:1–12

Rice JR, Johnson MA (1970) The role of large crack tip geometry changes in plane strain fracture. In: Kanninen MF (ed) Inelastic behavior of solids. McGraw-Hill, New York, pp 641–672

Rice JR, Paris PC, Merkle JG (1973) Some further results of *J*-integral analysis and estimates. ASTM STP 536:231–245

Rice JR (1976) Elastic–plastic fracture mechanics. In: Erdogan F (ed), The Mechanics of Fracture, AMD, vol 19. ASME, New York, pp 23–53

Rice JR (1979) The mechanics of quasi-static crack growth. In: Kelly RE (ed) Proceedings of the eighth U.S. National congress of applied mechanics. ASME, New York, pp 191–216

Rice JR, Drugan WJ, Sham TL (1980) Elastic–plastic analysis of growing cracks. ASTM STP 700:189–221

Riddell WT, Piascik RS, Sutton MA, Zhao W, McNeill SR, Helm JD (1999) Determining fatigue crack opening loads from near-crack-tip displacement measurements. In: McClung RC, Newman JC (eds), Advances in fatigue crack closure measurement and analysis, 2nd vol, ASTM STP, West Conshohocken, PA, pp 157–174

Ritchie RO, Suresh S, Moss CM (1980) Near-threshold fatigue crack growth in 2¼ Cr– 1 Mo pressure vessel steel in air and hydrogen. J Eng Mat Tech 102:293–299

Roychowdhury S, Dodds RH Jr (2005) Effects of an overload event on crack closure in 3-D small-scale yielding: finite element studies. Fatigue Fract Eng Mater Struct 28:891–907

Sadananda K, Vasudevan AK, Holtz RL, Lee EU (1999) Analysis of overload effects and related phenomena. Int J Fatigue 21:S233–S46

Schijve J (1960) Fatigue crack propagation in light alloy sheet material and structures. NRL Report 195 MP National Aeronautical Research Institute, Amsterdam, Holland

Schijve J (1962) Fatigue crack propagation in light alloy sheet material and structures. In: Advances in Aeronautical Sciences, vol. 3, Pergamon Press, 387–408

Schijve J (2009) Fatigue of structures and materials, 2nd ed. Springer, Netherlands

Schöngrundner R (2011) Numerische Studien zur Ermittlung der risstreibenden Kraft in elastisch–plastischen Materialien bei unterschiedlichen Belastungsbedingungen. Fortschritt-Berichte VDI, Reihe 18 Mechanik/Bruchmechanik, Nr. 329. VDI-Verlag, Düsseldorf

Schweizer C, Seifert T, Riedel H (2010) Simulation of fatigue crack growth under large-scale yielding conditions. J Phys Conf Ser 240(1):012043

Shan GX (2005) Post-processing program for calculating the configurational force with ABAQUS. Internal Report Institute of Mechanics, 1–10

Sehitoglu H, Sun W (1991) Modeling of plane strain fatigue crack closure. ASME J Eng Mater Technol 113:31–40

Siegmund T, Kolednik O, Pippan R (1990) Direkte Messung der Rissspitzenverformung bei wechselnder Belastung. Z Metallkde, Bd. 81 H.9, 677−683

Simha NK, Fischer FD, Kolednik O, Chen CR (2003) Inhomogeneity effects on the crack driving force in elastic and elastic–plastic materials. J Mech Phys Solids 51:209–240

Simha NK, Fischer FD, Kolednik O, Predan J, Shan GX (2005) Crack tip shielding due to smooth and discontinuous material inhomogeneities. Int J Fract 135:73–93

Simha NK, Fischer FD, Shan GX, Chen CR, Kolednik O (2008) *J*-integral and crack driving force in elastic–plastic materials. J Mech Phys Solids 56:2876–2895

Sistaninia M, Kolednik O (2014) Effect of a single soft interlayer on the crack driving force. Eng Fract Mech 130:21–41

Skorupa M (1998) Load interaction effects during fatigue crack growth under variable amplitude loading – A literature review. Part I: Empirical trends. Fatigue Fract Eng Mater Struct 21:987–1006

Solanki K, Daniewicz SR, Newman JC Jr (2003) Finite element modeling of plasticity-induced crack closure with emphasis on geometry and mesh refinement effects. Eng Fract Mech 70:1475–1489

Solanki K, Daniewicz SR, Newman JC Jr (2004) Finite element analysis of plasticity-induced fatigue crack closure: an overview. Eng Fract Mech 71:149–71

Stampfl J, Scherer S, Berchthaler M, Gruber M, Kolednik O (1996a) Determination of the fracture toughness by automatic image processing. Int J Fract 78:35−44

Stampfl J, Scherer S, Gruber M, Kolednik O (1996b) Reconstruction of surface topographies by scanning electron microscopy for application in fracture research. Appl Phys A 63:341−346

Suresh S, Ritchie RO (1982) A geometric model for fatigue crack closure induced by fracture surface morphology. Metall Trans 13A:1627–1631

Suresh S (1983) Micromechanisms of fatigue crack growth retardation following overloads. Eng Fract Mech 18:577–593.

Suresh S, Ritchie RO (1984) Near-threshold fatigue crack propagation: a perspective on the role of crack closure. In: Davidson DL, Suresh S, edotors. Fatigue Crack Growth Threshold Concepts, pp 227–261. Warrendale: The Metallurgical Society of the American Institute of Mining, Mineral and Petroleum Engineers

Suresh S (1998) Fatigue of materials, 2nd ed. Cambridge University Press, Cambridge, UK

Tanaka K (1983) The cyclic *J*-integral as a criterion for fatigue crack growth. Int J Fract 22:91–104

Tanaka K (1989) Mechanics and micromechanics of fatigue crack propagation. ASTM STP 1020:151–183

Truesdell C, Noll W (1965) The nonlinear field theories of mechanics, in: S. Flügge, ed, Encyclopedia of physics, vol III/3, Springer, Berlin

Turner CE, Kolednik O (1994) Application of energy dissipation rate arguments to stable crack growth. Fatigue Fract Eng Mater Struct 17:1089–1107

Tvergaard V (2005) Overload effects in fatigue crack growth by crack-tip blunting. Int J Fatigue 27:1389–1397

von Euw EFJ, Hertzberg RW, Roberts R (1972) Delay effects in fatigue crack propagation. In: Stress Analysis and Growth of Cracks, ASTM STP 513, part I. Philadelphia ASTM:230–59

Vormwald M (2014) Fatigue crack propagation under large cyclic plastic strain conditions. In: Procedia Materials Science 3, 20th European Conference on Fracture, ECF20, 301–306

Vormwald M (2015) Effect of cyclic plastic strain on fatigue crack growth. Int J Fatigue, In Press

Ward-Close CM, Ritchie RO (1988) On the role of crack closure mechanisms in influencing fatigue crack growth following tensile overloads in a titanium alloy: near threshold versus higher ΔK behavior. In: Newman JC Jr, Elber W, editors. Mechanics of Fatigue Crack Closure, ASTM STP 982. ASTM, 93–111

Ward-Close CM, Blom AF, Ritchie RO (1989) Mechanisms associated with transient fatigue growth under variable-amplitude loading: an experimental and numerical study. Eng Fract Mech 32:613–638

Wells AA (1963) Application of fracture mechanics at and beyond general yielding. Brit Welding J 10:563–570

Wüthrich C (1982) The extension of the *J*-integral concept to fatigue cracks. Int J Fract 20:R35–R37

Zappfe CA, Worden CO (1951) Fractographic registrations of fatigue. Transactions of the American Society of Metals 43:958–969

Zienkiewicz OC, Taylor RL (2005) The finite element method. Its basics and fundamentals, vol 1. Butterworth-Heinemann, 6th ed